

The background of the cover features a complex, three-dimensional molecular structure. It consists of numerous interconnected spheres (atoms) and thin rods (bonds). The spheres are rendered in shades of light blue, teal, and orange, while the rods are a dark, muted blue. The overall effect is a dense, geometric network that suggests the atomic-scale nature of nanomechanics.

IntechOpen

Nanomechanics

Edited by Alexander Vakhrushev



NANOMECHANICS

Edited by **Alexander Vakhrushev**

Nanomechanics

<http://dx.doi.org/10.5772/65466>

Edited by Alexander Vakhrushev

Contributors

Natalia Vladimirovna Kamanina, Şeref Doğuşcan Akbaş, Xiaohua Zhang, Manuel Cortez Valadez, R. Britto Hurtado, Mario Flores Acosta, Gerardo Calderon Ayala, L. P. Ramírez-Rodríguez, Pustan Marius, Cristian Dudesco, Corina Birleanu, Florina Rusu, Paolo Bergese, Stefania Federici, Vladimir Skripnyak, Evgeniya G. Skripnyak, Yuan Dong, Zeng-Yuan Guo, Bing-Yang Cao

© The Editor(s) and the Author(s) 2017

The moral rights of the and the author(s) have been asserted.

All rights to the book as a whole are reserved by INTECH. The book as a whole (compilation) cannot be reproduced, distributed or used for commercial or non-commercial purposes without INTECH's written permission.

Enquiries concerning the use of the book should be directed to INTECH rights and permissions department (permissions@intechopen.com).

Violations are liable to prosecution under the governing Copyright Law.



Individual chapters of this publication are distributed under the terms of the Creative Commons Attribution 3.0 Unported License which permits commercial use, distribution and reproduction of the individual chapters, provided the original author(s) and source publication are appropriately acknowledged. If so indicated, certain images may not be included under the Creative Commons license. In such cases users will need to obtain permission from the license holder to reproduce the material. More details and guidelines concerning content reuse and adaptation can be found at <http://www.intechopen.com/copyright-policy.html>.

Notice

Statements and opinions expressed in the chapters are these of the individual contributors and not necessarily those of the editors or publisher. No responsibility is accepted for the accuracy of information contained in the published chapters. The publisher assumes no responsibility for any damage or injury to persons or property arising out of the use of any materials, instructions, methods or ideas contained in the book.

First published in Croatia, 2017 by INTECH d.o.o.

eBook (PDF) Published by IN TECH d.o.o.

Place and year of publication of eBook (PDF): Rijeka, 2019.

IntechOpen is the global imprint of IN TECH d.o.o.

Printed in Croatia

Legal deposit, Croatia: National and University Library in Zagreb

Additional hard and PDF copies can be obtained from orders@intechopen.com

Nanomechanics

Edited by Alexander Vakhrushev

p. cm.

Print ISBN 978-953-51-3181-6

Online ISBN 978-953-51-3182-3

eBook (PDF) ISBN 978-953-51-4830-2

We are IntechOpen, the world's leading publisher of Open Access books Built by scientists, for scientists

3,500+

Open access books available

111,000+

International authors and editors

115M+

Downloads

151

Countries delivered to

Our authors are among the
Top 1%

most cited scientists

12.2%

Contributors from top 500 universities



WEB OF SCIENCE™

Selection of our books indexed in the Book Citation Index
in Web of Science™ Core Collection (BKCI)

Interested in publishing with us?
Contact book.department@intechopen.com

Numbers displayed above are based on latest data collected.
For more information visit www.intechopen.com



Meet the editor



Vakhrushev Alexander Vasilyevich received his PhD degree in Technical Sciences from Izhevsk Institute of Mechanical Engineering, Russia, in 1982, and degree of Doctor of Sciences in Physics and Mathematics from the Institute of Continuous Media Mechanics of Ural Branch of Russian Academy of Sciences, Russia, in 2003.

Now, he is the head of the Department of “Nanotechnology and Microsystems Technics” of Kalashnikov Izhevsk State Technical University and head of the Department of “Mechanics of Nanostructures” of the Institute of Continuous Media Mechanics of the Ural Branch of the Russian Academy of Sciences. He has over 400 publications to his name, including monographs, articles, reports, reviews, and patents. He has received several awards, including an Academician A. F. Sidorov Prize from the Ural Division of the Russian Academy of Sciences for significant contribution to the creation of the theoretical fundamentals of physical processes taking place in multilevel nanosystems and Honorable Scientist of the Udmurt Republic. He is currently a member of the editorial board of several journals, including Computational Continuum Mechanics, Chemical Physics and Mesoscopia, and Nanobuild. His research interests include multiscale mathematical modeling of physical-chemical processes into the nanoheterosystems at nano-, micro-, and macrolevels; static and dynamic interaction of nanoelements; and basic laws relating the structure and macrocharacteristics of nanoheterostructures.

Contents

Preface XI

- Chapter 1 **Interfacial Mechanical Behaviors in Carbon Nanotube Assemblies 1**
Xiaohua Zhang
- Chapter 2 **Mechanical Behavior of Nanostructured and Ultrafine-Grained Metal Alloy under Intensive Dynamic Loading 31**
Vladimir A. Skripnyak and Evgeniya G. Skripnyak
- Chapter 3 **Thermomass Theory: A Mechanical Pathway to Analyze Anomalous Heat Conduction in Nanomaterials 69**
Yuan Dong, Bingyang Cao and Zengyuan Guo
- Chapter 4 **Surface Nanomechanics of Biomolecules and Supramolecular Systems 89**
Paolo Bergese and Stefania Federici
- Chapter 5 **Nanocharacterization of the Mechanical and Tribological Behavior of MEMS Micromembranes 107**
Marius Pustan, Cristian Dudescu, Corina Birleanu and Florina Rusu
- Chapter 6 **Static, Vibration, and Buckling Analysis of Nanobeams 123**
Şeref Doğuşcan Akbaş
- Chapter 7 **Green Synthesis of Metallic and Carbon Nanostructures 139**
R. Britto Hurtado, G. Calderon-Ayala, M. Cortez-Valadez, L.P. Ramírez-Rodríguez and M. Flores-Acosta
- Chapter 8 **Perspective of the Structuration Process Use in the Optoelectronics, Solar Energy, and Biomedicine 167**
Natalia Vladimirovna Kamanina

Preface

In recent years, nanotechnology is the basis for the development of modern production. This determined the urgency of the intensive development of the new direction of mechanics and nanomechanics, for the scientific description of nanotechnological processes and the solution of a number of topical nanotechnology problems: reduction of time to prepare for the production, acceleration of technological processes, automation of technological processes, reduction in the cost of production, improvement in the quality of materials and products, preparation of high-performance materials, improvement of the ecology, etc. How are nanotechnological processes different from traditional technologies and how does nanomechanics fundamentally differ from classical mechanics? The specific feature of the physical processes in nanoscale is that the key phenomena determining the behavior of a nanoscale system in real time at the macroscale take place at small space and time scales. The properties of a nanoscale system depend not only on the properties of its constituent elements but also on the regularities of the spatial arrangement of the nanoscale system and the parameters of the nanoelement interaction. So, classical physical body mechanics, which is based on the hypothesis of continuum per that all the properties of a body are determined by the mechanics of continuum, cannot be applied to nanoscale systems. In this connection, it is obvious that describing of nanosystems requires the use of different physical models and mathematical methods and a detailed complex analysis of the "history" of the nanoscale material existence at different structural scales. Therefore, for nanosystems, we use currently nanomechanics, which allows to describe their behavior and properties at different structural levels. That is why, the development of nanomechanics is very necessary. Nanomechanics includes different physics and mathematics models: quantum mechanics, molecular dynamics, mesodynamics, and continuum mechanics. Because of the multilevel nature of nanotechnological processes, the problems of nanomechanics are very complex.

This book presents a collection of eight scientific papers on theoretical and practical advances in nanomechanics at different structural levels. Topics included in the book cover a wide range of research in the field of nanomechanics: thermomass theory of nanosystems, deformation of nanomaterials, interface mechanics of assembly carbon nanotube, nanomechanics on surface, molecular interactions and transformations, nanomechanical sensors, nanobeams and micromembranes, nanostructural organic and inorganic materials, green synthesis of metallic nanoparticles. The main goal of these works is the establishment of the nanosystem macroparameter dependence on its nanoparameters using nanomechanics.

Chapter 1 presents the complete material on the problem of interfacial mechanical behaviors in carbon nanotube assemblies. Chapter 2 presents the complete investigations on regularities of deformation at high strain rates and damage and fracture of ultrafine-grained alloys in static and in dynamic loading conditions. Chapter 3 presents the complete material on the

problem of changes in the parameters of thermal conductivity when the size of the nanosystem changes. In Chapter 4, it is shown how to single out small ligands able to inhibit protein misfolding, to measure energetics of surface-confined ferritin during iron loading, and to realize a universal probe for ammine-based designer medication. Chapter 5 presents the complete experimental investigation, analytical calculation, and numerical simulation by the method of MFE of micromembranes supported by serial-parallel connected hinges. Chapter 6 presents the modified couple stress theory for static, vibration, and buckling analysis of nanobeams. Chapter 7 presents the eco-friendly methods of obtaining nanostructures using plant experimental results of metallic and carbon nanostructures formation *ficus-indica* using the extract from *Opuntia cladodes*. Chapter 8 presents the results of experimental and simulation study of structure and properties of materials, surface of which was modified by oriented carbon nanotubes and, additionally, was treated by surface electromagnetic waves.

This book will be useful for engineers, technologists, and researchers interested in methods of nanomechanics and in advanced nanomaterials with complex behavior and their applications.

I would like to express my appreciation to all the contributors of this book. My special thanks to the Publishing Process Manager, Ms. Martina Usljebrka, and other staff of InTech publishing for their kind support and great efforts in bringing the book to completion.

Prof. Alexander Vakhruhev

Head of the Department of "Mechanics of Nanostructures"
Institute of Continuous Media Mechanics
of the Ural Branch of the Russian Academy of Sciences,
Ekaterinburg, Russia

Head of the Department of "Nanotechnology and Microsystems,"
Kalashnikov Izhevsk State Technical University,
Izhevsk, Russia

Interfacial Mechanical Behaviors in Carbon Nanotube Assemblies

Xiaohua Zhang

Additional information is available at the end of the chapter

<http://dx.doi.org/10.5772/67764>

Abstract

Interface widely exists in carbon nanotube (CNT) assembly materials, taking place at different length scales. It determines severely the mechanical properties of these assembly materials. In this chapter, I assess the mechanical properties of individual CNTs and CNT bundles, the interlayer or intershell mechanics in multiwalled CNTs, the shear properties between adjacent CNTs, and the assembly-dependent mechanical and multifunctional properties of macroscopic CNT fibers and films.

Keywords: carbon nanotube, assembly materials, mechanics, interface

1. Introduction

Carbon nanotubes (CNTs) are hollow cylinders consisting of single or multiple sheets of graphite (graphene) wrapped into a cylinder. After the first observation in 1991 by Iijima [1], extensive work has been carried out to CNTs toward their broad mechanical, electronic, thermal, and optical applications [2, 3]. The fundamental mechanical properties, such as their stiffness, strength, and deformability, have been investigated with extensive theoretical and experimental researches, and been well reviewed, in the past two decades [4–8]. Nowadays, for industrial and engineering applications, CNTs have been assembled into macroscopic materials such as fibers, films, forests, and gels [9–15]. Due to the assembly feature of these materials, the interfacial structure between CNTs always plays a crucial role in determining the tensile or compressive behavior, dynamic response, and coupling phenomenon between

multiple physical properties that take place at the interfaces. Therefore, the utilization efficiency of the mechanical property from individual CNTs to their assembly is a sophisticated function of the assembly structure and types of interfacial interactions.

In this chapter, I will review the mechanics of individual CNTs, discuss the sliding friction between CNTs, and report our recent progresses on the fabrication technique and mechanical properties of macroscopic CNT assembly materials. The general features of the assembly design and interface design will be illustrated from the perspective of interface engineering. The chapter is organized as follows. Section 2 contains a brief description of the mechanical properties of individual CNTs, in terms of modulus, strength, compressibility, and deformability. Section 3 describes the interlayer (intershell) sliding of multiwalled CNTs (MWCNTs) and intertube friction between adjacent CNTs, and the strategies to enhance the interfacial frictions. Section 4 discusses the recent investigations on the interfacial mechanics in macroscopic CNT assembly materials, especially CNT fibers and films where the CNTs are highly aligned or highly entangled. Finally, the chapter concludes with a brief summary and gives an outlook on future developments in the field.

2. Mechanical properties of carbon nanotubes

2.1. Young's modulus and tensile strength

The basic mechanical properties of CNT are strongly related to the basic properties of a graphene sheet. In these materials, carbon atoms are covalently bonded with three nearest carbon atoms in a hexagonal lattice by forming three σ bonds in the sheet plane and one delocalized π -bond over the basal plane. As the sp^2 σ bond is shorter and stronger even than the sp^3 bond in diamond, the axial elastic modulus of CNT and graphene is super high, as expected to be up to several TPa [6, 7]. The first experimental study on the modulus was based on the analysis of thermal vibration of MWCNTs, which showed a wide range of 0.4–4.15 TPa [16]. Later, the modulus was also estimated by the compressive response using micro Raman spectroscopy and was 2.8–3.6 TPa for singlewalled CNTs (SWCNTs) and 1.7–2.4 GPa for MWCNTs [17]. Direct tensile tests showed the modulus ranged from 270 to 950 GPa for individual MWCNTs [18], and from 320 to 1470 GPa when several SWCNTs bundled together as a CNT rope [19]. Besides the experimental evaluations, theoretical estimations also show the similar results. For example, by using an empirical Keating Hamiltonian with parameters determined from first principles, a modulus ranging from 1.5 to 5.0 TPa was estimated [20]. A molecular dynamics (MD) approach showed a modulus of ~ 1 TPa and a shear modulus of ~ 0.5 TPa and predicted that chirality, radius, and number of walls have little effect on the value of Young's modulus [21].

Different from the modulus estimation, measuring the tensile strength of CNTs is a very challenging task. Compared with experiment, it is easier to compute the strength by considering the effects of defects [22, 23], loading rate, temperature [24], and number of walls [25]. Typically, the fraction of CNT involves bond breakage and/or rotation, usually resulting in the formation of specific types of dislocation, such as the pentagon-heptagon (5-7), (5-7-7-5), (5-7-5-8-5) defects [26]. MD simulations showed that CNT under tension behaves as a brittle

material at high strain (15%) and low temperature (1300 K), or as a ductile material at low strain (3%) and high temperature (3000 K) [26–28]. Such tensile behaviors depend on the evolution of the dislocation. For example, the (5-7-7-5) dislocation can either separate into two (5-7) pairs to result in a ductile transformation or involve into a crack to result in a brittle fracture. An alternative pathway for the fracture of CNT was also proposed by the direct bond-breaking through the formation of a series of virtual defects at high tensions [23]. These studies were usually based on the consideration of the formation of energy for the dislocations. However, another MD study showed that the fracture behavior is almost independent of the separation energy and to depend primarily on the inflection point in the interatomic potential [22]. The fracture strength should be moderately dependent on tube chirality, and the strength and fracture strain were estimated to be 93.5–112 GPa and 15.8–18.7%, respectively. **Figure 1a** shows two different stress-strain curves for a (20,0) CNT, where the modified Morse potentials with interatomic force peaks at 19 and 13% strain were used. To show the effect of structural defect, a result for a missing atom is provided where the strength was reduced by about 25%.

The tensile strength and the fracture of CNT were also measured directly with experiment [18, 19]. The measurement of 19 MWCNTs showed a strength of 11–63 GPa and a strain at break up to 12% [18]. The failure of MWCNTs was described in term of the “sword-in-sheath” type fracture, where the outermost shell broke first followed by the pull out of the rest of the shells from the outermost shell. When SWCNTs were bundled to be a rope, the tensile strength was measured to be 13–52 GPa, based on 15 measurements, and the strain at break was up to 5.3%, see **Figure 1b** [19]. The stretchability of CNT was also experimentally obtained by deforming freely suspended SWCNT ropes, where the maximum strain was up to $5.8 \pm 0.9\%$ [29]. By measuring the stress-induced fragmentation of MWCNTs in a polymer matrix, the tube strength was up to 55 GPa [30]. Another pulling and bending tests on individual CNTs in-situ in a transition electron microscope (TEM) showed a tensile strength of ~ 150 GPa, suggesting that the strength is a large fraction of the elastic modulus [31].

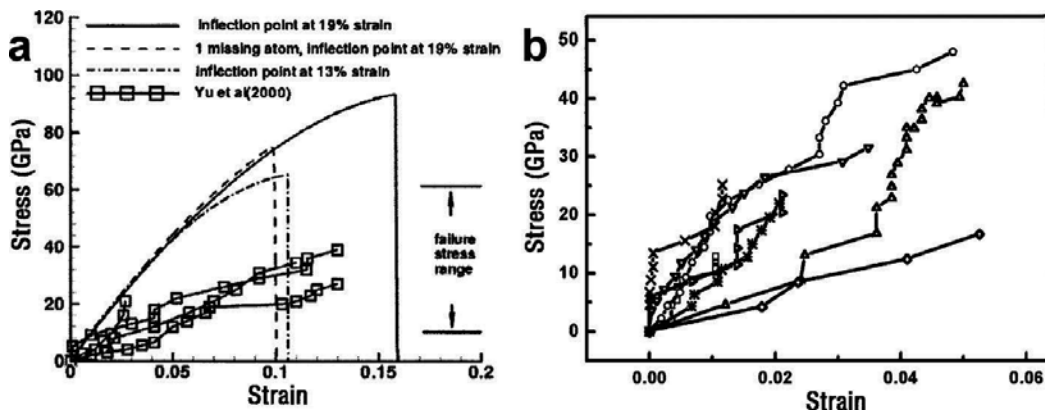


Figure 1. (a) A strong dependence on the inflection point in the interatomic potential can be seen from the stress-strain curves for a (20,0) CNT, and a missing atom has also a significant effect on strength, reducing it by about 25% [22]. Experimental measurements on MWCNTs are provided for comparison [18]. (b) Eight stress-strain curves obtained from the tensile-loading experiments on SWCNT ropes [19].

2.2. Compressibility and deformability

Different from the high rigidity and high strength along the axial direction, CNT is relatively compressible and deformable in the transverse direction. When individual SWCNTs are bundled together, significant deformation could occur by van der Waals (vdW) interaction between the adjacent tubes [32]. Fully collapsed MWCNTs were first observed with TEM [33]. Large diameter CNTs could also form the partial and full collapse on substrate [34–36]. The structural deformation can be induced by applying pressure. Various experiments on SWCNT bundles have shown clear evidence of structural deformation or transition [37–42]. MD simulations revealed that the compressibility and deformability are dependent on the tube diameter and the number of walls [43]. By applying a certain high pressure, there could be a circular-to-elliptical shape transition of the tube's cross section for either individual CNTs or their bundles [44–51]. These structural deformations are all reversible upon unloading the pressure. In a different way, a very large force exerted on CNT could still produce reversible and elastic deformation, and that radial mechanical forces might not be capable of cutting a CNT [43]. By examining the ballistic impact and bouncing-back processes, large diameter CNTs could withstand high bullet speeds [52].

Upon compressing, bending, or twisting, structural deformations of CNT become more complicated. With an increasing compression stress, different buckling patterns in CNT at the point of instabilities can be created [53]. As shown in **Figure 2**, each shape change corresponds

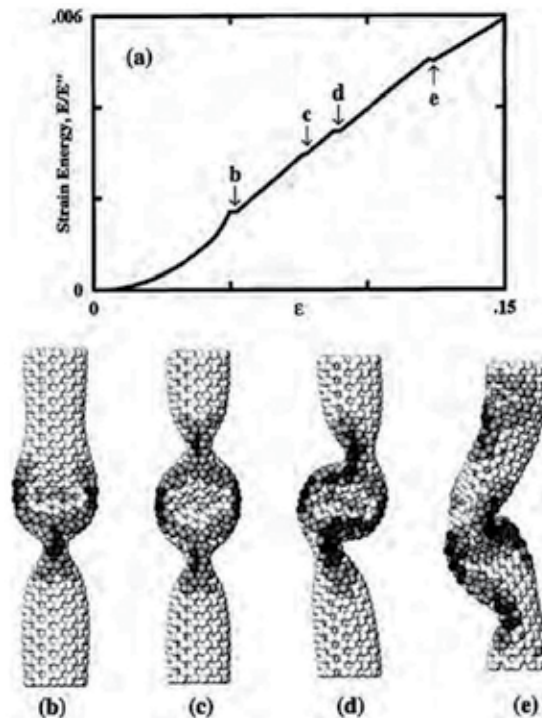


Figure 2. The strain energy (a) displays four singularities corresponding to shape changes (b–e) with increasing the axial compression [53].

to an abrupt release of energy and a singularity in the stress-strain curve. MD simulations showed that the presence of intertube vdW interactions tends to weaken the CNT bundles under compression [55]. On the other hand, with increasing the tube diameter, the bending modulus was found to decrease sharply [56], as a rippling mode becomes energetically favorable [57, 58]. The modeling on the wavelike distortion indicated that there is a critical diameter at a given load and a CNT length, for the emergence of the rippling mode [59]. It was also found that thick MWCNTs are very prone to develop rippling deformations in bending and twisting, governed by the interplay of strain energy relaxation and intertube interactions [58, 60]. **Figure 3** shows experimental observations of partially collapsed segments in freestanding and twisted MWCNTs with TEM [54].

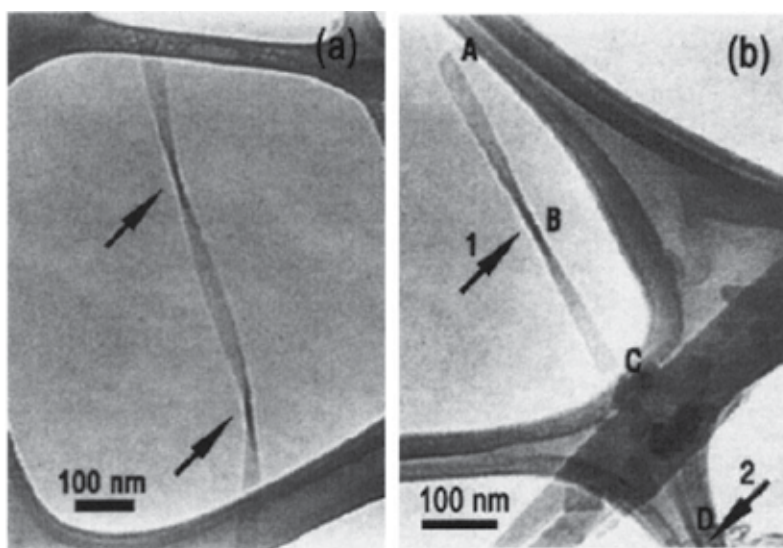


Figure 3. TEM images showing a suspended, fully collapsed, and twisted MWCNT (a), and a freestanding, fully collapsed, and twisted MWCNT (b) on a lacy carbon TEM grid [7, 54].

3. Interlayer and intertube interactions

3.1. Sliding between MWCNT shells

Different from SWCNTs, the interlayer interactions in MWCNTs exhibit interesting sliding phenomena during the tensile stretching and self-oscillation. By modeling of the interlayer interaction with different atomic potentials, such as the classic Lennard-Jones (LJ) potential and the registry-dependent Kolmogorov-Crespi (KC) potential (zeroth generation RDP0 [61] and first generation RPD1 [62]), could cause significantly different energy corrugation between graphitic layers [62–65]. Nevertheless, the interlayer sliding has been systematically studied despite the type of atomic potential. Experiments have also shown the interlayer sliding and superlubricity of CNTs.

Experimental measurements on the dependence of the sliding force against the contact length between the MWCNT shells suggested several responsible sources including the surface tension, the shear elastic force, and the edge (tube termination) effect force [66]. The shear strength was found to be 0.08–0.3 MPa depending on the interlayer commensurability. After the inner shells were pulled out from the outer shells, spontaneous retraction was observed with TEM due to the attractive vdW forces between these shells [67]. The interlayer static and dynamic shear strengths were estimated to be 0.43–0.66 MPa. The telescoping motion of an MWCNT also showed an ultralow friction, below 1.4×10^{-15} N per atom (8.7×10^{-4} meV \AA^{-1}) [68]. More direct observation of the superlubricity in doublewalled CNTs (DWCNTs) was conducted by extracting the inner shell out from a centimeters-long DWCNT, where the inner-shell friction (vdW force) was estimated to be 1.37–1.64 nN (the total number of atoms was unknown, yet could be over 10^8 – 10^9 for a tube length of 1 cm) [69], corresponding to a friction force of about 10^{-6} – 10^{-5} meV \AA^{-1} per atom. By following the low-friction induced telescoping, gigahertz oscillators were theoretically proposed based on the oscillatory extrusion and retraction of the inner shells [70–77], and the interlayer commensurability determines the rate of energy dissipation during the oscillation [71]. The friction force between oscillatory layers was estimated to range from 10^{-17} to 10^{-14} N per atom, about 6×10^{-6} –0.006 meV \AA^{-1} [73]. Similarly, the rotation between CNT shells and the rotational friction was observed or measured by experiments and simulations [78–81]. The rotational friction is a broadband phenomenon, as it does not depend strongly on a specific vibrational mode but rather appears to occur from the aggregate interactions of many modes at different frequencies [82].

At high sliding speeds, the friction between CNT layers was not hydrodynamical, in fact not even monotonic with the sliding speed [83]. A high speed can develop a sharp friction peak and onset parametric excitation of CNT's "breathing" phonon modes. **Figure 4a** shows that there is

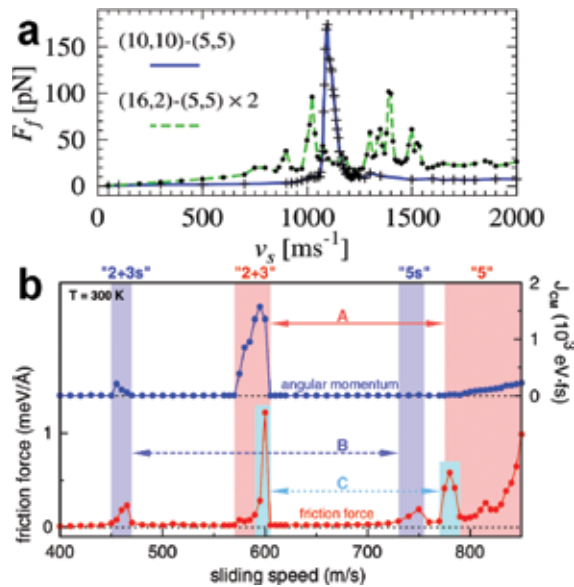


Figure 4. (a) There is a massive increase in friction at ~ 1100 m s^{-1} for the (5,5)@10,10 DWCNT [83]. (b) The center-of-mass angular momentum J_{CM} (top) and the sliding frictional force per inner tube atom (bottom) as functions of the sliding speed [84]. A, B, and C are three resonance regions related the giant friction forces.

a massive increase in sliding friction at a speed of $\sim 1100 \text{ m s}^{-1}$ for a (5,5)@(10,10) DWCNT. The highest friction force could be up to 170 pN, corresponding to $\sim 0.15 \text{ meV \AA}^{-1}$ per inner tube atom. The main source of the interlayer friction was believed to be the inner nanotube terminations [85], while the “bulk” friction was unfortunately considered to be irrelevant.

To understand the “bulk” frictional behavior, two groups of studies were carried out [65, 84, 86]; pulling simulations where a constant external force was applied on each atom of the inner tube along the tube axis, and rigid sliding simulations where the inner tube was constrained to slide as a whole at a fixed speed. The pulling simulation revealed a static friction (depinning) force of $0.02 \text{ meV \AA}^{-1}$ at 300 K and 0.1 meV \AA^{-1} at 50 K for the (5,5)@(10,10) DWCNT. After the depinning, the speed of the inner tube jumps directly to plateaus. Three speed plateaus are seen at $v \approx 450, 720, \text{ and } 780 \text{ m s}^{-1}$. This phenomenon is ubiquitous as it is also observed for an incommensurate case where a chiral (11,2) tube slides inside a (12,12). The general occurrence of plateaus and jumps is a natural consequence of frictional peaks for growing the speed. **Figure 4b** shows sharp frictional peaks near $v \approx 450, 570, 720$, and an important threshold onset near 780 m s^{-1} . These peaks are known to generally arise out of parametric excitation of the “breathing” phonon modes, classified by an angular momentum index n (for tangential quantization around the tube axis). Such nonmonotonic force-speed characteristics imply a “negative differential friction,” whereby an increasing applied force yields an inner tube sliding speed that grows by jumps and plateaus, rather than smoothly.

The surprise comes from analyzing the two parts of angular momentum $J = J_{\text{CM}} + J_{\text{pseudo}}$ around the tube axis such as its center-of-mass (rigid body rotation with angular velocity ω) and shape-rotation (“pseudorotational”) parts [65, 84]. Generally, zero at generic sliding speed due to lack of nanotube chirality, $J_{\text{pseudo}} = -J_{\text{CM}} = 0$, J_{pseudo} jumps to nonzero values at the frictional peaks and past the threshold, where $J_{\text{pseudo}} = -J_{\text{CM}} \neq 0$, see **Figure 4b**. This is a spontaneous breaking of chiral symmetry occurring in nanoscale friction, whose mechanism is from the third- and fourth-order energy nonlinearities. The inner-tube sliding causes a washboard frequency due to the lattice periodicity $a_{\text{CC}} = 2.46 \text{ \AA}$. At the critical frequencies, the ‘ $n = 5$ ’ or ‘ $2 + 3 = 5$ ’ excitations are observed, where the DWCNT’s $n = 5$ mode is resonantly excited or the $n = 2, 3, 5$ modes are jointly excited by the simple matching condition $2 + 3 = 5$. Besides these “normal” excitations (labeled A in **Figure 4b**), there are ‘ $n = 5s$ ’ and ‘ $2 + 3s = 5$ ’ excitations, where the $3s$ and $5s$ are the single outer tube’s phonon modes. These excitations are labeled B in **Figure 4b**. The two C-peaks in **Figure 4b** are ascribed to the phenomenon of strong stick-slip frictions, possibly related to the phonon modes along the tube axis.

3.2. Intertube friction

In most of the cases, individual CNTs are bundled together as a CNT rope, owing to the strong aggregation tendency between adjacent CNTs. As mentioned above, experimental measurement showed a tensile strength just up to 13–52 GPa [19], far below the ideal strength for individual CNTs. The easy sliding between adjacent CNTs has become a severe problem hindering their engineering applications. For example, slip rather than breakage of individual CNTs was observed in the fracture test of polymers reinforced by CNT bundles [87]. As CNTs can contact with each other in parallel way or at certain cross angles, the interfacial shear strengths between CNTs should be discussed separately.

The static and kinetic frictions between two perpendicular CNTs were investigated experimentally. A coefficient of friction of 0.006 ± 0.003 was obtained by sliding an MWCNT perpendicularly on a SWCNT surface, and the shear strength was derived to be 4 ± 1 MPa [88]. The shear strength was one to two orders of magnitude larger than the intershell shear strength of 0.05 MPa for MWCNTs in vacuum, possibly due to the presence of water at the intertube interface in ambient. A following experiment, namely a vertical friction loop measurement, was proposed to characterize the adhesion and friction properties between CNTs [89]. An MWCNT tip was ramped in the vertical direction against a suspended SWCNT. During ramping, a stick-slip motion was found to dominate the sliding, attributed to the presence of defect-induced or amorphous-carbon-associated high energy points on the tip surface. Surprisingly, the coefficients of static friction and shear strength were finally evaluated to be about 0.2 and 1.4 GPa, respectively.

MD simulations showed that the sliding behaviors and interfacial shear strengths between two crossly contacting CNTs are much more complicated than the frictions between CNTs and graphite, graphite and graphite, and the inner and outer shells of MWCNTs [90]. The simulation was performed on two SWCNTs in contact at different cross angles. For the parallel contact, the axial interfacial shear strengths between the zigzag-zigzag (~ 0.25 GPa) and armchair-armchair pairs (~ 0.5 GPa) are two orders of magnitude larger than those of CNTs having different chiralities (0.5–1 MPa). CNTs with diameters larger than 1 nm will slide relatively from an AB stacking position to the next nearest AB stacking position while smaller ones do not slide through AB stacking positions. For two cross contacting CNTs, the magnitude of interfacial shear strength is much less dependent upon tube chirality. The highest value of shear strength was reported to be about 1 GPa in SWCNT bundles, however, still as quite low as to be improved for applications in high-performance composite materials [91].

3.3. Strategies to improve the intertube load transfer

A molecular mechanics modeling showed that in order to make the strength of a CNT bundle as high as that of the lowest value of individual CNTs (11 GPa), the contact length should be up to ~ 3800 nm, by assuming the CNTs are bundled together without changing their circular cross sections [63]. With considering the vdW-force-induced radial deformation [32], the intertube distance-of-closest changes from 3.34 to 3.25 Å for (10,10) CNT bundles, the required contact distance for 11 GPa can decrease to ~ 1300 nm. This implies that the key to improve the intertube load transfer is the interface design between CNTs.

Twist is an effective way to induce strong radial deformation for CNT bundles. **Figure 5a** shows the cross sections obtained from MD simulations with increasing the twist level and **Figure 5b** shows the corresponding transferred load due to the shape deformation at twist angles of 0, 30, 60, 90, 120, 150, 180, and 210° [63]. It was observed that the individual CNTs start to collapse in the cross section, and therefore, more atoms are in close contact. For the case of no twist, a force of only ~ 0.048 eV Å⁻¹ is transferred to the center tube, while at 120° the transferred load increases to 1.63 eV Å⁻¹. Clearly, the radial deformation strongly depends on the twist angle, which consequently changes the nature of the contact and contributes to a new interlayer tribology.

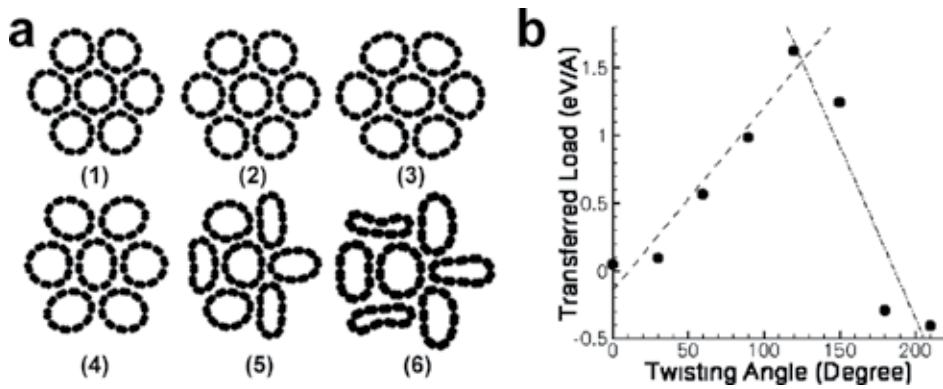


Figure 5. (a) Change in cross section at the mid-length of a SWCNT bundle with increasing the twist level and (b) the corresponding load transfer ability as a function of twist angle [63].

Even a slight structural deformation could cause an improved load transfer. For example, when a DWCNT was slightly bent into a curved one, the energy transfer between the two tubes becomes much faster than that between two straight tubes [81]. Slight displacement of the inner tube could add a large degree of disturbance to the DWCNT's original state of equilibrium and thus present strong inertia to oppose the extraction process, indicating the importance of the inner tube as structural support for the outer tube [92].

Pressure-induced structural phase transition could be a new strategy to improve the intertube load transfer [51]. For a CNT bundle containing 16 (23,0) SWCNTs, the intertube static friction can be improved from $0.1 \text{ eV } \text{Å}^{-1}$ per atom to $0.4\text{--}0.45 \text{ eV } \text{Å}^{-1}$ after all the tubes collapse under pressure higher than 0.5 GPa, see **Figure 6**. Due to the large tube diameter, the collapsed CNT structure

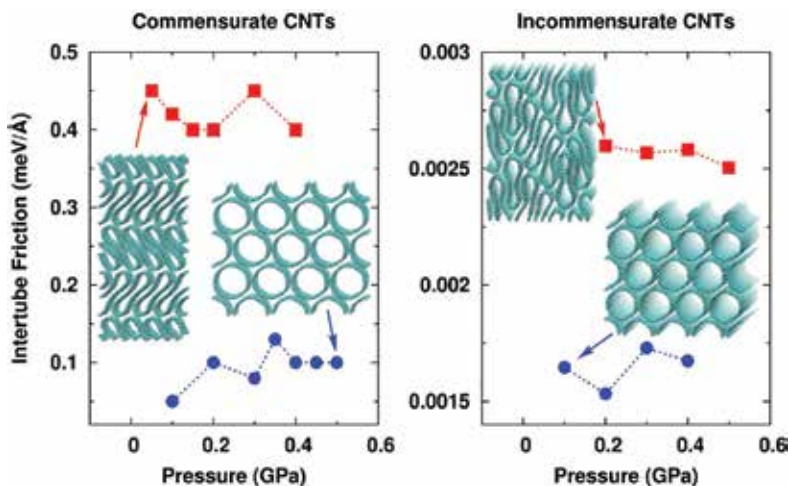


Figure 6. The intertube friction force can be increased by a factor of 1.5–4, depending on tube chirality and radius, when all tubes collapse above a critical pressure and when the bundle remains collapsed with unloading down to atmospheric pressure [51].

can be well maintained even by unloading the pressure down to 0.05 GPa. In order to realize a 10 GPa tensile strength, the minimum tube length should be just 167 nm, much smaller than the length of 1090 nm before the phase transition. For a CNT bundle containing totally different tube chiralities, the dynamic friction force can be improved from 0.0017 to 0.0026 eV Å⁻¹ after the phase transition. Such study also indicated that fewwalled large-diameter CNTs could be very important for engineering applications due to the easy ability to induce the collapse phase transition.

Covalent bonding between the shells in MWCNTs or between adjacent CNTs can increase the interlayer and intertube shear strength by several orders of magnitude [93–95]. The covalent intershell bonds can be formed due to the on-shell vacancies or intershell interstitials. According to the types of defect, the force needed to initiate sliding of the shells varies from 0.08 to 0.4 nN for a single vacancy to 3.8–7.8 nN for two vacancies, an intershell interstitial, and an intershell dimer [93]. Therefore, small-dose electron or ion irradiations are suggested to partially transfer the load to the nanotube inner shells. MD simulations revealed that interwall sp³ bonds and interstitial carbon atoms can increase load transfer between DWCNT walls and that interwall sp³ bonds are the most effective [95]. Similarly, by using moderate electron-beam irradiation inside a TEM, stable links between adjacent CNTs within bundles were covalently formed [94]. At a high irradiation energy of 200 keV, there was a substantial increase in effective bending modulus and thus an increase in shear modulus for low doses, while a long irradiation time rather damaged the well-ordered structure of tubes (**Figure 7**). At 80 keV, electrons were shown not to damage isolated CNTs but had enough energy to lead to the formation

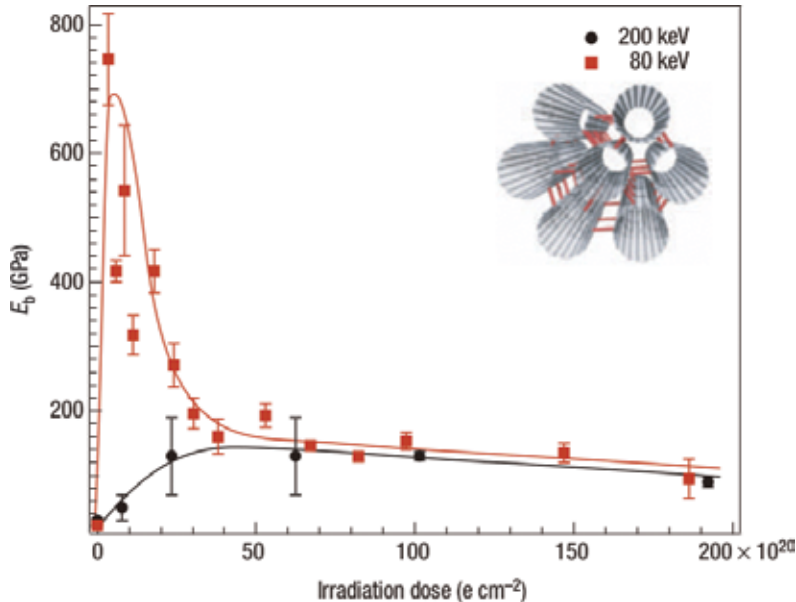


Figure 7. Behavior of bending modulus as a function of received dose for two incident electron energies [94]. For 200 keV, the modulus increases on short exposures, due to cross-linking and degrades at higher exposures because of structural damage. The bundle irradiated with 80-keV electrons shows a much stronger and sharper increase of the bending modulus.

of mobile interstitial atoms in the confined space between adjacent CNTs. As a result of the newly formed covalent bonds, a huge increase of the bending modulus by a factor of thirty was observed (**Figure 7**). However, a long-time dose at low energies could still cause the accumulation of damage to the structure, making the mechanical performance to decrease eventually.

Even without introducing covalent bonding between the sp^2 layers, the existence of structural defects in either CNT layer could lead to a sharp increase in friction and energy dissipation rate [64].

However, besides the tube structure, defect level, and intertube contact, there are many other issues in macroscopic CNT assembly materials. For example, the CNT packing density, alignment, entanglement, aggregation size, and surface functionalization could be important structural parameters, as to be discussed below.

4. Carbon nanotube assembly materials

So far, CNT fibers, films, forests, and gels are well-known and typical macroscopic assembly materials where the CNTs are the main constituents, especially at a mass fraction much more than 50% [10]. For example, CNT fiber is a one-dimensional assembly containing millions of individual tubes [9, 11–13, 15]. It has been found that CNT fibers could have much higher specific modulus and specific strength than those of commercial carbon and polymeric fibers. For the composite materials, there have been two different applications of CNTs such as a dispersion-based fabrication by using CNTs as reinforcing fillers in a polymer matrix [96, 97] and an assembly-based fabrication by directly assembling CNTs into composites [14]. In the former, the CNT content is strongly limited to be no larger than ~5 wt%, while in the latter, a small amount of polymer molecules (about 20–30 wt%) are used to strengthen the interfaces between CNTs. To describe these macroscopic CNT materials, different structural parameters are proposed and investigated in the past decade.

4.1. CNT fibers

CNT fiber can be produced by the coagulation-based “wet spinning” [98–101], the “direct spinning” from a CNT aerogel [102–104] or similarly from a pre-formed CNT film [105], and the “forest spinning” based on vertically aligned CNT forests [106–108]. A CNT fiber with a diameter of ~10 μm usually contains more than 10^6 individual CNTs. Such assembly feature is different from those well-known fibers for many years, which are usually a solid structure without internal interfaces. CNT fiber can also be considered a continuous length of interlocked “filaments” (CNT bundles), where the bundles are formed during the CNT growth rather than in the spinning process. As I have pointed out recently [109], although also being called as CNT yarn, CNT fiber is indeed not a yarn because the CNT bundles are not macroscopically processable. On the contrary, the basic components of a yarn, the long and parallel or interlocked filaments, are usually processable objects with a width larger than several micrometers [110].

Twist is the most fundamental treatment to make the CNTs assembled into a continuous fiber with a circular cross section. The as-spun fiber is relatively loose with noticeable spaces between CNTs or CNT bundles when the twist angle is small. Increasing the twist angle is an effective method to densify CNT fibers and thus improves the friction coefficient between the CNTs. **Figure 8** shows the strength-twist relationship for different CNT fibers [111–113]. All studies showed that the highest fiber strength was found at a twist angle of 15–20°. However, with further increasing the twist, the load (upon stretching) compresses the fiber rather than acts totally along the fiber axis due to the twist angle between the CNTs and the axis, making the utilization efficiency to decrease at high twist angles. The experimental observations that the strength initially increases with twist angle and then decreases are almost the same as those in traditional textile yarns. Nevertheless, the constituent CNTs are different from the filaments in a textile yarn; the CNTs are hollow cylinders and can deform the cross section under pressure due to a structural phase transition [44–49]. For those fibers spun from few-walled CNTs (wall numbers smaller than 6), it can be seen that beyond the optimal twist angle, an additional strength peak is at large twist angle of 27–30°. This second peak arises from the collapse transformation of the CNT hollow structure, which renders the CNT bundles much stronger and reduces the bundle cross-sectional area.

Solvent densification is another interfacial treatment to CNT assemblies, due to a large capillary force [114, 115]. Therefore, liquid infiltration by using water, ethanol, acetone, or dimethyl sulfoxide (DMSO) is also often used in the method of array spinning to densify CNT fibers [116–119]. Although the densification process does not improve nanotube orientation, it enhances the load transfer between the nanotubes, thus ensuring that most of them are fully load-bearing. For example, the fiber diameter was shrunk from 11.5 to 9.7 μm after acetone shrinking [117]. However, the role of solvent is hardly known as the capillary force can be influenced by the solvents volatility (boiling point), surface tension, and interaction with CNT surfaces. By comparing various solvents including the nonpolar solvents of *n*-hexane, cyclohexane, cyclohexene, toluene, and styrene, polar protic solvents of glycerine, methanol, ethanol, water, ethylene glycol, and 1,3-propanediol, and polar aprotic solvents of

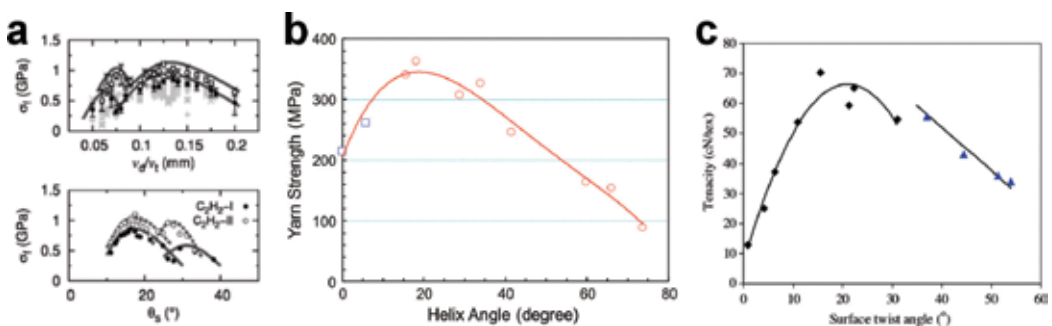


Figure 8. (a) Double-peak strength behavior of CNT fibers with increasing twist angles [111]. The surface twist angle (θ_s) depends on the twisting and drawing speeds (v_t and v_d) by $\theta_s = \arccos \{ (v_d/v_t) / [(\pi d_t)^2 + (v_d/v_t)^2]^{1/2} \}$, where d_t is the fiber diameter and is $>10.5 \mu\text{m}$. (b) Dependence of yarn tensile strength on helix angle for forest-spun MWCNT fibers [112]. The fiber diameter was $\sim 20 \mu\text{m}$. (c) Relationship between the fiber's specific strength and tenacity with the surface twist angle [113].

ethyl acetate, acetone, acetonitrile, *N,N*-dimethylformamide (DMF), DMSO, and *N*-methyl-2-pyrrolidone (NMP), only few highly polar solvents show high densifying ability to CNTs, namely DMF, DMSO, NMP, and ethylene glycol, despite of their high boiling points and low evaporation rates [118]. These solvents increased the fiber strength from 864 MPa (dry-spun) or 1.19 GPa (ethanol) to 1.14–1.35 GPa (DMF, DMSO, NMP) or 1.33–1.58 GPa (ethylene glycol). Clearly, the solvent polarity shows a key role in determining the capillary, as the polarity induced attractive binding energy with CNT (E_{ind}) goes up quadratically with the solvent's local dipole moment μ , by $E_{\text{ind}} = -\mu^2\alpha/(4\pi\epsilon_0)^2r^6$, where α is the static polarizability of CNT, ϵ_0 is the vacuum permittivity, and r is the distance between the dipole moment and the CNT surface [120, 121].

In addition to twisting and liquid densification, polymer impregnation is another effective treatment to enhance the mechanical properties of CNT fibers. The polymers are introduced to bridge nonneighboring CNTs, such as polyethyleneimine (PEI) [122], polydopamine (PDA) [123], polyvinyl alcohol (PVA) [105, 118, 124], polyacrylate [125], polyvinylidene fluoride (PVDF) [126], epoxy [105], polyimide (PI) [118, 127], and bismaleimide (BMI) [118, 128]. **Figure 9** shows several typical stress-strain curves for polymer-reinforced CNT fibers, such as PI, BMI, PEI, and PDA [118, 122, 123]. The enhanced mechanical properties of CNT fibers with polymer impregnation are attributed to couplings between the CNT network and polymer chains occurring at the molecular level. As a result, the sliding between CNTs can be remarkably hindered by the polymer network, especially that formed by the cured thermosetting polymers. Therefore, more external strain can be transferred to the CNTs as shown in **Figure 10**, where the Raman peaks of CNTs downshift to a lower wavenumber by different values under axial strains [105]. Both PVA and epoxy enhanced the downshifts, corresponding to the improved load transfer between CNTs. The cured thermosetting polymer network also shows advantages in improving the fiber modulus, as indicated by the largest change in G' -peak wavelength. Similarly, PI and BMI are other efficient thermosetting polymers for producing high-modulus CNT fibers [118, 127, 128]. However, other polymers might be good at improving the fiber's stretchability and toughness by preventing the sliding-induced fiber fracture, possibly due to the polymer wrapping around the CNT connections [126], cooperative deformation mechanisms of the soft and hard segments [125], iron-mediated covalent cross-linking [122], or cross-linked polymeric binders [123].

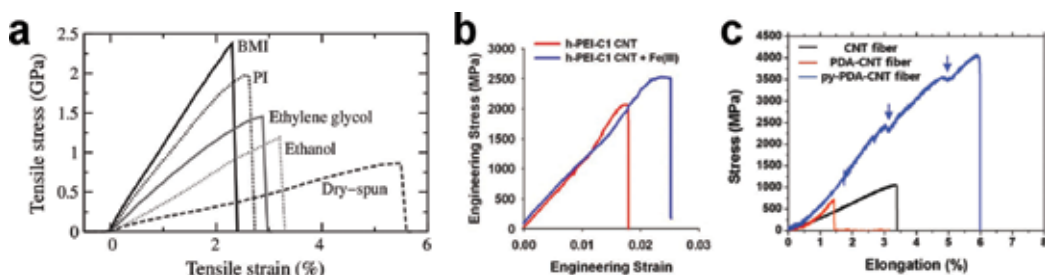


Figure 9. (a) Stress-strain curves of dry-spun, ethanol-densified, ethylene-glycol-densified, PI-reinforced, and BMI-reinforced CNT fibers [118]. (b) Stress-strain curves of PEI-catechol-reinforced CNT fibers, including one after addition of Fe(III) [122]. (c) Stress-strain curves of as-drawn CNT fiber, CNT/PDA fiber, and CNT/(pyrolyzed PDA) fiber [123].

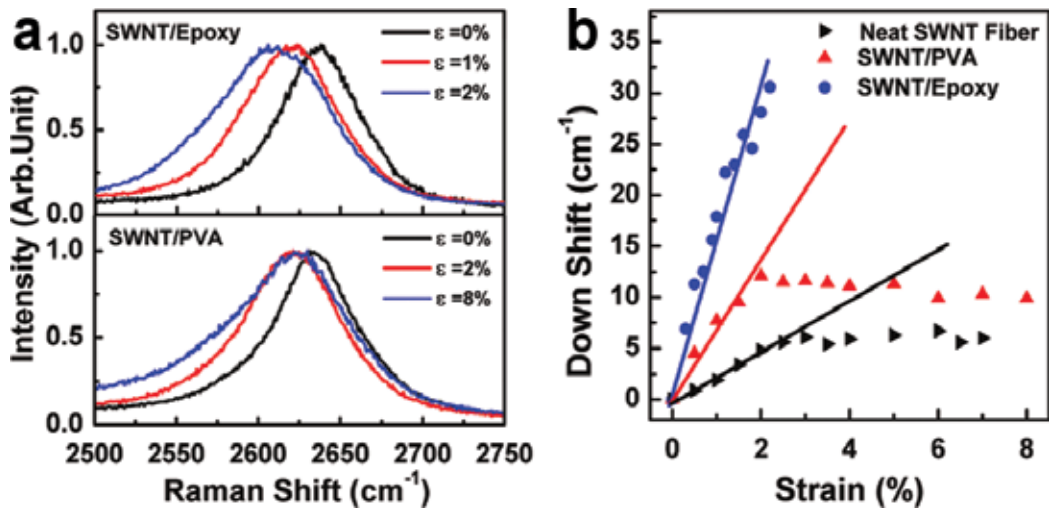


Figure 10. Variations of Raman spectra under strain in different systems [105]. (a) Typical G' band Raman spectra of epoxy- and PVA-infiltrated CNT fibers. (b) Downshifts of the peak position in different systems.

The structure of CNT fiber is hierarchical, with CNTs self-assembling into bundles and the bundles forming an aligned network in the fiber [129, 130]. Other assembly parameters also include the tube waviness or straightness [131], which can also result in different elasticity and modulus for CNT fibers. Notice that the above-mechanical improvements are irrelevant to the microstructure of individual CNTs but are relevant to the macroscopic assembly parameters. From the point of view of tube structure, fewwalled CNTs have shown advantages in producing high-performance fibers, rather than the ideal SWCNTs [131]. For the SWCNTs, usually 1–1.5 nm in diameter, simulations and experiments have shown that a certain high pressure (hundreds of MPa) is necessary to introduce even a slight deformation of their cross sections. That means, the intertube contact area is far limited compared with the overall circumference of the cross section. While for the fewwalled tubes, the tube diameter can be large up to ≥ 5 nm, making it much easy to deform the cross section and increase the contact area. Experiments even have shown, upon certain twisting and/or tensioning, collapse of fewwalled tubes were possibly introduced [111, 132].

Furthermore, covalent interface engineering could be an efficient posttreatment for the as-produced CNT fibers. Acid treatment could introduce rich hydroxyl, methyl/methylene, and carbonyl groups onto CNT surfaces, which also made CNT fibers shrunk slightly, or more densified. Such treatment enhanced the load transfer between CNTs, according to a theoretical study [94], and thus resulted in an increase in fiber strength and modulus [133]. Recently, by using an incandescent tension annealing process (ITAP), where the current-induced Joule heating increase the temperature of CNT fiber up to 2000°C in vacuum, sp³ covalent bonding was observed in CNT fibers [134]. As a result, the fiber modulus could be improved from 37 to 170 GPa, once the ITAP was performed with maintaining a high tension on the fiber.

In order to further improve the utilization efficiency of the individual CNT's mechanical properties in CNT fibers, more effort should be paid to the delicate combining of the choice

of CNT structure, controlling in CNT packing density, alignment, and straightness, and inter-tube mechanics engineering by polymers or covalent functionalization.

4.2. CNT films

CNT films are another important macroscopic material with high mechanical performances. Various processing methods have been developed to produce CNT films by using preformed CNT assemblies, among which these two methods are of great importance: the layer-by-layer stacking of aligned CNT sheets and the stretching on entangled CNT webs [14]. Despite of the fabrication methods, there are also many common problems concerning with the interface mechanics, as the CNT fibers do.

For instance, liquid densification is widely used to CNT films [135–137], and polymer impregnation can remarkably improve the interfacial load transfer [138–143]. Different from CNT fibers where the tubes are assembled with the aid of twisting, there is more freedom to tune the assembly structure. The CNTs can be got superaligned by stretching the films in a wet environment [135], or by microcombing before they are layer-by-layer stacked [136]. After improving the CNT alignment, the pure CNT films could be as strong as 3.2 GPa in tensile strength, with a Young’s modulus of 124–172 GPa [135, 136]. **Figure 11** shows the stress-strain curves for the CNT films being both densified and superaligned. Once these aligned CNTs were impregnated with polymers, especially thermosetting polymers, the film’s strength and modulus could be further improved. At a mass fraction of 50–55% for CNT, the CNT/BMI composite films exhibited a strength of 3.8 GPa and a modulus of 293 GPa [139]. Such superior properties are derived from the long length, high mass fraction, good alignment, and reduced waviness of the CNTs.

The stretching on entangled CNT webs is another way to obtain highly aligned CNT films. With the aid of BMI impregnation and curing, the strength and modulus of the CNT/BMI composite films could be improved from 620 MPa and 47 GPa (un-stretched) to 1600 MPa and

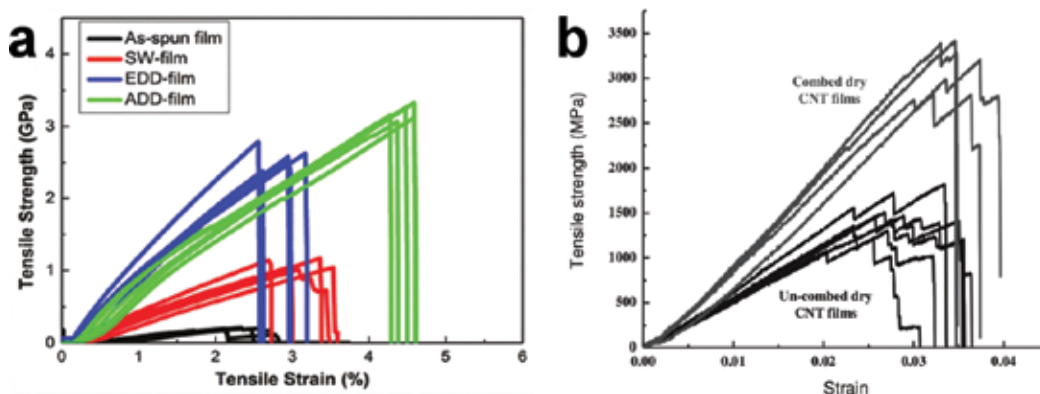


Figure 11. Stress-strain curves for CNT films obtained by a stretch-dip-drying method (a) [135] and a microcombing method (b) [136]. The films treated with acetone (ADD) and ethanol (EDD) were much stronger than the as-spun and spray-wound (SW) films. The films after microcombing had a larger Young’s modulus than the ADD and EDD films.

122 GPa, 1800 MPa and 150 GPa, and 2088 MPa and 169 GPa after being stretched by 30, 35, and 40%, respectively [140]. By further introducing surface functionalization for CNTs, the strength and modulus were surprisingly improved up to 3081 MPa and 350 GPa, respectively [141].

However, the direct stacking of CNT sheets and stretching on CNT webs could not avoid the CNT aggregation due to the vdW interactions. As shown in **Figure 12a** and **b**, the aggregation size was up to hundreds of nanometer [143]. Such aggregation of nanometer-sized components has become a severe problem in paving the way to stronger materials [144]. In the aggregation phase, the intertube load transfer is not as efficient as at the CNT-polymer interface. Thus, such aggregation phase becomes the weak parts in the composites and hinders further reinforcement. In an ideal structure, the nanometer-sized components should be uniformly distributed in the matrix without forming any aggregation phases. Therefore, all the interfaces can play roles in shear load transfer. As inspired by the formation process of natural composite structures, the BMI resins were infiltrated into CNT webs before any stretching was performed. Since the liquid treatment just densifies the CNT network without inducing CNT aggregation, the impregnation before stretching causes each CNT or CNT bundle uniformly covered by a thin layer of polymers. Therefore, the following stretching could just align the CNTs but avoid the aggregation due to the thin layer of polymer, resulting in an optimized composite structure. By adapting a multistep stretching process, the final

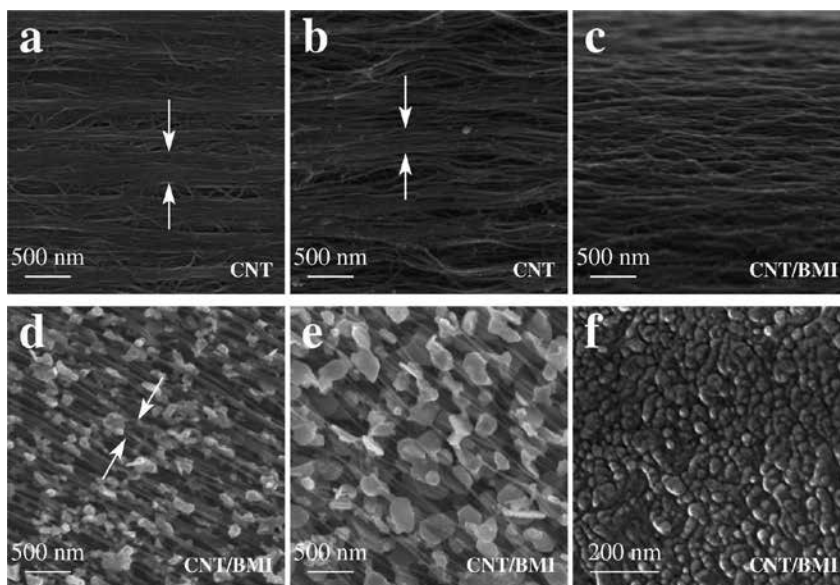


Figure 12. Comparison of CNT assembly structure for different films [143]. (a,b) CNT aggregation in the layer-by-layer stacking of array-drawn CNT sheets and the stretched dry films composed by entangled CNTs, respectively. (c) The small-sized CNT bundles did not aggregate but were surrounded by BMI polymers and uniformly distributed. (d, e) 750°C treated CNT/BMI composite films where the stretching was performed before and after resin impregnation, respectively, showing the aggregation and unaggregation. (f) Cross section of the optimal CNT/BMI composite structure by using focused ion beam treatment, indicating an aggregation size of 20–50 nm for the CNTs.

composite film exhibited superior mechanical performances. The highest tensile strength and modulus were up to 5.77–6.94 and 212–351 GPa at a CNT-to-resin mass ratio of 7:3 and a stretching magnitude of 34% [143].

Figure 12c shows the morphology of the optimized CNT/BMI composites, where the CNT bundles were found to be uniformly distributed and aligned. To characterize the aggregation of CNTs, thermal treatment and focused ion beam treatment were used. After being heated to 750°C to decompose the polymers, the remaining CNTs were found to be aggregated/unaggregated if the stretching was performed before/after the polymer impregnation, see **Figure 12d** and **e**. The direct observation of the cross section with focused ion beam treatment showed an aggregation size of just 20–50 nm (**Figure 12f**), a size for the bundling that was still difficult to avoid during the growth process.

On the whole, for the macroscopic CNT assemblies, the interface mechanics becomes much more complicated as the material exhibits a collective dynamics from the constituent CNTs. Assembly parameters, including CNT packing density, alignment and/or entanglement, twisting level, cross-linking, and aggregation size, are found to be critical for the mechanical properties. By controlling the interface mechanics in the CNT assemblies, we can not only optimize the mechanical properties, but also introduce multifunctionalities, as discussed below.

4.3. Multifunctionalization by interface engineering

Besides load transfer at the intertube interfaces, energy dissipation is also a common interfacial phenomenon. As CNT fiber is formed by assembling millions of individual tubes, the assembly features provide the fiber with rich interface structures and various ways of energy dissipation, including the internal viscosity and intertube friction [109]. Therefore, a modified Kelvin-Voigt model was adopted, where an elastic spring K , a viscous damping coefficient η , and an intertube friction f are connected in parallel [145]. Due to the friction, there exists a friction-dependent component in loss tangent, which is not dependent on the frequency. As shown in **Figure 13**, the loss tangent was nonzero (about 0.045) for the dry-spun CNT fibers, while that for the T300 carbon fiber was nearly zero due to the absence of interfaces. When the CNT fibers were densified

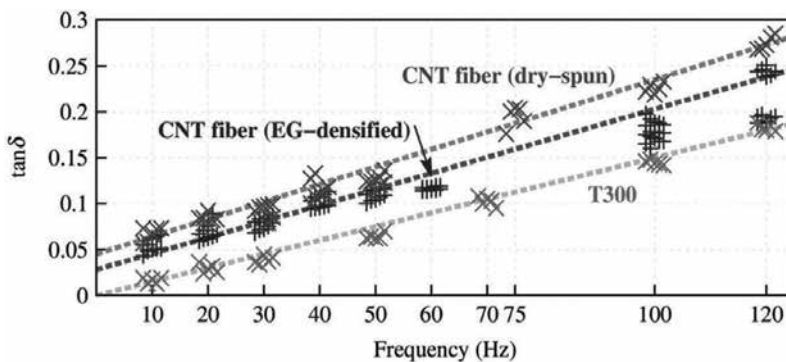


Figure 13. The frequency dependence of loss tangent for the dry-spun CNT fiber, ethylene-glycol-densified CNT fiber, and T300 carbon fiber [109].

by ethylene glycol, the CNTs became constrained, corresponding to reduced loss tangents, see **Figure 13**. Based on the friction-based Kelvin-Voigt model, the damping performance of CNT fibers can be tuned in a very wide range. The introduction of thermosetting polymers further decreases the loss tangent, while plying CNT fibers into a yarn increases the loss tangent [109].

The CNT entanglement provides another way to enhance the damping ability [146]. The as-produced CNT films based on an injection chemical vapor deposition exhibited a loss tangent of 0.37–0.42 at 200 Hz [146], or 0.2 at 50 Hz [143]. After the network was stretched and strengthened with BMI, the loss tangent could decrease remarkably down to about 0.05 at 50 Hz [143].

When an electric current is passing through CNT assemblies, there exist parallel currents along the aligned CNTs. The collective electromagnetic force between parallel current can cause a volume contraction for the assembly [147]. Based on such mechanism, CNT fibers can be developed as electromechanical actuator. Detailed study revealed that the electromechanical coupling is quite complicated beyond the actuation [128]. For example, when a current passes through a CNT fiber, the fiber's modulus could decrease remarkably due to the current-induced weakening in C–C σ bond. Besides the electromechanical coupling, the current could induce a strong Joule heating, making the fiber temperature to increase very sharply. Such electrothermal coupling can be used for fast curing to the impregnated thermosetting resins at a moderate temperature of 200–300°C [128], or for the formation of intertube sp^3 covalent bonding at a high temperature of 2000°C in vacuum [134].

5. Conclusion

The control of interface mechanics is a key strategy to develop high-performance CNT assembly structures. High tensile properties (strength up to 3–6 GPa and modulus up to 200–350 GPa) can be obtained for aligned CNT fibers and films, corresponding to an improved utilization efficiency of CNT's mechanical properties. Furthermore, the dynamical performance and multifunctionalities both depend strongly on the interface between CNTs, also in terms of CNT packing density, alignment, entanglement, twisting level, cross-linking, and aggregation size. For future development of high-performance CNT assembly materials, more delicate design on the multiscale interfaces is required. I hope this review could cast lights for the interface design ranging widely from the nanometer scale to the macroscopic scale.

Acknowledgements

The author thanks Prof. Xingao Gong of Fudan University, Prof. Erio Tosatti of the International School for Advanced Studies, and Prof. Qingwen Li of Suzhou Institute of Nano-Tech and Nano-Bionics for their kind collaborations, which are the important sources for this chapter. Financial supports from the National Natural Science Foundation of China (11302241, 51561145008), Youth Innovation Promotion Association of the Chinese Academy of Sciences (2015256), and National Key Research and Development Program of China (2016YFA0203301) are acknowledged.

Author details

Xiaohua Zhang

Address all correspondence to: zhangxhcm@gmail.com

1 Suzhou Institute of Nano-Tech and Nano-Bionics, Chinese Academy of Sciences, Suzhou, China

2 Jiangsu Key Laboratory of Engineering Mechanics and Department of Engineering Mechanics, School of Civil Engineering, Southeast University, Nanjing, China

References

- [1] Iijima S. Helical microtubules of graphitic carbon. *Nature*. 1991;**354**(6348):56–58
- [2] Baughman RH, Zakhidov AA, De Heer WA. Carbon nanotubes—the route toward applications. *Science*. 2002;**297**(5582):787–792
- [3] De Volder MFL, Tawfick SH, Baughman RH, Hart AJ. Carbon nanotubes: present and future commercial applications. *Science*. 2013;**339**(6119):535–539
- [4] Qian D, Wagner GJ, Liu WK, Yu M-F, Ruoff RS. Mechanics of carbon nanotubes. *Applied Mechanics Reviews*. 2002;**55**(6):495–533
- [5] Bernholc J, Brenner D, Nardelli MB, Meunier V, Roland C. Mechanical and electrical properties of nanotubes. *Annual Review of Materials Research*. 2002;**32**:347–375
- [6] Ruoff RS, Qian D, Liu WK. Mechanical properties of carbon nanotubes: theoretical predictions and experimental measurements. *Comptes Rendus Physique*. 2003;**4**(9):993–1008
- [7] Yu M-F. Fundamental mechanical properties of carbon nanotubes: current understanding and the related experimental studies. *Journal of Engineering Materials and Technology*. 2004;**126**(3):271–278
- [8] Kis A, Zettl A. Nanomechanics of carbon nanotubes. *Philosophical Transactions of the Royal Society London A*. 2008;**366**(1870):1591–1611
- [9] Behabtu N, Green MJ, Pasquali M. Carbon nanotube-based neat fibers. *Nano Today*. 2008;**3**(5–6):24–34
- [10] Liu L, Ma W, Zhang Z. Macroscopic carbon nanotube assemblies: preparation, properties, and potential applications. *Small*. 2011;**7**(11):1504–1520
- [11] Zhang X, Li Q. Toward multifunctional carbon nanotube fibers. In: Q. Zhang, editor. *Carbon Nanotubes and Their Applications*. Singapore: Pan Stanford Publishing; 2012. pp. 467–499. Chapter 14
- [12] Lu W, Zu M, Byun J-H, Kim B-S, Chou T-W. State of the art of carbon nanotube fibers: opportunities and challenges. *Advanced Materials*. 2012;**24**(14):1805–1833

- [13] Miao M. Yarn spun from carbon nanotube forests: production, structure, properties and applications. *Particuology*. 2013;**11**(4):378–393
- [14] Zhang X, Yu X, Zhao J, Li Q. Bio-inspired design and fabrication of super-strong and multifunctional carbon nanotube composites. In: Berber MR, Hafez IH, editors. *Carbon Nanotubes - Current Progress of Their Polymer Composites*. Rijeka, Croatia: InTech - Open Access; 2016. pp. 73–93. Chapter 3
- [15] Di J, Zhang X, Yong Z, Zhang Y, Li D, Li R, Li Q. Carbon-nanotube fibers for wearable devices and smart textiles. *Advanced Materials*. 2016;**28**(47):10529–10538
- [16] Treacy MMJ, Ebbesen TW, Gibson JM. Exceptionally high Young's modulus observed for individual carbon nanotubes. *Nature*. 1996;**381**(6584):678–680
- [17] Lourie O, Wagner HD. Evaluation of Young's modulus of carbon nanotubes by Micro-Raman spectroscopy. *Journal of Materials Research*. 1998;**13**(9):2418–2422
- [18] Yu M-F, Lourie O, Dyer MJ, Moloni K, Kelly TF, Ruoff RS. Strength and breaking mechanism of multiwalled carbon nanotubes under tensile load. *Science*. 2000;**287**(5453):637–640
- [19] Yu M-F, Files BS, Arepalli S, Ruoff RS. Tensile loading of ropes of single wall carbon nanotubes and their mechanical properties. *Physical Review Letters*. 2000;**84**(24):5552–5555
- [20] Overney G, Zhong W, Tománek D. Structural rigidity and low frequency vibrational modes of long carbon tubules. *Zeitschrift fur Physik D*. 1993;**27**(1):93–96
- [21] Lu JP. Elastic properties of carbon nanotubes and nanoropes. *Physical Review Letters*. 1997;**79**(7):1297–1300
- [22] Belytschko T, Xiao SP, Schatz GC, Ruoff RS. Atomistic simulations of nanotube fracture. *Physical Review B*. 2002;**65**(23):235430
- [23] Dumitrică T, Belytschko T, Yakobson BI. Bond-breaking bifurcation states in carbon nanotube fracture. *Journal of Chemical Physics*. 2003;**118**(21):9485–9488
- [24] Wei C, Cho K, Srivastava D. Tensile strength of carbon nanotubes under realistic temperature and strain rate. *Physical Review B*. 2003;**67**(11):115407
- [25] Liew KM, Wong CH, He XQ, Tan MJ, Meguid SA. Nanomechanics of single and multi-walled carbon nanotubes. *Physical Review B*. 2004;**69**(11):115429
- [26] Bernholc J, Brabec C, Nardelli MB, Maiti A, Roland C, Yakobson BI. Theory of growth and mechanical properties of nanotubes. *Applied Physics A*. 1998;**67**(1):39–46
- [27] Nardelli MB, Yakobson BI, Bernholc J. Brittle and ductile behavior in carbon nanotubes. *Physical Review Letters*. 1998;**81**(21):4656–4659
- [28] Nardelli MB, Yakobson BI, Bernholc J. Mechanism of strain release in carbon nanotubes. *Physical Review B*. 1998;**57**(8):R4277–4280

- [29] Walters DA, Ericson LM, Casavant MJ, Liu J, Colbert DT, Smith KA, Smalley RE. Elastic strain of freely suspended single-wall carbon nanotube ropes. *Applied Physics Letters*. 1999;**74**(25):3803–3085
- [30] Wagner HD, Lourie O, Feldman Y, Tenne R. Stress-induced fragmentation of multiwall carbon nanotubes in a polymer matrix. *Applied Physics Letters*. 1998;**72**(2):188–189
- [31] Demczyk BG, Wang YM, Cumings J, Hetman M, Han W, Zettl A, Ritchie RO. Direct mechanical measurement of the tensile strength and elastic modulus of multiwalled carbon nanotubes. *Materials Science and Engineering A*. 2002;**334**(1–2):173–198
- [32] Tersoff J, Ruoff RS. Structural properties of a carbon-nanotube crystal. *Physical Review Letters*. 1994;**73**(5):676–679
- [33] Chopra NG, Benedict LX, Crespi VH, Cohen ML, Louie SG, Zettl A. Fully collapsed carbon nanotubes. *Nature*. 1995;**377**(6545):135–138
- [34] Hertel T, Martel R, Avouris P. Manipulation of individual carbon nanotubes and their interaction with surfaces. *Journal of Physical Chemistry B*. 1998;**102**(6):910–915
- [35] Hertel T, Walkup RE, Avouris P. Deformation of carbon nanotubes by surface van der Waals forces. *Physical Review B*. 1998;**58**(20):13870–13873
- [36] Yu M-F, Kowalewski T, Ruoff RS. Structural analysis of collapsed, and twisted and collapsed, multiwalled carbon nanotubes by atomic force microscopy. *Physical Review Letters*. 2001;**86**(1):87–90
- [37] Chesnokov SA, Nalimova VA, Rinzler AG, Smalley RE, Fischer JE. Mechanical energy storage in carbon nanotube springs. *Physical Review Letters*. 1999;**82**(2):343–346
- [38] Venkateswaran UD, Rao AM, Richter E, Menon M, Rinzler A, Smalley RE, Eklund PC. Probing the single-wall carbon nanotube bundle: Raman scattering under high pressure. *Physical Review B*. 1999;**59**(16):10928–10934
- [39] Peters MJ, McNeil LE, Lu JP, Kahn D. Structural phase transition in carbon nanotube bundles under pressure. *Physical Review B*. 2000;**61**(9):5939–5944
- [40] Gaál R, Salvétat J-P, Forró L. Pressure dependence of the resistivity of single-wall carbon nanotube ropes. *Physical Review B*. 2000;**61**(11):7320–7323
- [41] Tang J, Qin L-C, Sasaki T, Yudasaka M, Matsushita A, Iijima S. Compressibility and polygonization of single-walled carbon nanotubes under hydrostatic pressure. *Physical Review Letters*. 2000;**85**(9):1887–1889
- [42] López MJ, Rubio A, Alonso JA, Qin L-C, Iijima S. Novel polygonized single-wall carbon nanotube bundles. *Physical Review Letters*. 2001;**86**(14):3056–3059
- [43] Lordi V, Yao N. Radial compression and controlled cutting of carbon nanotubes. *Journal of Chemical Physics*. 1998;**109**(6):2509–2512

- [44] Elliott JA, Sandler JKW, Windle AH, Young RJ, Shaffer MSP. Collapse of single-wall carbon nanotubes is diameter dependent. *Physical Review Letters*. 2004;**92**(9):095501
- [45] Zhang XH, Sun DY, Liu ZF, Gong XG. Structure and phase transitions of single-wall carbon nanotube bundles under hydrostatic pressure. *Physical Review B*. 2004;**70**(3):035422
- [46] Zhang XH, Liu ZF, Gong XG. Comment on collapse of single-wall carbon nanotubes is diameter dependent. *Physical Review Letters*. 2004;**93**(14):149601
- [47] Sun DY, Shu DJ, Ji M, Liu F, Wang M, Gong XG. Pressure-induced hard-to-soft transition of a single carbon nanotube. *Physical Review B*. 2004;**70**(16):165417
- [48] Ye X, Sun DY, Gong XG. Pressure-induced structural transition of double-walled carbon nanotubes. *Physical Review B*. 2005;**72**(3):035454
- [49] Gadagkar V, Maiti PK, Lansac Y, Jagota A, Sood AK. Collapse of double-walled carbon nanotube bundles under hydrostatic pressure. *Physical Review B*. 2006;**73**(8):085402
- [50] Chang T. Dominoes in carbon nanotubes. *Physical Review Letters*. 2008;**101**(17):175501
- [51] Zhang X, Li Q. Enhancement of friction between carbon nanotubes: an efficient strategy to strengthen fibers. *American Chemical Society Nano*. 2010;**4**(1):312–316
- [52] Mylvaganam K, Zhang LC. Ballistic resistance capacity of carbon nanotubes. *Nanotechnology*. 2007;**18**(47):475701
- [53] Yakobson BI, Brabec CJ, Bernholc J. Nanomechanics of carbon tubes: instabilities beyond linear response. *Physical Review Letters*. 1996;**76**(14):2511–2514
- [54] Yu M-F, Dyer MJ, Chen J, Qian D, Liu WK, Ruoff RS. Locked twist in multiwalled carbon-nanotube ribbons. *Physical Review B*. 2001;**64**(24):241403
- [55] Liew KM, Wong CH, Tan MJ. Tensile and compressive properties of carbon nanotube bundles. *Acta Materialia*. 2006;**54**(1):225–231
- [56] Poncharal P, Wang ZL, Ugarte D, De Heer WA. Electrostatic deflections and electromechanical resonances of carbon nanotubes. *Science*. 1999;**283**(5407):1513–1516
- [57] Lourie O, Cox DM, Wagner HD. Buckling and collapse of embedded carbon nanotubes. *Physical Review Letters*. 1998;**81**(8):1638–1641
- [58] Arroyo M, Belytschko T. Nonlinear mechanical response and rippling of thick multiwalled carbon nanotubes. *Physical Review Letters*. 2003;**91**(21):215505
- [59] Liu JZ, Zheng Q, Jiang Q. Effect of bending instabilities on the measurements of mechanical properties of multiwalled carbon nanotubes. *Physical Review B*. 2003;**67**(7):075414
- [60] Qian D, Liu WK, Subramoney S, Ruoff RS. Effect of interlayer potential on mechanical deformation of multiwalled carbon nanotubes. *Journal of Nanoscience and Nanotechnology*. 2003;**3**:185–191

- [61] Kolmogorov AN, Crespi VH. Smoothest bearings: interlayer sliding in multiwalled carbon nanotubes. *Physical Review Letters*. 2000;**85**(22):4727–4730
- [62] Kolmogorov AN, Crespi VH. Registry-dependent interlayer potential for graphitic systems. *Physical Review B*. 2005;**71**(23):235415
- [63] Qian D, Liu WK, Ruoff RS. Load transfer mechanism in carbon nanotube ropes. *Composites Science and Technology*. 2003;**63**(11):1561–1569
- [64] Guo W, Zhong W, Dai Y, Li S. Coupled defect-size effects on interlayer friction in multiwalled carbon nanotubes. *Physical Review B*. 2005;**72**(7):075409
- [65] Zhang XH, Santoro GE, Tartaglino U, Tosatti E. Dynamical phenomena in fast sliding nanotube models. *Philosophical Magazine*. 2013;**93**(8):922–948
- [66] Yu M-F, Yakobson BI, Ruoff RS. Controlled sliding and pullout of nested shells in individual multiwalled carbon nanotubes. *Journal of Physical Chemistry B*. 2000;**104**(37):8764–8767
- [67] Cumings J, Zettl A. Low-friction nanoscale linear bearing realized from multiwall carbon nanotubes. *Science*. 2000;**289**(5479):602–604
- [68] Kis A, Jensen K, Aloni S, Mickelson W, Zettl A. Interlayer forces and ultralow sliding friction in multiwalled carbon nanotubes. *Physical Review Letters*. 2006;**97**(2):025501
- [69] Zhang R, Ning Z, Zhang Y, Zheng Q, Chen Q, Xie H, Zhang Q, Qian W, Wei F. Superlubricity in centimetres-long double-walled carbon nanotubes under ambient conditions. *Nature Nanotechnology*. 2013;**8**(12):912–916
- [70] Zheng Q, Jiang Q. Multiwalled carbon nanotubes as gigahertz oscillators. *Physical Review Letters*. 2002;**88**(4):045503
- [71] Guo W, Guo Y, Gao H, Zheng Q, Zhong W. Energy dissipation in gigahertz oscillators from multiwalled carbon nanotubes. *Physical Review Letters*. 2003;**91**(12):125501
- [72] Legoas SB, Coluci VR, Braga SF, Coura PZ, Dantas SO, Galvão DS. Molecular-dynamics simulations of carbon nanotubes as gigahertz oscillators. *Physical Review Letters*. 2003;**90**(5):055504
- [73] Zhao Y, Ma C-C, Chen G, Jiang Q. Energy dissipation mechanisms in carbon nanotube oscillators. *Physical Review Letters*. 2003;**91**(17):175504
- [74] Rivera JL, McCabe C, Cummings PT. Oscillatory behavior of double-walled nanotubes under extension: a simple nanoscale damped spring. *Nano Letters*. 2003;**3**(8):1001–1005
- [75] Liu P, Zhang YW, Lu C. Oscillatory behavior of gigahertz oscillators based on multiwalled carbon nanotubes. *Journal of Applied Physics*. 2005;**98**(1):014301
- [76] Zhao X, Cummings PT. Molecular dynamics study of carbon nanotube oscillators revisited. *Journal of Chemical Physics*. 2006;**124**(13):134705

- [77] Li B, Chang T. Tunable dual-frequency oscillators of carbon nanotubes. *Journal of Applied Physics*. 2010;**108**(5):054304
- [78] Fennimore AM, Yuzvinsky TD, Han W-Q, Fuhrer MS, Cumings J, Zettl A. Rotational actuators based on carbon nanotubes. *Nature*. 2003;**424**(6947):408–410
- [79] Zhang S, Liu WK, Ruoff RS. Atomistic simulations of double-walled carbon nanotubes (DWCNTs) as rotational bearings. *Nano Letters*. 2004;**4**(2):293–297
- [80] Servantie J, Gaspard P. Rotational dynamics and friction in double-walled carbon nanotubes. *Physical Review Letters*. 2006;**97**(18):186106
- [81] Cai K, Cai H, Yin H, Qin QH. Dynamic behavior of curved double-wall carbon nanotubes with rotating inner tube. *Royal Society of Chemistry Advances*. 2015;**5**(38):29908–29913
- [82] Cook EH, Buehler MJ, Spakovszky ZS. Mechanism of friction in rotating carbon nanotube bearings. *Journal of the Mechanics and Physics of Solids*. 2013;**61**(2):652–673
- [83] Tangney P, Cohen ML, Louie SG. Giant wave-drag enhancement of friction in sliding carbon nanotubes. *Physical Review Letters*. 2006;**97**(19):195901
- [84] Zhang XH, Santoro GE, Tartaglino U, Tosatti E. Dynamical chiral symmetry breaking in sliding nanotubes. *Physical Review Letters*. 2009;**102**(12):125502
- [85] Tangney P, Louie SG, Cohen ML. Dynamic sliding friction between concentric carbon nanotubes. *Physical Review Letters*. 2004;**93**(6):065503
- [86] Zhang X-H, Tartaglino U, Santoro GE, Tosatti E. Velocity plateaus and jumps in carbon nanotube sliding. *Surface Science*. 2007;**601**(18):3693–3696
- [87] Ajayan PM, Schadler LS, Giannaris C, Rubio A. Single-walled carbon nanotube polymer composites: strength and weakness. *Advanced Materials*. 2000;**12**(10):750–753
- [88] Bhushan B, Ling X, Jungen A, Hierold C. Adhesion and friction of a multiwalled carbon nanotube sliding against single-walled carbon nanotube. *Physical Review B*. 2008;**77**(16):165428
- [89] Bhushan B, Ling X. Adhesion and friction between individual carbon nanotubes measured using force-versus-distance curves in atomic force microscopy. *Physical Review B*. 2008;**78**(4):045429
- [90] Li C, Liu Y, Yao X, Ito M, Noguchi T, Zheng Q. Interfacial shear strengths between carbon nanotubes. *Nanotechnology*. 2010;**21**(11):115704
- [91] Salvétat J-P, Briggs GAD, Bonard J-M, Bacsá RR, Kulik AJ, Stöckli T, Burnham NA, Forró L. Elastic and shear moduli of single-walled Carbon nanotube ropes. *Physical Review Letters*. 1999;**82**(5):944–947
- [92] Kok ZKJ, Wong CH. Molecular dynamics simulation studies of mechanical properties of different carbon nanotube systems. *Molecular Simulation*. 2016;**42**(15):1274–1280

- [93] Huhtala M, Krasheninnikov AV, Aittoniemi J, Stuart SJ, Nordlund K, Kaski K. Improved mechanical load transfer between shells of multiwalled carbon nanotubes. *Physical Review B*. 2004;**70**(4):045404
- [94] Kis A, Csányi G, Salvétat J-P, Lee T-N, Couteau E, Kulik AJ, Benoit W, Brugger J, Forró L. Reinforcement of single-walled carbon nanotube bundles by intertube bridging. *Nature Materials*. 2004;**3**(3):153–157
- [95] Fonseca AF, Borders T, Baughman RH, Cho K. Load transfer between cross-linked walls of a carbon nanotube. *Physical Review B*. 2010;**81**(4):045429
- [96] Coleman JN, Khan U, Blau WJ, Gun'ko YK. Small but strong: a review of the mechanical properties of carbon nanotube-polymer composites. *Carbon*. 2006;**44**(9):1624–1652
- [97] Moniruzzaman M, Winey KI. Polymer nanocomposites containing carbon nanotubes. *Macromolecules*. 2006;**39**(16):5194–5205
- [98] Vigolo B, Pénicaud A, Coulon C, Sauder C, Pailler R, Journet C, Bernier P, Poulin P. Macroscopic fibers and ribbons of oriented carbon nanotubes. *Science*. 2000;**290**(5495):1331–1334
- [99] Dalton AB, Collins S, Muñoz E, Razal JM, Ebron VH, Ferraris JP, Coleman JN, Kim BG, Baughman RH. Super-tough carbon-nanotube fibres. *Nature*. 2003;**423**(6941):703–703
- [100] Ericson LM, Fan H, Peng H, Davis VA, Zhou W, Sulpizio J, Wang Y, Booker R, Vavro J, Guthy C, Parra-Vasquez ANG, Kim MJ, Ramesh S, Saini RK, Kittrell C, Lavin G, Schmidt H, Adams WW, Billups WE, Pasquali M, Hwang WF, Hauge RH, Fischer JE, Smalley RE. Macroscopic, neat, single-walled carbon nanotube fibers. *Science*. 2004;**305**(5689):1447–1450
- [101] Behabtu N, Young CC, Tsentlovich DE, Kleinerman O, Wang X, Ma AWK, Bengio EA, Ter Waarbeek RF, De Jong JJ, Hoogerwerf RE, Fairchild SB, Ferguson JB, Maruyama B, Kono J, Talmon Y, Cohen Y, Otto MJ, Pasquali M. Strong, light, multifunctional fibers of carbon nanotubes with ultrahigh conductivity. *Science*. 2013;**339**(6116):182–186
- [102] Zhu HW, Xu CL, Wu DH, Wei BQ, Vajtai R, Ajayan PM. Direct synthesis of long single-walled carbon nanotube strands. *Science*. 2002;**296**(5569):884–886
- [103] Li Y-L, Kinloch IA, Windle AH. Direct spinning of carbon nanotube fibers from chemical vapor deposition synthesis. *Science*. 2004;**304**(5668):276–278
- [104] Koziol K, Vilatela J, Moisala A, Motta M, Cunniff P, Sennett M, Windle A. High-performance carbon nanotube fiber. *Science*. 2007;**318**(5858):1892–1895
- [105] Ma W, Liu L, Zhang Z, Yang R, Liu G, Zhang T, An X, Yi X, Ren Y, Niu Z, Li J, Dong H, Zhou W, Ajayan PM, Xie S. High-strength composite fibers: realizing true potential of carbon nanotubes in polymer matrix through continuous reticulate architecture and molecular level couplings. *Nano Letters*. 2009;**9**(8):2855–2861

- [106] Jiang K, Li Q, Fan S. Spinning continuous carbon nanotube yarns. *Nature*. 2002;**419**(6909):801–801
- [107] Zhang M, Atkinson KR, Baughman RH. Multifunctional carbon nanotube yarns by downsizing an ancient technology. *Science*. 2004;**306**(5700):1358–1361
- [108] Li Q, Zhang X, DePaula RF, Zheng L, Zhao Y, Stan L, Holesinger TG, Arendt PN, Peterson DE, Zhu YT. Sustained growth of ultralong carbon nanotube arrays for fiber spinning. *Advanced Materials*. 2006;**18**(23):3160–3163
- [109] Zhao J, Zhang X, Pan Z, Li Q. Wide-range tunable dynamic property of carbon-nanotube-based fibers. *Advanced Materials Interfaces*. 2015;**2**(10):1500093
- [110] Hearle JWS, Hollick L, Wilson DK. *Yarn Texturing Technology*. Boca Raton: CRC Press; 2001
- [111] Zhao J, Zhang X, Di J, Xu G, Yang X, Liu X, Yong Z, Chen M, Li Q. Double-peak mechanical properties of carbon nanotube fibers. *Small*. 2010;**6**(22):2612–2617
- [112] Fang S, Zhang M, Zakhidov AA, Baughman RH. Structure and process-dependent properties of solid-state spun carbon nanotube yarns. *Journal of Physics: Condensed Matter*. 2010;**22**(33):334221
- [113] Miao M, McDonnell J, Vuckovic L, Hawkins SC. Poisson's ratio and porosity of carbon nanotube dry-spun yarns. *Carbon*. 2010;**48**:2802–2811
- [114] Liu H, Li S, Zhai J, Li H, Zheng Q, Jiang L, Zhu D. Self-assembly of large-scale micropatterns on aligned carbon nanotube films. *Angewandte Chemie International Edition*. 2004;**43**(9):1146–1149
- [115] Chakrapani N, Wei B, Carrillo A, Ajayan PM, Kane RS. Capillarity-driven assembly of two-dimensional cellular carbon nanotube foams. *Proceedings of the National Academy of Sciences*. 2004;**101**(12):4009–4012
- [116] Zhang X, Jiang K, Feng C, Liu P, Zhang L, Kong J, Zhang T, Li Q, Fan S. Spinning and processing continuous yarns from 4-inch wafer scale super-aligned carbon nanotube arrays. *Advanced Materials*. 2006;**18**(12):1505–1510
- [117] Liu K, Sun Y, Zhou R, Zhu H, Wang J, Liu L, Fan S, Jiang K. Carbon nanotube yarns with high tensile strength made by a twisting and shrinking method. *Nanotechnology*. 2010;**21**(4):045708
- [118] Li S, Zhang X, Zhao J, Meng F, Xu G, Yong Z, Jia J, Zhang Z, Li Q. Enhancement of carbon nanotube fibres using different solvents and polymers. *Composites Science and Technology*. 2012;**72**(12):1402–1407
- [119] Qiu J, Terrones J, Vilatela JJ, Vickers ME, Elliott JA, Windle AH. Liquid infiltration into carbon nanotube fibers: effect on structure and electrical properties. *American Chemical Society Nano*. 2013;**7**(10):8412–8422

- [120] in het Panhuis M, Maiti A, Dalton AB, van den Noort A, Coleman JN, McCarthy B, Blau WJ. Selective interaction in a polymer—single-wall carbon nanotube composite. *Journal of Physical Chemistry B*. 2003;**107**(2):478–482
- [121] Israelachvili JN. *Intermolecular and Surface Forces*. 2nd ed. San Diego: Academic Press; 1991.
- [122] Ryu S, Lee Y, Hwang J-W, Hong S, Kim C, Park TG, Lee H, Hong SH. High-strength carbon nanotube fibers fabricated by infiltration and curing of mussel-inspired catecholamine polymer. *Advanced Materials*. 2011;**23**(17):1971–1975
- [123] Ryu S, Chou JB, Lee K, Lee D, Hong SH, Zhao R, Lee H, Kim S-G. Direct insulation-to-conduction transformation of adhesive catecholamine for simultaneous increases of electrical conductivity and mechanical strength of CNT fibers. *Advanced Materials*. 2015;**27**(21):3250–3255
- [124] Liu K, Sun Y, Lin X, Zhou R, Wang J, Fan S, Jiang K. Scratch-resistant, highly conductive, and high-strength carbon nanotube-based composite yarns. *American Chemical Society Nano*. 2010;**4**(10):5827–5834
- [125] Naraghi M, Filleter T, Moravsky A, Locascio M, Loutfy RO, Espinosa HD. A multi-scale study of high performance double-walled nanotube-polymer fibers. *American Chemical Society Nano*. 2010;**4**(11):6463–6476
- [126] Zou J, Zhang X, Zhao J, Lei C, Zhao Y, Zhu Y, Li Q. Strengthening and toughening effects by strapping carbon nanotube cross-links with polymer molecules. *Composites Science and Technology*. 2016;**135**:123–127
- [127] Fang C, Zhao J, Jia J, Zhang Z, Zhang X, Li Q. Enhanced carbon nanotube fibers by polyimide. *Applied Physics Letters*. 2010;**97**(18):181906
- [128] Meng F, Zhang X, Li R, Zhao J, Xuan X, Wang X, Zou J, Li Q. Electro-induced mechanical and thermal responses of carbon nanotube fibers. *Advanced Materials*. 2014;**26**(16):2480–2485
- [129] Vilatela JJ, Elliott JA, Windle AH. A model for the strength of yarn-like carbon nanotube fibers. *American Chemical Society Nano*. 2011;**5**(3):1921–1927
- [130] Deng W-L, Qiu W, Li Q, Kang Y-L, Guo J-G, Li Y-L, Han S-S. Multi-scale experiments and interfacial mechanical modeling of carbon nanotube fiber. *Experimental Mechanics*. 2014;**54**(1):3–10
- [131] Jia J, Zhao J, Xu G, Di J, Yong Z, Tao Y, Fang C, Zhang Z, Zhang X, Zheng L, Li Q. A comparison of the mechanical properties of fibers spun from different carbon nanotubes. *Carbon*. 2011;**49**(4):1333–1339
- [132] Motta M, Moisala A, Kinloch IA, Windle AH. High performance fibres from ‘dog bone’ carbon nanotubes. *Advanced Materials*. 2007;**19**(21):3721–3726

- [133] Meng F, Zhao J, Ye Y, Zhang X, Li Q. Carbon nanotube fibers for electrochemical applications: effect of enhanced interfaces by an acid treatment. *Nanoscale*. 2012;**4**(23):7464–7468
- [134] Di J, Fang S, Moura FA, Galvão DS, Bykova J, Aliev A, de Andrade MJ, Lepró X, Li N, Haines C, Ovalle-Robles R, Qian D, Baughman RH. Strong, twist-stable carbon nanotube yarns and muscles by tension annealing at extreme temperatures. *Advanced Materials*. 2016;**28**(31):6598–6605
- [135] Wang Y, Li M, Gu Y, Zhang X, Wang S, Li Q, Zhang Z. Tuning carbon nanotube assembly for flexible, strong and conductive films. *Nanoscale*, 2015;**7**(7):3060–3066
- [136] Zhang L, Wang X, Xu W, Zhang Y, Li Q, Bradford PD, Zhu Y. Strong and conductive dry carbon nanotube films by microcombing. *Small*. 2015;**11**(31):3830–3836
- [137] Di J, Hu D, Chen H, Yong Z, Chen M, Feng Z, Zhu Y, Li Q. Ultrastrong, foldable, and highly conductive carbon nanotube film. *American Chemical Society Nano*. 2012;**6**(6):5457–5464
- [138] Liu W, Zhang X, Xu G, Bradford PD, Wang X, Zhao H, Zhang Y, Jia Q, Yuan F-G, Li Q, Qiu Y, Zhu Y. Producing superior composites by winding carbon nanotubes onto a mandrel under a poly(vinyl alcohol) spray. *Carbon*. 2011;**49**(14):4786–4791
- [139] Wang X, Yong ZZ, Li QW, Bradford PD, Liu W, Tucker DS, Cai W, Wang H, Yuan FG, Zhu YT. Ultrastrong, stiff and multifunctional carbon nanotube composites. *Materials Research Letters*. 2013;**1**(1):19–25
- [140] Cheng Q, Bao J, Park J, Liang Z, Zhang C, Wang B. High mechanical performance composite conductor: multi-walled carbon nanotube sheet/bismaleimide nanocomposites. *Advanced Functional Materials*. 2009;**19**(20):3219–3225
- [141] Cheng Q, Wang B, Zhang C, Liang Z. Functionalized carbon-nanotube sheet/bismaleimide nanocomposites: mechanical and electrical performance beyond carbon-fiber composites. *Small*. 2010;**6**(6):763–767
- [142] Jiang Q, Wang X, Zhu Y, Hui D, Qiu Y. Mechanical, electrical and thermal properties of aligned carbon nanotube/polyimide composites. *Composites Part B*. 2014;**56**:408–412
- [143] Han Y, Zhang X, Yu X, Zhao J, Li S, Liu F, Gao P, Zhang Y, Zhao T, Li Q. Bio-inspired aggregation control of carbon nanotubes for ultra-strong composites. *Scientific Reports*. 2015;**5**:11533
- [144] Wagner HD. Nanocomposites: paving the way to stronger materials. *Nature Nanotechnology*. 2007;**2**(12):742–744
- [145] Murayama T. Dynamic measurement of interfilament friction on staple yarns. *Journal of Applied Polymer Science*. 1979;**24**(6):1413–1417

- [146] Liu Q, Li M, Gu Y, Wang S, Zhang Y, Li Q, Gao L, Zhang Z. Interlocked CNT networks with high damping and storage modulus. *Carbon*. 2015;**86**:46–53
- [147] Guo W, Liu C, Zhao F, Sun X, Yang Z, Chen T, Chen X, Qiu L, Hu X, Peng H. A novel electromechanical actuation mechanism of a carbon nanotube fiber. *Advanced Materials*. 2012;**24**(39):5379–5384

Mechanical Behavior of Nanostructured and Ultrafine-Grained Metal Alloy under Intensive Dynamic Loading

Vladimir A. Skripnyak and Evgeniya G. Skripnyak

Additional information is available at the end of the chapter

<http://dx.doi.org/10.5772/intechopen.68291>

Abstract

Researches of the last years have allowed to establish that the laws of deformation and fracture of bulk ultrafine-grained (UFG) and coarse-grained (CG) materials are various both in static and in dynamic loading conditions. The influence of average grain size on the yield stress, the tensile strength, and the compression strength was established for metal alloys with a face-centered cubic (FCC), a body-centered cubic (BCC), and a hexagonal close-packed (HCP) structures. The study of the microstructure of the alloys after severe plastic deformation (SPD) by the electron backscatter diffraction (EBSD) technique showed the presence of a bimodal grain size distribution in the UFG alloys. Metal alloys with a bimodal grain size distribution possess a negative strain rate sensitivity of the yield stress and higher ductility at quasi-static strain rates. In this chapter, we will discuss the regularities of deformation at high strain rates, damage, and fracture of ultrafine-grained alloys.

Keywords: nanostructured metals, ultrafine-grained alloys, severe plastic deformation, high strain rates, yield stress, spall strength

1. Introduction

During the last decade, the interest in research of mechanical behavior of ultrafine-grained (UFG) and nanostructured (NS) metal alloys has been risen sharply [1–13]. Compared to their coarse-grained counterparts, UFG and NS metals exhibit significantly higher static yield strength, hardness, but lower tensile elongation. Ultrafine-grained materials produced by severe plastic deformation (SPD) methods exhibit a high strength, good damping properties, and superplastic properties over a limited range of strain rates at high temperatures. The increase of UFG material strength can be explained on the behavior of dislocation at submicrometer grain size. Laws of plastic deformation operating at room temperature for

coarse-grained metals usually are based on dislocation mechanisms [1–9]. When grain size is decreased in nanometer range, dislocation activity becomes difficult. Therefore, plastic deformation resulting to dislocation nucleation and motion limits ductility of NS and UFG materials. Strain rate sensitivity of flow stress also depends on grain size [9–11].

Similarity of mechanical behavior of materials in wide range of loading conditions takes place for metals combining into several groups [14]. Metal alloys with face-centered cubic (FCC), body-centered cubic (BCC), and hexagonal close-packed (HCP) crystalline lattices can be related to three groups. Mechanical behavior of these groups of metals has to be described by various constitutive models [2–4]. We can expect that UFG metals with FCC, BCC, and HCP lattices will have various laws of plastic deformation at high strain rates also.

Mechanical behavior of NS and UFG materials under shock wave loading requires understanding of fundamental laws of the deformation and failure mechanisms at high strain rates.

2. Mechanical behavior of nanostructured and ultrafine-grained metal alloys

Important information about mechanical behavior of nanostructured and ultrafine-grained materials under dynamic loading is contained in the experimental data on high-speed interaction of plates; results of tests on compression and tension by using a split-Hopkinson pressure bar (SHPB), also known as Kolsky bar test; and results of tests using high-rate servo-hydraulic machine Instron VHS.

Experimental results obtained from the tests of metals and alloys by these methods showed that the patterns of deformation in ultrafine-grained and coarse-grained materials are different not only under quasi-static but also intense dynamic loading.

The free surface profiles of shock wave in the UFG Ti-6Al-2Sn-2Zr-2Mo-Si titanium alloy are shown in **Figure 1**.

The metal plate was loaded with shock pulses, which were obtained by the impact of thin aluminum. The metal plate was loaded with shock pulses, which were obtained at impact thin aluminum plates at a speed of $650 \pm \text{m/s}$ [13, 15].

The movement of the back surface of the plates when exposed to a shock pulse was recorded using a laser Doppler interferometer VISAR with subnanosecond time resolution [15].

Shock wave in UFG alloys has the two-wave structure as in CG alloys. The shock wave in the UFG alloys has a double structure in coarse-grained alloys. Elastic precursor propagates with the longitudinal sound speed. The bulk compression wave or the plastic wave propagates through compressed material with the bulk speed of sound.

Curves 1 and 2 correspond to specimens with grain size $\sim 300 \text{ nm}$, and the Curve 3 corresponds to coarse-grained specimen with grain size of $20 \mu\text{m}$ [13, 15]. The thicknesses of UFG specimens 1 and 2 were 0.835 and 6.36 mm, respectively. The thickness of coarse-grained specimen was 10 mm.

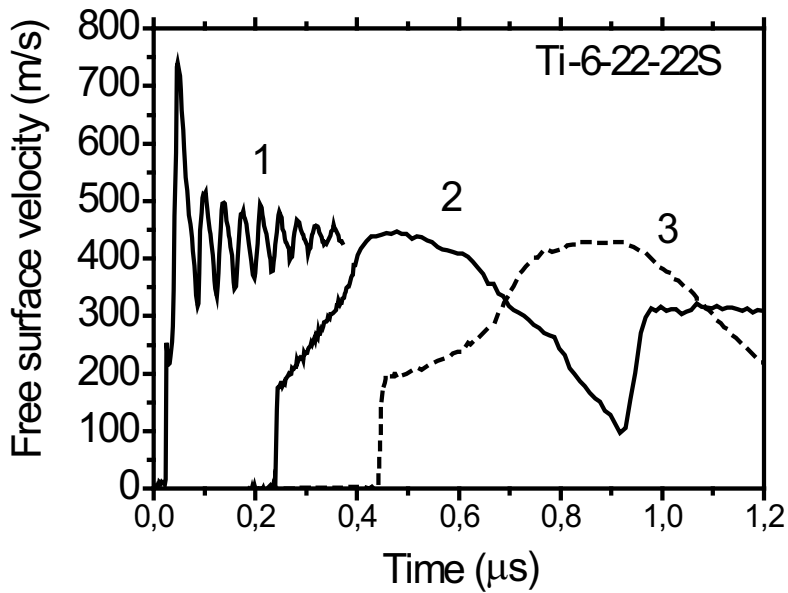


Figure 1. Free surface velocity profiles.

The Hugoniot elastic limit (HEL) (dynamic elastic limit) for an elastic plastic material can be calculated by the formula [15, 16]

$$\sigma_{HEL} = (1/2)\rho_0 C_L u_{pHEL} \tag{1}$$

where σ_{HEL} is the Hugoniot elastic limit, ρ_0 is the initial mass density, C_L is the longitudinal speed of sound, and $u_{pHEL} = u_{fsHEL}/2$ is the maximum particle velocity in the elastic precursor.

The average strain rate in the elastic precursor is measured by the ratio [16]

$$\dot{\epsilon}_{eq}^{HEL} = \frac{1}{2} \frac{u_{pHEL}}{C_L \Delta t_{HEL}}, \tag{2}$$

where Δt_{HEL} is a time, which is achieved by the amplitude of the elastic precursor.

The calculated ratio of the bulk modulus of nanostructured titanium to the bulk modulus of coarse-grained titanium agrees with experimental data. Sound velocities of materials can be calculated by relations [16]

$$c_s = \sqrt{\mu/\rho}, \quad c_b = \sqrt{B/\rho}, \quad c_L = \sqrt{c_b^2 + (4/3)c_s^2} \tag{3}$$

where C_s , C_b , C_L are the shear, bulk, and longitudinal sound velocities; B is the bulk modulus; and μ is the shear modulus.

The effective bulk modulus B of nanostructured material can be determined by the equation

$$B = B^{(c)}C^{(c)} + B^{(g)}C^{(g)} + B^{(tj)}C^{(tj)}, \quad (4)$$

where $B^{(c)}$ is the isentropic bulk modulus of a crystalline phase; $B^{(g)} \approx 0.45B^{(c)}$ and $B^{(tj)} \approx 0.5B^{(c)}$ are the bulk modulus of a grain boundary phase and the bulk modulus of material near the triple junctions correspondingly; and $C^{(c)}$, $C^{(g)}$, and $C^{(tj)}$ are the volume fractions of these phases correspondingly.

The volume fraction of the triple junction and the volume fraction of grain boundaries were described by the equations

$$C^{(g)} = \beta^{(g)} \exp(-\alpha^{(g)} d_g / b), \quad (5)$$

$$C^{(tj)} = \beta^{(tj)} \exp(-\alpha^{(tj)} d_g / b), \quad (6)$$

where d_g is the grain size; b is the modulus of the Burgers vector; and $\beta^{(g)}$, $\beta^{(tj)}$, $\alpha^{(g)}$, and $\alpha^{(tj)}$ are the constants of a material.

The values of $C^{(g)}$ and $C^{(tj)}$ versus grain size are shown in **Figure 2**.

As the grain size is decreased into the nanometer range (<100 nm), the volume of grain interfaces sufficiently increased. The calculated ratio of the bulk modulus of nanostructured materials to the bulk modulus of coarse-grained materials is demonstrated in **Figure 2**.

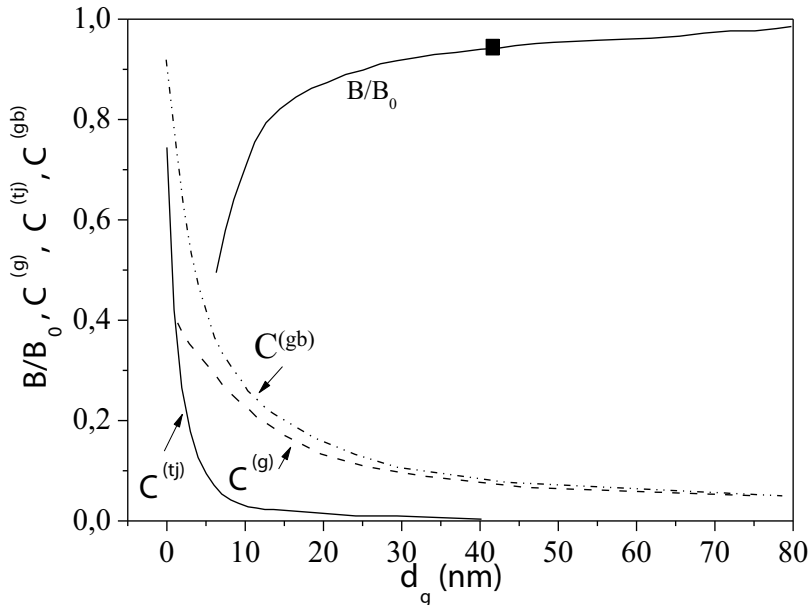


Figure 2. Volume fractions of grain boundary phases versus grain size for titanium. Filled square denotes the experimental data [17].

From Eqs. (3)–(6), it follows that the longitudinal and bulk sound velocities for the UFG and CG alloys differ insignificantly. Thus, in the absence of pores and microcracks, UFG and CG alloys have close values of mass density, elastic moduli, and sound velocities C_s , C_b , and C_L .

The dynamic yield stress of the material σ_y acting on the shock adiabat is determined by the formula [15, 16]

$$\sigma_Y = \sigma_{HEL} \frac{1 - 2\nu}{1 - \nu}, \quad (7)$$

where ν is Poisson's ratio.

The experimental results in **Figure 1** showed that the UFG and CG titanium alloys have similar amplitude values of the elastic precursors at the equivalent distances to the free surface of the samples. Thus, the Hugoniot elastic limits of UFG and CG titanium alloys can be the same. But the quasi-static yield strength of titanium alloys depends on grain size in accordance with the Hall-Petch relation, as shown in **Figure 3**.

Filled symbols show experimental data for titanium alloys [13, 18] and magnesium alloys [7, 8, 19].

Experimental investigations indicate that the prevailing deformation mechanisms are changed for the grain size below ~100 nm. The Hall-Petch relation (Eq. (8)) is satisfied for many polycrystalline materials, but the values of coefficients σ_0 and k are changed at the

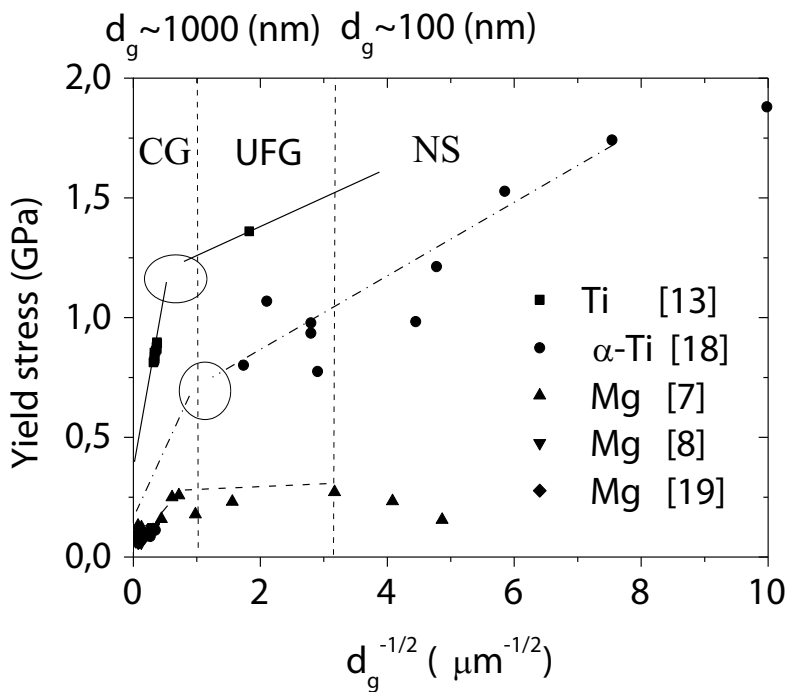


Figure 3. The yield strength of HCP alloys versus the inverse square root of the grain size.

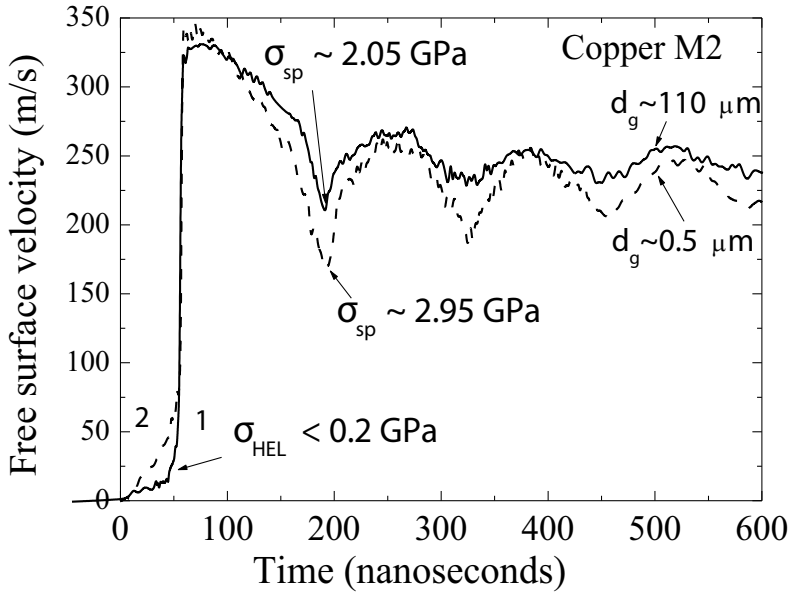


Figure 4. Free surface velocity versus time in UFG and CG copper.

grain size about several hundred nm (range UFG) and 30–20 nm (range NS) as shown in **Figure 3**. Filled symbols show experimental data for titanium alloys [13, 18] and magnesium alloys [7, 8, 19]:

$$\sigma_s = \sigma_0 + kd_g^{-1/2}, \quad (8)$$

where σ_0 is the yield strength, d_g is the grain size, σ_0 , and k are the material constants.

Figure 4 shows shock wave profiles in UFG and CG copper specimens [15, 20, 21]. Copper refers to isomechanical group of materials with the FCC lattice [15]. Curve 1 corresponds to UFG structure of specimen with grain size of ~ 500 nm. Curve 2 is received for a material in which fine grains occupied only 85% of volume. These experimental results testify that the Hugoniot elastic limit (HEL) and the spall strength (σ_{sp}) of copper sharply decrease with the decrease of the relative volume occupied with UFG structure.

The solid Curve 1 corresponds to CG specimen, and dashed Curve 2 corresponds to UFG specimen. The HEL of UFG copper M2 (~ 0.4 GPa) is about twice that of polycrystalline alloy.

Precipitate-strengthened aluminum, magnesium alloys, copper, and some other metals possess a high strength and ductility. The presence of nanoparticles and precipitate phases influences on the yield stress and the spall strength of UFG alloys under shock wave loadings.

In **Figure 5**, shock wave profiles in precipitate-strengthened aluminum alloy AA6063T6- $AlMg_{0.5}Si_{0.4}$ are shown [6].

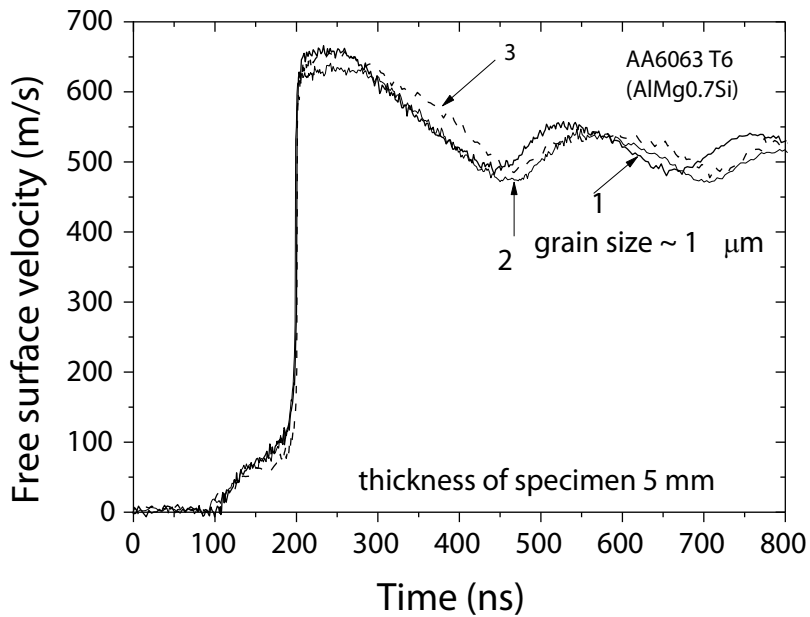


Figure 5. Free surface velocities versus time in UFG and CG aluminum alloy AA6063 T6.

Curves 1, 2, and 3 correspond to AA6063T6 alloy after two and eight passes of equal-channel angular pressing (ECAP) and without ECAP, respectively. Coarse-grained alloy specimens had a grain size of $\sim 100 \mu\text{m}$. UFG structure was created by repeated ABC ECAP passes. Nanoparticles of Mg_2Si were formed by means of thermal treatment of alloy before ECAP treatment. The HEL of coarse-grained AA6063T6 was equal to $\sim 0.33 \text{ GPa}$, and the spall strength was equal to $\sim 1.29 \text{ GPa}$, whereas the HEL values of UFG alloy were $\sim 5.7\%$ higher ($\sim 0.35 \text{ GPa}$), and the spall strength was equal to $\sim 1.48 \text{ GPa}$. Thus, the spall strength and the yield strength of UFG alloys depend not only on grain size but also on concentration and sizes of phase precipitates.

The Hugoniot elastic limit of ultrafine-grained metal alloys and their coarse-grained counterparts is not significantly different. The rate of elastic precursor attenuation is above in UFG alloys, than in coarse-grained counterparts.

The tensile strength at high strain rate can be determined from the analysis of shock wave profiles shown in **Figures 1, 4, and 5**. These values correspond to the spall strength. The spall strength is determined by formulas [15, 16]

$$\sigma_{sp} = (1/2)\rho_0 C_b (\Delta u_{fs} + \delta), \quad \delta = (h/C_b - h/C_L) \cdot |\dot{u}_1|, \quad (9)$$

where σ_{sp} is the spall strength; ρ_0 is the initial mass density; C_b is the bulk speed of sound in the shock-compressed material; Δu_{fs} is the difference between the maximum speed of the free surface of the target and speed in front of the spall pulse; δ is the amendment, to account for

the velocity gradients at the free surface in front of spall pulse and in the front; h is the thickness of the target; C_L is the longitudinal sound velocity; and \dot{u}_1 is the change in the free surface velocity in time in front of the spall pulse.

The spall strength σ_{sp} of copper specimen with grain size of 500 nm is ~ 2.95 GPa, whereas the spall strength of specimen with grain size of 100 μm is only ~ 2.05 GPa. The spall strength of UFG and CG copper is shown in **Figure 6**.

The spall strength of UFG and CG and single crystal aluminum alloys is shown in **Figure 7**.

Filled symbols show experimental data for Al single crystal [15], AD1 [15], AMg6 [15], and AA6063T6 [6].

These results correlate with data on the increasing of the quasi-static yield stress of FCC metals at a decrease of grain sizes (**Figure 8**). Experimental data [4–6, 18, 20, 21] for copper and aluminum alloys are shown by the filled symbols.

Changes of curve slope both FCC and HCP metal alloys (**Figures 3 and 8**) testify to peculiarities of the mechanical behavior of UFG alloys when the grain size varied from 1000 to ~ 10 nm.

Bulk UFG alloys usually have a dispersion of grain size appearing at their manufacturing by severe plastic deformation (SPD) methods. A specific volume, which is occupied with UFG structure, influences on the HEL and the spall strength of alloys.

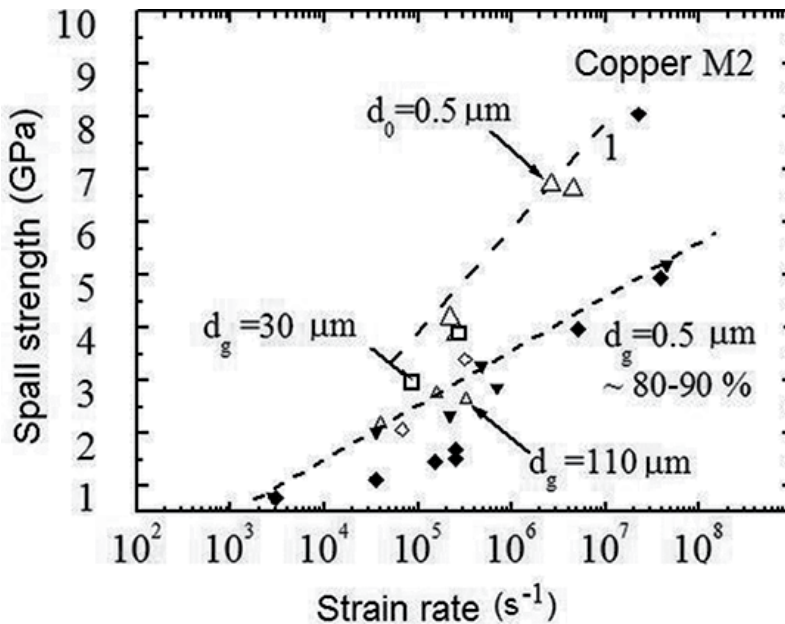


Figure 6. The spall strength of UFG and CG copper.

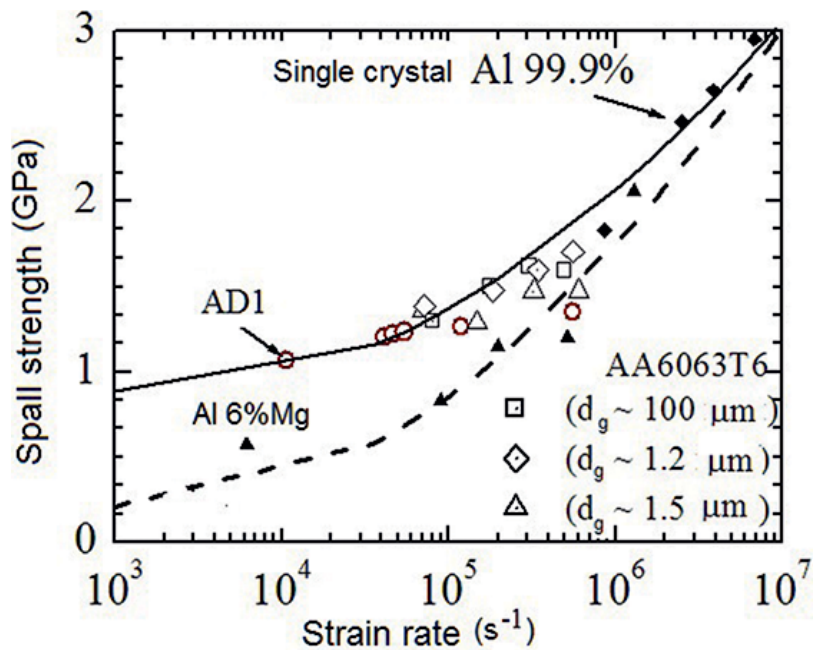


Figure 7. The spall strength of UFG and CG aluminum alloy AA6063 T6.

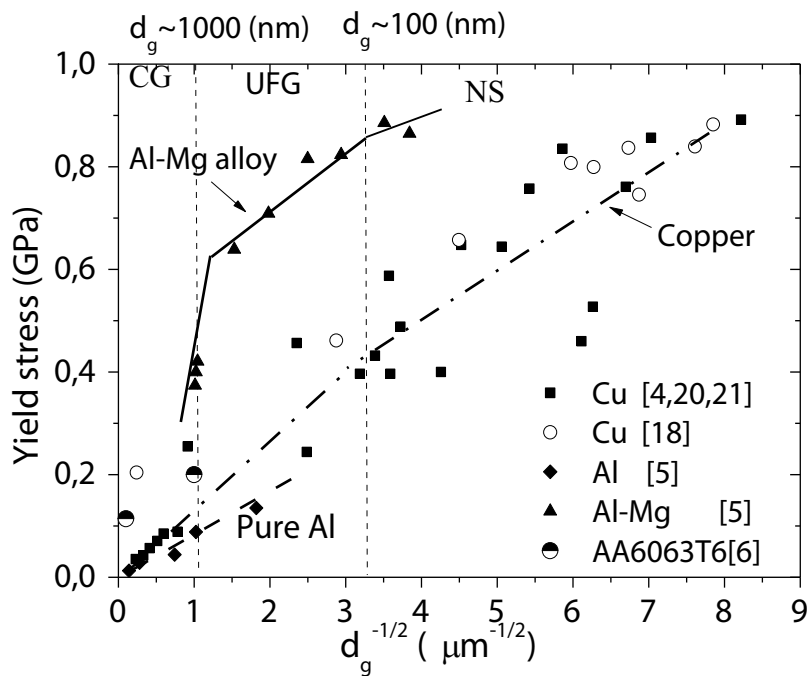


Figure 8. The yield strength versus the inverse square root of the grain size.

3. Dissipation of mechanical energy during deformation of ultrafine-grained and coarse-grained titanium and zirconium alloys

Research of deformation localization and fracture mechanisms of NS and UFG alloys was investigated by a combination of structure-sensitive methods [1, 2, 22–27]. The high sensitivity of modern infrared (IR) thermal vision systems in combination with the opportunity of noncontact continuous temperature and strain measurements gives us important information on processes of damage and fracture. Recently, it has been shown that UFG titanium has a peak of an internal friction at temperatures of 450–500°C, which results from the processes of recovery and recrystallization [22]. Experimental data were obtained about the deformation and thermal characteristics of the UFG and CG VT1-0 alpha titanium alloy and E110 zirconium alloy [26–28]. The mechanical tests were performed by means of servo-hydraulic machine Instron VHS 40/50–20. These specimens were nanostructured by means of a combined method of severe plastic deformation (SPD).

The residual stresses in the specimens were relieved by means of annealing. Samples from UFG titanium and zirconium were converted to coarse grain using a high-temperature annealing. The forces were registered by the sensor DYNACELL with accuracy up to 0.2%.

The obtained curves of true stress—true strain were used for determination of the yield strength, the strength, and the strain to failure. The temperature distributions on the specimen surface under tension with constant strain rate were registered by using the FLIR system SC7700M series infrared camera.

IR thermograms were registered with maximum recording frequency of 115 Hz. The resolution was ~20 micron and the image format is of 640 × 512 mm.

The thermal camera was at a distance of 0.4 m from the specimen. The software of the FLIR system SC7700M was used for interpretation of the registered data [24]. The reflection surface of the samples was close to the “absolutely black body” through the use of carbon blackening.

The thermal vision system allowed one to record not only the specimen’s surface temperature distribution but also the current dimensions of specimen during the deformation. The specimen size, the loading force, and the loading times were recorded in the process of quasi-static tensile tests. Engineering true stress, strain, and true strain were calculated using recorded data.

True stress-strain curves of coarse-grained VT1-0 titanium and E110 zirconium specimens under tension are shown in **Figures 9** and **10**, respectively. True stress-true strain curves are marked as Curve 1. Curve 2 corresponds to the engineering stress and strain diagrams. **Figures 9** and **10** also showed the temperature distribution on the surface of the samples for several increasing strains.

Temperature change is caused by dissipation of mechanical energy during plastic deformation.

The stress-strain curve has a parabolic ascending branch, which passes into the descending portion having a negative coefficient of strain hardening. True stress-strain diagrams of UFG

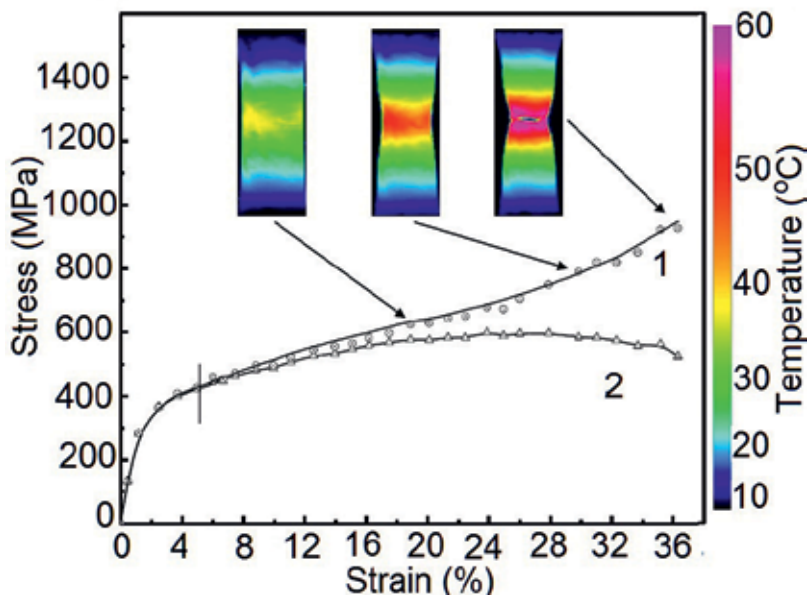


Figure 9. Stress-strain curves of coarse-grained VT1-0 titanium.

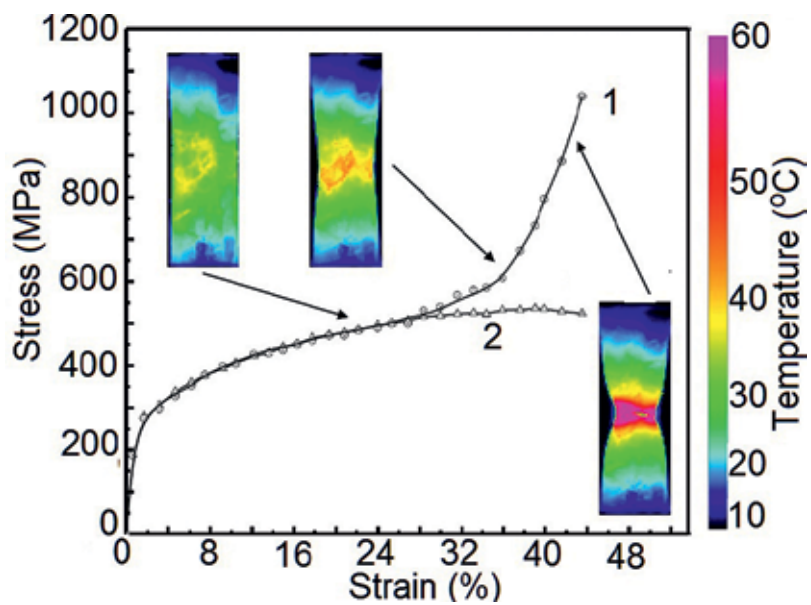


Figure 10. Stress-strain curves of coarse-grained E110 zirconium.

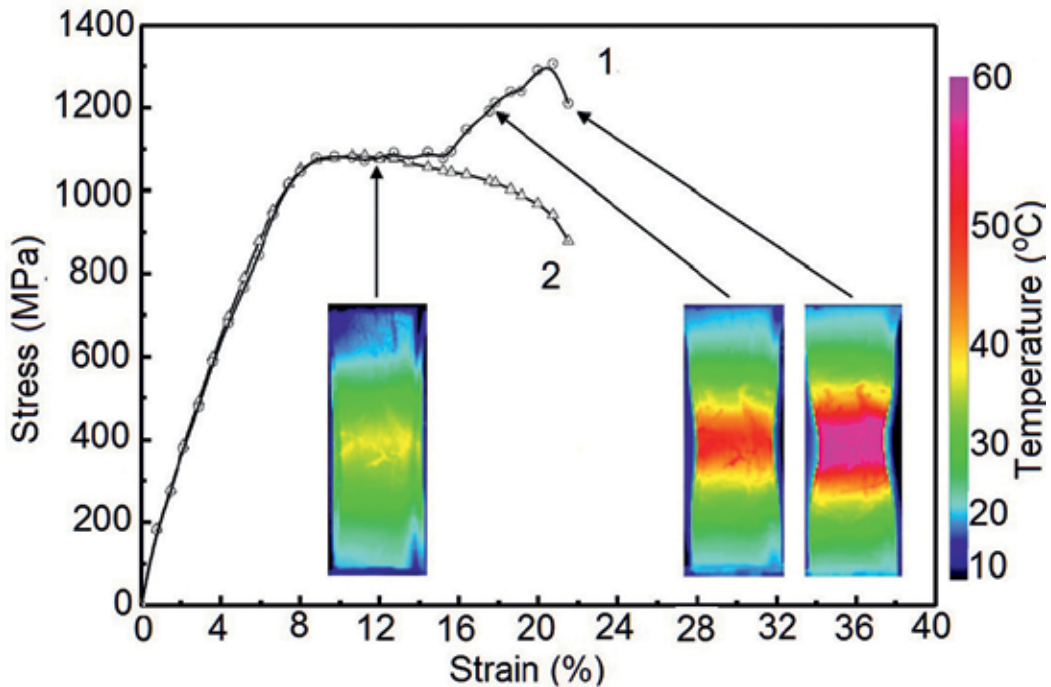


Figure 11. Stress-strain diagrams of ultrafine-grained VT1-0 titanium alloy.

VT1-0 titanium and E110 zirconium specimens under tension are shown in **Figures 11** and **12**, respectively.

Curves of true stress-true strain are shown as Curve 1. Curves of engineering stress and strain are marked as Curve 2. The insets show the temperature distribution on the specimen surface under certain deformations.

Dimensions of specimens at thermograms for UFG titanium and zirconium alloys showed that the fractional decrease in the area at fracture of specimens is twice less ones in comparison with values of CG alloys. Deformation localization in the zone of necking caused a significant growth of true flow stress and increase of the hardening coefficient. Deformation localization is accompanied by local temperature rise.

The maximum temperature on the surface of CG titanium specimen raised proportionally to the strain rate up to a certain level (in the range from 50 to 55°C) and then increased sharply on ~5–10°C (up to the temperature 58.45–60.54°C) due to the localization of the plastic deformation near damages or crack.

The analyses of IR thermograms showed that character of temperature changing under deformation of UFG and CG titanium specimens is different. These results indicate that macroscopic regularities of strain localization in the UFG and CG titanium and zirconium alloys differ.

The maximum temperature of the UFG sample is directly proportional to strain rate and reaches a temperature of 50–58 °C, after that the temperature did not change much [28].

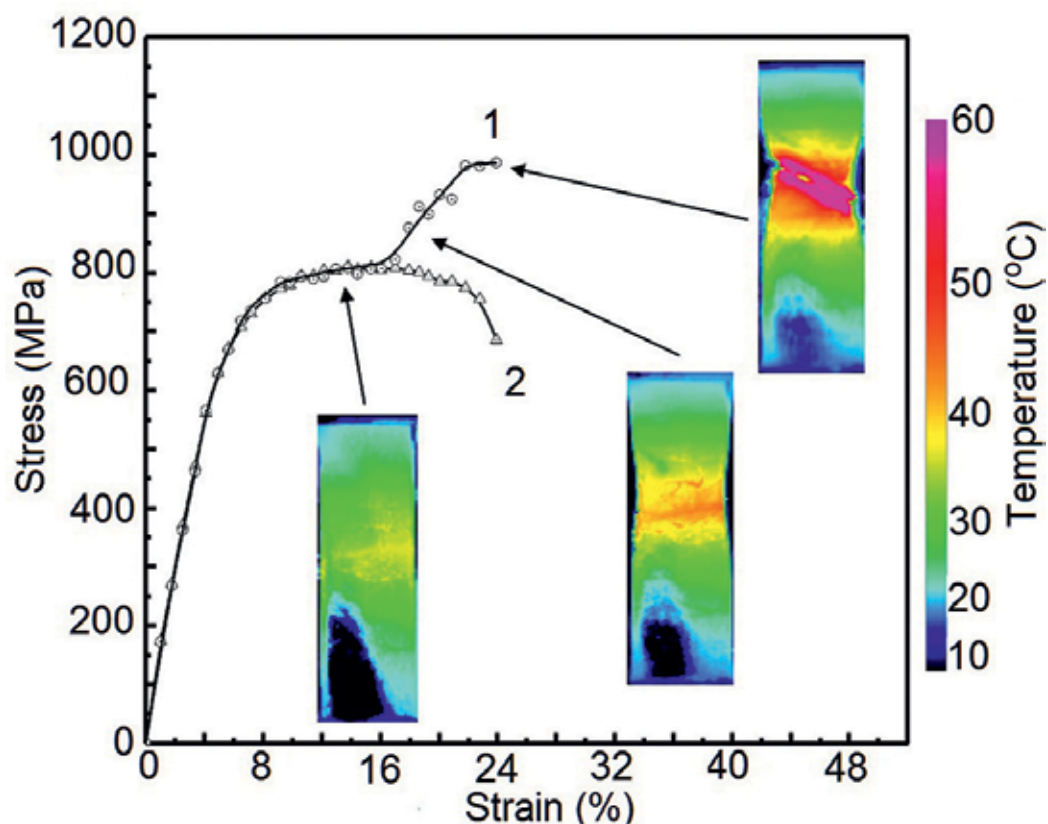


Figure 12. The diagram of ultrafine-grained E110 zirconium alloy.

Figure 13 shows the SEM images of fracture surfaces of UFG titanium alloy and UFG zirconium alloy. Chains of micropores and microcracks are present on the fracture surface.

The maximum temperature at the surface of UFG zirconium alloy specimen increased from 40 to 68°C; then, there was an abrupt temperature decrease. This effect is caused by rapid damage accumulation and formation of macrocrack.

The grain size distributions of UFG zirconium and titanium specimens differ due to imperfect process of the intensive plastic deformation [29].

The results of the SEM study of fracture surface confirmed the difference of damage in the samples of UFG titanium and zirconium alloys.

The results of fractographic studies of the fracture surfaces and the results of quasi-static and dynamic tests prove that the fracture of UFG FCC and HCP alloys has the ductile character.

The experimental and theoretical results can be used to develop in defining equations for the UFG alloys over the last decade.

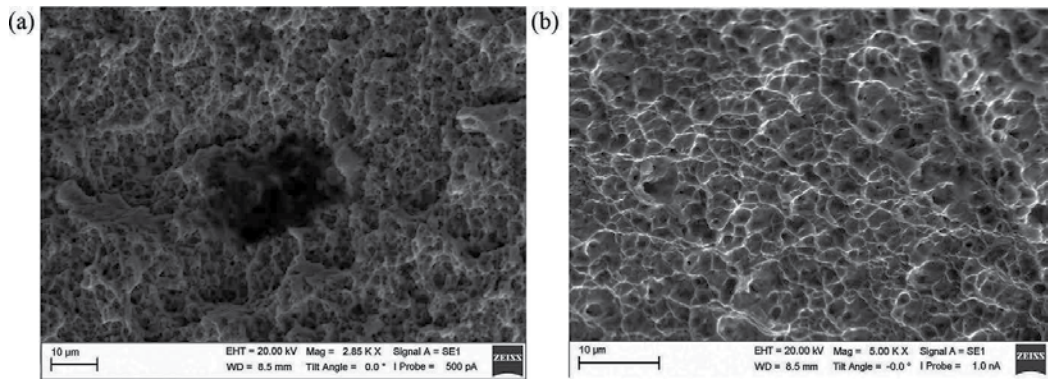


Figure 13. SEM image of the fracture surface. (a) Specimen of UFG VT1-0 titanium and (b) specimen of UFG E110 zirconium.

4. The constitutive equation for ultrafine-grained alloys covering a wide range of strain rates

The computational model is required to predict the mechanical behavior of ultrafine-grained FCC, HCP, and BCC alloys under dynamic loading. Therefore, constitutive equations taking into account the grain size of metal alloys were offered by Meyers et al. [4, 18], Armstrong and Zerilli [30], and Khan et al. [31, 32]. Mishra et al. modified the model of Johnson-Cook [33]. A satisfactory quantitative description of the mechanical behavior of FCC and HCP alloys with coarse-grained and ultrafine-grained structure can be achieved by changing parameters of the materials. This limits opportunities to use models for the prediction of mechanical behavior of ultrafine-grained titanium alloys under dynamic loadings.

Obtaining realistic predictions of yield and strength in a wide range of strain rates remains an important problem.

We have developed model of mechanical behavior of the alloys for studying of laws of deformation and fracture of UFG alloys in a wide range of strain rates [12, 34–36].

The approach of damaged medium with stress relaxation for numerical simulation of solid response under shock wave loading was used. The stress of material particle is considered as a result of two competitive processes. Increasing of stresses and internal energy is caused by external impacts. Relaxation of the shear stress and energy dissipation are caused by the increments of inelastic deformation.

The model uses the effective parameters of mechanical state and averaged parameters of mechanical properties (mass density, elastic constants, Grüneisen parameter, etc.).

We consider the possibility of damage accumulation during inelastic deformation of NS and UFG metals in consequence of limited ductility.

The local damage parameter D was used in the scalar form

$$D = \Delta \varepsilon^p / \varepsilon_f, \quad (10)$$

where $\Delta \varepsilon^p = \int_{t_0}^t \dot{\varepsilon}_{eq}^p dt$, $\dot{\varepsilon}_{eq}^p$ is the equivalent of inelastic strain rate tensor, and ε_f is the average value of an inelastic strain of a material particle at fracture.

The local failure criterion of a material particle was used in the form

$$D = 1 \quad (11)$$

The constitutive equation of UFG alloy was determined for material particle in the form

$$\sigma_{ij} = \sigma_{ij}^{(m)} \varphi(D), \quad \sigma_{ij}^{(m)} = -p^{(m)} \delta_{ij} + S_{ij}^{(m)}, \quad (12)$$

where σ_{ij} is components of the stress tensor, p is the pressure, S_{ij} is components of the deviatoric part of the stress tensor, δ_{ij} is the Kronecker delta, $\varphi(D)$ is the function of damage, and the parameters with index m correspond to the condensed phase of the damaged material.

The equation of state, Mie-Grüneisen, was used to calculate the pressure [16]. The relaxation equation was used to calculate the deviator of the stress tensor in the undamaged phase material:

$$dS_{ij}^{(m)} / dt = 2\mu^{(m)} (\dot{\varepsilon}_{ij}^{(m)} - \dot{\varepsilon}_{ij}^{p(m)}), \quad (13)$$

where d/dt is the Jaumann derivative, $\mu^{(m)}$ is the shear modulus of the undamaged phase material, $\dot{\varepsilon}_{ij}^{(m)}$ is components of the strain rate tensor, and $\dot{\varepsilon}_{ij}^{p(m)}$ is components of the inelastic strain rate tensor.

The deviator of the inelastic strain rate tensor was calculated in the framework of the theory of Hencky-Ilyushin:

$$\dot{\varepsilon}_{ij}^{p(m)} = (3/2) [S_{ij}^{(m)} \dot{\varepsilon}_{eq}^{p(m)} / \sigma_{eq}], \quad (14)$$

$$\sigma_{eq} = [(3/2) S_{ij}^{(m)} S_{ij}^{(m)}]^{1/2}. \quad (15)$$

The scalar function $\dot{\varepsilon}_{eq}^{p(m)}$ is defined by the sum of the components basing on physical modes of inelastic deformation by relations:

$$\begin{aligned} \dot{\varepsilon}_{eq}^{p(m)} &= \sum_k [\dot{\varepsilon}_{eq}^p]_k \Delta F_k, \\ [\dot{\varepsilon}_{eq}^p]_k &= [\dot{\varepsilon}_{eq}^p]_{disl} + [\dot{\varepsilon}_{eq}^p]_{disl\ nucl} + [\dot{\varepsilon}_{eq}^p]_{tw}, \\ \Delta F_k &= \int_{d_{gk-1}}^{d_{gk+1}} f(d_g) d(d_g), \end{aligned} \quad (16)$$

where $f(d_g) = 1 - \exp(-[(d_g - d_{g \min})/\delta]^{-n})$ and δ , $d_{g \min}$, and n are parameters of grain size distribution function, $\dot{\epsilon}_{eq}^p$ is the equivalent rate of plastic strain rate, $\left[\dot{\epsilon}_{eq}^p\right]_{disl}$ is the equivalent rate of plastic strain rate due to dislocation movement, $\left[\dot{\epsilon}_{eq}^p\right]_{dislnucl}$ is the equivalent rate plastic strain rate due to heterogeneous dislocation nucleation, and $\left[\dot{\epsilon}_{eq}^p\right]_{tw}$ is the equivalent rate of plastic strain rate due to twinning.

We used experimental function $f(d_g)$ of grain size distribution in UFG metal alloys treated by the equal channel angular pressing (ECAP). The grain size distribution and the average grain size are varied after several passes of ECAP [4]. Therefore, the total increments of inelastic deformation will depend on specific volume of small grains.

Peculiarity of deformation laws of FCC and HCP groups of metals has to be described by various kinetics (Eq. (17)). Equations can be used in phenomenological relation forms [12, 14]:

$$\begin{aligned}
 \left[\dot{\epsilon}_{eq}^p\right]_{dislmov} &= gbv\rho_m \exp(-\Delta G_1/RT), \\
 \Delta G_1 &= \Delta G_0 [1 - (\sigma_{eq}/\sigma^*)^{n_1}]^q, \\
 \left[\dot{\epsilon}_{eq}^p\right]_{dislnucl} &= gb\dot{\rho}(\ell) \exp(-\Delta G_2/kT), \\
 \left[\dot{\epsilon}_{eq}^p\right]_{tw} &= A_{tw} \exp(-\Delta G_3/RT) \times [1 - \sigma_{eff}/\sigma^{**}(d_{gk}, T, P)]^{m_1}, \\
 \sigma_{eq}^* &= \sigma_{eq}^* 0 + kd_{gk}^{-1/2}, \quad \sigma_{eff} = \sigma_{eq} - \Delta\sigma_{bs}, \\
 \sigma^{**} &= \sigma_0^* + k_1 d_{gk}^{-1/2} + k_2 (\epsilon_{eq}^p)^{1/2} + k_3 p^{1/2}, \\
 \Delta\sigma_{bs} &= k_1 d_{gk}^{-1/2} + k_2 (\epsilon_{eq}^p)^{1/2} + \Delta\sigma_{bspr},
 \end{aligned} \tag{17}$$

where R is the gas constant; k is the Boltzmann constant; T is temperature; b is the modulus of Burgers vector; $g \approx 0.5$ is the orientation coefficient; G_0 and G_2 are specific activation energy of dislocation movement and nucleation, respectively; v is the average dislocation velocity; G_3 is the specific activation energy of twinning; d_g is the grain size; ρ_m is a density of dislocation movement; $\dot{\rho}$ is the rate of dislocation nucleation; and A_{tw} , n_1 , m_1 , q are the material constants.

Constants n , q , ΔG_0 , and ΔG_2 are varied for FCC and HCP metals [14].

The precipitate hardening of metals can be described by Orowan's equation [37]:

$$\Delta\sigma_{bspr} = 0.4\mu bM \ln(2r/b) / (\pi\lambda\sqrt{1-\nu}), \quad \lambda = \left(\sqrt{3\pi/4f} - 1.64\right)r, \tag{18}$$

where μ is the shear modulus, b is the modulus of Burgers vector, M is the material constant, r is the radius of particles, f is the concentration of particles, and ν is Poisson's ratio.

In Refs. [12–14], numerical values of model parameters have been discussed for UFG titanium alloys. Used numerical method has been discussed in [12]. Chemical composition of alloys is shown in **Table 1**.

The grade	Element wt.-%										
	Al	Sn	Zr	Mo	Cr	Si	Fe	O	N	C	Other
Ti-6-22-22S	5.75	1.96	1.99	2.15	2.10	0.13	0.04	0.082	0.006	0.009	
VT1-0	-	-	-	-	-	0.08	0.12	0.1	0.04	0.05	0.1

Table 1. Chemical composition of Ti-6-22-22S and VT1-0 titanium alloys.

Eqs. (10)–(17) were used for numerical simulation of high velocity impacts of plates. Calculated profiles of shock pulses in UFG titanium alloy are shown in **Figure 14**.

In simulated loading condition, UFG Ti-6-22-22S of 0.835 and 6.36 mm thicknesses was impacted by aluminum plates with 0.12 and 0.835 mm thicknesses at impact velocities of about 1250 and 680 m/s [15]. Dashed and solid curves indicate calculated and experimental profiles, respectively.

Results of computer simulation of shock loading of UFG alloys testify that fast relaxation of elastic precursor amplitude takes place at the first millimeter. Fast attenuation of elastic precursor can be explained by high rate of dislocation nucleation at grain sizes of several hundreds of nanometers.

Unlike coarse-grained alloys, strain hardening of fine-grained alloys at deformation under shock loading of several GPa is not enough. Satisfactory description of spall fracture was

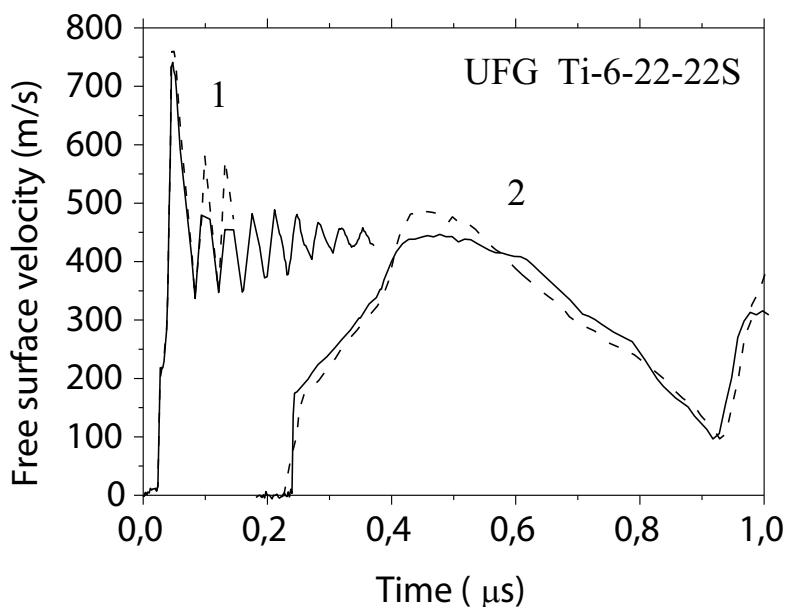


Figure 14. Measured (solid lines) and simulated (dashed lines) free surface velocity histories for UFG Ti-6-22-22S [12].

achieved in calculation too, in spite of a quasi-elastic unloading. We have not found considerable Bauschinger effect.

Figure 15 showed calculated stress-strain curves for Ti-6-22-22S. Solid curves correspond to experimental data. Dashed curves correspond to results of calculation.

Stress-strain curves for UFG Ti-6-22-22S have a good agreement with experimental data at strain rates within the range from 10^{-3} to 10^3 s^{-1} . Eqs. (15)–(16) allow us to describe the work hardening of titanium alloys in the range of deformation before necking.

Figure 16 showed calculated stress-strain curves for VT1-0 titanium alloy.

Eqs. (15)–(16) describe the flow stress dependence on the strain rates and the plastic strains. Results of simulation of deformation of VT1-0 titanium alloy are shown in **Figure 16**.

Experimental stress-strain curves are shown as solid curves. The dashed lines 1 were obtained under assumption that k in the relation (Eq. (8)) is the constant for UFG and CG alloys. The dashed line 2 was obtained under assumption that k decreased when grain size became less $1 \mu\text{m}$. These results are consistent with the experimental data for the UFG alloy, shown in **Figure 3**.

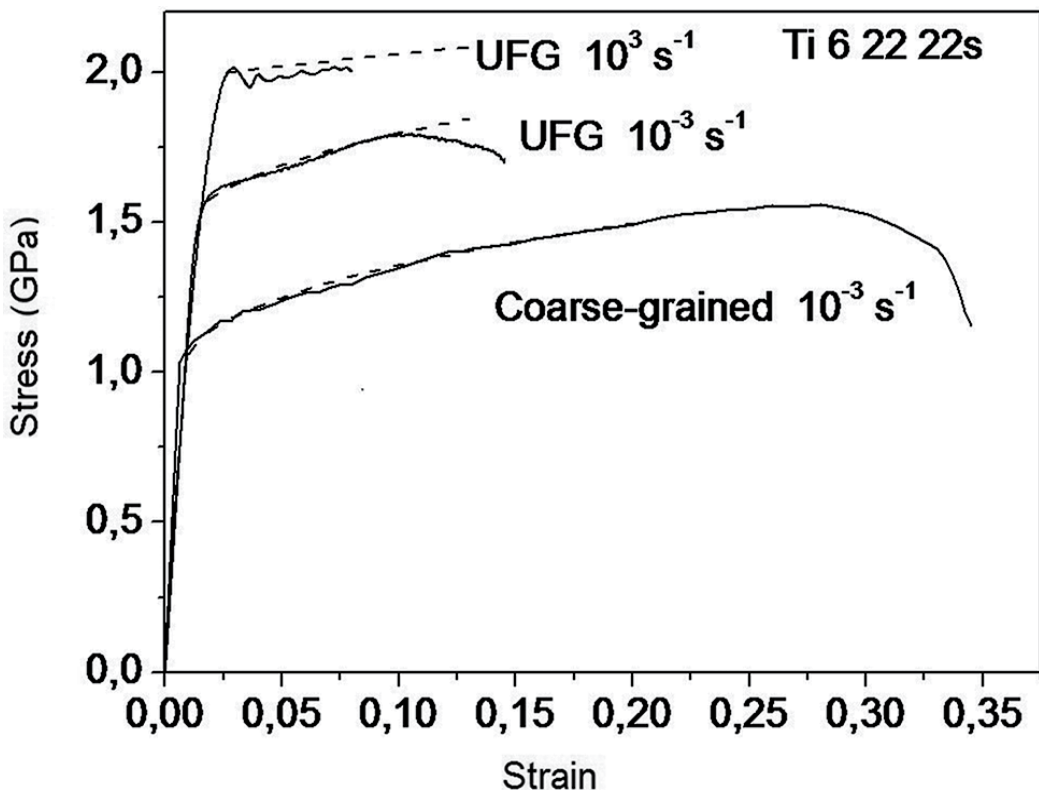


Figure 15. Stress versus strain of Ti-6-22-22S titanium alloy.

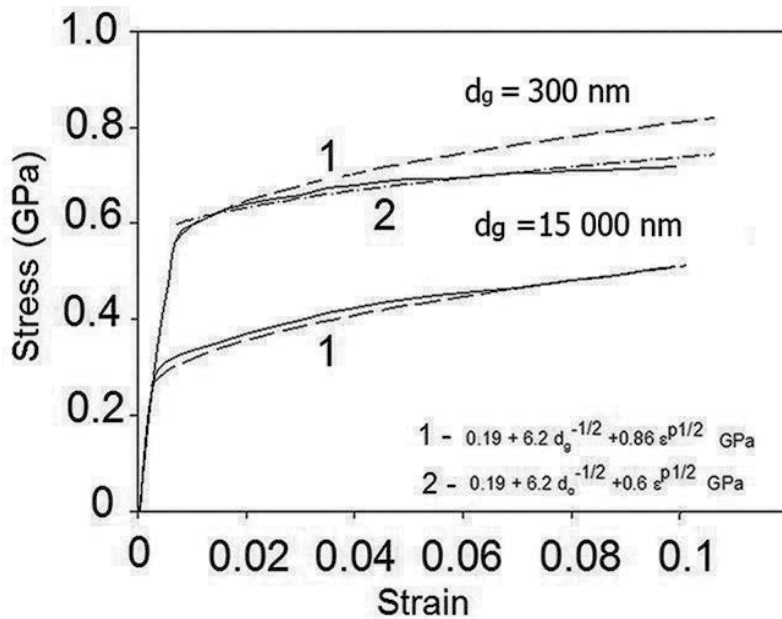


Figure 16. Stress versus strain of titanium alloy VT1-0 at strain rate 10^{-3} s^{-1} .

Figure 17 shows the logarithm of the shear stress versus the logarithm of normalized strain rate for coarse grain and UFG Ti-6-22-22S alloys. Experimental data are shown by symbols [12, 13, 38]. Curves 1 and 2 correspond to UFG and CG alloy, respectively. For normalization of the equivalent, strain rate was used $\dot{\epsilon}_{eq}^p = 1 \text{ s}^{-1}$. Analysis of the stress-strain rate data shows that the parameter $m = d(\lg \sigma_{eq}) / d(\lg \dot{\epsilon}_{eq}^p) \Big|_{T, \epsilon_{eq}^p}$ of strain rate sensitivity is less than that of CG Ti-6-22-22S alloy.

Change of curve slope at strain rates above $\sim 10^3 \text{ s}^{-1}$ testifies the change of dominant physical mechanisms of shear stress relaxation in both CG and UFG alloys. Thus, the constitutive equations for ultrafine-grained FCC and HCP metal alloys should have various forms likewise for coarse-grained counterparts.

The strain rate sensitivity index of the flow stress is determined by the relation

$$m = \frac{d(\ln \sigma_s)}{d \ln(\dot{\epsilon}_{eq} / \dot{\epsilon}_0)} \Big|_{T, \epsilon_{eq}^p} = m_0 + C_m d_g^{-1/2}, \quad (19)$$

where σ_s is the flow stress; $\dot{\epsilon}_{eq} = [(2/3)\dot{\epsilon}_{ij}\dot{\epsilon}_{ij}]^{1/2}$ is the equivalent strain rate; and $\dot{\epsilon}_0 = 1.0 \text{ s}^{-1}$, m_0 , and C_m are the material parameters.

The strain rate sensitivity index of the yield strength is a private parameter value m at a predetermined value of $\epsilon_{eq}^p = 0.002$.

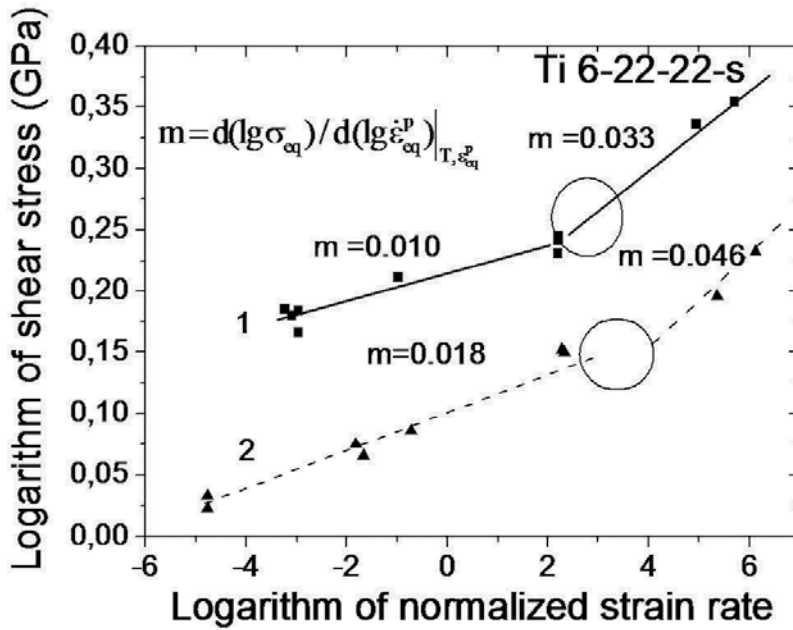


Figure 17. Strain rate sensitivity of UFG and CG Ti-6-22-22S titanium alloy.

Figure 18 shows the dependence of the strain rate sensitivity index m of the yield strength versus the inverse square root of the grain size. Experimental data are shown by symbols [39, 40].

Curve 1 corresponds to HCP alloys; Curve 2 corresponds to FCC alloys. Filled triangles are experimental data [39]; filled squares are experimental data [40].

The tensile deformation to fracture under static loading increases with the decrease of grain size, as shown in Figure 19 [40]:

$$\epsilon_{f \text{ static}} = \epsilon_{f0} \left[1 + D_{ef} d_g^{-1/2} \right] / (1 - \theta), \tag{20}$$

where $\epsilon_{f \text{ static}}$ is the limit of plastic deformation to fracture under tension, d_g is the average grain size, ϵ_{f0}, D_{ef} are structure-sensitive parameters of the material, $\theta = (T - T_r) / (T_m - T_r)$ T is the temperature in absolute scale, $T_r = 295$ K is the room temperature, and T_m is the melting temperature.

The decrease of the strain to fracture under tension of UFG alloys is proportional to the logarithm of the strain rate in the range from 10^{-3} to 10^3 s^{-1} [5, 41]. Experimental data on the normalized ultimate tensile strain versus the logarithm of normalized strain rate for the UFG and NC aluminum and magnesium alloys are shown in Figure 19.

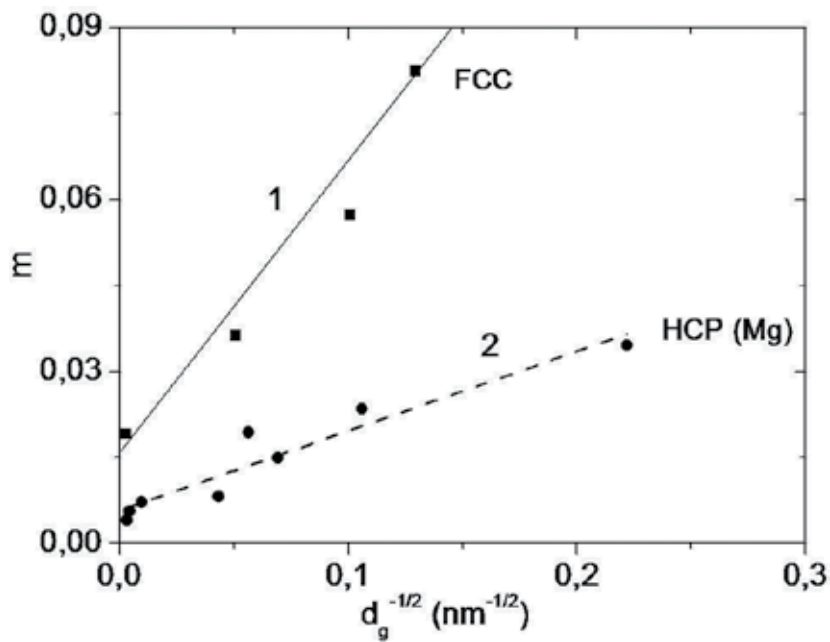


Figure 18. The strain rate sensitivity index of the yield strength versus the inverse square root of the grain size.

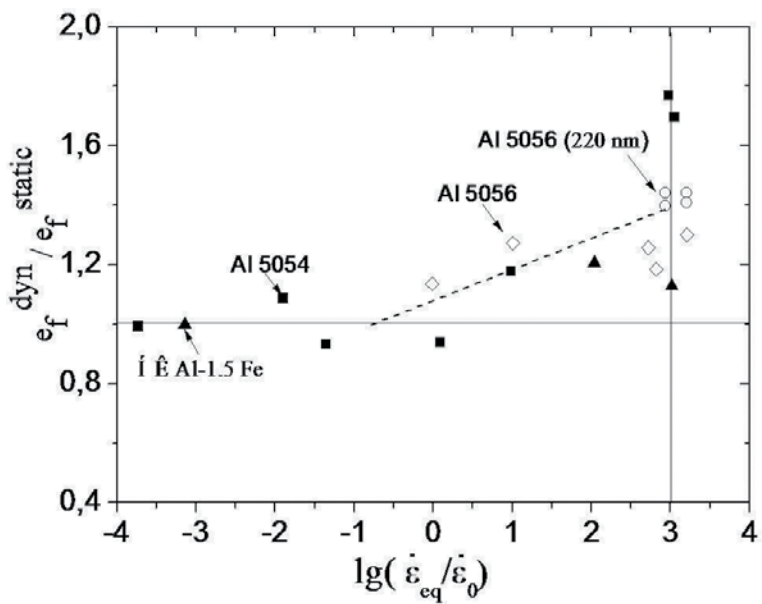


Figure 19. Normalized ultimate tensile strain versus the logarithm of normalized strain rate for the UFG and NC aluminum and magnesium alloys.

The dashed curve shows data obtained according to the formula

$$\varepsilon_{f \text{ static}} / \varepsilon_{f \text{ dynamic}} = [1 + C_{ef} \ln(\dot{\varepsilon}_{eq} / \dot{\varepsilon}_0)] / (1 - \theta), \quad (21)$$

where ε_f is the strain to fracture, $\dot{\varepsilon}_{eq} = [(2/3)\dot{\varepsilon}_{ij}\dot{\varepsilon}_{ij}]^{1/2}$ is the equivalent strain rate, $\dot{\varepsilon}_0 = 1.0 \text{ s}^{-1}$, and C_{ef} is material parameter.

In the aluminum, magnesium, and titanium alloys, the formation of mesoscopic cracks is preceded by the stage of nucleation and growth of micro-voids. In this regard, the width of the plastic zone in the considered alloys will be determined by the critical size of voids.

Valiev et al. reported the log-normal grain size distributions for fine-grained polycrystalline metals processed by equal channel angular extrusion (ECAE) [42]. The distribution effect of grain size on the flow stress, ultimate strength at compression and tension, and elongation to failure has been shown to CG and UFG alloys [43, 44].

Starting with the pioneering work of Tellkamp et al. [45], the formation of bimodal distribution of grain size is used to produce ultrafine-grained and nanostructured alloys with high strength and satisfactory ductility. A bimodal distribution of grain size in UFG aluminum and magnesium alloys is the cause of several anomalies of the mechanical behavior. Negative strain rate sensitivity of plastic flow stress and increase of the ductility in a wide range of strain rates (from 10^{-4} to 1 s^{-1}) were revealed for UFG Al-7.5 wt.% Mg, Al 5083, and magnesium alloys Mg-7wt.%Y [46-52].

The threshold value for the strain to fracture can be calculated by the ratio

$$\varepsilon_f^n(d_g) / \varepsilon_{f0}^{CG} = A_2 + (A_1 + A_2) / (1 + \exp[(x - x_0) / \bar{x}]), \quad \varepsilon_{f0}^{CG} = D_1(P^* + T^*)^{D_2}, \quad (22)$$

where ε_{f0}^{CG} is the strain to fracture of CG alloy; x is equal to $d_g^{-1/2}$; A_1 , A_2 , x_0 , and \bar{x} are material constants; $T^* = \sigma_{sp} / P_{HEL}$, $P^* = p / P_{HEL}$, and P_{HEL} are the pressure in elastic precursor; and D_1 and D_2 are material constants.

Increased crack growth resistance in Al-Mg alloys with a bimodal grain size distribution is a result of deflection of microcracks on borders between UFG and coarse-grained (CG) zones [53]. As a result of it, resistance to crack growth at mesoscale level increases with the increase of the plastic deformation.

Features of mechanical behavior of UFG alloys with bimodal grain size distribution are defined by shear band formation, nucleation and growth of damages, coalescence damages under formation of mesoscale, and macroscale cracks.

Thus, processes of shear banding in UFG alloys with bimodal and unimodal grain size distributions depend on strain rates.

5. Multiscale model of mechanical behavior of UFG alloys under dynamic loadings

The mechanisms of dynamic fracture in alloys with bimodal grain size distributions are poorly investigated. We present computational model and results of numerical simulation of damage and fracture of aluminum and magnesium alloys under dynamic loading.

The multilevel computer simulation method was used for numerical research on damage and formation of cracks within structured representative volume element (RVE) of the alloy [34–36, 54]. Several types of grain structure that take place in alloys after severe plastic deformation were simulated.

Grain size distributions of aluminum and magnesium alloys after various numbers of passes of equal channel angular pressing (ECAP) are reported in Refs. [41–49]. The analysis of grain size distributions has shown that there are several types of grain structures. The model-structured RVE of alloys was created using the experimental data on grain structures.

Models of RVE have the volume fraction of coarse grains: 0, 5, 10, 15, 30, 50, 75, and 100%. When volume fraction of coarse grains exceeds the percolation limit (~0.25), the cell grain structures were taken into consideration. Mechanical behavior of alloy is described by means of averaging the mechanical response of structured RVE at the mesoscale level under loading of high strain rates. 3D models of representative volume element (RVE) of alloys with a bimodal grain size distribution have a dimension of $100 \times 100 \times 5 \text{ (}\mu\text{m)}^3$.

Dynamics of RVE is described within approach of a continuum mechanics [14]. Smooth particle hydrodynamic (SPH) method was used for the simulation [54]. The kinematic boundary condition (Eq. (23)) is convenient when using SPH method. The boundary conditions (Eq. (23)) can be used for load combination of compression, shear, and tension. The scheme of boundary conditions is shown in **Figure 20**:

$$u_k(x_k, t) = u_k(x_k, t), \quad x_k \in \Gamma_4, x_k \in \Gamma_2, x_k \in \Gamma_3, \quad (23)$$

where x_k is Cartesian coordinates, t is time, and u_k is components of particle velocity vector.

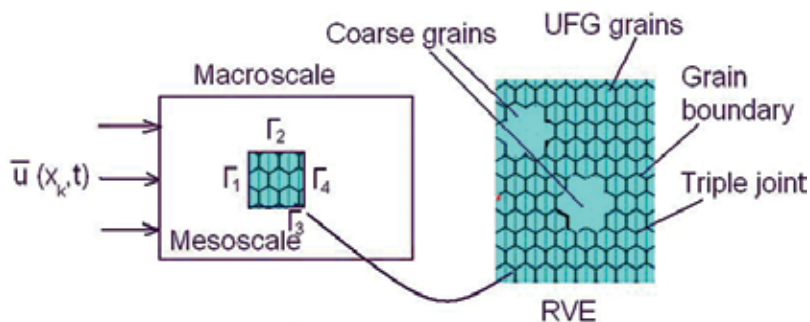


Figure 20. Scheme of boundary conditions.

The system of equations of continuum mechanics is applied to describe the deformation of the structured representative volume under loading conditions. Components of the strain rate tensor are described by the relation

$$\dot{\varepsilon}_{ij} = \frac{1}{2} \left(\nabla_i u_j + \nabla_j u_i \right), \quad (24)$$

where $\dot{\varepsilon}_{ij}$ is the strain rate tensor component, u_i is the particle velocity vector component, and ∇_i is the Hamilton operator.

Components of strain rate tensor are expressed by the sum of the elastic and the inelastic parts:

$$\dot{\varepsilon}_{ij} = \dot{\varepsilon}_{ij}^e + \dot{\varepsilon}_{ij}^n, \quad (25)$$

where $\dot{\varepsilon}_{ij}^e$ is the elastic strain rate tensor component and $\dot{\varepsilon}_{ij}^n$ is the inelastic strain rate tensor component.

The bulk inelastic strain rate is described by the relation

$$\dot{\varepsilon}_{kk}^n = \frac{1}{3} \frac{\dot{D}}{(1-D)}, \quad (26)$$

where \dot{D} is the rate of change of the damage parameter.

The bulk inelastic strain rate will be equal to zero at $\dot{D} = 0$ as follows from Eq. (26). In this case, to describe the plastic flow can be used in the theory of plasticity, which assumes the implementation of the postulate of constant volume for plastic deformation. However, the plastic deformation of NS or UFG alloys is accompanied by the damage (microcrack) nucleation and accumulation due to the limited ductility of the grains.

However, plastic deformation of NS or UFG alloys is accompanied by the nucleation and accumulation of microdamage (microcracks or pores) due to the limited ductility of man-sized grains.

The damage parameter D was introduced in the form

$$D = \int_0^{t_f} \frac{\dot{\varepsilon}_{eq}^n}{\varepsilon_f^n} dt. \quad (27)$$

A local fracture criterion (Eq. (11)) was used for the UFG and the NS alloy with unimodal and bimodal distribution of grain size. The model uses Eq. (28) and phenomenological relation for the threshold inelastic strain ε_f^n .

Damage parameter is defined by the relation

$$D = \frac{1}{C_1} \int_0^{\varepsilon_{f0}^n + kd_s^{-1/2}} \exp\left(-\frac{p}{\sigma_{eq}} C_2\right) d\varepsilon_{eq}^n, \quad (28)$$

where d_g is the grain size of mesoscale region with the unimodal distribution of grain sizes; p is the pressure; and ε_{f0}^n , k , C_1 , and C_2 are the parameters for the local volumes of the material with unimodal distribution of grain size: $e_{ij}^p = \left[(2/3)e_{ij}^n e_{ij}^n\right]^{1/2}$, $\varepsilon_{ij}^n = (1/3)\varepsilon_{kk}^n \delta_{ij} + e_{ij}^n$, $\sigma_{eq} = [3/2S_{ij}S_{ij}]^{1/2}$, $\sigma_{ij} = -p\delta_{ij} + S_{ij}$, and δ_{ij} is the Kronecker delta.

Eq. (12) was used as a constitutive equation of material particles. The pressure was calculated by polynomial equation of state [12]. The stress tensor deviator is calculated by Eq. (13). The deviator of the inelastic strain rate tensor is calculated by Eq. (14).

The scalar function $e_{eq}^{p(m)}$ is defined by the sum of components based on physical mechanisms of inelastic deformation by Eq. (16).

The total plastic work per volume unit under high strain rates was calculated by the relation

$$W^p = (1/2) \int_0^{t_f} \sigma_{ij} \dot{\varepsilon}_{ij}^n dt, \quad (29)$$

where σ_{ij} is the stress tensor component, $\dot{\varepsilon}_{ij}^n$ is the inelastic strain rate tensor component, and t_f is the time of inelastic deformation before local fracture.

The local increment of temperature due to dissipation of plastic work at high strain rate was calculated by the equation

$$\Delta T(t) = (\beta/\rho C_p) \int_0^t \sigma_{ij} \dot{\varepsilon}_{ij}^n dt, \quad (30)$$

where ΔT is the temperature increment associated with plastic deformation, β is a phenomenological parameter, C_p is the specific heat of material, and ρ is the mass density:

$$\beta(\varepsilon_{eq}^p) = 1 - n \left(\frac{\varepsilon_{eq}^p}{\varepsilon_0}\right)^{n-1}, \quad (31)$$

where ε_0 is the yield strain and n is the hardening exponent of the material.

Eqs. (10)–(15) and (24)–(31) were used for describing mechanical response of structured RVE of FCC and HCP alloys under dynamic loadings.

The distribution of grain sizes is specified in the model of a representative volume of the alloys.

Model RVE of alloys with a bimodal grain size distribution includes separate large grains and the volumes consisting of fine grains. RVEs taking into account the distribution of grain size similar to those identified in samples of UFG aluminum alloy Al 1560 (Al-Mg) and magnesium

alloy MA2-1 (Mg-Al-Zn) were used for model calibration. Parameters of materials in constitutive equations were discussed in Refs. [12, 34, 53]. Numerical method was discussed in Refs. [12, 34–36].

The equivalent stresses in UFG magnesium alloy with quasi-regular grains structure at the time ~ 15.7 ns under shock wave loading with peak stress of 3.8 GPa are shown in **Figure 21**.

The width of shock wave front is less than the average grain size ~ 300 nm in the model of NS aluminum alloy with regular grain structure. Mechanical behavior of aluminum alloys with similar grain structure under quasi-static loading was discussed in Ref. [55].

A distribution of material particle velocities was found on the mesoscale level. The distribution of particle velocities arises from the wave interaction with grain boundaries and triple joints of grains.

The distribution of the parameter of damage behind the front of a shock wave with a peak stress of 3.2 GPa is shown in **Figure 22**. Two large grains with size of ~ 20 μm are contained in the model volume of the alloy. These large grains were surrounded by UFG phase with average grain size ~ 1 μm .

Deformation of RVE occurred nonuniformly under shock compression. Shear bands have been formed in the UFG phase at high strain rates. Damage to the mesoscale shear band was formed in 40 ns. The damage parameter increased rapidly when the local tensile stresses acted in areas filled with small grains and on the border between large grains and fine grains. Fracture of RVE is a result of the formation of flat clusters of damaged particles.

The distribution of grains size affects on the formation of damage and the distribution of the specific plastic work per unit volume over the RVE. The distribution of specific plastic work in RVE is shown in **Figure 23**. The size of large grains and its specific volume was ~ 20 μm and $\sim 38\%$, respectively.

The damage parameter increased in local areas where the maximum values of plastic work have been achieved. Fracture mechanisms of alloys with bimodal distribution of grain size are similar in compression and tension. Damage also accumulates in the zones of plastic strain

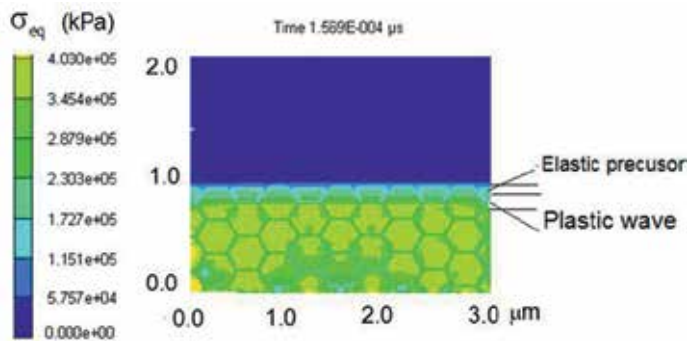


Figure 21. Stress in UFG magnesium alloy with quasi-regular grain structure.

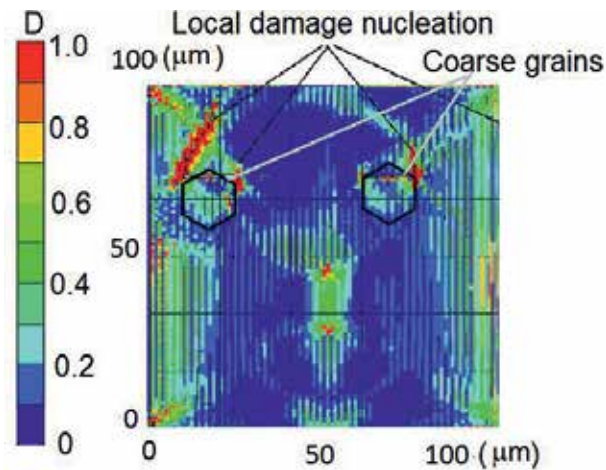


Figure 22. Damage in Al 1560 alloy under shock wave loading with peak stress of 3.2 GPa.

localization near borders of large grains of alloys with a bimodal distribution of grains. Specific plastic work per unit volume and equivalent plastic strain are shown in **Figures 23 and 24**, respectively.

Therefore, kinetics of fracture depends on the specific volume of coarse grains.

The equivalent plastic strain in RVE of Al 1560 alloy under shock compression with peak stress of 3.2 GPa is shown in **Figure 24**. The average intensity of plastic deformation in coarse grains is higher than in the volume filled with fine grains. The maximum equivalent plastic strain is localized in a fine-grained phase near the boundaries of large grains.

Figure 25 shows the calculated plastic work under the tension of RVE at high strain rates. The tensile loading at high strain rates is realized in the spall zone where interaction of unloading waves takes place.

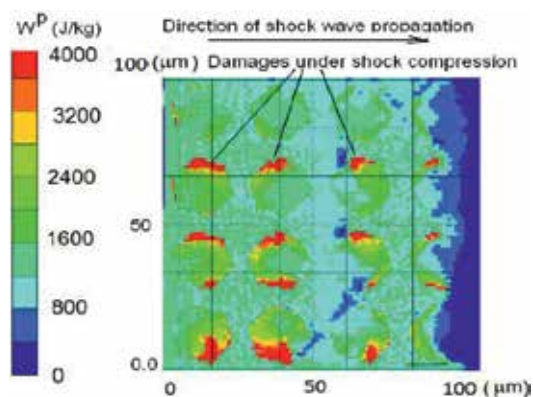


Figure 23. Specific plastic work per unit volume in Al 1560 alloy under shock wave loading with peak stress of 3.2 GPa.

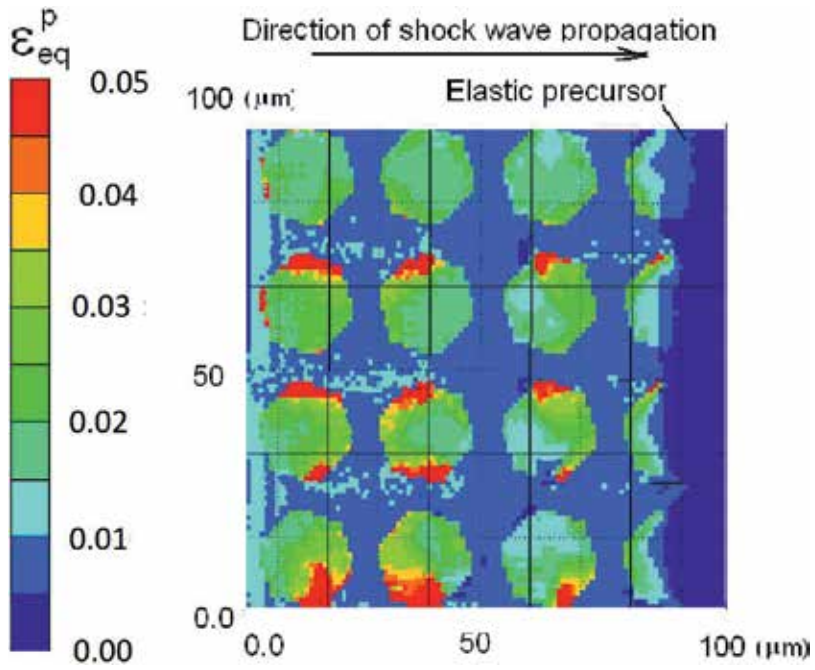


Figure 24. The equivalent plastic strain in RVE under shock wave loading with peak stress of 3.2 GPa.

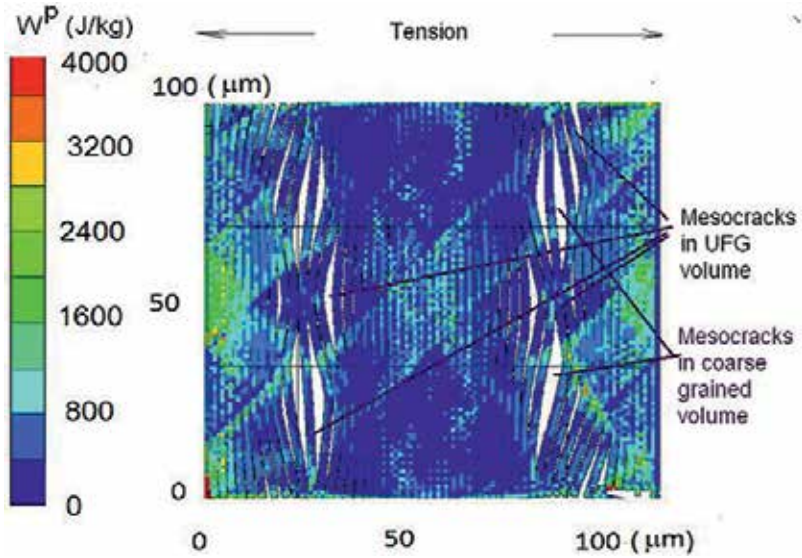


Figure 25. Specific work per unit volume under tension of RVE of Al 1560 aluminum alloy.

Mesoscale cracks in fine-grained volume formed under a tensile strain rates above $\sim 10^3 \text{ s}^{-1}$. The presence of large grains prevents the rapid growth of these cracks and leads to an increase in plastic work per unit volume. Thus, UFG alloys with bimodal distribution of grain sizes under dynamic loading have a higher ductility compared to UFG counterparts with unimodal distribution of grain sizes.

Tensile stress in the spall zone is shown in **Figure 26**. The representative volume of Al 1560 aluminum alloy consisted from $\sim 75\%$ of large grains with a size $\sim 20 \mu\text{m}$. The average size of fine grains was assumed equal to $1 \mu\text{m}$. The relaxations of stresses in a spall zone have been accelerated by the damage accumulation.

The use of multi-pass ECAP leads to stochastic distribution of large grains in the volume of alloys. As a result, fracture of UFG alloys with bimodal grain size distribution under dynamic loading has probabilistic character. Large grains can be formed in the NS and UFG alloys as a result of dynamic recrystallization [56, 57].

In the used model, Eq. (18) takes into account the influence of nanostructured precipitates on dislocation kinetics. Wang et al. showed that in the UFG Al the deformation mechanism is operated by the dislocation interactions at high strain rates, while in the lower strain rate range, the deformation mechanism may be related to grain boundary sliding [58].

The increase in the concentration of nano-size precipitates leads to the growth of the yield stress of both large and small grains of alloys. The concentration of precipitates in UFG alloys affects the grain size distribution and the distance between the shear bands. These results agree

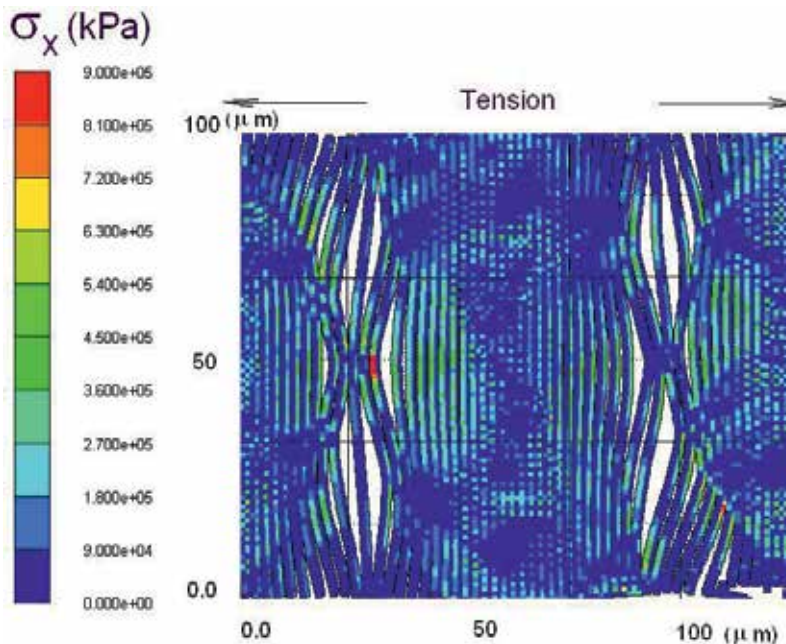


Figure 26. Tensile stress in RVE of Al 1560 aluminum alloy.

with experimental data [59]. Chrominski et al. showed that the grain size, grain boundary character, and dislocation substructure are strongly depended on the precipitation in 6082 aluminum alloy. It was found that needlelike precipitates are homogeneously distributed in the grains of micron-size [59].

The ductility of UFG alloys increases when a specific volume of coarse grains is decreased. The ductility versus specific volume of coarse grains in Al-Mg alloy with a bimodal grain size distribution is shown in **Figure 27**. Experimental data [45, 48, 49] are shown by filled symbols. Decreasing of the specific volume of large grains in RVE of UFG alloy is accompanied by a decrease of average strain to failure under quasi-static and dynamic loading.

Figure 28 shows the dependence of strain to fracture of aluminum and magnesium alloys on logarithm of strain rates.

Experimental data reported by Ulacia for coarse-grained magnesium alloy AZ31 are marked by filled symbols [60]. Data for aluminum alloys are shown in circular and triangular symbols [48, 49]. UFG Al-Mg alloys have fine-grained size of $1\ \mu\text{m}$ and coarse-grained size of $20\ \mu\text{m}$.

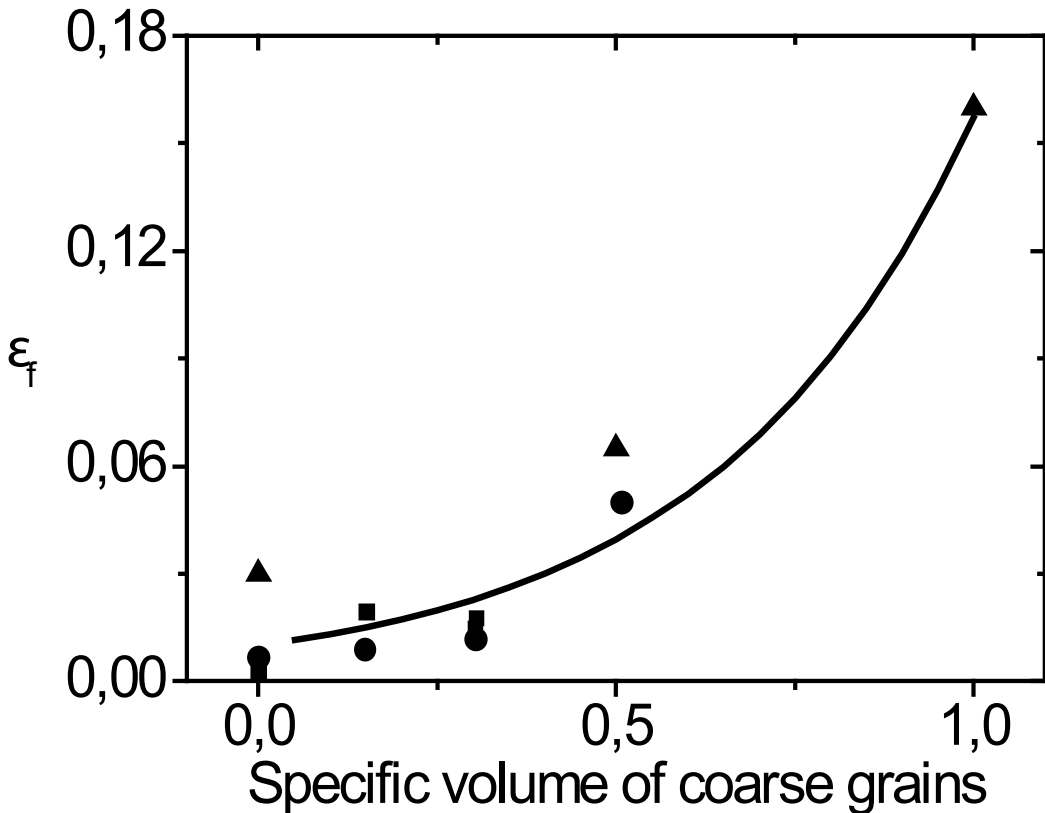


Figure 27. The strain to fracture of Al-Mg alloy with a bimodal grain size distribution versus specific volume of coarse grains.

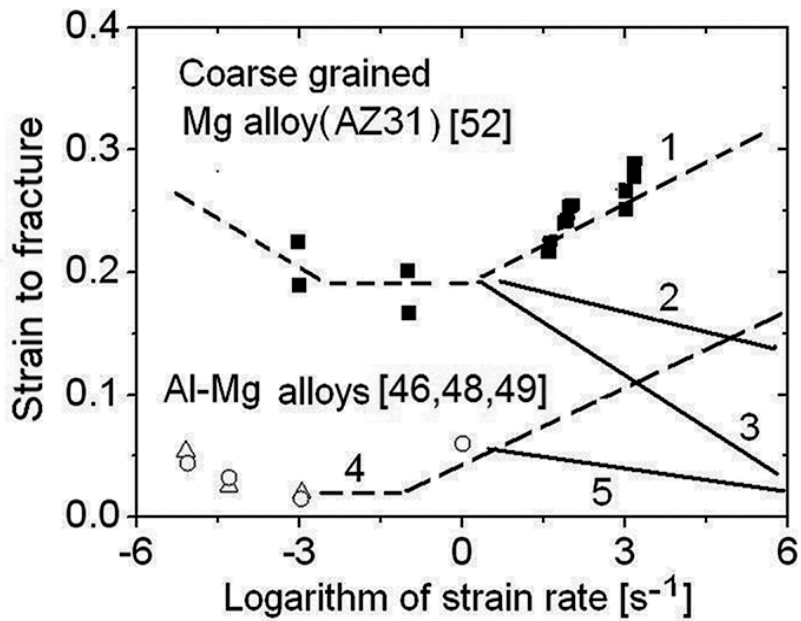


Figure 28. Strain to fracture of aluminum and magnesium alloys versus logarithm of strain rate.

The calculated values of total strain to failure of coarse-grained magnesium alloy AZ31 versus the logarithm of strain rate are depicted by dashed Curve 1 in **Figure 28**. Rodriguez [61] later received that the experimental values of strain to failure of AZ31 alloy at quasi-static loading conditions confirmed the adequacy of the prediction.

Curve 2 shows the calculated strain to fracture of Ma2-1 magnesium alloy with volume concentration of large grains about ~70%. Curve 3 shows strain to fracture for magnesium alloy with specific volume of large grains about ~10%.

Curve 4 shows the ductility of Al-Mg alloys with a bimodal grain structure in a wide range of strain rates. Curve 5 displays decreasing dynamic ductility of Al-Mg alloys with a bimodal grain structure and specific volume of large grains ~10%.

The plasticity of the alloys under quasi-static tension increases when specific volume of large grains in UFG Al-Mg alloy is more than 30%.

The calculated strain to failure for Al-M alloys can be described by the equation

$$\varepsilon_f^n = 0.01 \exp(C_{cg}/0.363), \quad (32)$$

where ε_f^n is the strain to failure under quasi-static tension and C_{cg} is the specific volume of coarse-grained size.

Eq. (32) describes ductility of UFG Al-Mg alloys with a bimodal grain distribution versus the specific volume of large grains. Results of simulation agree with the available experimental data [48, 49, 52].

6. Conclusions

The study of the mechanical behavior of NS and UFG alloys under intensive dynamic loadings allows you to deepen understanding of the basic laws of deformation and failure of alloys in extreme states.

Experimental studies have shown that the difference between the Hugoniot elastic limits of alloys with UFG and CG structure can be negligible.

The spall strength and the yield strength of UFG alloys are depended not only on grain size but also on distribution of grain sizes, a concentration of a nano-sized precipitates.

Fine precipitates in alloys not only affect the hardening but also lead to change the influence of the grain size distribution on volume concentration of shear bands.

Multiscale computer modeling can be used to study the regularities of deformation and fracture of advanced structural alloys at high strain rates.

It was shown that the use of models taking into account the unimodal and bimodal distribution of grain size allows predicting the strength and ductility of a UFG alloys at high strain rates under compression and tension.

The results of computer simulation showed that the dynamic strength and ductility depend on the distribution of grain size in the HCP and FCC alloys processed by severe plastic deformation.

Experimental and numerical studies have shown that strain to failure of UFG alloys with a bimodal grain size distribution nonlinearly decreases with the increase of specific volume of submicrometer grains.

The dynamic ductility of UFG alloys is decreased when specific volume of submicrometer grains is above ~70%.

It should be noted that researches on the influence of grain size distribution of UFG alloys on dynamic strength and ductility are at an early stage. The peculiarities of the mechanical behavior of UFG alloys under dynamic loading at elevated temperatures are insufficiently studied.

Author details

Vladimir A. Skripnyak* and Evgeniya G. Skripnyak

*Address all correspondence to: skrp2006@yandex.ru

National Research Tomsk State University, Russia

References

- [1] Li Z, Wang B, Zhao S, Valiev RZ, Vecchio KS, Meyers MA. Dynamic deformation and failure of ultrafine-grained titanium. *Acta Materialia*. 2017;**125**:210–218.
- [2] Xu Y, Meyers MA. Nanostructural and microstructural aspects of shear localization at high-strain rates for materials adiabatic shear localization. In *Adiabatic Shear Localization: Frontiers and Advances* (eds. B. Dodd, Y Bai). 2nd ed.; 2012. pp. 111–171.
- [3] Asaro RJ, Suresh S. Mechanistic models for the activation volume and rate sensitivity in metals with nanocrystalline grains and nano-scale twins. *Acta Materialia*. 2005;**53**:3369–3382.
- [4] Meyers MA, Mishra A, Benson DJ. Mechanical properties of nanocrystalline materials. *Progress in Materials Science*. 2006;**51**:427–556.
- [5] Mukai T, Higashi K. Ductility enhancement of ultrafine-grained aluminum under dynamic loadings. *Scripta Materialia*. 2001;**44**:1493–1496.
- [6] Meyer LW, Hockauf M, Krüger L, Schneider I. Compressive behavior of ultrafine-grained AA6063T6 over a wide range of strains and strain rates. *International Journal of Materials Research*. 2007;**98**(3):191–199.
- [7] Choi HJ, Kim Y, Shin JH, Bae DH. Deformation behavior of magnesium in the grain size spectrum from nano- to micrometer. *Materials Science and Engineering: A*. 2010;**527**(6):1565–1570.
- [8] Ono N, Nowak R, Miura S. Effect of deformation temperature on Hall–Petch relationship registered for polycrystalline magnesium. *Materials Letters*. 2004;**58**(1–2):39–43.
- [9] Wei Q, Cheng S, Ramesh KT, Ma E. Effect of nanocrystalline and ultrafine grain sizes on the strain rate sensitivity and activation volume: FCC versus BCC metals. *Materials Science and Engineering: A*. 2004;**381**(1–2):71–79.
- [10] Valle del JA, Ruano OA. Influence of the grain size on the strain rate sensitivity in an Mg–Al–Zn alloy at moderate temperatures. *Scripta Materialia*. 2006;**55**(5):775–778.
- [11] Skripnyak VA, Skripnyak EG, Nazarov MN, Mechanical behavior of nanostructured materials at high strain rates. Computer simulation. In: Furnish MD, Elert ML, Russell TP, and White CT, editors. *Proceedings of the Shock Compression of Condensed Matter*. part I; 2006. pp. 503–506.
- [12] Herzig N, Meyer LW, Halle MT, D Musch, Skripnyak VA, Skripnyak EG, Razorenov SV, Krüger L. Modeling of mechanical behavior of ultra-fine grained titanium alloys at high strain rates. *Proceedings of the 3rd International Conference on High Speed Forming*; 2008. pp. 141–154.
- [13] Herzig N, Meyer LW, Musch D, Halle T, Skripnyak VA, Skripnyak EG, Razorenov SV, Krüger L. The mechanical behaviour of ultrafine-grained titanium alloys at high strain

- rates. Proceedings of the 3rd International Conference on High Speed Forming; 2008. pp. 65–74.
- [14] Frost HJ, Ashby MF. Deformation Mechanism Maps. The Plasticity and Creep of Metals and Ceramics. Oxford–New York–Toronto–Sydney–Paris–Frankfurt: Pergamon Press; 1982. pp. 166.
- [15] Kanel GI, Razorenov SV, Utkin AV, Fortov VE. Experimental Profiles of Shock Waves in Condensed Substances. Moscow: FIZMATLIT; 2008. pp. 246.
- [16] Kanel GI, Razorenov SV, Fortov VE. Shock Wave Phenomena and The Properties of Condensed Matter. Berlin-NY: Springer-Verlag; 2004. pp. 322.
- [17] Cao HS, Hunsinger JJ, Elkdim O. Determination of elastic modulus of nanocrystalline iron and titanium by means of acoustic microscopy. Scripta Materialia. 2003;**48**:531–537.
- [18] Meyers MA, Vöhringer O, Lubarda VA. The onset of twinning in metals: a constitutive description. Acta Materialia. 2001;**49**(19):4025–4039.
- [19] Lee CD. Dependence of tensile properties of AM60 magnesium alloy on microporosity and grain size. Materials Science and Engineering: A. 2007;**454–455**:575–580.
- [20] Garkushin GV, Razorenov SV, Kanel GI, Ignatova ON, Ivanchina GI. Study of elastic-plastic and strength properties of copper M1 at the shock-wave loading. Proceedings of the III International School-Conference Physical Science. Nanomaterials for Technical and Medical Purposes. Togliatti; 2007. pp. 190–192.
- [21] Garkushin GV, Razorenov SV, Ignatova ON. The influence of the internal structure of copper M1 on elastic-plastic and strength properties under shock wave loading. Proceedings of the International conference “Zababakhin scientific talks 2007”. Snezhinsk; 2007. pp. 5-15. <http://www.vniitf.ru/rig/konfer/9zst/s5/s-5.htm>
- [22] Naimark OB, Yu V, Bayandin, Leontiev VA, Panteleev IA, Plekhov OA. Structural-scaling transitions and thermodynamic and kinetic effects in submicro-(nano-)crystalline bulk materials. Physical Mesomechanics. 2009;**12**(5–6):239–248.
- [23] Gunderov DV, Polyakov AV, Sitdikov VD, Churakova AA, Golovin IS. Internal friction and evolution of ultrafine-grained structure while annealing titanium Grade 4 under severe plastic deformation. The Physics of Metals and Metallography. 2013;**114** (12):1078–1085.
- [24] Chrysochoos A. Infrared thermography applied to the analysis of material behavior: A brief overview. Quantitative InfraRed Thermography. 2012. Editions Hermes;**9**(2):193–208.
- [25] Oliferuk W, Maj M, Zembrzycki K. Determination of the energy storage rate distribution in the area of strain localization using infrared and visible imaging. Experimental Mechanics. 2015;**55**(4): 753–760.
- [26] Yu P, Sharkeev VP, Vavilov VA, Skripnyak VA, Klimenov OA, Belyavskaya DA, Nesteruk AA, Kozulin AI, Tolmachev. Evolution of the temperature field during deformation and

- fracture of specimens of coarse grained and ultrafine-grained titanium. *Russian Journal of Nondestructive Testing*. 2011;**47**(10):701–706.
- [27] Sharkeev YP, Eroshenko AY, Kulyashova KS, Fortuna SV, Suvorov KA, Epple M, Prymak O, Sokolova V, Chernousova S. Microstructure, mechanical and biological properties of zirconium alloyed with niobium after severe plastic deformation. *Material wissenschaft und Werkstofftechnik*. 2013;**44**:198–204.
- [28] Sharkeev YP, Vavilov VP, Belyavskaya OA, Skripnyak VA, Nesteruk DA, Kozulin AA, Kim VM. Analyzing deformation and damage of VT1-0 titanium in different structural states by using infrared thermography. *Journal of Nondestructive Evaluation*. 2016;**35**(3):42.
- [29] Danilov VI, Eroshenko AY, Sharkeev YP. Peculiarities of deformation and fracture of ultrafine-grained Ti and Zr-based alloys. *Physical Mesomechanics*. 2014;**17**(4): 77–85.
- [30] Armstrong RW, Zerilli FJ. Dislocation mechanics aspects of plastic instability and shear banding. *Mechanics of Materials*. 1994;**17**:319–327.
- [31] Liu J, Khan AS, Takacs L, Meredith CS. Mechanical behavior of ultrafine-grained / nanocrystalline titanium synthesized by mechanical milling plus consolidation: Experiments, modeling and simulation. *International Journal of Plasticity*. 2015;**64**:151–163.
- [32] Khan AS, Liu J. A deformation mechanism based crystal plasticity model of ultrafine-grained/nanocrystalline FCC polycrystals. *International Journal of Plasticity*. 2016;**86**:56–69.
- [33] Mishra A, Martin M, Thadhani NN, Kad BK, Kenik EA, Meyers MA. High-strain-rate response of ultra-fine-grained copper. *Acta Materialia*. 2008;**56**(12):2770–2783.
- [34] Skripnyak VA, Skripnyak EG, Skripnyak NV, Vaganova IK, Skripnyak VV. Failure mechanisms of light alloys with a bimodal grain size distribution. *Proceedings of the 11th World Congress on Computational Mechanics (WCCM XI), 5th European Conference on Computational Mechanics (ECCM V), 6th European Conference on Computational Fluid Dynamics (EFCD VI), (IV)*; 2014:3915-3925. doi: 10.4028/www.scientific.net
- [35] Skripnyak VA, Skripnyak NV, Skripnyak EG. Mechanical behavior of light alloys with bimodal grain size distribution. *Applied Mechanics and Materials*. 2015;**756**:205-213
- [36] Skripnyak NV, Skripnyak VV, Skripnyak VA. Fracture of thin metal sheets with distribution of grain sizes in the layers. In: Papadrakakis M, Papadopoulos V, Stefanou G, Plevris V, editors. *Proceedings of the ECCOMAS Congress 2016, VII European Congress on Computational Methods in Applied Sciences and Engineering*. Crete Island, Greece; 2016. Vol. 1. pp. 355–365.
- [37] Martin JW. *Precipitation Hardening: Theory and Applications*. 2nd ed. Oxford: Butterworth-Heinemann; 1998. p. 221.
- [38] Krüger L, Meyer LW, Razorenov SV, Kanel GI. Investigation of dynamic flow and strength properties of Ti-6-22-22S at normal and elevated temperatures. *International Journal of Impact Engineering*. 2003;**28**:877–890.

- [39] Zhu B, Asaro RJ, Krysl P, Bailey R. Transition of deformation mechanisms and its connection to grain size distribution in nanocrystalline metals. *Acta Materialia*. 2005;**53**:4825–4838.
- [40] Lukač P, Trojanova Z. Influence of grain size on ductility of magnesium alloys, *Materials Engineering*. 2011;**18**:110–114.
- [41] Mukai T, Suresh S, Kita K, Sasaki H, Kobayashi N, Higashi K, Inoue A. Nanostructured Al–Fe alloys produced by e-beam deposition: Static and dynamic tensile properties. *Acta Materialia*. 2003;**51**(14):4197–4208.
- [42] Valiev RZ, Islamgaliev RK, Alexandrov IV. Bulk nanostructured materials from severe plastic deformation. *Progress in Material Science*. 2000;**45**:103–189.
- [43] Ramtani S, Dirras G, Bui HQ. A bimodal bulk ultra-fine-grained nickel: Experimental and micromechanical investigations. *Mechanical Material*. 2010;**42**:522–536.
- [44] Agnew SR, Horton JA, Lillo TM, Brown DW. Enhanced ductility in strongly textured magnesium produced by equal channel angular processing. *Scripta Materialia*. 2004;**50**:77–381.
- [45] Tellkamp VL, Melmed A, Lavernia EJ. Mechanical behavior and microstructure of a thermally stable bulk nanostructured Al alloy. *Metallurgical and Material Transactions A*. 2001;**32**:2335–2343.
- [46] Fan GJ, Choo H, Liaw PPK, Lavernia EJ. Plastic deformation and fracture of ultrafine-grained Al–Mg alloys with a bimodal grain size distribution. *Acta Materialia*. 2006;**54**:1759–1766.
- [47] Ahn B, Lavernia EJ, Nutt SR. Dynamic observations of deformation in an ultrafine-grained Al–Mg alloy with bimodal grain structure. *Journal of Material Science*. 2008;**43**:7403–7408.
- [48] Lee ZH, Radmilovic V, Ahn B, Lavernia EJ, Nutt SR. Tensile deformation and fracture mechanism of bulk bimodal ultrafine-grained Al–Mg alloy. *Metallurgical and Material Transactions A*. 2010;**41**:795–801.
- [49] Han BQ, Lee Z, Witkin D, Nutt SR, Lavernia EJ. Deformation behavior of bimodal nanostructured 5083 Al alloys. *Metallurgical and Material Transactions A*. 2005;**36**:57–965.
- [50] Han BQ, Huang JY, Zhu YT, Lavernia EJ. Strain rate dependence of properties of cryomilled bimodal 5083 Al alloys. *Acta Materialia*. 2006;**54**:3015–3024.
- [51] Fu H, Li H, Fang D, Cai X, Peng Q. High ductility of a bi-modal Mg-7wt.%Y alloy at low temperature prepared by high pressure boriding and semi-solid extrusion. *Materials and Design*. 2016;**92**:240–245.
- [52] Zhu L, Lu J. Modelling the plastic deformation of nanostructured metals with bimodal grain size distribution. *International Journal of Plasticity*. 2012;**30–31**:166–184.

- [53] Skripnyak VA. Mechanical behavior of nanostructured and ultrafine-grained materials under shock wave loadings. Experimental data and results of computer simulation. *Shock Compression of Condensed Matter. AIP Conference Proceedings*. **1426**; 2012. pp. 965–970.
- [54] Parshikov AN, Medin SA. Smoothed particle hydrodynamics using interparticle interparticle contact algorithms. *Journal of Computational Physics*. 2002;**180**:358–382.
- [55] Sabirov I, Yu M. Murashkin, Valiev RZ. Nanostructured aluminium alloys produced by severe plastic deformation: New horizons in development. *Materials Science & Engineering A*. 2013;**560**:1–24.
- [56] Lin Y, Liu W, Wang L, Lavernia EJ. Ultra-fine grained structure in Al–Mg induced by discontinuous dynamic recrystallization under moderate straining. *Materials Science & Engineering A*. 2013;**573**:197–204.
- [57] Sakai T, Belyakov A, Kaibyshev R, Miura H, Jonas JJ. Dynamic and post-dynamic recrystallization under hot, cold and severe plastic deformation conditions. *Progress in Materials Science*. 2014;**60**:130–207.
- [58] Wang M, Shan A. Effect of strain rate on the tensile behavior of ultra-fine grained pure aluminum. *Journal of Alloys and Compounds Letter*. 2008;**455**:L10–L14.
- [59] Chrominski W, Kulczyk M, Lewandowska M, Kurzydowski KJ. Precipitation strengthening of ultrafine-grained Al–Mg–Si alloy processed by hydrostatic extrusion. *Materials Science & Engineering A*. 2014;**609**:80–87.
- [60] Ulacia CP, Salisbury I, Hurtado MJ, Worswick, Tensile characterization and constitutive modeling of AZ31B magnesium alloy sheet over wide range of strain rates and temperatures. *Journal of Materials Processing Technology*. 2011;**211**:830–839.
- [61] Rodriguez AK, Ayoub B, Mansoor GA, Benzerga AA. Effect of strain rate and temperature on fracture of magnesium alloy AZ31 B. *Acta Materialia*. 2016;**112**:194–208.

Thermomass Theory: A Mechanical Pathway to Analyze Anomalous Heat Conduction in Nanomaterials

Yuan Dong, Bingyang Cao and Zengyuan Guo

Additional information is available at the end of the chapter

<http://dx.doi.org/10.5772/67780>

Abstract

The synthesis and measurements of nanomaterials have yielded significant advances in the past decades. In the area of thermal conduction, the nanomaterials exhibit anomalous behavior such as size-dependent thermal conductivity, thermal rectification, and ultra-high thermoelectric properties. The theoretical understanding and modeling on these behaviors are much desired. In this chapter, we study the thermal conduction in nanomaterials through the thermomass theory, which models the heat transfer from a fluid mechanics viewpoint. The control equations of the equivalent mass of the thermal energy are formulated following the continuum mechanics principles, which give the general heat conduction law. It incorporates nonlinear effects such as spatial acceleration and boundary resistance, which can overcome the drawbacks of the traditional Fourier's law in nanoscale systems. By the thermomass theory, we successfully model the size-dependent effective thermal conductivity in nanosystems. Furthermore, the thermal rectification as well as the thermoelectric enhancement in nanosystems is also discussed with the present framework.

Keywords: thermomass theory, nanomaterial, thermal conductivity, thermal rectification, thermoelectric

1. Introduction

The Fourier law proposed in 1822 [1] is the fundamental of thermal conduction. It indicates that the heat flux passing through a material is proportional to the local gradient of temperature

$$q = -\kappa \nabla T \quad (1)$$

where q is the heat flux, ∇T is the local temperature gradient, and κ is the thermal conductivity, which represents the material capability of transferring heat. In a long term, the Fourier law can accurately model the heat conduction. In the middle of twentieth century, theoretical

physicists started to question the Fourier law because of its contradiction to the second law of thermodynamics [2]. After that, the heat waves were observed in low-temperature experiments [3] and aroused people's interest as well as controversy. In 1980s, the short pulse laser experiment stimulated a lot of research and led to several relaxational [4], hyperbolic [5], or lagging types [6] of models, which can be regarded as the generalization of Fourier law. The above research focused on the distortion of ordinary heat transfer in short time scales. On the other hand, the shrink of space scales caused another type of distortion and began to be realized in the early 1990s, when sign of failure of Fourier law was perceived in thin dielectric films [7]. The phenomena of anomalous heat transfer in small scale materials can be fundamentally understood through the kinetic theory of phonons, that is, the thermal conductivity of dielectric materials can be formulated as [8, 9]

$$\kappa = \frac{1}{3} C v \lambda \quad (2)$$

where C is the specific heat per unit volume, v is the average group velocity of phonon, and λ is the phonon mean free path (MFP). When the material size is much larger than MFP, the MFP can be regarded as a constant and is dominated by the intrinsic phonon-phonon scattering and phonon-defect scattering rates. Therefore, the thermal conductivity is independent on the system size. In contrast, when the material size reduces to comparable value with the MFP, the phonon-boundary scattering becomes considerable. In this condition, the smaller system size induces higher boundary scattering rates and consequently shorter effective phonon MFP. By using Eq. (2) one figures out the reduction of thermal conductivity of nanomaterials.

The reduced thermal conductivity of nanofilms is a disadvantage for the heat dissipation in IC chips or semiconductor lasers. Nevertheless, it is an advantage for the thermoelectric devices. Experiments showed that the silicon nanowires have very high figure of merit (ZT) [10, 11]. The nanocomposites also demonstrate considerable ZT benefiting from the nano-sized superlattice or grains significantly scatter the phonons and reduce the effective thermal conductivity [12, 13]. Therefore, a lot of effort has been made to fabricate materials with ultra-low thermal conductivity through nanotechnology with the target at high ZT for the applications in advanced heating and cooling, waste heat recovery [14], as well as solar thermoelectric generators [15].

Due to the fast growth of energy-related nanomaterial synthesis and its transition from laboratory to industrial applications, modeling the thermal conducting behavior in nanosystems is in urgent need. Ideally, it should rise from a perspective of characterizing the fundamental physics and approach to simply structured theory which can be conveniently used by engineers. Nevertheless, this goal has not been satisfactorily achieved and current research is paving toward it. The gray model proposed by Majumdar is a pioneer work in this path. It predicts the effective thermal conductivity as [7]

$$\frac{\kappa_{\text{eff}}}{\kappa_0} = \frac{1}{1 + \beta \frac{\lambda}{L}} = \frac{1}{1 + \beta \text{Kn}} \quad (3)$$

where κ_{eff} is the effective thermal conductivity, κ_0 is the thermal conductivity of the bulk material, L is the characteristic size of system, and β is a dimensionless parameter. Except that

the temperature is much lower than the Debye temperature, the phonon scattering at most engineering surfaces can be regarded as diffusive. In this case, it was derived that for the in-plane heat conductivity of nanofilms, $\beta = 3/8$. For the cross-plane heat conductivity of nanofilms, $\beta = 4/3$. For the longitudinal heat conductivity of nanowires, β can be selected as $4/3$ [16]. Kn is the Knudsen number, which is the ratio of MFP over L . Kn is actually a concept in gas dynamics, and it is well known that rarefaction effects should be considered in high Kn situations [17]. Eq. (3) was derived from an analogy between photons and phonons as wave packets of energy. Therefore, radiative transfer was assumed for phonons. It is easily found that Eq. (3) retreats to the Fourier law when the system size is much larger than MFP, that is, at the bulk limit. When the system size is comparable with the MFP, Eq. (3) delineates the size dependency of thermal conductivity. However, along with the progress in measuring the thermal conductivity of thin silicon films [18–21], the accuracy of Eq. (3) was questioned. It was claimed that the MFP of monocrystalline silicon should be around 300 nm to match the experiment results [19], while the value based on Eq. (2) is around 42 nm. Chen et al. [22–24] proposed that the phonon MFPs of single-crystal Si at room temperature should be 210–260 nm considering that the phonons of different frequencies contribute differently to the heat conduction. This amendment partly resolves the inaccuracy of gray model. However, it still exhibits considerable deviations to predict the experiment value of nanowires [25]. McGaughey et al. [16] developed a model which accounts the full dispersion relation and the directional dependent scattering chances with surfaces. This model matches well with experiments for nanofilms, while still overestimating the experiments for nanowires.

The phonon hydrodynamics [26–31] is another pathway to model the nanoscale heat conduction. It originates from the solving of linearized Boltzmann equation. An additional term representing the second order spatial derivative of heat flux, $\nabla^2 q$, is involved in the governing equation of heat conduction. Since the heat flux is similar to a fluid flow flux, $\nabla^2 q$ is in analogy with the viscous dissipation term in Navier-Stokes equation for fluid mechanics. Therefore, the heat flux could be nonuniform in the heat transfer cross-section due to the drag from the boundary, forming a Poiseuille flow of heat. This behavior induces the terminology of “phonon hydrodynamics.” The analysis based on phonon hydrodynamics indicated the effective thermal conductivity of nanosystems should be inversely proportional to the square of Kn due to the nonuniform distribution of heat flux profile. However, the experiments indicated that the effective thermal conductivity is approximately linear to the characteristic size rather than the square of size. It is thereby further elucidated that the boundary velocity slip would happen in case of large Kn [29, 31]. By introducing the slip boundary condition into the governing equation, the linear size-dependent effective thermal conductivity can be achieved. The drawbacks of present phonon hydrodynamics analysis are: 1. The arbitrary in choosing the style and parameters of slip boundary condition. 2. The deviation from the physical picture of original derivation of Boltzmann equation, where it was the normal (N) scattering processes that induced the second order spatial derivative of heat flux. The present phonon hydrodynamic models just simply use the MFP of resistive (R) scattering processes as the parameter of $\nabla^2 q$.

Upon the abovementioned progresses and their defects, the development of better models characterizing heat conducting in nanomaterials should base on capturing the essential feature of its

physics. In recent years, the thermomass theory has been developed in our group, which proposes a mechanical analysis framework for heat transfer [32–35]. The generalized heat conduction governing equations are established based on such analysis. In the following sections, we will present the application of thermomass theory in nanomaterial heat conduction. The size dependency of thermal conductivity, thermal rectification, and thermoelectric effects will be addressed.

2. Thermomass theory

In history, the nature of heat was regarded as either a fluid, that is, caloric theory. The caloric theory regards heat as a weightless, self-repulsive fluid. In the eighteenth and the first half of nineteenth centuries, the caloric theory was the mainstream theory. It was extinct after the mid-nineteenth century and replaced by the dynamic theory that the nature of heat is the random motion of particles in a body. In twentieth century, Einstein's relativity theory introduced the well-known mass-energy equivalence relation, $E = mc^2$, where c is the speed of light. According to this theory, the thermal energy should correspond to a certain amount of mass. To illustrate his theory, Einstein elucidated "a piece of iron weighs more when red hot than when cool" [36], which means the adding of the thermal energy into material, that is, raise its temperature and at the same time increase the mass. The mass increase induced by heat was defined as "thermomass," which is very small in ordinary conditions. For example, the thermomass of Si at room temperature is 10^{-12} of the total mass. Such small amount of mass is negligible when dealing with the dynamic problem, like movement and balance of the body. However, the heat conduction is the movement of thermomass itself relative to molecular or the lattice. It is driven by the pressure gradient induced by the concentration difference of thermomass among the materials. The forces and inertia of thermomass are comparable and lead to the limited acceleration and drift velocity of it. The advantage to bring in the concept of thermomass is that the analysis of heat conduction can follow a mechanical framework. The corresponding forces, velocities, accelerations, and momentums can be properly defined.

Consider the dielectric solids, the phonons are the main heat carriers. In this case, the internal energy per unit volume, e , is the summation of all phonon energies [9]

$$\begin{aligned} e &= CT = (2\pi)^{-3} \sum_n \int [\hbar\omega^n f^n(k, x, t)] d^3k \\ &= \sum_n \int_k \hbar\omega^n f^n(k, x, t) \end{aligned} \quad (4)$$

where \hbar is the reduced Planck constant (Dirac constant), ω is the phonon frequency, k is the wave vector, and n denotes the index of phonon branches. f is the phonon distribution function. In equilibrium state, f obeys the Bose-Einstein distribution

$$f_0 = [\exp(\hbar\omega/k_B T) - 1]^{-1} \quad (5)$$

where k_B is the Boltzmann constant. The density of the thermomass, that is, the equivalent mass of the phonon gas, is obtained by using the Einstein's mass-energy equivalence relation

$$\rho_{TM} = \frac{CT}{c^2} \quad (6)$$

It should be reminded that the frequently used expression for thermal conductivity of phonon systems, Eq. (2), is from the analogy between gas and heat carriers. The scattering of phonons induces resistance on heat transport. Generally, the scattering accounted for thermal resistance is the R processes, including the Umklapp scattering, defect scattering, and boundary scattering. These scattering events eliminate the quasi-momentum of phonons. The MFP defined in Eq. (2) refers to the traveled distance of a phonon between succeeding R scatterings. However, in ideal gas systems, the collision among gas molecules does not perish the momentums. Therefore, the R processes of phonons are more resemble to the collision of gas molecules to residential barriers. It is the case when a gas flows through a porous medium. The collision frequency between gas molecules and material skeleton determines the resistance experienced by the gas flow. In the porous flow, the Darcy's law describes the effective flow velocity is proportional to the pressure gradient

$$u \propto -\nabla p \quad (7)$$

The pressure gradient can be regarded as the driving force of flow. From a viewpoint of force balance, the driving force is actually balanced by the friction force. Thereby Eq. (7) essentially depicts that the friction force is proportional to the flow velocity. It is a general case in laminar flow.

In analogy to the gas flow in porous medium, the velocity of thermomass is defined as

$$u_{TM} = \frac{q}{CT} \quad (8)$$

The mass and momentum balance equations of thermomass can be derived as [32–34]

$$\frac{\partial \rho_{TM}}{\partial t} + \nabla \cdot (\rho_{TM} u_{TM}) = 0 \quad (9)$$

$$\rho_{TM} \frac{\partial u_{TM}}{\partial t} + (\rho_{TM} u_{TM} \cdot \nabla) u_{TM} + \nabla p_{TM} = f_{TM} \quad (10)$$

where p_{TM} is the phonon gas pressure, and f_{TM} is the friction force impeding the phonon gas. Eq. (9) gives the energy conservation equation by applying Eqs. (6) and (8). Eq. (10) characterizes the heat transport, which is the motion of thermomass through the materials. To obtain the explicit heat transport governing equation, the pressure and friction terms need to be determined. If the phonons are viewed as moving particles with finite mass, the pressure of them can be derived by accounting the momentum change when these particles hit and rebound from a unit area of the container surface, in analogy to the kinetic theory of gas. In a result, the pressure of phonon gas can be expressed as

$$p_{TM} = \frac{1}{3} \frac{v_g^2}{c^2} CT = \frac{1}{3} v_g^2 \rho_{TM} \quad (11)$$

where v_g is the group velocity of phonons. For bulk material, the friction experienced by thermomass can be extracted from Eq. (7). When discussing the nanosystems, the boundary

effect needs to be considered. The Darcy's law for porous flow was extended to Darcy-Brinkman relation when the boundary effect is nonnegligible [37, 38]

$$-\nabla p = \frac{\mu}{K}u - \mu\nabla^2 u \quad (12)$$

where μ is the viscosity, K is the permeability with a unit of m^2 . Eq. (12) indicates that the boundary slip velocity attenuates from the boundary with a characteristic length of $K^{1/2}$ to the uniform velocity in the porous medium. The introducing of a second-order spatial derivative term also makes Eq. (12) the same order as the governing equations for free flow. In the steady flow, the driving force is balanced with the friction force. Following the form of Eq. (12), when the boundary effect is considered, the friction of thermomass can be formulated as

$$f_{\text{TM}} = -\chi\rho_{\text{TM}}u_{\text{TM}} + \mu_{\text{TM}}\nabla^2 u_{\text{TM}} \quad (13)$$

where χ is the friction factor. The permeability of the thermomass in heat conducting medium is

$$K_{\text{TM}} = \frac{\mu_{\text{TM}}}{\chi\rho_{\text{TM}}} \quad (14)$$

In large systems, the boundary effect is negligible. Then, Eq. (13) reduces to the Darcy's law with the first term much more important than the second term on the right hand side.

When the spatial gradient and changing rate of physical quantities are not significant, the first and second terms in Eq. (10) can be neglected. In this case, Eq. (10) exhibits the balance between driving force and friction force. The heat conduction is steady in such a nonequilibrium system. Combining Eqs. (13) and (10) leads to

$$\chi q = -\nabla\left(\frac{1}{3}v_g^2 CT\right) \quad (15)$$

For the simplest case, v_g and C are assumed to be temperature independent. Then, Eq. (15) actually gives the Fourier law with

$$\chi = v_g^2 C / 3\kappa \quad (16)$$

When the boundary effect is considerable, the second term in Eq. (13) needs to be accounted. In this case, the combination of Eqs. (13) and (10) gives

$$-\kappa\nabla T = q - l_B^2\nabla^2 q \quad (17)$$

where l_B equaling to the square root of K_{TM} is a characteristic length.

Eq. (17) is a generalization of Fourier law when boundary effect needs to be considered. It predicts the reduction of effective thermal conductivity in nanosystems by the additional resistance term. When the system size is bigger, the spatial gradient of q is smaller. Thus, κ_{eff} increases with the system size growing larger. Nevertheless, to quantitatively predict the size dependency

of κ_{eff} and compare it with experiments, the exact value of l_B needs to be determined for certain material. The thermal conductivity is a macroscopic physical quantity, which is usually obtained by experiments. Similarly, with plenty of experimental data, the value of thermomass permeability and l_B could be evaluated. However, nowadays the experiments in nanosystems are still expensive and have large uncertainty. Therefore, in the following, a bottom-up strategy, namely, raising from microscopic phonon properties, is used to extract the value of l_B .

3. Phonon Boltzmann derivation

For dielectric solids, the Boltzmann equation describes the evolution of phonon density of state as in Ref. [26, 27]

$$Df(k, x, t) = Cf(k, x, t) \tag{18}$$

where D is the drift operator and C is the collision operator. Eq. (18) indicates that the phonon gas can freely drift without the disturbance of collision. The drift operator is

$$Df(k, x, t) = \left(\frac{\partial}{\partial t} + v_k^n \cdot \nabla \right) f^n \tag{19}$$

where v_k is the phonon velocity in one Cartesian direction. The collision, such as the phonon-phonon scattering, reshapes the phonon distribution function. In phonon theory, the collisions can be sorted to R and N processes. The R processes break the phonon quasi-momentum, while the N processes conserve it. In this sense, the collision operator can be simply formulated as

$$Cf(k, x, t) = \frac{f_0^n - f^n}{\tau_R} + \frac{f_D^n - f^n}{\tau_N} \tag{20}$$

where τ_R and τ_N are the characteristic relaxation time between succeeding R and N events. f_0 is the equilibrium distribution given by Eq. (5), f_D is the displaced distribution

$$f_D = \frac{1}{\exp[(\hbar\omega - \hbar k \cdot u_D)/k_B T] - 1} \tag{21}$$

where u_D is the drift velocity of phonon gas. Eq. (20) illustrates that the R processes tend to bring f back to f_0 , while N processes tend to bring f to f_D .

If f can be approximated with f_D , a solution of Eq. (20) can be obtained with a second-order Taylor expansion of f_D around f_0 and then integrating [33]

$$\frac{\partial q_i}{\partial t} + \frac{15}{16} \nabla_j \frac{q_i q_j}{e} + \frac{1}{3} v_g^2 C \nabla_i T = - \frac{q_i}{\tau_R} \tag{22}$$

If the friction force in Eq. (10) only has the first term, which is linear to the thermomass velocity, Eq. (22) is identical to Eq. (10) except the coefficient 15/16 in ahead of the second term on the

left hand side. This difference is caused by the Doppler Effect during the drift motion of phonon gas. From this perspective, the phonon gas is slightly different from the real gas. The phonon energy varies due to the dispersion, causing the “eclipse” of the convection term. In a nondispersive medium, the frequency is independent of k . Then, Eq. (22) is consistent with Eq. (10). Nevertheless, the second-order spatial derivative term, like in Eq. (17), is dismissed. In nanosystems, the boundary condition should be considered in solving Eq. (18). For example, if the boundary is completely diffusive, the drift velocity in Eq. (21) is dragged to zero. In this case, the phonon distribution function is assumed to have the following form.

$$f = f_D + v_g \tau_N \nabla f_D \quad (23)$$

It indicates that with the diffusive boundary, the N processes induce a deviation from f_D , with the relaxation length $\lambda_N = v_g \tau_N$, i.e., the MFP of N processes. The additional term in Eq. (23) gives a second-order spatial derivative term. By the integration of Eq. (18), one gets

$$\frac{\partial q_i}{\partial t} + \frac{15}{16} \nabla_j \frac{q_i q_j}{e} + \frac{1}{3} v_g^2 C \nabla_i T = -\frac{q_i}{\tau_R} + \frac{\tau_N v_g^2}{5} \nabla^2 q_i \quad (24)$$

Keep in mind that the thermal conductivity in bulk limit is expressed by Eq. (2), in steady state, one-dimensional heat conduction case, Eq. (24) can be simplified to

$$-\kappa \nabla T = q - \frac{\lambda_R \lambda_N}{5} \nabla^2 q \quad (25)$$

Eq. (25) can be regarded as the first order Chapman-Enskog expansion [17] of the phonon distribution function. In fluid mechanics, the viscous term in Navier-Stokes equation can be derived from the first order Chapman-Enskog expansion of the state distribution function of fluid molecular. Without the Chapman-Enskog expansion, the solution of Boltzmann equation gives the Euler equation, which is the dynamic equation without the viscous dissipation. This case happens when the interested region is far away from the boundary, or the boundary layer thickness is negligible compared with the flow region, like the large Reynolds number flow around the aircrafts. The difference between the thermomass flow and ordinary gas flow is that the R processes causes residential friction forces to the flow, which makes the transfer diffusive. In low temperature crystals, or low dimensional materials, such as graphene, the R processes can be rare. Then the heat conduction will exhibit obvious hydrodynamic behaviors. Therefore, based on the phonon Boltzmann derivation, the value of l_B in Eq. (17) can be determined as $l_B^2 = \lambda_R \lambda_N / 5$.

4. Phonon gas flow in Si nanosystems

Based on Eq. (25) we can calculate the effective thermal conductivity of nanosystems. The silicon nanofilms and nanowires are investigated here because the experimental results are available for comparison. The geometries of nanofilms and nanowires are shown in **Figure 1**. The direction of heat conduction is in-plane for nanofilms and longitudinal for nanowires.

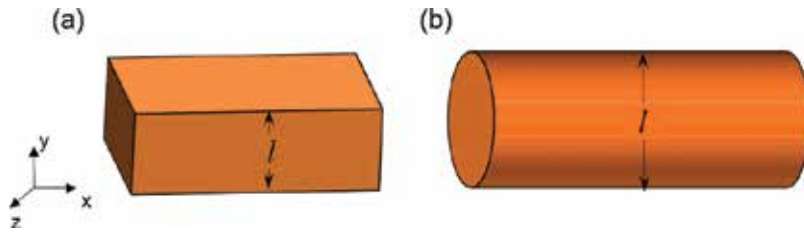


Figure 1. Heat conduction in nanosystems. (a) In-plane nanofilm; (b) nanowire.

Assume the boundary is completely diffusive, i.e., the phonon gas drift velocity is zero on the boundary. The solution of Eq. (25) for a nanofilm is [39]

$$q(y) = -\kappa_0 \nabla T \left[1 - \frac{\cosh(y/l_B)}{\cosh(l/2l_B)} \right] \quad (26)$$

$$\kappa_{\text{eff}}^{\text{nf}} = \frac{\int_l q dy}{-\nabla T l} = \kappa_0 [1 - 2Br \cdot \tanh(1/2Br)] \quad (27)$$

where l is the thickness of film and $Br = l_B/l$ is the Brinkman number. The solution for nanowire is

$$q(y) = -\kappa_0 \nabla T \left[1 - \frac{J_0(iy/l_B)}{J_0(il/2l_B)} \right] \quad (28)$$

$$\kappa_{\text{eff}}^{\text{nw}} = \kappa_0 \left[1 - (4Br) \cdot \frac{J_1(i/2Br)}{iJ_0(i/2Br)} \right] = \kappa_0 \left[1 - \frac{\sum_{t=0}^{\infty} \frac{(4Br)^{-2t}}{t!(t+1)!}}{\sum_{t=0}^{\infty} \frac{(4Br)^{-2t}}{t!t!}} \right] \quad (29)$$

where l is the diameter (thickness) of the wire and J is the cylindrical Bessel function

$$J_n(x) = \left(\frac{x}{2}\right)^n \sum_{t=0}^{\infty} \frac{(-1)^t (x/2)^{2t}}{t!(t+n)!} \quad (30)$$

Eqs. (26) and (28) show the heat flux is nonuniform at the cross-section. If the system size is much larger than l_B , $q(y)$ tends to be constant. Then, the effective thermal conductivity renders the bulk limit, κ_0 . If the system size is comparable with l_B , $q(y)$ is significantly affected by the boundary. Thereby, κ_{eff} is strongly reduced.

The analytical derivation of Eqs. (26)–(30) is based on the assumption that the l_B is constant. However, in nanosystems, the phonon would scatter with boundary, which shortens the MFPs. For the pure diffusive boundary, the scattering on boundary will terminate the MFPs. It can be seen as the additional collision event into the ordinary scatterings. If the boundary is located at r away from the originating point, the effective MFP of phonons can be expressed as

$$\frac{\lambda_{\text{eff}}}{\lambda_0} = 1 - \exp\left(-\frac{r}{\lambda_0}\right) \quad (31)$$

In this way, the effective MFPs in nanosystems can be obtained by integrating over the sphere angle. For nanofilms, the local value of MFPs is [40]

$$\frac{\lambda_{\text{eff}}(y)}{\lambda_0} = 1 + \frac{1}{2} [(\alpha - 1)e^{-\alpha} + (\beta - 1)e^{-\beta} - \alpha^2 E_i(\alpha) - \beta^2 E_i(\beta)] \quad (32)$$

where $\alpha = (l/2 - y)/\lambda_0$, $\beta = (l/2 + y)/\lambda_0$, and $E_i(x) = \int_1^\infty t^{-1} e^{-tx} dt$. For nanowires, we have

$$\frac{\lambda_{\text{eff}}(y)}{\lambda_0} = \frac{1}{\pi} \int_0^\pi \int_0^{\frac{\pi}{2}} \left[1 - \exp\left(-\frac{y \cos \theta + \sqrt{l^2/4 - y^2 \sin^2 \theta}}{\lambda_0 \sin \varphi}\right) \right] \sin \varphi d\varphi d\theta \quad (33)$$

Therefore, the MFPs are significantly shortened in nanosystems. It reveals that the boundary has dual effects on heat conduction in nanosystems. First, the second spatial derivative of heat flux, which represents the viscous effect of phonon gas, imposes additional resistance on heat transfer due to the nonslip boundary condition. Second, the collision on boundary changes the effective MFPs. This effect is similar to the rarefaction of gas flow in high Kn case. By accounting both the dual effects, the thermal conduction in nanosystems is described as

$$-\frac{\lambda_{\text{R,eff}}(r)}{\lambda_{\text{R},0}} \kappa_0 \nabla T = q(r) - \frac{\lambda_{\text{R,eff}}(r) \lambda_{\text{N,eff}}(r)}{5} \nabla^2 q(r) \quad (34)$$

It is worth noting that in fluid mechanics, the rarefaction is not necessarily happened at the same time of viscous effect based on the Darcy-Brinkman relation. Consider the water flow in porous material. The permeability of porous flow is determined by the size of pores, which typically is in the order of micrometers. The MFP among water molecule is typically subnanometer. Therefore, the square root of permeability differs much from the MFP. The effects of Darcy-Brinkman boundary layer and rarefaction can be unconjugated. On the other hand, if the fluid is replaced by gas, the MFP of fluid could be comparable to the square root of permeability. In this case, the Darcy-Brinkman boundary layer and the rarefaction should be considered simultaneously. For the phonon gas flow, the relative magnitude of λ_{R} , λ_{N} , and l decides the conjugation of boundary layer and rarefaction. λ_{R} represents the "size of pores" while λ_{N} represents the viscosity of phonon gas. The bulk limit is achieved when $l \gg \lambda_{\text{R}}$ and $l \gg \lambda_{\text{N}}$. If $\lambda_{\text{R}} \gg l \gg \lambda_{\text{N}}$, the first term on the right hand side of Eq. (34) is less important than the second term. The flow mimics a dense fluid passing through a sparse medium. The boundary transmits momentum efficiently across the flow region. The phonon hydrodynamics can be observed. If $\lambda_{\text{N}} \gg l \gg \lambda_{\text{R}}$, the flow mimics a dilute fluid passing through a dense medium. The velocity profile will be close to linear. In this case, only the rarefaction effect needs to be considered. If $\lambda_{\text{N}} \gg l$ and $\lambda_{\text{R}} \gg l$, both the rarefaction and boundary drag affect the resistance on flow and need to be modeled simultaneously.

The numerical solution of Eq. (34) gives the effective thermal conductivity for Si nanofilms and nanowires at room temperature, as shown in **Figure 2**. The physical properties are adopted as $\kappa_0 = 148\text{W}/(\text{m K})$ (standard experiment value for monocrystalline Si), $\lambda_{R,0} = 42\text{ nm}$ (according to the direct calculation based on Eq. (2)), $\lambda_{N,0} = 360\text{ nm}$. The predictions based on the gray model [7], McGaughey model [16], and Ma model [31] are also presented in **Figure 2**. It shows the gray model and McGaughey model overestimate the thermal conductivities. Ma model gives close results to experiments. However, Ma model assumes a MFP of 210 nm, which is lack of physical support. It also shows an unreasonable drop at $D = 1000\text{--}2000\text{ nm}$ for nanowires. According to **Figure 2**, our model achieves the best agreement with current available experiment and numerical results.

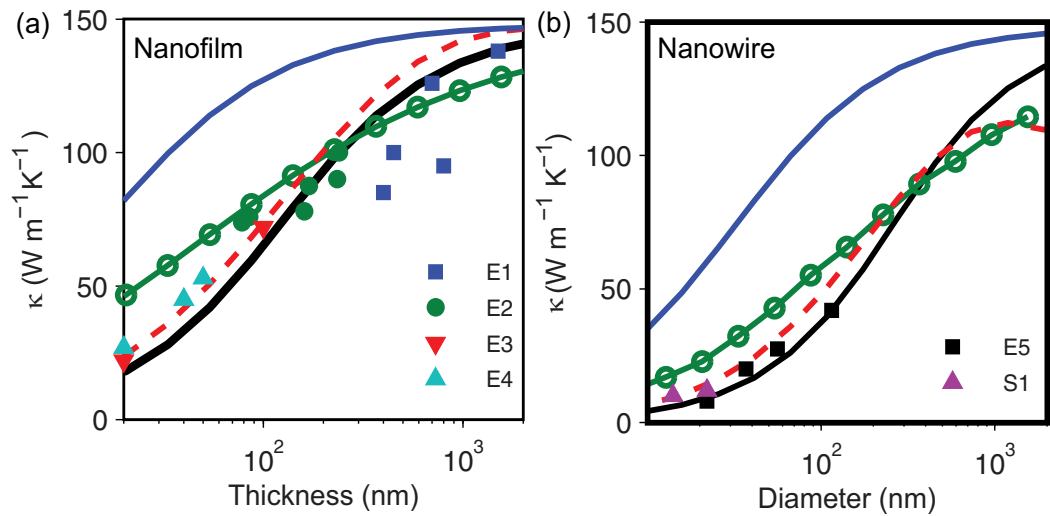


Figure 2. Effective in-plane thermal conductivities of single crystal Si nanosystems at room temperature. Bottom solid line: present model (Eq. (34)); top solid line: gray model [7]; solid and circle: McGaughey model [16]; dash line: Ma model [31]. (a) Nanofilm. Symbols E1–E4 are experimental results from Refs. [18–21]. (b) Nanowire. Square is experimental results from Ref. [25]. Triangle is numerical results from Refs. [41, 42].

5. Thermal rectification in nanosystems

Thermal rectification refers that the heat conduction in one direction of the device leads to higher heat flux than following the opposite direction, even though the same temperature difference is applied. It currently raises much interest since the first experimental report by carbon nanotubes [43]. The thermal rectification effect is anticipated to realize thermal diode [44], thermal logic gate [45], or thermal transistors [46, 47]. Though much effort has been paid for searching useful mechanisms and realizing considerable rectification ratio, the ambitious goal that controlling heat as electricity is still far away [48].

The mechanism of thermal rectification has been widely studied. It is found that various effects can induce rectification, such as the different temperature dependences of the thermal conductivity at the different parts of the device [49], the asymmetric transmission rates of

phonons across the interfaces [50], and the temperature dependence of electromagnetic resonances [51]. Here, another rectification mechanism is proposed through the thermomass theory, following an analogy to fluid mechanics. In Navier-Stokes equations, the convective acceleration term indicates when the fluid experiences speed up or slow down. Therefore, if the cross-section area of a flow channel is changing (e.g. the trapezoidal channel), the flow rate under the same pressure difference is different in the convergent direction or in the divergent direction. In the convergent direction, the channel serves as a nozzle, which accelerates the fluid and converts part of its potential energy to the kinetic energy. In the divergent direction, the channel serves as a diffuser, which decelerates the fluid and converts part of its kinetic energy to the potential energy. The acceleration of fluid increases the velocity head and consumes the dynamic head of flow. Therefore, the total fluid flux in the convergent direction will be less than that in the divergent direction. In terms of thermal conduction, it means that with the same temperature difference between the heat source and sink, the total heat flux in the wide-to-narrow direction is smaller than that in the narrow-to-wide direction, which is the thermal rectification. Nevertheless, it should be stressed that for a flow channel with large angle of divergence, the flow separation could happen when the fluid velocity is high. In case of flow separation, the effective resistance of the diffuser will be much increased. It may cause the total heat flux in the wide-to-narrow direction larger than that in the narrow-to-wide direction, that is, the reverse of rectification.

In steady state, the generalized conduction law, Eq. (10), can be reformulated as

$$-\tau_R \nabla_j \frac{q_i q_j}{e} - \kappa \nabla T = q_i - l_B^2 \nabla^2 q \quad (35)$$

The difference between Eqs. (35) and (25) is the additional convective term, $-\tau_R \nabla_j q_i q_j / e$. The first term on the left hand side mimics to the spatial inertia term in fluid mechanics. It induces rectification effect. Consider a trapezoidal material with heat conducting through the symmetry axis, as shown in **Figure 3**. The thickness of the material is H ; the widths at the narrow and the wide ends are L_W and L_N , respectively, and the separation between these ends is L . If L is much larger than L_N and L_W , the heat conduction can be assumed as quasi-one-dimensional. The mainstream of heat flux is in the x direction, $q_x \gg q_y$. The total heat flux (Q) at each cross-section perpendicular to x direction is constant. Due to the boundary friction, the Laplacian of q_x in the y direction is much larger than in the x direction. Then, the x component of Eq. (35) is

$$-\kappa \frac{\partial T}{\partial x} = q_x \left(1 + \tau_R \frac{\partial q_x}{\partial x CT} \right) - l_B^2 \frac{\partial^2}{\partial y^2} q_x = q_x (1 + C_R) - l_B^2 \frac{\partial^2}{\partial y^2} q_x \quad (36)$$

where C_R consists of two terms

$$C_R = \frac{\tau_R}{CT} \frac{\partial q_x}{\partial x} - \frac{\tau_R q_x}{CT^2} \frac{\partial T}{\partial x} \quad (37)$$

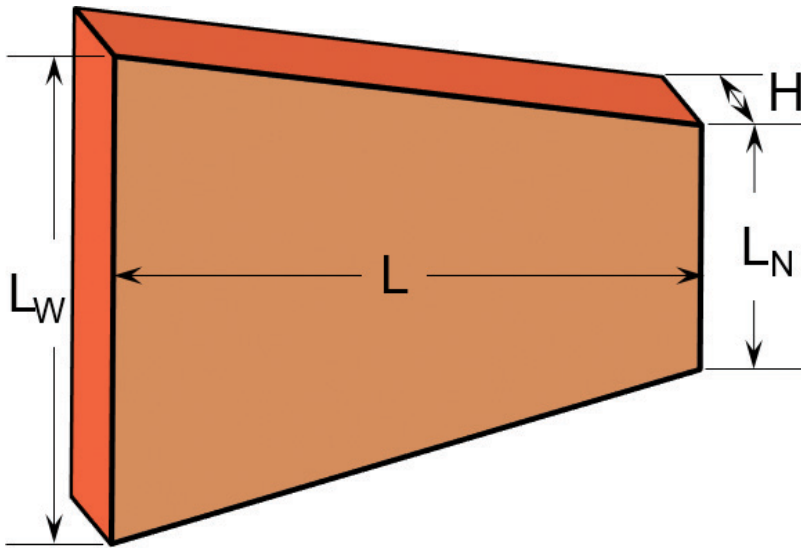


Figure 3. Trapezoidal nanoribbon for demonstrating thermal rectification.

The sign of the first term of C_R will be positive for the heat conduction in a convergent channel, which means the acceleration of heat flux creates additional effective resistance, and reduces the total heat flux. Oppositely, heat conduction in a divergent channel will increase the total heat flux. The second term of C_R will not change sign with the direction of heat transport. It characterizes the acceleration due to density variation since thermomass is compressible. It is insignificant except for the case of ultra-high heat flux [52].

To enhance the thermal rectification, the directional sensitive part in Eq. (36) should be amplified over the directional non-sensitive part. If the diffusive boundary condition is replaced with slip boundary condition, or the system size is large compared with the boundary layer, the Laplacian term of heat flux can be neglected. In room temperature, the second term of C_R is usually much less than the first term. In this case, Eq. (36) can be simplified to

$$-\kappa \frac{\partial T}{\partial x} = q_x \left(1 + \frac{\tau_R}{CT} \frac{\partial q_x}{\partial x} \right) \quad (38)$$

Consider a silicon ribbon with the average temperature 300 K. Assume that $H = 1000$ nm, $L = 300$ nm, $L_N = 300$ nm, L_W varies from 300 to 2000 nm. The relaxation time τ_R is set as $1.5e-10$ s based on experimental results [53]. The temperatures on both ends are 330 and 270 K, respectively. By numerically solving Eq. (38), we can get the rectification ratio (defined as the thermal conductance in narrow-to-wide direction over that in the opposite direction), as shown in **Figure 4**. It shows that the rectification ratio grows with L_W from zero to a considerable value of 32.3%. This value is large enough to construct thermal diode or thermal logic gate.

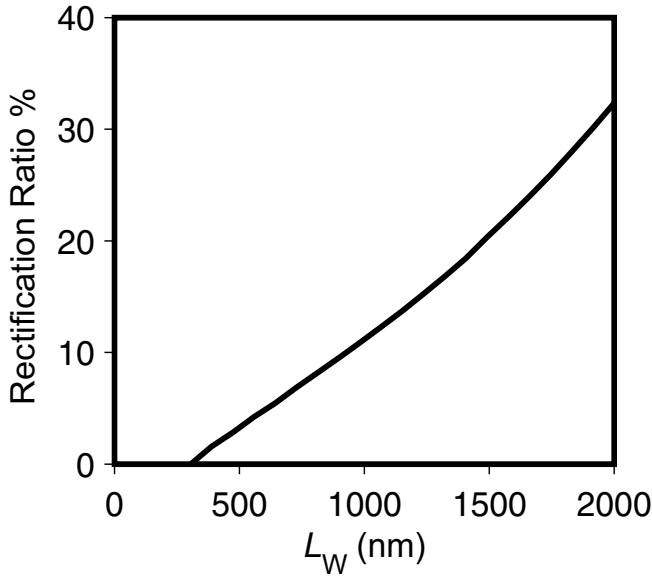


Figure 4. Thermal rectification ratio depending on L_w of the trapezoidal silicon ribbon.

6. Thermoelectricity of nanosystems

The ZT for nanomaterials could be much enhanced [10–13]. The mechanism of such enhancement can be that the nanostructures reduce the thermal conductivity by strong phonon-boundary scattering while maintaining the electrical conductivity. Although a lot of work has been done in searching high ZT materials through nanotechnology, the thermodynamic analysis and the role of nonlocal and nonlinear transports, which are highly possible to happen in nanosystems, are not fully discussed [54, 55]. In recent years, the nonlocal effects raised by the MFP reduction due to geometry constraint [56], the electron and phonon temperature [57], and the breakdown of Onsager reciprocal relation (ORR) [58, 59] in nanosystems have been investigated from the framework of extended irreversible thermodynamics (EIT). These works showed that the nonlinear and nonlocal effects influence the efficiency of devices. The breakdown of ORR not only possesses theoretical importance but also shed light on approaches to further increase efficiency.

Here, we analyze the thermoelectric effect from the thermomass theory perspective. There could be various effects when the individual motion of phonon gas and electron gas is separately considered. The most apparent one is the energy exchange between phonons and electrons [60]. In a one-dimensional thermoelectric medium, the conservation of energy gives

$$\nabla q - IE = 0 \quad (39)$$

where I is the electrical current and E is the electrical field. IE equals the adding or subtracting rate of thermal energy. Dividing Eq. (39) by c^2 illustrates that the electrical current performs as

the mass source or sink of thermomass. The nonconservation of mass brings additional term in Eq. (10). In steady state, we obtain the governing equation of thermomass momentum as

$$(\rho_{TM} u_{TM} \cdot \nabla) u_{TM} + u_{TM} \nabla \cdot (\rho_{TM} u_{TM}) + \nabla p_{TM} = f_{TM} \quad (40)$$

The second term on the left hand side is nonzero because of the energy conversion. It increases the spatial inertia of thermomass. For simplicity, we do not consider the Brinkman extension of the friction force and assume the material cross-section is constant, and then Eq. (40) turns to

$$-\kappa \frac{\partial T}{\partial x} = q_x (1 + C_R) \quad (41)$$

where

$$C_R = \frac{2\tau_R}{CT} IE - \frac{\tau_R q_x}{CT^2} \frac{\partial T}{\partial x} \quad (42)$$

Compared with Eq. (37), the first term of C_R has a coefficient 2 because of the energy exchange between phonons and electrons. The electrical current couples with the heat flux and induces additional spatial acceleration force on the thermomass flow. This inertia increase is insignificant in ordinary conditions due to the small value of τ_R . It could be considerable in case of strong power thermoelectric convertor with large electrical current and intense electrical field. Neglecting the second term of C_R , it can be derived that the effective thermal conductivity and Seebeck coefficient change to

$$\kappa' = (1 + C_R)^{-1} \kappa \quad (43)$$

$$S' = (1 + C_R)^{-1} S \quad (44)$$

Since ZT is $S^2\sigma/\kappa T$, the effective ZT is $(1 + C_R)^{-1}$ of the original one without considering the inertia effect of thermomass. Therefore, when $IE > 0$, the electrical energy converts to thermal energy. It is typically the case of thermoelectric cooler. The heat flux is additionally impeded. The ZT is decreased. When $IE < 0$, the temperature gradient drives electric current. It is typically a thermoelectric generator. The heat flux is further pumped, and the effective ZT is enhanced. The inertia effect could be beneficial for a higher ZT of the device in this case.

7. Conclusion

In this chapter, we present a mechanical analysis on the thermal conduction in nanosystems with the thermomass theory. Firstly, the boundary resistance in nanosystems on heat flow is modeled with the Darcy-Brinkman analogy. The permeability of thermomass in materials is derived based on the phonon Boltzmann equation. The size-dependent effective thermal conductivity of Si nanosystems thereby is accurately predicted with the present model. Then, the spatial inertia effect of thermomass is shown to induce the thermal rectification in

asymmetry nanosystems. The predicted rectification ratio can be as high as 32.3% in a trapezoidal Si nanoribbon. Finally, the energy conversion in thermoelectric devices can be coupled with the spatial inertia of thermomass flow. The ZT tends to be increased in case of a thermoelectric generator.

Acknowledgements

This work was financially supported by the National Natural Science Foundation of China (nos. 51136001, 51356001) and the Tsinghua University Initiative Scientific Research Program.

Author details

Yuan Dong^{1*}, Bingyang Cao² and Zengyuan Guo²

*Address all correspondence to: dony327@163.com

1 Department of Mechanical & Aerospace Engineering, University of Missouri, Columbia, Missouri, USA

2 Key Laboratory for Thermal Science and Power Engineering of Ministry of Education, Department of Engineering Mechanics, Tsinghua University, Beijing, China

References

- [1] Fourier J. *Analytical Theory of Heat*. New York: Dover Publications; 1955.
- [2] Cattaneo, C. Sulla conduzione del calore. In *Some Aspects of Diffusion Theory*, pp. 485. Berlin: Springer; 2011.
- [3] Ackerman CC, Bertman B, Fairbank HA, Guyer R. Second sound in solid helium. *Physical Review Letters*. 1966;16(18):789.
- [4] Joseph DD, Preziosi L. Heat waves. *Reviews of Modern Physics*. 1989;61(1):41.
- [5] Qiu T, Tien C. Femtosecond laser heating of multi-layer metals—I. Analysis. *International Journal of Heat and Mass Transfer*. 1994;37(17):2789-2797.
- [6] Tzou DY. *Macro-to Microscale Heat Transfer: The Lagging Behavior*. Chichester: John Wiley & Sons; 2014.
- [7] Majumdar A. Microscale heat conduction in dielectric thin films. *Journal of Heat Transfer*. 1993;115(1):7-16.
- [8] Ziman JM. *Electrons and Phonons: The Theory of Transport Phenomena in Solids*. Oxford: Oxford University Press; 2001.
- [9] Kittel C. *Introduction to Solid State Physics*. 7th ed. New York: Wiley; 1996.

- [10] Boukai AI, Bunimovich Y, Tahir-Kheli J, Yu JK, Goddard Iii WA, Heath JR. Silicon nanowires as efficient thermoelectric materials. *Nature*. 2008;451(7175):168-171.
- [11] Hochbaum AI, Chen R, Delgado RD, Liang W, Garnett EC, Najarian M, et al. Enhanced thermoelectric performance of rough silicon nanowires. *Nature*. 2008;451(7175):163-167.
- [12] Poudel B, Hao Q, Ma Y, Lan Y, Minnich A, Yu B, et al. High-thermoelectric performance of nanostructured bismuth antimony telluride bulk alloys. *Science*. 2008;320(5876):634-638.
- [13] Liu W, Yan X, Chen G, Ren Z. Recent advances in thermoelectric nanocomposites. *Nano Energy*. 2012;1(1):42-56.
- [14] Bell LE. Cooling, heating, generating power, and recovering waste heat with thermoelectric systems. *Science*. 2008;321(5895):1457-1461.
- [15] Baranowski LL, Snyder GJ, Toberer ES. Concentrated solar thermoelectric generators. *Energy & Environmental Science*. 2012;5(10):9055-9067.
- [16] McGaughey AJ, Landry ES, Sellan DP, Amon CH. Size-dependent model for thin film and nanowire thermal conductivity. *Applied Physics Letters*. 2011;99(13):131904.
- [17] Chapman S, Cowling TG. *The Mathematical Theory of Non-Uniform Gases: An Account of the Kinetic Theory of Viscosity, Thermal Conduction and Diffusion in Gases*. Cambridge: Cambridge University Press; 1970.
- [18] Asheghi M, Leung Y, Wong S, Goodson K. Phonon-boundary scattering in thin silicon layers. *Applied Physics Letters*. 1997;71(13):1798-1800.
- [19] Ju Y, Goodson K. Phonon scattering in silicon films with thickness of order 100 nm. *Applied Physics Letters*. 1999;74(20):3005-3007.
- [20] Liu W, Asheghi M. Phonon-boundary scattering in ultrathin single-crystal silicon layers. *Applied Physics Letters*. 2004;84(19):3819-3821.
- [21] Ju YS. Phonon heat transport in silicon nanostructures. *Applied Physics Letters*. 2005;87(15):153106.
- [22] Chen G. Thermal conductivity and ballistic-phonon transport in the cross-plane direction of superlattices. *Physical Review B*. 1998;57(23):14958.
- [23] Yang R, Chen G. Thermal conductivity modeling of periodic two-dimensional nanocomposites. *Physical Review B*. 2004;69(19):195316.
- [24] Dames C, Chen G. Theoretical phonon thermal conductivity of Si/Ge superlattice nanowires. *Journal of Applied Physics*. 2004;95(2):682-693.
- [25] Li D, Wu Y, Kim P, Shi L, Yang P, Majumdar A. Thermal conductivity of individual silicon nanowires. *Applied Physics Letters*. 2003;83(14):2934-2936.
- [26] Guyer RA, Krumhansl J. Solution of the linearized phonon Boltzmann equation. *Physical Review*. 1966;148(2):766.

- [27] Guyer R, Krumhansl J. Thermal conductivity, second sound, and phonon hydrodynamic phenomena in nonmetallic crystals. *Physical Review*. 1966;148(2):778.
- [28] Alvarez F, Jou D, Sellitto A. Phonon hydrodynamics and phonon-boundary scattering in nanosystems. *Journal of Applied Physics*. 2009;105(1):014317.
- [29] Jou D, Criado-Sancho M, Casas-Vázquez J. Heat fluctuations and phonon hydrodynamics in nanowires. *Journal of Applied Physics*. 2010;107(8):084302.
- [30] Sellitto A, Alvarez F, Jou D. Second law of thermodynamics and phonon-boundary conditions in nanowires. *Journal of Applied Physics*. 2010;107(6):064302.
- [31] Ma Y. Size-dependent thermal conductivity in nanosystems based on non-Fourier heat transfer. *Applied Physics Letters*. 2012;101(21):211905.
- [32] Cao BY, Guo ZY. Equation of motion of a phonon gas and non-Fourier heat conduction. *Journal of Applied Physics*. 2007;102(5):053503.
- [33] Dong Y, Cao BY, Guo ZY. Generalized heat conduction laws based on thermomass theory and phonon hydrodynamics. *Journal of Applied Physics*. 2011;110(6):063504.
- [34] Wang M, Yang N, Guo ZY. Non-Fourier heat conduction in nanomaterials. *Journal of Applied Physics*. 2011;110(6):064310.
- [35] Dong Y. *Dynamical Analysis of Non-Fourier Heat Conduction and Its Application in Nanosystems*. Berlin: Springer; 2015.
- [36] Einstein A, Infeld L. *The Evolution of Physics: The Growth of Ideas from Early Concepts to Relativity and Quanta*. New York: Simon and Schuster; 1938.
- [37] Brinkman HA. Calculation of the viscous force exerted by a flowing fluid on a dense swarm of particles. *Flow, Turbulence and Combustion*. 1949;1(1):27.
- [38] Nield DA, Bejan A. *Convection in Porous Media*. Berlin: Springer; 2006.
- [39] Dong Y, Cao BY, Guo ZY. Size dependent thermal conductivity of Si nanosystems based on phonon gas dynamics. *Physica E: Low-Dimensional Systems and Nanostructures*. 2014;56:256-262.
- [40] Guo Z, Shi B, Zheng CG. An extended Navier-Stokes formulation for gas flows in the Knudsen layer near a wall. *EPL (Europhysics Letters)*. 2007;80(2):24001.
- [41] Moore AL, Saha SK, Prasher RS, Shi L. Phonon backscattering and thermal conductivity suppression in sawtooth nanowires. *Applied Physics Letters*. 2008;93(8):083112.
- [42] He Y, Galli G. Microscopic origin of the reduced thermal conductivity of silicon nanowires. *Physical Review Letters*. 2012;108(21):215901.
- [43] Chang C, Okawa D, Majumdar A, Zettl A. Solid-state thermal rectifier. *Science*. 2006;314(5802):1121-1124.
- [44] Li B, Wang L, Casati G. Thermal diode: rectification of heat flux. *Physical Review Letters*. 2004;93(18):184301.

- [45] Wang L, Li B. Thermal logic gates: computation with phonons. *Physical Review Letters*. 2007;99(17):177208.
- [46] Lo WC, Wang L, Li B. Thermal transistor: heat flux switching and modulating. *Journal of the Physical Society of Japan*. 2008;77(5):054402.
- [47] Joulain K, Drevillon J, Ezzahri Y, Ordóñez-Miranda J. Quantum thermal transistor. *Physical Review Letters*. 2016;116(20):200601.
- [48] Li N, Ren J, Wang L, Zhang G, Hänggi P, Li B. Colloquium: phononics: manipulating heat flow with electronic analogs and beyond. *Reviews of Modern Physics*. 2012;84(3):1045.
- [49] Dames C. Solid-state thermal rectification with existing bulk materials. *Journal of Heat Transfer*. 2009;131(6):061301.
- [50] Hu M, Koblinski P, Li B. Thermal rectification at silicon-amorphous polyethylene interface. *Applied Physics Letters*. 2008;92(21):211908.
- [51] Basu S, Francoeur M. Near-field radiative transfer based thermal rectification using doped silicon. *Applied Physics Letters*. 2011;98(11):113106.
- [52] Wang HD, Cao BY, Guo ZY. Heat flow choking in carbon nanotubes. *International Journal of Heat and Mass Transfer*. 2010;53(9):1796-1800.
- [53] Sahasrabudhe G, Lambade S. Temperature dependence of the collective phonon relaxation time and acoustic damping in Ge and Si. *Journal of Physics and Chemistry of Solids*. 1999;60(6):773-785.
- [54] Tzou D, Puri P. Macro-to microscale heat transfer: the lagging behavior. *Applied Mechanics Reviews*. 1997;50:B82-B.
- [55] Casas-Vázquez J, Lebon G, Jou D. *Extended Irreversible Thermodynamics*. Berlin: Springer; 2010.
- [56] Jou D, Cimmelli V, Sellitto A. Nonlocal heat transport with phonons and electrons: application to metallic nanowires. *International Journal of Heat and Mass Transfer*. 2012;55(9):2338-2344.
- [57] Sellitto A, Cimmelli V, Jou D. Influence of electron and phonon temperature on the efficiency of thermoelectric conversion. *International Journal of Heat and Mass Transfer*. 2015;80:344-352.
- [58] Cimmelli V, Sellitto A, Jou D. A nonlinear thermodynamic model for a break-down of the Onsager symmetry and the efficiency of thermoelectric conversion in nanowires. *Proc. R. Soc. A*. 2014;470:20140265.
- [59] Sellitto A. Crossed nonlocal effects and breakdown of the Onsager symmetry relation in a thermodynamic description of thermoelectricity. *Physica D: Nonlinear Phenomena*. 2014;283:56-61.
- [60] Dong Y. Clarification of Onsager reciprocal relations based on thermomass theory. *Physical Review E*. 2012;86(6):062101.

Surface Nanomechanics of Biomolecules and Supramolecular Systems

Paolo Bergese and Stefania Federici

Additional information is available at the end of the chapter

<http://dx.doi.org/10.5772/intechopen.68293>

Abstract

Surface nanomechanics of biomolecules and supramolecular systems is an interdisciplinary and vital area of current research, with implications/applications spanning from synthetic biology to regenerative medicine, from smart surfaces to molecular machines. Biomolecule surface transformations and nanomachinery arise upon “wiring” them onto surfaces and interfaces. Surface confinement of biomolecules is a common feature of biological systems (e.g., cell membranes) and often a mandatory step for translating their properties into real-world applications (e.g., biosensors). On surfaces biomolecules undergo peculiar transformations and interactions which they do not experience in solution. Such unedited effects open challenges in synthetic systems, for example, by altering or hindering the designed/expected property, but also disclose a wealth of opportunities and surprises. Based on our latest research, this chapter will bring fresh excerpts from the field. It will start with an accessible description of thermodynamics of surface nanomechanics of biomolecules and supramolecular systems and then will show how it can be implemented to gain understanding of grow factor cell signaling, to single out small ligands able to inhibit protein misfolding, to measure energetics of surface confined ferritin during iron loading, and to realize a universal probe for ammine-based designer drugs.

Keywords: molecular transformations, surface, nanomechanics, nanomechanical sensors, grow factors, ferritin, abiotic supramolecular receptors, designer drugs

1. Describing and probing molecule collective surface nanomechanics

The section introduces the description of surface molecule transformations by classical interfacial thermodynamics. This will be helpful to better grasp the working principle of nanomechanical sensors, which will be presented in the next subsection. Nanomechanical sensors are

the basic technology used to probe and quantify molecule collective surface nanomechanics. The level of the treatment is kept concise and accessible to a wide readership; those interested in the throughout treatment are redirected to Refs. [1–3].

For simplicity, let us restrict to the case of a solid supported monolayer of proteins that can only switch between two conformational states, A and B. The switch from A to B can be directed by changing the electrolyte (salt) molar concentration of the solution in which the system is immersed. This changes the amount of ions bound to the protein and the Debye-Hückel screening of the charge interactions on the protein, which in turn trigger the exposition to the solution of peptide groups that were buried in conformation A, driving the protein into conformation B.

With the visual help of **Figure 1**, it can be intuitively seen that the switch from state A to state B involves a change of the in-plane interactions between the proteins, because the switch is intertwined with several nanoscale and subnanoscale changes, such as intermolecular distances, surface charge and monolayer thickness. This can be thermodynamically described by an additional surface work that accompanies the surface transformation with respect to the same transformation occurring in “free” solution. In particular, it can be shown [2, 3] that the surface standard molar Gibbs energy, $\Delta_r G_0^s$, of the surface switch from state A to state B is composed by the sum of an excess surface work, W^s , and the molar Gibbs energy of the same transformation occurring in bulk solution, $\Delta_r G_0^o$:

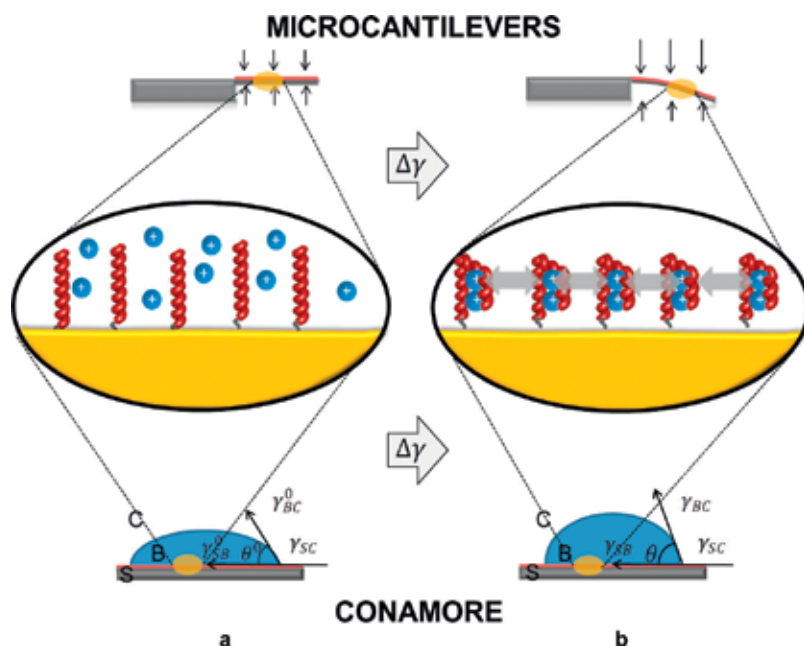


Figure 1. Working principle of nanomechanical sensors in the representative case of a solid supported monolayer of proteins switching between state A (left images) to state B (right images) upon binding to cations. The switch drives the overall variation of surface tension $\Delta\gamma$, triggered at the nanoscale by the change of in-plane interactions between proteins.

$$\Delta_r G_0^\sigma = \Delta_r G_0^b + W^\sigma \quad (1)$$

In addition, W^σ can be further detailed as [2, 3]

$$W^\sigma = \frac{\Delta\gamma}{\Gamma_B} \quad (2)$$

where $\Delta\gamma$ is the thermodynamic surface tension, for simplicity hereafter referred as surface tension, that gathers both the mechanical, $\Delta\sigma$, and electrostatic, ω_e^σ , contributions, and Γ_B is the surface density of proteins in state B. From a (nano)mechanical view point, one can say that $\Delta\gamma$ exerts a surface stress on the surface that supports the molecular monolayer or thin film.

The above considerations and equations have general validity. Molecular transformations, recognition, binding and nanomachinery at a solid-liquid interface involve nanomechanical work with point of application at the surface. This arises from a very complex co-operative action of electrostatic, steric (hydration) and thermal fluctuation (entropic) forces triggered by the transformation that macroscopically appear as a variation of the surface tension, or the applied surface stress. The nature of the forces is determined by the specific solid-solution interfacial environment, that is, by the molecules and their binding partners, the molecule surface density, the solution composition and ionic strength, the solid surface and modification chemistry, the solid geometry and nanostructure, and so on. This phenomenon is leveraged by static nanomechanical sensors [4]. In particular, the molecular transformations confined on the sensor surface cumulate and perform an overall surface tension change in the order of mN/m [2] that can be probed and translated by tensiometric techniques such as contact angle [5] or microcantilever (MC) beams [6], as sketched in **Figure 1**.

The working principle of MC biosensor is quite simple: the MC surface is functionalized with a receptor that can selectively bind the target species. Adsorption and binding site interactions of the targets change the mechanical response of the MC system (because of the surface stress generated by changes in Gibbs free energy), providing the transduction/sensing mechanism. CONAMORE (CONtact Angle MOlecularREcognition) technique is based on the sessile drop contact angle principle. When a droplet containing the target species is placed onto a solid surface functionalized with a receptor, it reaches equilibrium with the surface and the surroundings under the action of the interfacial tensions at the contact line at which drop, surface, and surroundings meet, forming a definite contact angle [5].

The variation of the overall surface tension $\Delta\gamma$ can be directly determined by CONAMORE measurement, where the molecular transformations can be univocally associated with the differential of the solid-solution interfacial tensions of the systems represented in **Figure 1a** and **b**. In case of MC experiments, $\Delta\gamma$ can be easily calculated through the relation between $\Delta\gamma$ and MC deflection, Δz , given by the Stoney equation [7]:

$$\Delta\gamma = -\frac{\Delta z E t^2}{4 L^2(1-\nu)} \quad (3)$$

where Δz is the cantilever deflection (with the z axis individuated by the unitary vector normal to the top surface of the cantilever base, i.e., $\Delta z < 0$ for a downward cantilever bending), E is the cantilever Young's modulus, t is the cantilever thickness, L is the cantilever length, and ν is the cantilever Poisson's ratio.

Application of nanomechanical sensors to biosensing has become in the last 15 years a breakthrough in biochemistry, life science and medicine, depicting how nanomechanics and biology can grow together [6, 8, 9]. Research in this direction is growing substantially after the milestone work of Fritz and coworkers in 2000, in which they report the specific transduction driven by the surface stress change of DNA hybridization without reported labels [6]. Several experiments have been successfully performed afterwards, revealing DNA hybridization and DNA switch [10–12], detecting proteins and antibodies [5, 13, 14], single virus particles [15] or bacteria [16].

2. Surface nanomechanics of biomolecules

2.1. Role of nanomechanics in the activation of cell membrane growth factors

Ligand-receptor protein interactions are a fundamental mechanism for every biological system, in both physiological and pathological conditions. In particular, the interaction between cell membrane growth factor receptors and their key ligands plays an important role in different processes, including cancer [17]. The growth, survival, and metastatic spreading of solid tumors strongly depend on the formation of a novel vessel network (tumor angiogenesis), making the pro-angiogenic molecular machinery a target for new strategies in cancer therapy [18, 19]. This approach requires to disentangle the complex array of transduction signals activated by the interaction of pro-angiogenic growth factors with their cognate cell membrane tyrosine kinase receptors [20].

In view of this, a nanoliter CONAMORE assay was assessed to investigate the interactions of the vascular endothelial growth factor receptor-2 (VEGFR2), which is the major pro-angiogenic receptor expressed by endothelial cells [21], with the canonical ligand VEGF-A, which is the major pro-angiogenic factor of the VEGF family. The activated complex has a crucial role in physiological and pathological angiogenesis through distinct signal transduction pathways regulating endothelial cell survival, proliferation, migration, vascular permeability, tubulogenesis, and gene expression [22].

The CONAMORE assay scheme and working principle are sketched in **Figure 2**. The recognition between the VEGF-A ligand at nanomolar concentration and the surface confined VEGFR2 was characterized in different scenarios: in the presence of noninteracting proteins, in competitive binding experiments and testing the detection of binding of small peptide ligands to VEGFR2 [23]. In particular, the VEGFR2/VEGFA recognition was clearly detectable in the presence of a ten-fold molar excess of an unrelated protein (1.0 μ M BSA) and combined with irrelevant immunoglobulins. It was also distinguished from the nonspecific interactions occurring after denaturation of the receptors. The specificity and robustness of the

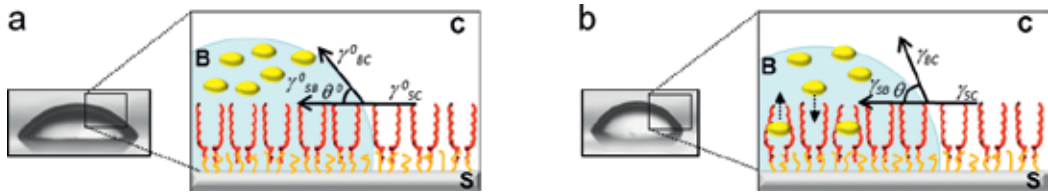


Figure 2. Scheme of the CONAMORE assay in sessile drop configuration for quantification of the nanomachinery of VEGF-A/VEGFR2 surface recognition. (a) Initial state with ligands free in solution. (b) Ligand-receptor recognition equilibrium.

technique were confirmed also by a competition experiment, where the interaction VEGF-A/VEGFR2 was suppressed by a neutralizing anti-VEGF-A antibody, and by a successful detection of an interaction between VEGFR2 and a low molecular weight (LMW) molecule (2 k Dacyclo-peptide).

These preliminary studies set the basis to investigate the role of nanomechanics in the activation of cell membrane growth factors [24]. We started from observations that identified the bone morphogenic protein-antagonist gremlin as a novel pro-angiogenic ligand of VEGFR2, distinct from canonical VEGFs, increasing the complexity of extracellular interactions involving this receptor [24].

VEGF-A/VEGFR2 and gremlin/VEGFR2 surface recognition were first characterized by Surface Plasmon Resonance (SPR) spectroscopy, which is a gold-standard mass-based biosensor [25]. The SPR isotherms of VEGF-A and gremlin overlapped, demonstrating that a similar number of VEGF-A and gremlin molecules interacting with VEGFR2 (VEGF-A and gremlin have very close masses). But, to the contrary, we found the interactions significantly differentiate in terms of binding kinetics and in-plane intermolecular forces, suggesting that the binding of VEGF-A or gremlin induces different VEGFR2 conformational changes and/or clustering in respect to gremlin. Such nanomechanical differences resulted exactly mirrored and supported by the in-vitro experiments. In fact, we showed that VEGF-A triggers a more rapid receptor clustering and a more potent biological response in endothelial cells with respect to gremlin. The key nanomechanical experimental and results are summarized below.

The SPR dose-response experiments were repeated with CONAMORE, by exploiting the fact that with CONAMORE technique is possible to perform the nanomechanical sensing on the same chips used for SPR experiments. **Figure 3a** shows the typical binding curves obtained by plotting $\Delta\gamma_{sb}$ as a function of ligand concentration. In view of the SPR data, the extent of binding of VEGF-A and gremlin matches at any concentration. Therefore, the isotherms indicate that for the same extent of binding to surface-immobilized VEGFR2, VEGF-A exerts a $\Delta\gamma_{sb}$ (blue dots) that is two- to fivefold higher than the $\Delta\gamma_{sb}$ exerted by gremlin (red reverse triangle). At 100 nM, $\Delta\gamma_{sb}$ is (8.3 ± 2.1) mN/m and (3.7 ± 0.4) mN/m for VEGF-A and gremlin, respectively. Remarkably, these values are consistent with MC measurements of cooperative surface mechanical work performed by protein conformational changes [26].

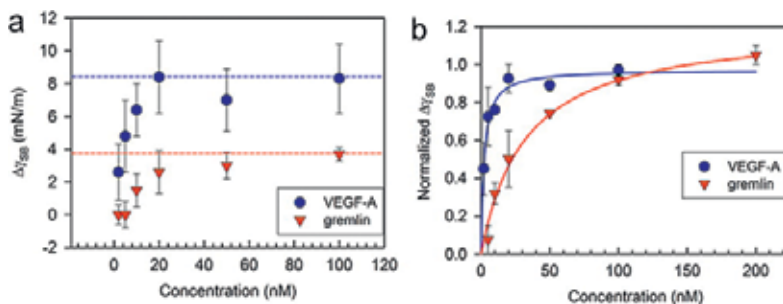


Figure 3. Results of VEGF-A/VEGFR2 and gremlin/VEGFR2 surface recognition. (a) CONAMORE binding isotherms of VEGF-A (blue circles) and gremlin (red reverse triangles) with VEGFR2 immobilized on surface. (b) Normalized $\Delta\gamma_{SB}$ binding isotherms.

Figure 3b shows the normalized $\Delta\gamma_{SB}$ isotherms and the resulting fitting curves with a Langmuir-like equation for monovalent binding. It is possible to estimate an apparent equilibrium constant that explains the nanomechanical aspects of ligand/VEGFR2 surface recognition, named surface nanomechanical affinity, $K_d^{\sigma mech}$, and its reciprocal, $K_a^{\sigma mech} = 1/K_d^{\sigma mech}$, named surface nanomechanical dissociation constant. The VEGF-A isotherm features a sharply steeper rise with respect to the gremlin one, indicating a significant difference in terms of $K_d^{\sigma mech}$. This is supported by the fitting results, which give $K_d^{\sigma mech} = (2.0 \pm 0.7)$ nM and $K_d^{\sigma mech} = (32 \pm 9)$ nM, for VEGF-A and gremlin, respectively. Thus, VEGF-A has about 16-fold higher surface nanomechanical affinity for VEGFR2 with respect to gremlin.

2.2. Nanomechanics and protein folding disorders

Protein conformational changes are a key event in protein's activity, and their characterization is a central goal of biology. Several diseases arise from protein misfolding, in which the misfolded protein self-associates and becomes deposited in amyloid-like aggregates in diverse organs, inducing tissue damage and organ dysfunction.

Beta2-microglobulin ($\beta 2$ -m) is a key protein acting in the onset of the dialysis related amyloidosis (DRA), that is a severe complication occurring in patients subjected to chronic hemodialysis, where insoluble and toxic $\beta 2$ -m amyloid deposits (fibrils) localize in the skeletal tissues [27]. The fibrils formation follows a complex and still unclear mechanism, where protein conformational changes, among other factors, play a crucial role.

MCs biosensors are suited to probe protein conformational changes, as the biomolecular transformation confined on MC surface can be directly translate in MC bending [6]. In particular, silicon MCs with *ad hoc* copolymer coating were employed to probe the effect of an unfolded intermediate of $\beta 2$ -m, driven by pH changes, and in turn to single out within a pilot set of LMW ligands the ones able to influence or even suppress such effect. The working concept is presented in the cartoon in **Figure 4**.

The set of small ligands were selected in order to cover the most relevant scenarios: congo red, a dye that probes fibril formation, speeds up the protein refolding kinetics and can abolish in

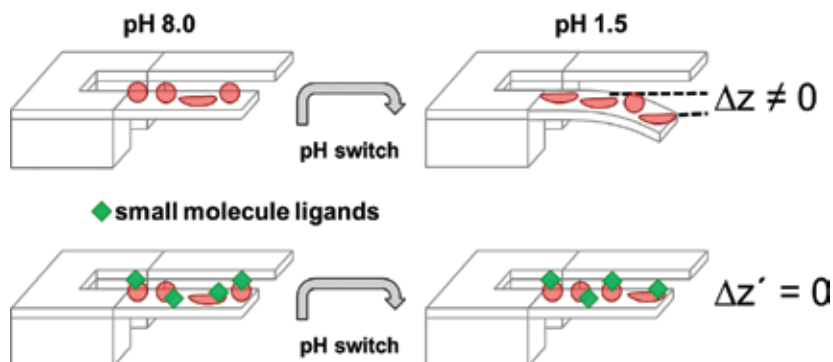


Figure 4. Cartoon representing the effect of small ligands on $\beta 2$ -m conformational stability probed by MC sensors during pH switch. In the top scheme, the pH switch between 8.0 and 1.5 induces a $\beta 2$ -m conformational change that drives MC deflection. In the bottom scheme, the presence of small molecule ligands prevents the protein conformational transformation and in turn MC deflection.

vitro fibril deposition [28], suramin, a urea derivative which also binds the protein but does not interfere with its refolding and without anti-amyloid activity [28], and a reference sulfonated molecule that does not bind the protein, hereafter referred as nonbinder.

The pH switch, set between 8.0 and 1.5, drives the MCs functionalized with the native form of $\beta 2$ -m to a mean differential deflection of $\Delta z = (-8 \pm 2)$ nm (**Figure 5** “no ligand”). To test the

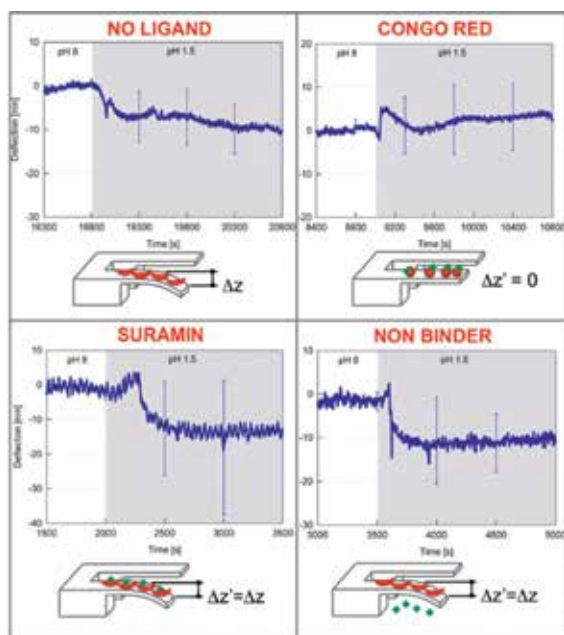


Figure 5. Experimental MC results and related binding-conformational scenarios of incubation of $\beta 2$ -m with the selected small molecule ligands. See the main text for the explanation.

activity of the selected set of small ligands, the β 2-m MCs were incubated *ex situ* in a 6 μ M solution of congo red, suramin or nonbinder (see Ref. [29] for the ligand concentration). Then, the β 2-m MCs system was exposed again to the pH switch. **Figure 5** reports the results and cartoons to explain the different binding-conformation scenarios. The β 2-m MCs incubated with congo red show no differential deflection ($\Delta z = 0$) after the pH switch. To the contrary, β 2-m MCs incubated with suramin and nonbinder drive a deflection of about -10 nm, that is compatible with the deflection of the native β 2-m MCs. MC deflection therefore indicates that only congo red is able to stabilize the β 2-m in its native conformation and prevent the conformational change upon the applied pH shift, while suramin and the nonbinder compound fail. Remarkably, it is known that suramin binds to β 2-m with the same binding affinity of congo red (in order of 10^{-5} M) [29, 30], but only congo red exerts an *in vitro* anti-amyloid activity [28], matching the nanomechanical results.

These findings demonstrate how nanomechanical sensors can be an extraordinary platform for the screening small ligands of proteins involved in pathological processes.

2.3. The nanomechanical side of ferritin iron loading

Sections 2.1 and 2.2 refer to nanomechanical biomolecular recognition driven by ligand-receptor interactions and molecular switches, where deflection is determined mostly by biomolecular conformational changes. Instead, in the following section, the study of a class of proteins with negligible conformational rearrangements is presented. In the particular case herein discussed, the surface energy change does not take origin from conformational changes, but is related to the electrostatic interaction between the inorganic new-born nanocores in ferritin cage proteins and other nonspecific short range forces, such as steric, bridging and depletion forces. These findings give the first observation on the in-plane forces arising upon ferritin iron loading confined at a solid-liquid interface [31].

Ferritin is a mineralization protein dedicated to the storage of intracellular free iron and peroxides, protecting the cell from oxidative damage [32]. Mammalian ferritin is made of 24 subunits that self-assemble in a 12 nm shell structure with an inner cavity of 8 nm in diameter able to accommodate up to about 4500 iron atoms [33]. The potential application of ferritin in the field of nanotechnology and nanomedicine [34], together with the rapid development of novel nanomaterials [35, 36], increases the need to understand and control the properties, interactions and iron loading activity of surface confined ferritin.

The rationale depicted in **Figure 6** shows a ferritin-MC assay based on recombinant human ferritin H chain (FTH) and a mutant without ferroxidase activity (Mutant). A thin film of active FTH (green circles) is deposited onto a MC, which balances by bending the variation of surface energy triggered by iron loading. A control MC is prepared by the surface functionalization with the Mutant that is not able to take up iron in the experimental conditions (light blue circles).

Figure 7a reports in dark gray line the absolute deflection of the MC modified with FTH (FTH-MC), in light gray line the absolute deflection of the reference MC modified with the

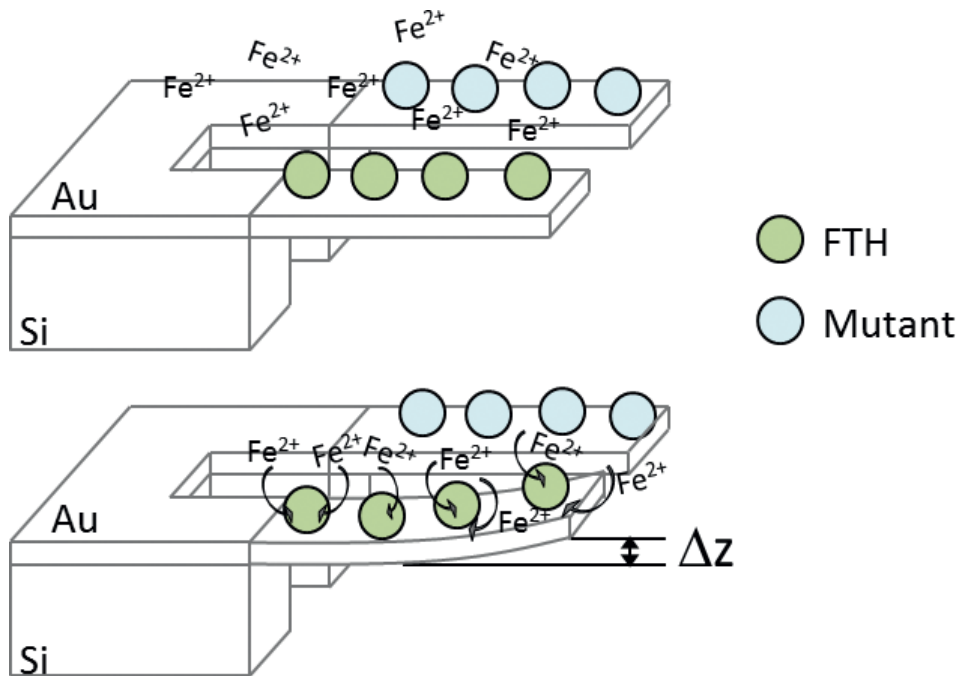


Figure 6. Cartoon depicting the ferritin-MC assay based on recombinant human ferritin H chain (FTH, green circles) and a mutant without ferroxidase activity (Mutant, light blue circles). The variation of surface energy triggered by the iron loading in FTH drives the FTH MC deflection, Δz .

Mutant (ref-MC), and in red line the differential deflection between the two signals, Δz . Vertical arrows indicate a sequential injections of Fe(II) solution necessary to reach a progressive iron loading and to limit the oxidation of nonloaded Fe(II) on the outer structure of the protein leading to Fe(III) precipitation. The presentation of Δz signal reduces any contribution to MCs deflection due to unspecific adsorption of Fe(II) and/or other components of the buffer solution. The trend depicted in **Figure 7a** is confirmed by the bar chart plot in **Figure 7b** that shows the mean equilibrium Δz over 4 replicate MC (the error bars represent the SD of the mean). The Δz value reaches a plateau value at $\Delta z = (28.1 \pm 9.6)$ nm, corresponding to a net tensile surface stress change, $\Delta\sigma = (6.0 \pm 1.5)$ mJ/m². By further calculation (see Ref. [31] for details) is possible to convert the Δz value at saturation in in-plane interferritin interactions force of about $40 k_b T$ at room temperature, coming along the formation of iron cores. This value indicates long-lived van der Waals and electrostatic interactions [37], consistent with reports on nanomechanical biomolecular recognition. Finally, by building up a purely attractive model between the iron cores, described by van der Waals (VDW) interaction potential, it comes out that the 40% of the measured energy variation of the interactions can be ascribed to VDW attractive forces between the newborn ferritin iron cores, and the remaining part ascribed to nonspecific short-range forces typical of biomolecule surface confined systems, such as hydration, steric, bridging and depletion forces [37, 38].

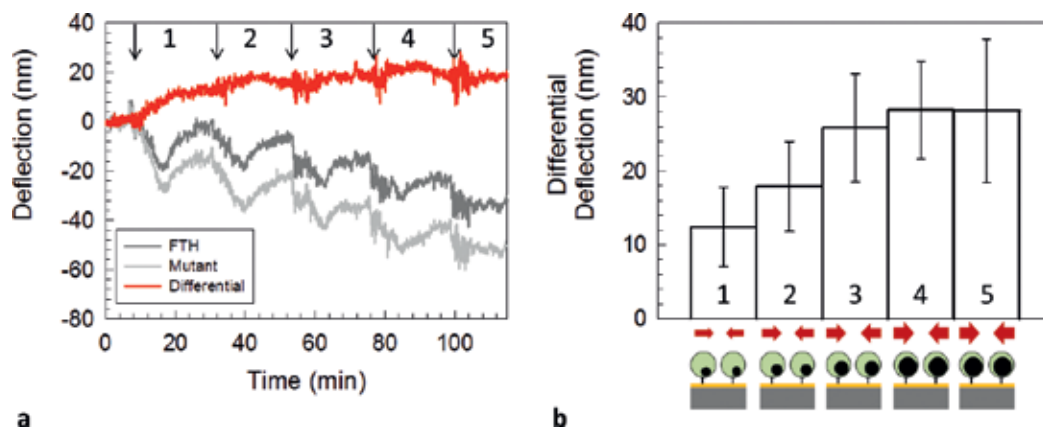


Figure 7. MC responses upon sequential injection of Fe(II). (a) Single MC deflection signals of: FTH-MC (dark gray line), ref-MC (light gray line) and differential deflection (red line). (b) Mean differential deflection, Δz , signals at equilibrium at each injection step.

3. Breaking good. Probing designer drug family with a unique supramolecular nanomechanical sensor

The systems presented in previous sections relate in general to biological systems and, in particular, to interactions of biomolecules confined at solid-solution interface, neglecting the large pool of available synthetic receptors. Nanomechanical sensors are limited, in fact, by the availability of coatings that interact selectively with the target analyte. By introducing the phosphonate cavitands as a versatile class of synthetic receptors [39] that are capable of binding inorganic and organic cations [40, 41] as well as neutral molecules [42] is possible to extend the surface nanomechanics to supramolecular systems.

Phosphonate cavitands are synthetic abiotic receptors (hosts) [39, 40, 43] with molecular recognition properties that have been exploited in gas sensing [44], supramolecular polymers [45, 46], surface self-assembly [47], and product protection [48]. They are specifically designed to target small molecules bearing amino-functionalities via a synergistic combination of weak interactions such as H-bonding, dipole-dipole, and CH- π interactions. Probing small molecules bearing amino-functionalities is a key issue from both the fundamental and the applied sides. N-Methylated moieties, in particular, are present in a broad range of biologically active compounds, from drugs [49] to cancer biomarkers [50] and neurotransmitters [51].

In the Section 3.1, we will present the preliminary study toward the viability of cavitand-MC nanomechanical sensors for probing small molecules bearing amino-functionalities. In Section 3.2, we show how we implemented these results to realize a nanomechanical device for label-free detection of amine-based illicit and designer drug in water.

3.1. Alkyl ammonium series

Figure 8 sketches a label-free selective detection of N-methyl-ammonium salts in methanol attained thanks to the use of MCs functionalized with tetraphosphonate cavitands. These molecules are LMW species of a mass equal to or lower than 150 Da, differing only by a methyl group, which is 15 Da.

The bar chart reported in **Figure 9a** shows the mean value of the deflection peaks of MCs functionalized with the cavitand. The highest interaction intensity is obtained when methylbutyl ammonium chloride is injected, $\Delta z = (-80 \pm 10)$ nm. A comparable deflection is measured with dimethylbutyl ammonium chloride and butyl ammonium chloride, with deflection values of $\Delta z = (-55 \pm 6)$ nm, and the weakest response comes from trimethyl butyl ammonium chloride, $\Delta z = (-10 \pm 2)$ nm. The trend is confirmed also by independent ITC experiments shown in **Figure 9b**. Deflection results can be read in terms of the applied surface stress driven by the host-guest complexation, determined to be $\Delta\sigma = (-17 \pm 2)$ mJ/m² for methylbutyl ammonium chloride, and $\Delta\sigma = (-12 \pm 1)$ mJ/m² for the interaction with dimethylbutyl ammonium chloride and butyl ammonium chloride. The stress was much lower for the interaction between the cavitand and the last guest, $\Delta\sigma = (-2 \pm 0.4)$ mJ/m². At the molecular level, the overall surface stress is triggered by the interplay between host-guest complexation, cavitand desolvation, and interface adsorption, as also suggested by the order of magnitude of $\Delta\sigma$, which falls in the range of intermolecular forces [52].

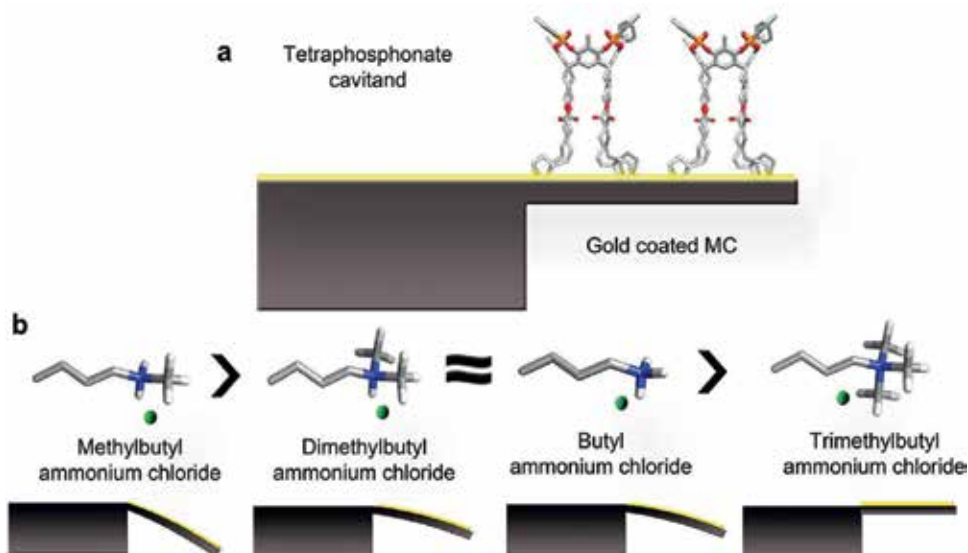


Figure 8. Scheme of the detection of N-methylammonium salts by cavitand-functionalized MCs. (a) Cavitand-MC architecture and (b) MC deflections driven by the different binding energies of N-methyl-ammonium salts and cavitands complexation.

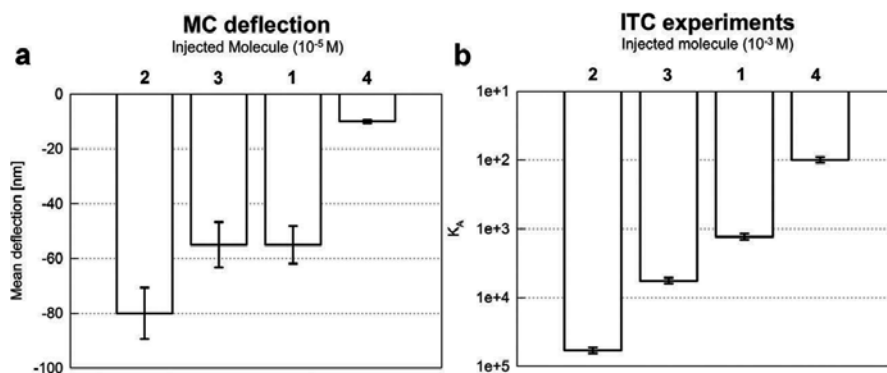


Figure 9. Bar chart of (a) the mean value of the deflection peaks of MCs functionalized with the cavitand and of (b) the mean value of K_A evaluated by ITC experiments.

3.2. Illicit and designer drugs

The next level application of the supramolecular nanomechanical device based on the combination of tetrakisphosphonate cavitands and silicon MCs depicted in previous section can be enrolled to the frontier of designer drugs identification.

Designer drugs pose serious challenges when it comes to recognizing them with the current assays, which are tailored for identification of currently illicit substances but poorly effective, or even useless, for novel designer drugs. Actually, designer variants, featuring minor modifications with respect to an existing drug, show a different chemical composition and are currently not illegal in many jurisdictions. The cavitand-MC system overcomes this shortcoming for methamphetamines, being capable to recognize the methyl-amine portion that is common to the entire drug family [53].

Data reported in **Figure 10** show the implementation of the cavitand-MC system on the detection of ecstasy (MDMA), cocaine and amphetamine in the presence of an interferent,

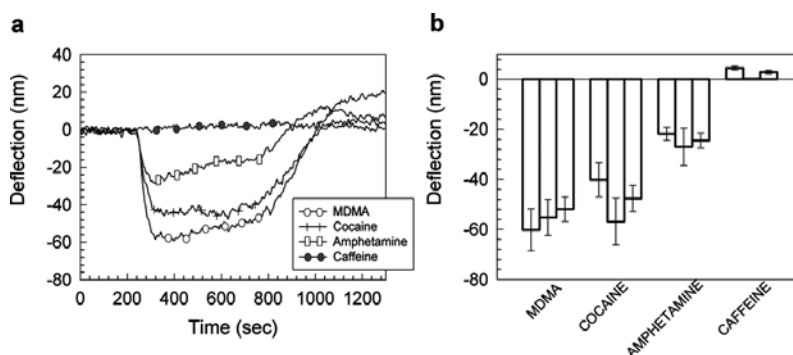


Figure 10. (a) Absolute deflection signal of cavitand-MC system upon injection of MDMA, Cocaine, Amphetamine and Caffeine and (b) mean deflection signal referring to different replicates.

such as caffeine. The different drugs drive MC responses with the same kinetics but different final equilibrium values (**Figure 10a**). Namely, the latter range from an average of 55 nm for MDMA and cocaine to 22 nm for amphetamine (with a 10% of uncertainty). The surface stress generated by the interaction gives (in modulus) $\Delta\sigma = 12 \text{ mN m}^{-1}$ for MDMA and cocaine and $\Delta\sigma = 5 \text{ mN m}^{-1}$ for amphetamine, in fully agreement with several previously reported studies, all related to biomolecules, where it is reported that recognition triggers $1 \text{ mN m}^{-1} < \Delta\sigma < 50 \text{ mN m}^{-1}$ [26, 54–56]. Other common excipients used in drug formulation, such as lactose and glucose, were investigated with the cavitand-MC system, and both MDMA and cocaine are recognized with high fidelity in the presence of the excipients [53].

Finally, the device was tested against a real “street” sample, containing 45% of 3-fluoromethamphetamine (3-FMA) and glucose as excipient. Signals reported in **Figure 11** (as absolute deflection curves in **Figure 11a** and related bar chart in **Figure 11b**) show the successful detection of the drug also directly in a real sample.

This research, that moves from advanced understanding of molecular recognition at the solid-liquid interface to complement the analytical toolbox for small molecules bearing amino functionalities, has broader horizons, including neurotransmitters and cancer biomarkers.

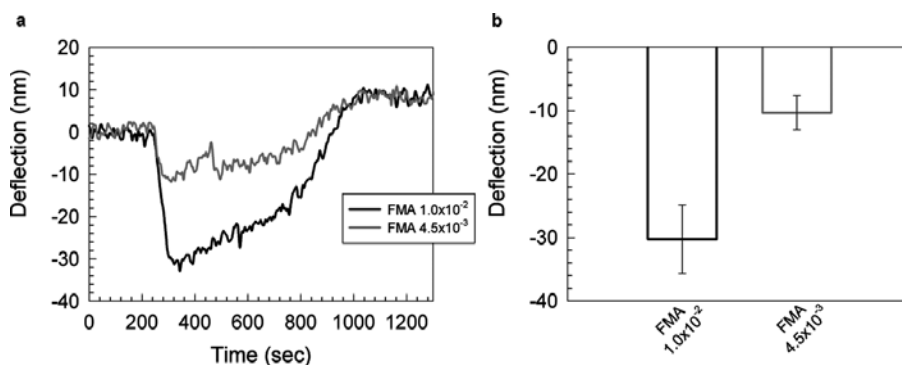


Figure 11. (a) Absolute deflection signal of cavitand-MC system upon injection of the street sample at two different concentrations and (b) mean deflection signal referring to different replicates.

Acknowledgements

The authors wish to thank all the colleagues and collaborators who participated to the presented researches; without their contribution, they would have been not just impossible, but unimaginable. Warm acknowledgments first of all to Laura E. Depero, Giulio Oliviero and Daniele Maiolo and then to Marcella Chiari, Ersilia De Lorenzi, Marco Presta, Paolo Arosio, Enrico Dalcanale Guido Condorelli and their research groups.

Author details

Paolo Bergese^{1*} and Stefania Federici²

*Address all correspondence to: paolo.bergese@unibs.it

1 Department of Molecular and Translational Medicine, INSTM, CSGI, University of Brescia, Brescia, Italy

2 Department of Mechanical and Industrial Engineering, INSTM, University of Brescia, Brescia, Italy

References

- [1] Bergese P, Oliviero G, Alessandri I, Depero LE. Thermodynamics of mechanical transduction of surface confined receptor/ligand reactions. *Journal of Colloid and Interface Science*. 2007;**316**:1017–1022. DOI: 10.1016/j.jcis.2007.08.048
- [2] Federici S, Oliviero G, Maiolo D, Depero LE, Colombo I, Bergese P. On the thermodynamics of biomolecule surface transformations. *Journal of Colloid and Interface Science*. 2012;**375**:1–11. DOI: 10.1016/j.jcis.2012.02.013
- [3] Bergese P, Colombo I. Thermodynamics of (nano) interfaces. In: Berti D, Palazzo G, editors. *Colloidal Foundations of Nanoscience*. Elsevier; 2014. pp. 1–31. ISBN: 978-0-444-59541-6
- [4] Arlett JL, Myers EB, Roukes ML. Comparative advantages of mechanical biosensors. *Nature Nanotechnology*. 2011;**6**:203–215. DOI: 10.1038/nnano.2011.44
- [5] Bergese P, Oliviero G, Colombo I, Depero LE. Molecular recognition by contact angle: Proof of concept with DNA hybridization. *Langmuir*. 2009;**25**:4271–4273. DOI: 10.1021/la900428u
- [6] Fritz J. Cantilever biosensors. *Analyst*. 2008;**133**:855–863. DOI: 10.1039/B718174D
- [7] Stoney GG. The tension of metallic films deposited by electrolysis. *Proceedings of the Royal Society A*. 1909;**83**:172–175. DOI: 10.1098/rspa.1909.0021
- [8] Carrascosa LG, Moreno M, Alvarez M, Lechuga LM. Nanomechanical biosensors: A new sensing tool. *Trends in Analytical Chemistry*. 2006;**25**:196–206. DOI: 10.1016/j.trac.2005.09.006
- [9] Álvarez M, Carrascosa LG, Moreno M, Calle A, Zaballos A, Lechuga LM, Martínez-A C, Tamayo J. Nanomechanics of the formation of DNA self-assembled monolayers and hybridization on microcantilevers. *Langmuir*. 2004;**20**:9663–9668. DOI: 10.1021/la0489559

- [10] McKendry R, Zhang J, Arntz Y, Strunz T, Hegner M, Lang HP, Bailer MK, Certa U, Meyer E, Guntherodt HJ, Gerber C. Multiple label-free biodetection and quantitative DNA-binding assays on a nanomechanical cantilever array. *Proceedings of the National Academy of Sciences USA*. 2002;**99**:9783–9788. DOI: 10.1073/pnas.152330199
- [11] Oliviero G, Federici S, Colombi P, Bergese P. On the difference of equilibrium constants of DNA hybridization in bulk solution and at the solid-solution interface. *Journal of Molecular Recognition*. 2010;**24**:182–187. DOI: 10.1002/jmr.1019
- [12] Maiolo D, Federici S, Ravelli L, Depero LE, Hamad-Schifferli K, Bergese P. Nanomechanics of surface DNA switches probed by captive contact angle. *Journal of Colloid and Interface Science*. 2013;**402**:334–339. DOI: 10.1016/j.jcis.2013.03.069
- [13] Arntz Y, Seelig JD, Lang HP, Zhang J, Hunziker P, Ramseyer JP, Meyer E, Hegner M, Gerber C. Label-free protein assay based on a nanomechanical cantilever array. *Nanotechnology*. 2003;**14**:86–90. DOI: 10.1088/0957-4484/14/1/319
- [14] Maiolo D, Mitola S, Leali D, Oliviero G, Ravelli C, Bugatti A, Depero LE, Presta M, Bergese P. Role of nanomechanics in canonical and noncanonical pro-angiogenic ligand/VEGF receptor-2 activation. *Journal of the American Chemical Society*. 2012;**134**:14573–14579. DOI: 10.1021/ja305816p
- [15] Ilic B, Yang Y, Craighead HG. Virus detection using nanoelectromechanical devices. *Applied Physics Letters*. 2004;**85**:2604–2606. DOI: 10.1063/1.1794378
- [16] Gfeller KY, Nugaeva N, Hegner M. Micromechanical oscillators as rapid biosensor for the detection of active growth of *Escherichia coli*. *Biosensors and Bioelectronics*. 2005;**21**:528–533. DOI: 10.1016/j.bios.2004.11.018
- [17] Xu A, Huang P. Receptor tyrosine kinase coactivation networks in cancer. *Cancer Research*. 2010;**15**:3857–3860. DOI: 10.1158/0008-5472
- [18] Folkman J. Angiogenesis in cancer, vascular, rheumatoid and other disease. *Nature Medicine*. 1995;**1**:27–31. DOI: 10.1038/nm0195-27
- [19] Chung AS, Lee J, Ferrara N. Targeting the tumour vasculature: Insights from physiological angiogenesis. *Nature Reviews Cancer*. 2010;**10**:505–514. DOI: 10.1038/nrc2868
- [20] Tvorogov D, et al. Effective suppression of vascular network formation by combination of antibodies blocking VEGFR ligand binding and receptor dimerization. *Cancer Cell*. 2010;**18**:630–640. DOI: 10.1016/j.ccr.2010.11.001
- [21] Ferrara N, Gerber HP, LeCouter J. The biology of VEGF and its receptors. *Nature Medicine*. 2003;**9**:669–676. DOI: 10.1038/nm0603-669
- [22] Olsson AK, Dimberg A, Kreuger J, Claesson-Welsh L. VEGF receptor signalling in control of vascular function. *Nature Reviews Molecular Cell Biology*. 2006;**7**:359–371. DOI:10.1038/nrm1911

- [23] Oliviero G, Maiolo D, Leali D, Federici S, Depero LE, Presta M, Mitola S, Bergese P. Nanoliter contact angle probes tumor angiogenic ligand–receptor protein interactions. *Biosensors and Bioelectronics*. 2010;**26**:1571–1575. DOI: 10.1016/j.bios.2010.07.115
- [24] Maiolo D, Mitola S, Leali D, Oliviero G, Ravelli C, Bugatti A, Depero LE, Presta M, Bergese P. Role of nanomechanics in canonical and noncanonical pro-angiogenic ligand/VEGF receptor-2 activation. *Journal of the American Chemical Society*. 2012;**134**:14573–14579. DOI: 10.1021/ja305816p
- [25] Rusnati M, Bugatti A, Mitola S, Leali D, Bergese P, Depero LE, Presta M. Exploiting surface plasmon resonance (SPR) technology for the identification of fibroblast growth factor-2 (FGF2) antagonists endowed with antiangiogenic activity. *Sensors*. 2009;**9**:6471–6503. DOI: 10.3390/s90806471
- [26] Federici S, Oliviero G, Hamad-Schifferli K, Bergese P. Protein thin film machines. *Nanoscale*. 2010;**2**:2570–2574. DOI: 10.1039/C0NR00616E
- [27] Merlini G, Bellotti V. Molecular mechanisms of amyloidosis. *The New England Journal of Medicine*. 2003;**349**:583–596. DOI: 10.1056/NEJMra023144
- [28] Carazzone C, Colombo R, Quaglia M, Mangione P, Raimondi S, Giorgetti S, Caccialanza G, Bellotti V, De Lorenzi E. Sulfonated molecules that bind a partially structured species of β_2 -microglobulin also influence refolding and fibrillogenesis. *Electrophoresis*. 2008;**29**:1502–1510. DOI: 10.1002/elps.200700677
- [29] Quaglia M, Carazzone C, Sabella S, Colombo R, Giorgetti S, Bellotti V, De Lorenzi E. Search of ligands for the amyloidogenic protein β_2 -microglobulin by capillary electrophoresis and other techniques. *Electrophoresis*. 2005;**26**:4055–4063. DOI: 10.1002/elps.200500313
- [30] Regazzoni L, Bertolotti L, Vistoli G, Colombo R, Aldini G, Serra M, Carini M, Caccialanza G, De Lorenzi E. A combined high-resolution mass spectrometric and insilicoapproach for the characterisation of small ligands of β_2 -microglobulin. *ChemMedChem*. 2010;**5**:1015–1025. DOI: 10.1002/cmdc.201000082
- [31] Federici S, Padovani F, Poli M, Carmona Rodriguez F, Arosio P, Depero LE, Bergese P. Energetics of surface confined ferritin during iron loading. *Colloids and Surfaces B: Biointerfaces*. 2016;**145**:520–525. DOI: 10.1016/j.colsurfb.2016.05.044
- [32] Arosio P, Levi S. Cytosolic and mitochondrial ferritins in the regulation of cellular iron homeostasis and oxidative damage. *Biochimica et Biophysica Acta*. 2010;**1800**:783–792. DOI: 10.1016/j.bbagen.2010.02.005
- [33] Chasteen ND, Harrison PM. Mineralization in ferritin: An efficient means of iron storage. *Journal of Structural Biology*. 1999;**126**:182–194. DOI: 10.1006/jsbi.1999.4118
- [34] Jutz G, van Rijn P, Santos Miranda B, Boker A. Ferritin: A versatile building block for bionanotechnology. *Chemical Reviews*. 2015;**115**:1653–1701. DOI: 10.1021/cr400011b

- [35] Knez M, Kadri A, Wege C, Gösele U, Jeske H, Nielsch K. Atomic layer deposition on biological macromolecules: Metal oxide coating of tobacco mosaic virus and ferritin. *Nano Letters*. 2006;**6**:1172–1177. DOI: 10.1021/nl060413j
- [36] Yamashita I, Iwahori K, Kumagai S. Ferritin in the field of nanodevices. *Biochimica et Biophysica Acta*. 2010;**1800**:846–857. DOI: 10.1016/j.bbagen.2010.03.005
- [37] Leckband D, Israelachvili JN. Intermolecular forces in biology. *Quarterly Reviews of Biophysics*. 2001;**34**:105–267. DOI: 10.1017/S0033583501003687
- [38] Briscoe WH. Depletion forces between particles immersed in nanofluids. *Current Opinion in Colloid & Interface Science*. 2015;**20**:46–53. DOI: 10.1016/j.cocis.2014.12.002
- [39] Pinalli R, Suman M, Dalcanale E. Cavitands at Work: From Molecular Recognition to Supramolecular Sensors. *Eur. J. Org. Chem*. 2004;2004:451–462. DOI: 10.1002/ejoc.200300430
- [40] Dutasta JP. New phosphorylated hosts for the design of new supramolecular assemblies. *Topics in Current Chemistry*. 2004;**232**:55–91. DOI: 10.1007/b13779
- [41] Vachon J, Harthong S, Jeanneau E, Aronica C, Vanthuynne N, Roussel C, Dutasta JP. Inherently chiral phosphonatecavitands as artificial chemo- and enantio-selective receptors of natural ammoniums. *Organic & Biomolecular Chemistry*. 2011;**9**:5086–5091. DOI: 10.1039/C1OB05194F
- [42] Maffei F, Betti P, Genovese D, Montalti M, Prodi L, De Zorzi R, Geremia S, Dalcanale E. Highly selective chemical vapor sensing by molecular recognition: Specific detection of C₁–C₄ alcohols with a fluorescent phosphonate cavitand. *Angewandte Chemie International Edition*. 2011;**50**:4654–4657. DOI: 10.1002/anie.201100738
- [43] Nifant'ev EE, Maslennikova VI, Merkulov RV. Design and study of phosphocavitands – A new family of cavity systems. *Accounts of Chemical Research*. 2005;**38**:108–116. DOI: 10.1021/ar0401810
- [44] Melegari M, Suman M, Pirondini L, Moiani D, Massera C, Ugozzoli F, Kalenius E, Vainiotalo P, Mulatier JC, Dutasta JP, Dalcanale E. Supramolecular sensing with phosphonate cavitands. *Chemistry – A European Journal*. 2008;**14**:5772–5779. DOI: 10.1002/chem.200800327
- [45] Yebeutchou RM, Tancini F, Demitri N, Geremia S, Mendichi R, Dalcanale E. Host–guest driven self-assembly of linear and star supramolecular polymers. *Angewandte Chemie International Edition*. 2008;**47**:4504–4508. DOI: 10.1002/ange.200801002
- [46] Tancini F, Yebeutchou RM, Pirondini L, De Zorzi R, Geremia S, Scherman OA, Dalcanale E. Host–guest-driven copolymerization of tetraphosphonatecavitands. *Chemistry – A European Journal*. 2010;**16**:14313–14321. DOI: 10.1002/chem.201002237
- [47] Tancini F, Genovese D, Montalti M, Cristofolini L, Nasi L, Prodi L, Dalcanale E. Hierarchical self-assembly on silicon. *Journal of the American Chemical Society*. 2010;**132**:4781–4789. DOI: 10.1021/ja9099938

- [48] Yebeutchou RM, Dalcanale E. Highly selective monomethylation of primary amines through host–guest product sequestration. *Journal of the American Chemical Society*. 2009;**131**:2452–2453. DOI: 10.1021/ja809614y
- [49] ATLAS on Substance Use (2010) – Resources for the prevention and treatment of substance use disorders; World Health Organization; 2011
- [50] Sreekumar A, et al. Metabolomic profiles delineate potential role for sarcosine in prostate cancer progression. *Nature*. 2009;**457**:910–914. DOI: 10.1038/nature07762
- [51] Von Bohlen und Halbach O, Dermietzel R. Neurotransmitters and Neuromodulators: Handbook of Receptors and Biological Effects. Weinheim: Wiley-VCH; 2006
- [52] Israelachvili JN. Intermolecular and Surface Forces, with Applications to Colloidal and Biological Systems. London: Academic Press; 1985
- [53] Biavardi E, Federici S, Tudisco C, Menozzi D, Massera C, Sottini A, Condorelli GG, Bergese P, Dalcanale E. Cavitand-grafted silicon microcantilevers as a universal probe for illicit and designer drugs in water. *Angewandte Chemie International Edition*. 2014;**53**:9183–9188. DOI: 10.1002/anie.201404774
- [54] Godin M, Tabard-Cossa C, Miyahara Y, Monga T, Williams PJ, Beaulieu LY, Lennox RB, Grutter P. Cantilever-based sensing: The origin of surface stress and optimization strategies. *Nanotechnology*. 2010;**21**:075501–075509. DOI: 10.1088/0957-4484/21/7/075501
- [55] de Puig H, Federici S, Baxamusa SH, Bergese P, Hamad-Schifferli K. Quantifying the Nanomachinery of the Nanoparticle–Biomolecule Interface. *Small*. 2011;**7**:2477–2484. DOI: 10.1002/smll.201100530
- [56] Kang K, Sachan A, Nilsen-Hamilton M, Shrotriya P. Aptamer functionalized microcantilever sensors for cocaine detection. *Langmuir*. 2011;**27**:14696–14702. DOI: 10.1021/la202067y

Nanocharacterization of the Mechanical and Tribological Behavior of MEMS Micromembranes

Marius Pustan, Cristian Dulescu,
Corina Birleanu and Florina Rusu

Additional information is available at the end of the chapter

<http://dx.doi.org/10.5772/intechopen.68292>

Abstract

This chapter presents the experimental investigation and numerical simulation of micromembranes supported by serial-parallel connected hinges. The micromembranes can be used in optical applications or as the flexible mechanical element in radio frequency micro-electromechanical system switches. A method to determine the micromembrane stiffness is presented. Experimentally, the out-of-plane micromembranes deflection is performed using an atomic force microscope. The dependence between deflection and the applied force gives the sample stiffness. The flexible plate of micromembranes is directly deflected to substrate, and the adhesion force is measured. The micromembranes are electroplated with gold, and two series of the serial connected hinges are investigated. Each of them has different parallel connected hinges. The experimental results of stiffness and adhesion force are compared with analytical and numerical results. The presented method is also applied to determine the stiffness of micromembranes supported by other types of hinges.

Keywords: micromembrane, stiffness, modeling, experimental investigation

1. Introduction

The micromembranes are microelectromechanical system (MEMS) components that accomplish one double role of supporting other components, which are regularly rigid and of providing the necessary flexibility in a microdevice that has moving parts [1–3]. A micromembrane has three significant parts: the mobile plate that is moved in different planes in response of an acting signal, the anchors that connect the flexible structures to substrate, and the hinges that connect the mobile

plate to anchors. Micromembranes have their thickness much smaller than in plane dimensions and can be implemented in RF-MEMS switches, MEMS accelerometer, or in optical applications [3]. The micromembranes are mechanically characterized here by means of their stiffness. Tribological investigations include the adhesion force measurement between micromembranes and their substrate.

The reliability issue concerning on MEMS has been developed in recent years. First step to understand MEMS reliability is to know the failure modes. The failure of a microsystem depends on the behavior of integrated microcomponents. For different MEMS applications, the mechanical flexible microcomponents are integrating on the same structure with electrical, optical, thermal, or magnetic components. In such systems, a multiphysics interaction occurs and the failure of one microcomponent means the failure of all system [4]. The flexible mechanical microcomponents from a MEMS device, such as sensor or actuator, can be a microcantilever, a microbridge, or micromembranes with different geometrical configurations. These structure MEMS are sensitive from mechanical structure point of view to phenomena like creep, fatigue, delamination, wear or adhesion [5].

Two of the main failure causes of micromembranes under large deflections are excessive stress in hinges and the stiction. Stiction is one of the most important and unavoidable failure problems of micromembranes under large deflection. Stiction is the adhesion of contacting surfaces due to surface forces (van der Waals, capillary forces, Casimir forces, hydrogen bridging, and electrostatic forces) [6]. The restorative force (pull-off force) of a micromembrane from substrate, opposite to the adhesion force, depends on the micromembrane stiffness.

There are several applications which include micromembranes as mechanical flexible component. For example, in a pressure sensor, a capacitive micromembrane deflects when the pressure is applied, changing the distance between electrodes and the capacitance. In optical MEMS, the micromembranes are used as micromirrors supported by hinges with high mobility. In an interferometer, where the laser light brought into the sensor by optical fiber and the light beam crosses a micromembrane, the deformation of micromembrane changes the light properties, and different propagation speed can result in phase shift. Micromembrane surface stress sensors from chemical and biological applications are fabricated from thin gold layer. The molecular interaction between probe and target molecules generates a surface stress on micromembrane. This surface stress causes the structural deflection of micromembrane which generates the capacitance change in electrical sensing [4].

One important parameter characteristic to micromembranes is their mechanical stiffness. The micromembrane stiffness is related to the geometry and material properties. Of micromembranes that are connected by hinges to the anchors, their mechanical stiffness is given by the geometrical and structural characteristics of hinges. Microhinges are utilized as joints in MEMS that provide relative motion between two adjacent rigid links through elastic deformation. The geometrical configuration of hinges has influence on the micromembrane response related to the mechanical stiffness. Hinges are deformed in bending or torsion as a function of the applied force.

This chapter presents a study case of micromembranes supported by serial-parallel connected hinges. The analysis includes theoretical approach, and numerical analysis of the out-of-plane stiffness of micromembranes is followed by experimental tests performed using an atomic force

microscope (AFM). Moreover, the adhesion effect between flexible part of micromembranes and substrate is experimentally determined and compared with analytical results. In order to compute the analytical adhesion force, the roughness of the contact surfaces is measured using the AFM tapping mode. Discussions and comparison with the other micromembranes supported by other type of hinges with different geometry is included at the end of chapter.

2. Geometry and dimensions of micromembrane with serial-parallel connected hinges

The samples for experimental tests are electroplated gold micromembranes with two different serial-parallel connected hinges (**Figure 1**). The flexible part of investigated micromembranes is suspended at $2\ \mu\text{m}$ above a silicone substrate. Gold is the most used material from optical and electrical MEMS applications.

The geometrical dimensions of investigated micromembranes according to **Figure 2** are the following:

- lengths: $l_1 = 65\ \mu\text{m}$, $l_2 = 100\ \mu\text{m}$, $l_3 = 85\ \mu\text{m}$, $l_4 = 50\ \mu\text{m}$;
- widths: $w_1 = 18\ \mu\text{m}$, $w_2 = 180\ \mu\text{m}$ (**Figure 1a**), and $288\ \mu\text{m}$ (**Figure 1b**);
- thickness: $t = 3\ \mu\text{m}$;
- number of hinges n_1 is 2 for the first investigated micromembrane and 4 for the second micromembrane (**Figure 1a**);
- number of hinges n_2 is 4 for the first investigated micromembrane and 6 for the second micromembrane (**Figure 1b**).

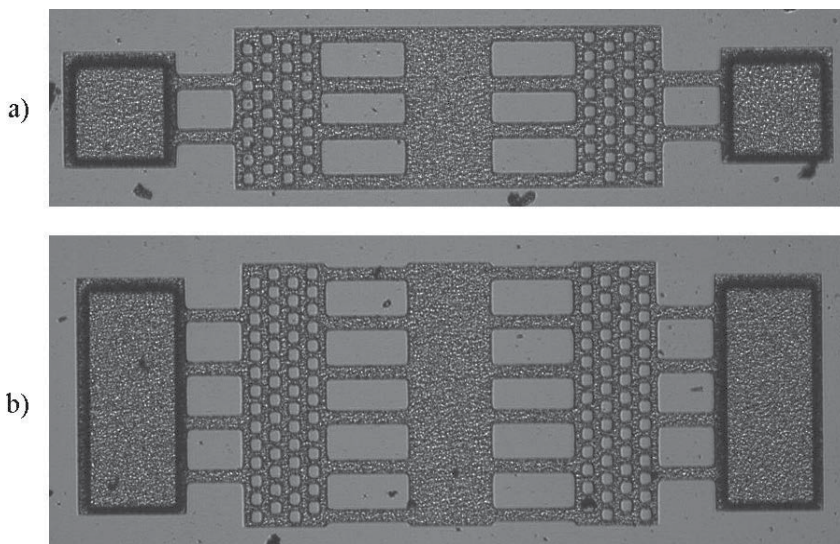


Figure 1. Micromembranes supported by serial-parallel connected hinges: (a) micromembrane supported by 2×4 connected hinges; (b) micromembrane supported by 4×6 connected hinges.

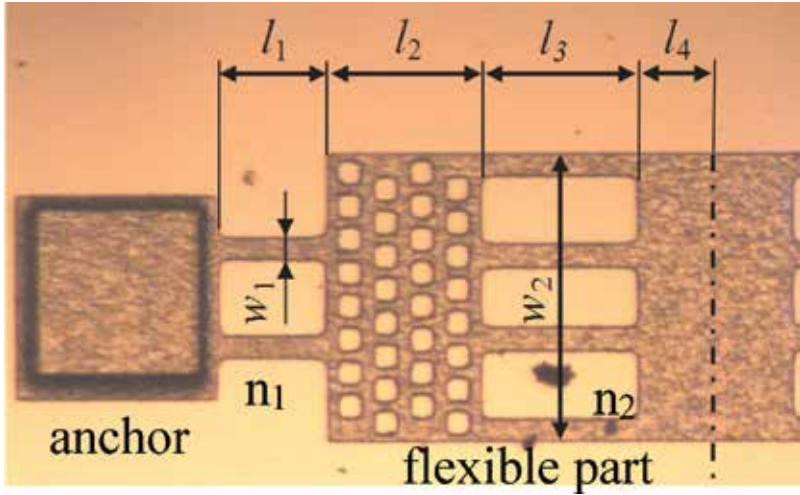


Figure 2. Dimensions of the micromembrane supported by connected hinges (half geometry).

3. Analytical and numerical analysis of stiffness of micromembranes with serial-parallel connected hinges

Castigliano’s second theorem, known as the displacement theorem, is utilized herein to derive the stiffness of investigated micromembranes and to compute the dependence between force and the sample-bending deflection. The force is considered to be applied in the mid position of the mobile plate as in experimental investigations [3]. A general formulation is derived here enabling stiffness computation for any combination of serial-parallel connected hinges. The analytical results of micromembranes with 2×4 and 4×6 serial-parallel connected hinges are compared in Section 6 of this chapter, with numerical and experimental results. As a consequence, a bending stiffness expression of micromembranes supported by serial-parallel connected hinges is obtained as following:

$$k_b = \frac{2}{(S_1 + S_2 + S_3 + S_4)} \tag{1}$$

where

$$S_1 = \frac{\left(\frac{(l_4+l_3+l_2+l_1)^3 - (l_4+l_3+l_2)^3}{3} - A\left((l_4 + l_3 + l_2 + l_1)^2 - (l_4 + l_3 + l_2)^2\right) + A^2l_1\right)}{EI_1},$$

$$S_2 = \frac{\left(\frac{(l_4+l_3+l_2)^3 - (l_4+l_3)^3}{3} - A\left((l_4 + l_3 + l_2)^2 - (l_4 + l_3)^2\right) + A^2l_2\right)}{EI_2},$$

$$S_3 = \frac{\left(\frac{(l_4+l_3)^3 - l_4^3}{3} - A\left((l_4 + l_3)^2 - l_4^2\right) + A^2l_3\right)}{EI_3}, S_4 = \frac{\left(\frac{l_4^3}{3} - Al_4^2 + A^2l_4\right)}{EI_4}, \text{ and}$$

$$A = \frac{\left(\frac{(l_4 + l_3 + l_2 + l_1)^2 - (l_4 + l_3 + l_2)^2}{I_1} + \frac{(l_4 + l_3 + l_2)^2 - (l_4 + l_3)^2}{I_2} + \frac{(l_4 + l_3)^2 - l_4^2}{I_3} + \frac{l_4^2}{I_4} \right)}{2 \cdot \left(\frac{l_1}{I_1} + \frac{l_2}{I_2} + \frac{l_3}{I_3} + \frac{l_4}{I_4} \right)}$$

In these expressions, $l_1, l_2, l_3,$ and l_4 are the characteristic lengths of hinges and mobile plates (**Figure 2**), and $I_1, I_2, I_3,$ and I_4 are the bending moments of inertia given by the micromembrane thickness and widths and influenced by the number of connected hinges n_1 and n_2 as:

$$I_1 = n_1 \cdot \frac{w_1 t^3}{12}, \quad I_2 = I_4 = \frac{w_2 t^3}{12}, \quad I_3 = n_2 \cdot \frac{w_1 t^3}{12}$$

Using the stiffness expression given by Eq. (1), a theoretical analysis of the number of connected hinges influence on the membrane stiffness is performed (**Figure 3**). As the number of hinges increases, the stiffness increases respectively.

A numerical analysis of micromembranes stiffness was performed by Finite Element Analysis (FEA) using the static structural module in ANSYS Workbench 13 software. The mesh of the FEA model for the micromembrane with 2×4 serial-parallel connected hinges (**Figure 1a**) consists of 318,200 nodes and 58,786 hexahedral elements with a size of $2 \mu\text{m}$. For the micromembrane with 4×6 serial-parallel connected hinges (**Figure 1b**), the created mesh has 534,835 nodes and 102,601 hexahedral elements with the same size. Boundary conditions applied on the bottom surface of the anchors correspond to a fixed support. A unitary force ($1 \mu\text{N}$) is applied in the mid position of the mobile plate, and the out-of-plane displacement is simulated. Considering the applied force and the resulting displacement, the bending stiffness is computed. The simulation is performed considering a value of modulus of elasticity equal by 72 GPa [7]. The own weight of the mobile plate upon the hinge deformation is very small and has been neglected.

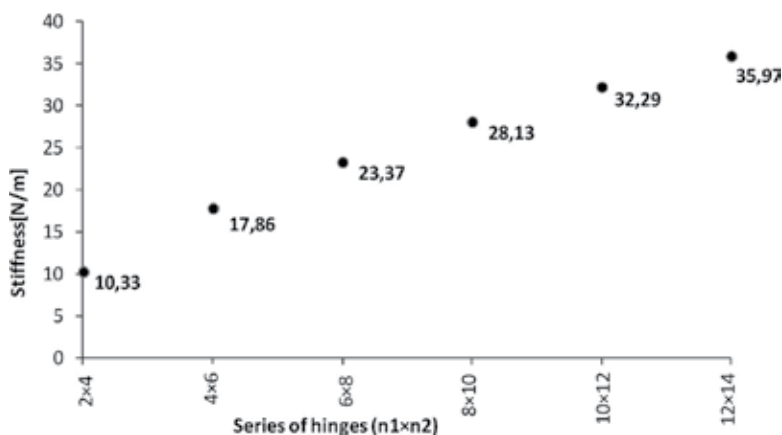


Figure 3. Analytical stiffness variation as a function of the number of connected hinges $n_1 \times n_2$ (n_1 represents the number of hinges that connect the membrane to anchor and n_2 represents the number of hinges between mobile plates).

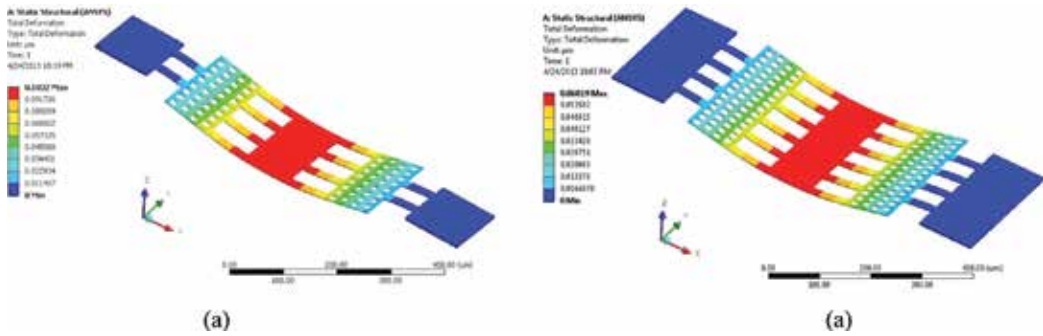


Figure 4. Finite element analysis of micromembrane supported by: (a) 2×4 connected hinges; (b) 4×6 connected hinges. The force is applied in the mid position of the mobile plate.

A maximum displacement of 103.2 nm is simulated of the investigated micromembrane supported by 2×4 connected hinges (**Figure 4a**) that give a numerical stiffness equal by 9.69 N/m. For the investigated micromembrane supported by 4×6 connected hinges, an out-of-plane displacement of 60.19 nm is obtained (**Figure 4b**) for a unitary force applied in the mid position of the central mobile plate that gives a bending stiffness equal to 16.61 N/m.

4. Experimental investigations on stiffness of micromembranes with serial-parallel connected hinges

The aim of experimental investigations is to estimate the mechanical stiffness of micromembranes using an atomic force microscope (AFM) type XE-70 fabricated by Park System Co. The AFM probe used to deflect the micromembranes is TD21562 with a nominal value of the spring constant equal to 144 Nm^{-1} , the radius of tip smaller than 25 nm, the tip height of 109 μm , the length of cantilever 782 μm , and the thickness 24 μm . The tests were performed at room temperature (22°C) and a relative humidity (RH) of 40%. During experimental tests, a mechanical force given by the bending deflection of AFM probe and its stiffness is applied in the mid position of the central plate and deflect it directly to substrate (**Figure 5**).

During experimental tests, the vertical displacement of the scanning head (D_z) is controlled, and the deflection of AFM probe (D_{AFM}) is optically monitored (**Figure 6**).

The experimental AFM curve gives the dependence between vertical displacement of scanning head that is controlled by software and the bending deflection of AFM probe detected by a photodetector. The experimental AFM curve has two different slopes (**Figure 7**). First part of the curve (A and B) from the loading curve (lower curve) corresponds to the bending of AFM probe and samples (position b from **Figure 6**), and the second part (B and C) is given by the bending only of AFM probe (position c from **Figure 6**) [3]. In the point B (**Figure 7**), the sample reaches the substrate. After the point C, the scanning head and the AFM probe are coming to the initial position (the blue curve).

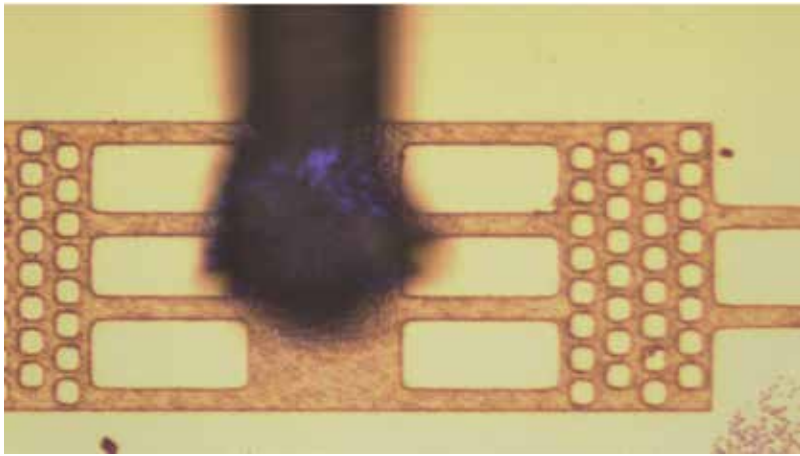


Figure 5. AFM probe in contact with the micromembrane supported by $n_1 \times n_2 = 2 \times 4$ connected hinges.

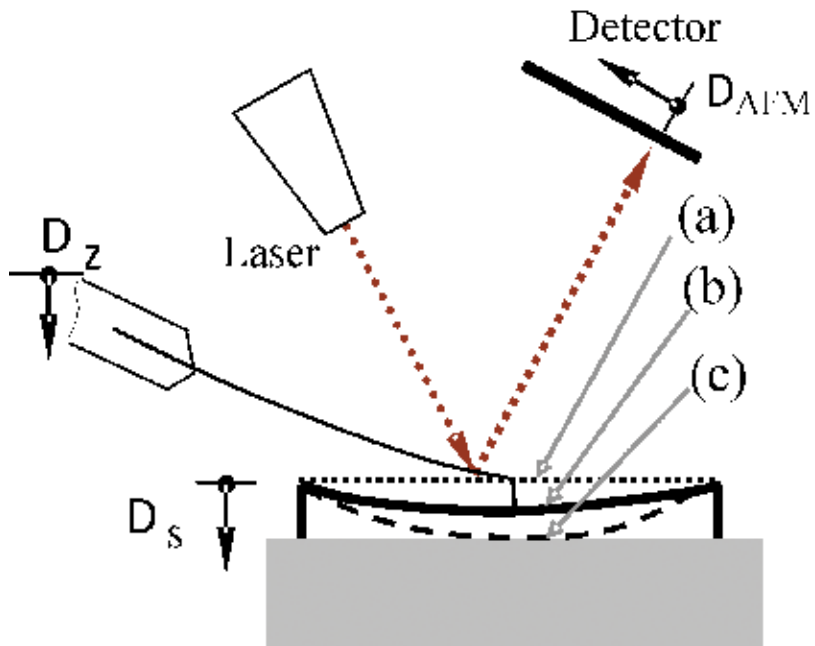


Figure 6. Bending deflection of AFM probe and investigated micromembranes: (a) the initial contact between AFM probe and sample; (b) bending of AFM probe together with sample; (c) bending only of AFM probe (the sample touch the substrate).

The AFM data from the first part of curve (A and B) are used to estimate the sample deflection (D_s) as the difference between the controlled displacement of the scanning head (D_z) and the detected deflection of AFM probe (D_{AFM}).

$$D_s = D_z - D_{AFM} \quad (2)$$

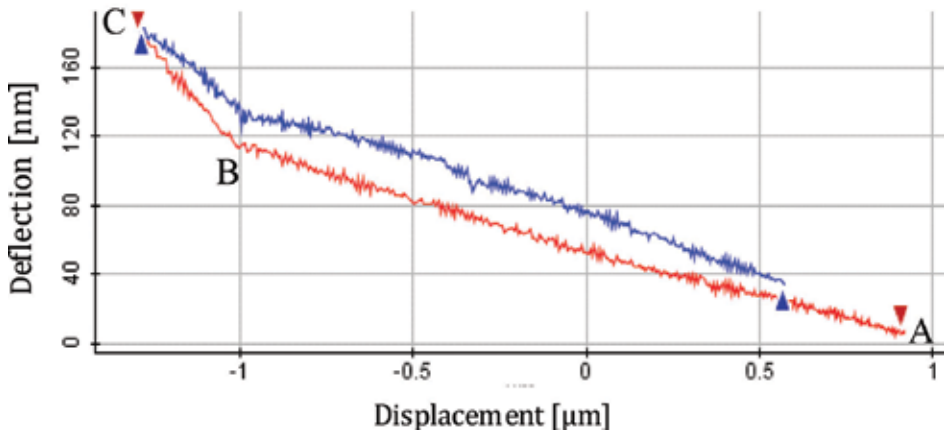


Figure 7. AFM experimental dependence between vertical displacements of the scanning head [μm] versus deflection of AFM probe [nm] for the investigated micromembrane with 2×4 connected hinges.

The force used in experiment can be determined based on the known stiffness of AFM probe and its bending deflection. This force and the determined deflection of sample given by Eq. (2) are used to compute the sample stiffness as:

$$k = \frac{F}{D_s} \tag{3}$$

The experimental dependence between the sample deflection and the applied AFM force is presented in **Figure 8**. The slope of this curve gives the micromembrane bending stiffness.

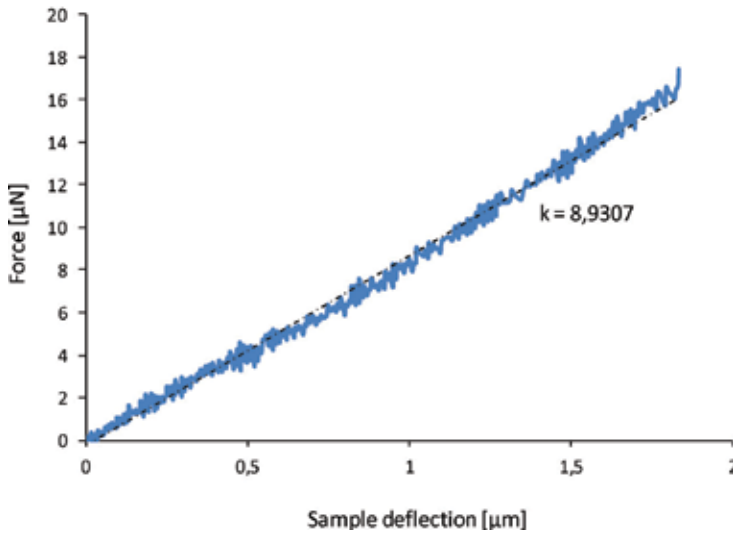


Figure 8. Force [μN] versus deflection [μm] of the micromembrane with 2×4 connected hinges. The slope of experimental curve represents the bending stiffness.

The stiffness of the investigated micromembrane supported by 2×4 serial-parallel connected hinges (**Figure 1a**) is 8.930 7N/m (**Figure 8**). The same experiment is performed in order to estimate the stiffness of the micromembrane supported by 4×6 serial-parallel connected hinges (**Figure 1b**). For this micromembrane, a bending stiffness equal to 18.18 N/m is determined if the force is applied in the mid position of the mobile plate (**Figure 5**). The tests were repeated several times, and the results of micromembrane stiffness have closed values.

5. Analysis of adhesion force between micromembrane with serial-parallel connected hinges and the silicon substrate

Stiction is one of the main failure causes in MEMS, and it occurs when surface forces are too large and, as a consequence, the surfaces brought in contact cannot be separated again. Intensive experimental and theoretical research has been conducted in order to determine the effect of the main factors on the surface forces especially on the adhesion force. For example, the influence of material properties, surface characteristics, and environmental conditions on the adhesion force has been experimentally determined and mathematically validated for several MEMS structures [8].

Researchers have developed several mathematical models for computing the adhesion force by taking into consideration the possible contact types between surfaces. For example, if two surfaces are characterized by high roughness, their contact was approximated by the contact between two elastic spheres (see DMT and JKR models [9]). Another example is the case of the elastic contact between a surface with high roughness and a surface with low roughness. The already mentioned mathematical models can be easily customized for this case [10]. However, the ideal case of elastic contact is rare at micro and nano scale, determining in some cases large differences between experimental and theoretical values. As mentioned in [8], when two surfaces are brought in contact, the highest asperities suffer a plastic deformation. Therefore, in order to correctly estimate the adhesion force between two rough surfaces, a plastic adhesion index has to be computed [8]:

$$\lambda = \frac{\pi^2 H^4 r_a \sigma}{8 \Delta \gamma^2 E^{*2}} \quad (4)$$

where H is the material hardness, r_a is the mean radius of curvature of asperities, σ is the standard deviation of peak heights, $\Delta \gamma$ is the work of adhesion, E^* is the equivalent Young's module given by:

$$E^* = \left(\frac{1 - \nu_1^2}{E_1} + \frac{1 - \nu_2^2}{E_2} \right) \quad (5)$$

$E_{1,2}$ are Young's moduli and $\nu_{1,2}$ are Poisson's ratios of the two surfaces. The work of adhesion is computed according to [10]:

$$\Delta\gamma = \gamma_1 + \gamma_2 - \gamma_{12} \tag{6}$$

where γ_1 and γ_2 are the surface energies of the two materials brought in contact, and $\gamma_{1,2}$ is the interface energy of contacting materials and was computed according to [11].

Considering the plastic deformation and assuming an exponential distribution of asperity heights, the adhesion force is expressed as a function of the compression force F as follows:

$$F_{ad} = F \left(-1 + \frac{1 + \lambda}{\lambda} \exp \left(-\frac{1}{\lambda} \right) \right) \tag{7}$$

while the total real contact area per unit area is given by:

$$A_r = 2\pi nr_n \sigma \tag{8}$$

and n is the number of asperities in contact per unit area.

The experimental determination of the adhesion force between the flexible part of the gold micromembrane and the silicon substrate was conducted using the spectroscopy in point mode of the AFM for the micromembrane with 2×4 connected hinges (**Figure 9**).

On the unloading AFM curve (**Figure 7**), the detachment of the micromembrane from substrate is delayed based on the adhesion effect that occurs. This effect gives a jump in the bending deflection of AFM probe that is directly proportional to the adhesion force. A zoom of the experimental AFM curve obtained when performing the spectroscopy in point is illustrated in **Figure 9**, and the blue part corresponds to the unloading test. In the same figure, the experimental value of the corresponding adhesion force given by the AFM software can be observed, and it is equal to 1.278 μN .

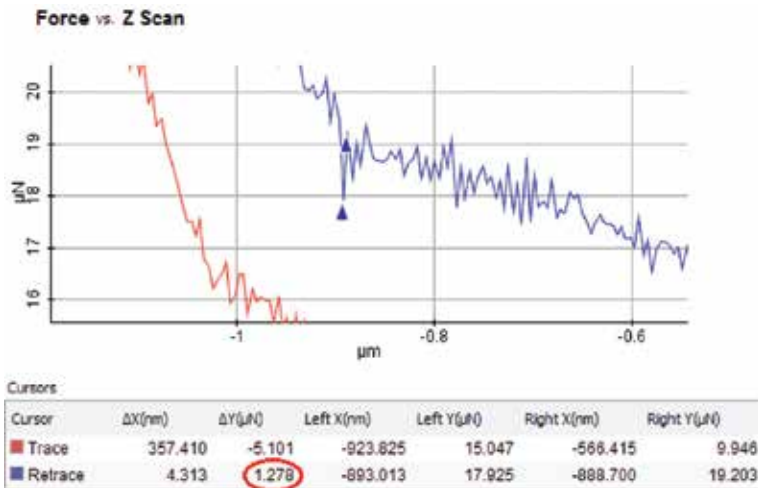


Figure 9. Adhesion force between the central part of micromembrane and the substrate in the case of micromembrane with 2×4 connected hinges.

In order to compute the adhesion force, the roughness of the contact surfaces is needed. To perform this step, a micromembrane is cut close to anchor and moved with the backside up to scan the contact surfaces [12]. The topography of the contact surfaces is taken using the tapping mode of AFM. The 3D images for each of the two surfaces that come in contact are provided in **Figures 10** and **11**, respectively, together with the statistical parameters provided for roughness by the software used for interpreting the experimental data (XEI Image Processing Tool for SPM).

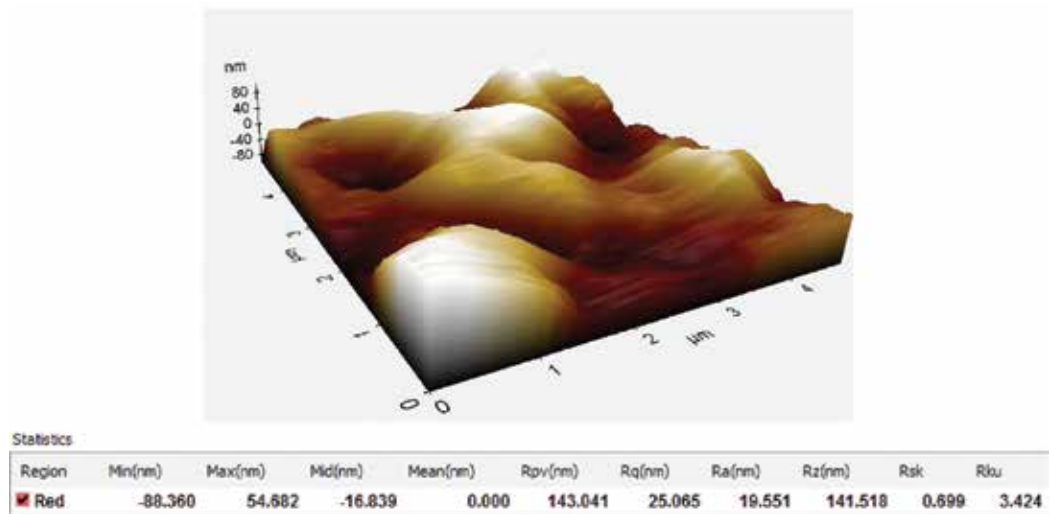


Figure 10. AFM images and the surface parameters of the backside of flexible plate (gold).

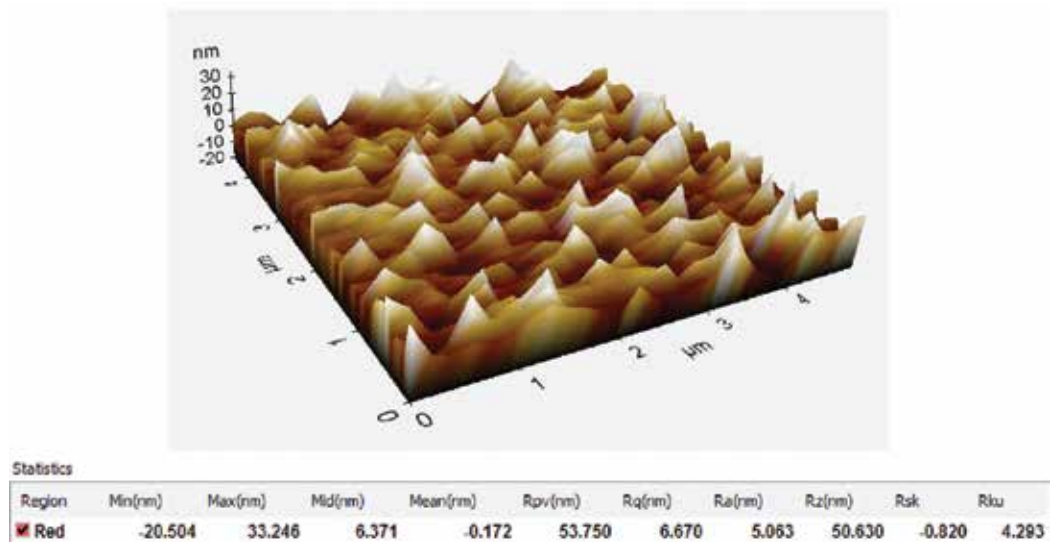


Figure 11. AFM images and the surface parameters of the substrate (silicon).

The theoretical value for the adhesion force was obtained using the mathematical model presented above. First, the work of adhesion was computed using a surface energy of 1.51 J/m^2 [13] for the silicon substrate and of 1 J/m^2 [14] for the gold micromembrane, while the equivalent Young's module was computed using a value of 150 GPa for Young's module and 0.17 for Poisson's ratio for the silicon substrate and a value of 72 GPa for Young's module and 0.42 for Poisson's ratio for the gold membrane. Then, the adhesion force was computed for the micromembrane with 2×4 connected hinges considering the real contact area between the surfaces. Knowing that the compression force was $17.28 \text{ }\mu\text{N}$, an adhesion force of $1.34 \text{ }\mu\text{N}$ was obtained in good agreement with the experimental ones.

6. Results and discussions

First, using the AFM technique, the effect of geometrical configuration of hinges on the bending stiffness of gold micromembranes was investigated. A method to estimate the out-of-plane stiffness by AFM is provided in this chapter, including its validation by analytical and numerical approaches. The mechanical force used to bend the flexible part of micromembrane is given by bending deflection of AFM probe and its stiffness. Second, by considering Castigliano's deformation theorem, an expression to compute the bending stiffness of micromembranes supported by serial-parallel connected hinges is provided. Moreover, simulation and finite element analysis is developed using a unitary force applied in the mid position of the mobile plate as in the experiments. The results obtained for out-of-plane stiffness in investigated samples are in good agreement as observed in **Table 1**.

The differences between results are influenced by the accuracy of the experimental tests and the differences of Young's modulus. In analytical and numerical analysis, a value of Young's modulus taken from literature is used, and it can differ by its experimental value. Moreover, the analytical model does not consider the influence of the holes from the plates. In any way, the holes have a negligible effect on the samples stiffness as confirmed by numerical analysis. An important influence of the holes can be observed if the micromembranes are dynamically actuated, because the damping given by surrounding medium decreases. Using different serial-parallel connected hinges to support the flexible part of micromembrane, different mechanical responses can be obtained. The stiffness of samples depends on the number of hinges and their connection.

The adhesion force for the contact between the flexible part and the silicon substrate of the gold micromembrane with 2×4 connected hinges was determined both experimentally and theoretically, and the results are in good agreement. The pull-off force of micromembranes from

Samples	Stiffness [N/m]		
	Experimental	Analytical	Simulation
Micromembrane 2×4	8.93	10.33	9.69
Micromembrane 4×6	18.18	17.86	16.61

Table 1. Bending stiffness of investigated micromembranes.

substrate depends on the adhesion force and the samples stiffness. Adhesion effect is influenced by the roughness of contact surfaces and the operating conditions. The roughness is the same for investigated micromembranes.

Depending on the micromembrane application, different types of hinges can be chosen in order to obtain different stiffness for in-plane and/or out-of-plane movement. The same methodology as presented in Section 3 of this chapter was applied to determine the stiffness of micromembrane with the other types of hinges.

Micromembranes supported by serpentine hinges are characterized by the possibility of in-plane and out-of-plane movements of the mobile plate [15]. Micromembranes supported by two and four serpentine hinges are presented in **Figure 12**. The number of hinges as well as their length have influence the micromembranes deflection under a mechanical force. Using the AFM tests, the displacement of the central plate is monitored under a mechanical force, and the micromembrane stiffness was determined. As the number of hinges and their length are modified, the stiffness is changed. The micromembrane 1 with two short hinges (**Figure 12a**) has an out-of-plane stiffness equal to 64.4 N/m. If the length of hinges increases for the micromembrane 2 (**Figure 12b**), the bending stiffness decreases 4.3 times. In the case of the same micromembrane, but supported by four hinges, the stiffness is modified. The micromembrane 3 with four short hinges (**Figure 12c**) is characterized by a stiffness of 127.5 N/m, and its value decreases five times if the length of hinges increases as in the case of the micromembrane 4 (**Figure 12d**). It can be noticed that longer hinges ensure more flexibility and the number of hinges multiply the stiffness.

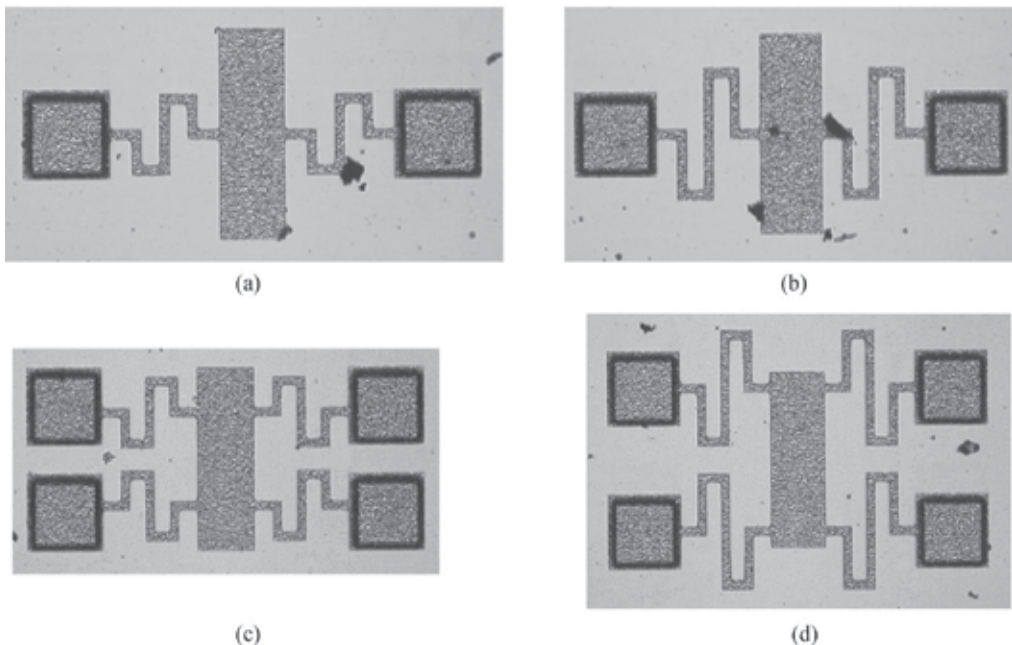


Figure 12. Micromembranes supported by serpentine hinges: (a) Micromembrane-1; (b) Micromembrane-2; (c) Micromembrane-3; (d) Micromembrane-4.

The other investigations using the same AFM method were performed on micromembranes supported by bent beam hinges electroplated with gold in different geometrical dimensions are presented in **Figure 13** [16]. The structures are characterized by different widths of hinges and different lengths of the central plate. Stiffness analysis considers fixed anchors and a central force perpendicular to the central plate of micromembranes. Different stiffness of micromembranes can be obtained if the geometrical dimensions are modified. The stiffness of micromembrane increases with the dimensions of hinges and decreases for a longer mobile plate.

Other example, presented in **Figure 14**, is a micromembrane supported by folded hinges [3]. The same AFM tests were performed to determine the micromembrane behavior under a

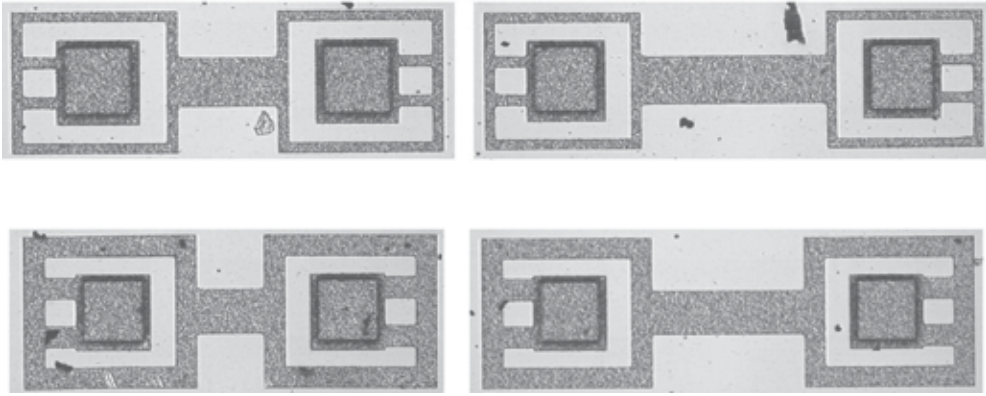


Figure 13. Micromembranes supported by bent beam hinges.

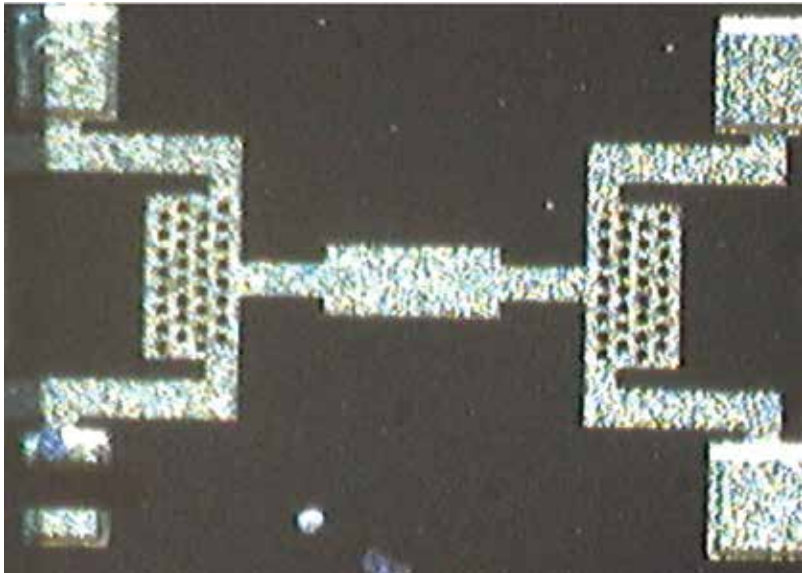


Figure 14. Micromembranes supported by folded hinges.

mechanical force. The stiffness was experimentally determined and validated by numerical and analytical results. As in the case of investigated micromembrane with serial-parallel connected hinges, the holes have a small influence upon stiffness under static deflection fact demonstrated by the numerical simulation. The holes have significant effect on the dynamic modulation because the mass of micromembrane is changed and the quality factor given by the air damping is improved [17].

Acknowledgements

This work was supported by a grant of the Romanian National Authority for Scientific Research and Innovation, CNCS-UEFISCDI, project number PN-II-RU-TE-2014-4-1271.

Author details

Marius Pustan*, Cristian Dudescu, Corina Birleanu and Florina Rusu

*Address all correspondence to: Marius.Pustan@omt.utcluj.ro

Technical University of Cluj-Napoca, Cluj-Napoca, Romania

References

- [1] Rebeiz GM. RF MEMS. Theory, Design, and Technology. John Wiley & Sons Ltd; 2003
- [2] Lobontiu N, Garcia E. Mechanics of Microelectromechanical Systems. Springer US; 2004
- [3] Pustan M, Dudescu C, Birleanu C. Nanomechanical and nanotribological characterization of a MEMS micromembrane supported by two folded hinges. *Analog Integrated Circuits and Signal Processing*. 2015;**82**:627–635
- [4] Pustan M, Birleanu C, Dudescu C, Belcin O. Mechanical and tribological characterizations for reliability design of micromembranes. In: *The 13th International Thermal Mechanical and Multi-Physics Simulation and Experiments in Microelectronics and Microsystems; EUROSIME 2012*. Cascais, Portugal; 2012
- [5] Somà A. MEMS design for reliability: Mechanical failure modes and testing. 2011. In: *Proceedings of 7th International Conference on Perspective Technologies and Methods in MEMS Design, MEMSTECH 2011*. art. 5960284; 2011. pp. 91–101
- [6] Pustan M, Dudescu C, Birleanu C. Static response and stiction analysis of MEMS micromembranes for optical applications. *Physica Status Solidi (c)*. 2015;**12**:1322–1327. DOI: 10.1002/pssc.201510096

- [7] Li X, Bhushan B, Takashima K, Baek CW, Kim YK. Mechanical characterization of micro/nanoscale structures for MEMS/NEMS applications using nanoindentation techniques. *Ultramicroscopy*. 2003;**97**: 481–494
- [8] Rusu F, Pustan M, Birleanu C, Müller R, Voicu R, Baracu A. Analysis of the surface effects on adhesion in MEMS structures. *Applied Surface Science*. 2015;**358**:634–640
- [9] Grierson DS, Flater EE, Carpick RW. Accounting for the JKR–DMT transition in adhesion and friction measurements with atomic force microscopy. *Journal of Adhesion Science and Technology*. 2005;**19**:291–311
- [10] Zhang LX, Zhao YP. Adhesion of rough surfaces with plastic deformation. *Journal of Adhesion Science and Technology*. 2004;**18**:715–729
- [11] Gutierrez-Miravete E. Adhesion between Contacting Surfaces, Chapter 4 [Internet], 2012. Available from: <http://www.ewp.rpi.edu/hartford/~ernesto/F2012/FWM/Notes/ch04.pdf> [Accessed: 25 January 2017]
- [12] Pustan M, Birleanu C, Dudescu C. Nanocharacterization of the adhesion effect and bending stiffness in optical MEMS. *Applied Surface Science*. DOI: 10.1016/j.apsusc.2016.12.021
- [13] Jaccodine RJ. Surface Energy of Germanium and Silicon. *Journal of the Electrochemical Society*. 1963;**110**:524–527
- [14] Jonas U. Introduction to Surface Chemistry [Lecture]. 2012. Available from: http://esperia.iesl.forth.gr/~ujonas/Master_Surf_Chem/lecture_IntroSurfChem_1c.pdf [Accessed: 25 January 2017]
- [15] Pustan M, Birleanu C, Dudescu C, Rusu F. Investigation on the contact behaviour of MEMS micromembrane with serpentine hinges. In: *The 13th International Conference on Tribology; ROTRIB 2016*. Galati, Romania; 2016
- [16] Pustan M, Dudescu C, Birleanu C, Rusu F, Chiorean R, Craciun S. Effect of geometrical dimensions on the tribomechanical response of a gold micromembrane with bent beam hinges. *IOP Conference Series: Materials Science and Engineering*. 2016;**147**(1):012022. DOI: 10.1088/1757-899X/147/1/012022
- [17] Pustan M, Birleanu C, Dudescu C, Golival JC. Dynamical behavior of smart MEMS in industrial applications. In: Nihitnov S, Estepa AL, editors. *Smart Sensors and MEMS: Intelligent Devices and Microsystems for Industrial Applications*. Woodhead Publishing; 2013. pp. 349–365. DOI:10.1533/9780857099297.2.349

Static, Vibration, and Buckling Analysis of Nanobeams

Şeref Doğuşcan Akbaş

Additional information is available at the end of the chapter

<http://dx.doi.org/10.5772/67973>

Abstract

Static, vibration, and buckling analysis of nanobeams is studied based on modified couple stress theory (MCST) in this chapter. The inclusion of an additional material parameter enables the new beam model to capture the size effect. The new nonclassical beam model reduces the classical beam model when the length scale parameter is set to zero. The finite element formulations are derived for static, free vibration, and buckling problems of nanobeams within MCST and the Euler-Bernoulli beam theory. The effect of the material length scale parameter and geometry parameters on the static, vibration, and buckling responses of the nanobeam is investigated in both the classical beam theory (CBT) and MCST by using finite element method. Also, the difference between the classical beam theory (CBT) and modified couple stress theory is investigated.

Keywords: nanobeams, couple stress theory, finite element method, static, vibration, buckling

1. Introduction

With the great advances in technology in recent years, micro and nanostructures have found many applications. In these structures, micro beams and micro tubes are widely used in nanoscale electromechanical systems such as sensors (Zook et al. [1], Pei et al. [2]), actuators (Senturia [3], Rezazadeh et al. [4]). In investigation of micro and nanostructures, the classical continuum mechanics are not effort of describing of the size-dependent mechanics. Nonclassical continuum theories such as higher-order gradient theories and the couple stress theory are capable of explanation of the size-dependent behaviors, which occur in micro/nanoscale structures.

At the present time, the experimental investigations of the micro/nano materials are still a challenge because of difficulties confronted in the micro/nanoscale. Therefore, mechanical

theories and atomistic simulations have been used for nanostructural analysis. The process of the atomistic simulations is very difficult and takes much time. So, continuum theory is the most preferred method for the analysis of the micro and nanostructures. Classical continuum mechanics does not contain the size effect, because of its scale-free character. The nonlocal continuum theory initiated by Eringen [5] has been widely used to mechanical behavior of micro/nanostructures.

The size effect is very effective in the mechanical behavior of nanostructures at nanometer scale that the classic theory has failed to consider when the size reduces from macro to nano (Toupin [6], Mindlin [7, 8], Fleck and Hutchinson [9], Yang et al. [10], Lam et al. [11]). Therefore, higher-order theories of modified couple stress theory (MCST) and modified strain gradient are used in the mechanical model of the nano/microstructures (Yang et al. [10], Lam et al. [11]).

The determination of the micro/nanostructural material length scale parameters is very difficult experimentally. So, Yang et al. [10] studied the strain energy of the MCST with one length scale parameter. After this, the MCST and the strain gradient elasticity theories have been widely applied to static and dynamic analysis of beams (Park and Gao [12], Ma et al. [13], Kong et al. [14], Wang et al. [15], Asghari et al. [16], Wang [17], Simsek [18], Kahrobaiyan et al. [19], Xia et al. [20], Ke et al. [21], Li et al. [22], Akgöz and Civalek [23, 24], Ansari et al. [25], Dos Santos and Reddy [26], Simsek et al. [27], Wang et al. [28], Kocatürk and Akbas [29], Kong [30], Daneshmehr et al. [31], Akgöz and Civalek [32], Ziaee [33], Islam et al. [34], Miandoab et al. [35], Liu et al. [36], Tang et al. [37], Hosseini and Rahmani [38], Akbas [39, 40]).

The objective of this paper is to investigate static, vibration, and buckling solutions of nanobeams based on modified couple stress theory (MCST). The finite element formulations are derived for static, free vibration, and buckling problems of nanobeams within MCST and the Euler-Bernoulli beam theory. The effect of the material length scale parameter and geometry parameters on the static, vibration, and buckling responses of the nanobeam are investigated in both the classical beam theory (CBT) and MCST. Also, the difference between the classical beam theory and modified couple stress theory is investigated.

2. Theory and formulations

A simple supported nanobeam of length L , width b , and height h , with X, Y, Z cartesian coordinate system is shown in **Figure 1**.

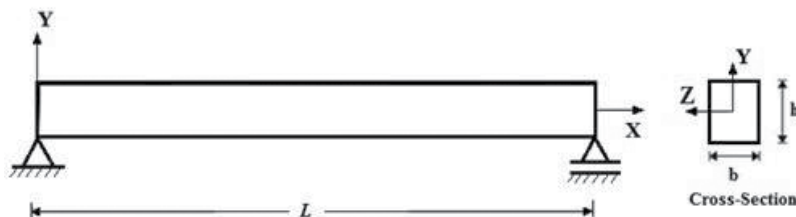


Figure 1. A simple supported nanobeam with X, Y, Z cartesian coordinate system and cross section.

The modified couple stress theory was proposed by Yang et al. [10]. Based on this theory, the strain energy density for a linear elastic material which is a function of both strain tensor and curvature tensor is introduced for the modified couple stress theory;

$$U = \int_V (\boldsymbol{\sigma} : \boldsymbol{\varepsilon} + \mathbf{m} : \boldsymbol{\chi}) dV \quad (1)$$

where $\boldsymbol{\sigma}$ is the stress tensor, $\boldsymbol{\varepsilon}$ is the strain tensor, \mathbf{m} is the deviatoric part of the couple stress tensor, $\boldsymbol{\chi}$ is the symmetric curvature tensor, defined by

$$\boldsymbol{\sigma} = \lambda \text{tr}(\boldsymbol{\varepsilon})\mathbf{I} + 2\mu\boldsymbol{\varepsilon} \quad (2)$$

$$\boldsymbol{\varepsilon} = \frac{1}{2}[\nabla\mathbf{u} + (\nabla\mathbf{u})^T] \quad (3)$$

$$\mathbf{m} = 2l^2\mu\boldsymbol{\chi} \quad (4)$$

$$\boldsymbol{\chi} = \frac{1}{2}[\nabla\boldsymbol{\theta} + (\nabla\boldsymbol{\theta})^T] \quad (5)$$

where λ and μ are Lamé's constants, l is a material length scale parameter which is regarded as a material property characterizing the effect of couple stress, \mathbf{u} is the displacement vector and $\boldsymbol{\theta}$ is the rotation vector, given by

$$\boldsymbol{\theta} = \frac{1}{2}\text{curl } \mathbf{u} \quad (6)$$

The parameters λ and μ in the constitutive equation are given by

$$\lambda = \frac{E\nu}{(1+\nu)(1-2\nu)}, \quad \mu = \frac{E}{2(1+\nu)} \quad (7)$$

where E is the modulus of elasticity and ν is the Poisson's ratio. According to the coordinate system (X, Y, Z) shown in **Figure 1**, based on Euler-Bernoulli beam theory, the axial and the transverse displacement field are expressed as

$$u(X, Y, t) = u_0(X, t) - Y \frac{\partial v_0(X, t)}{\partial X} \quad (8)$$

$$v(X, Y, t) = v_0(X, t) \quad (9)$$

$$w(X, Y, t) = 0 \quad (10)$$

where u, v, w are the $x, y,$ and z components of the displacements, respectively; u_0 and v_0 are the axial and the transverse displacements in the mid-plane; and t indicates time. Because the transversal surfaces of the beam are free of stress,

$$\sigma_{zz} = \sigma_{yy} = 0 \quad (11)$$

By using Eqs. (3) and (8)–(10), the strain-displacement relation can be obtained:

$$\varepsilon_{xx} = \frac{\partial u}{\partial X} = \frac{\partial u_0(X, t)}{\partial X} - Y \frac{\partial^2 v_0(X, t)}{\partial X^2} \quad (12a)$$

$$\varepsilon_{yy} = \varepsilon_{zz} = Y \frac{\partial^2 v_0(X, t)}{\partial X^2} \quad (12b)$$

$$\varepsilon_{xz} = \varepsilon_{yz} = \varepsilon_{xy} = 0 \quad (12c)$$

By using Eqs. (6) and (8)–(10),

$$\theta_z = \frac{\partial v_0(X, t)}{\partial X} \theta_x = \theta_y = 0 \quad (13)$$

Substituting Eq. (13) into Eq. (5), the curvature tensor χ can be obtained as follows:

$$\chi_{xz} = \frac{1}{2} \frac{\partial^2 v_0(X, t)}{\partial X^2} \chi_{xx} = \chi_{xy} = \chi_{yy} = \chi_{yz} = \chi_{zz} = 0 \quad (14)$$

According to Hooke's law, the constitutive equations of the nanobeam are as follows:

$$\sigma_{xx} = E\varepsilon_{xx} = E \left[\frac{\partial u_0(X, t)}{\partial X} - Y \frac{\partial^2 v_0(X, t)}{\partial X^2} \right] \quad (15)$$

where σ_{xx} and ε_{xx} are the normal stresses and normal strains in the X direction, respectively. Substituting Eq. (14) into Eq. (4), the couple stress tensor can be obtained as follows:

$$m_{xz} = l^2 \mu \frac{1}{2} \frac{\partial^2 v_0(X, t)}{\partial X^2} \quad (16a)$$

$$m_{xx} = m_{xy} = m_{yy} = m_{yz} = m_{zz} = 0 \quad (16b)$$

where μ is the shear modulus defined by Eq. (7). The elastic strain energy (U_i) of the nanobeam is expressed as

$$U_i = \frac{1}{2} \int_0^L \int_A (\sigma_{ij} \varepsilon_{ij} + m_{ij} \chi_{ij}) dA dX \quad (17)$$

By substituting Eqs. (12) and (14)–(16) into Eq. (17), elastic strain energy (U_i) can be rewritten as follows:

$$U_i = \frac{1}{2} \int_0^L \left[EA \left(\frac{\partial u_0(X, t)}{\partial X} \right)^2 + EI \left(\frac{\partial^2 v_0(X, t)}{\partial X^2} \right)^2 + \frac{1}{4} l^2 \mu A \left(\frac{\partial^2 v_0(X, t)}{\partial X^2} \right)^2 \right] dX \quad (18)$$

where A is the area of the cross section, and I is the moment of inertia.

$$T = \frac{1}{2} \int_0^L \left[\rho A \left(\frac{\partial u_0}{\partial t} \right)^2 + \rho A \left(\frac{\partial v_0}{\partial t} \right)^2 + \rho I \left(\frac{\partial^2 v_0}{\partial X \partial t} \right)^2 \right] dX \quad (19)$$

The potential energy of the external load can be written as

$$U_e = \int_0^L \left[f v(x) + P \left(\frac{\partial v}{\partial x} \right) \right] dX + Q_i v_i \quad (20)$$

where f is load function, Q_i is point loads which contains point forces and moments, P is axial compressive load for buckling case. The nodal displacements q for a two-node beam element contain three degrees of freedom at each node, as shown in **Figure 2**, namely,

$$\{q(t)\}_e = [u_i^{(e)}(t), v_i^{(e)}(t), \theta_i^{(e)}(t), u_j^{(e)}(t), v_j^{(e)}(t), \theta_j^{(e)}(t)]^T \quad (21)$$

The displacement field of the finite element is expressed in terms of the nodal displacements as follows:

$$u^{(e)}(X, t) = \varphi_1^{(U)}(X) u_i(t) + \varphi_2^{(U)}(X) u_j(t) = [\varphi^{(U)}] \begin{Bmatrix} u_i \\ u_j \end{Bmatrix} = [\varphi^{(U)}] \{q\}_U \quad (22)$$

$$v^{(e)}(X, t) = \varphi_1^{(V)}(X) v_i(t) + \varphi_2^{(V)}(X) \theta_i(t) + \varphi_3^{(V)}(X) v_j(t) + \varphi_4^{(V)}(X) \theta_j(t) \quad (23a)$$

$$[\varphi^{(V)}] \begin{Bmatrix} v_i \\ \theta_i \\ v_j \\ \theta_j \end{Bmatrix} = [\varphi^{(V)}] \{q\}_V \quad (23b)$$

where u_i , v_i , and θ_i are the axial displacements, transverse displacements, and slopes at the two end nodes of the beam element, respectively, and $\varphi_i^{(U)}$ and $\varphi_i^{(V)}$ are the Hermite shape functions for the axial and transverse displacements, respectively. The interpolation functions for the axial displacement are,

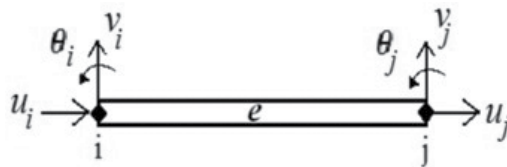


Figure 2. Two-node beam element.

$$\varphi^{(U)}(X) = \left[\varphi_1^{(U)}(X) \varphi_2^{(U)}(X) \right]^T \quad (24)$$

where

$$\varphi_1^{(U)}(X) = \left(-\frac{X}{L_e} + 1 \right) \quad (25a)$$

$$\varphi_2^{(U)}(X) = \left(\frac{X}{L_e} \right) \quad (25b)$$

The interpolation functions for the transverse displacement are

$$\varphi^{(V)}(X) = \left[\varphi_1^{(V)}(X) \varphi_2^{(V)}(X) \varphi_3^{(V)}(X) \varphi_4^{(V)}(X) \right]^T \quad (26)$$

where

$$\varphi_1^{(V)}(X) = \left(1 - \frac{3X^2}{L_e^2} + \frac{2X^3}{L_e^3} \right) \quad (27a)$$

$$\varphi_2^{(V)}(X) = \left(-X + \frac{2X^2}{L_e} - \frac{X^3}{L_e^2} \right) \quad (27b)$$

$$\varphi_3^{(V)}(X) = \left(\frac{3X^2}{L_e^2} - \frac{2X^3}{L_e^3} \right) \quad (27c)$$

$$\varphi_4^{(V)}(X) = \left(\frac{X^2}{L_e} - \frac{X^3}{L_e^2} \right) \quad (27d)$$

with L_e indicating the length of the beam element. The Lagrangian functional of the problem is given as follows:

$$I = T - (U_i + U_e) \quad (28)$$

After substituting Eqs. (22) and (23) into Eq. (28) and then using the Lagrange's equations, one obtains the following equation:

$$\frac{\partial I}{\partial q_k^{(e)}} - \frac{\partial}{\partial t} \frac{\partial I}{\partial \dot{q}_k^{(e)}} = 0, \quad k = 1, 2, 3, 4, 5, 6, \quad (29)$$

where $\dot{q}_k^{(e)}$ indicates the time derivative of the nodal displacements q .

The Lagrange's equations can be employed to yield the system of equations of motion for the finite element. By the usual assemblage procedure, the equations of motion can be obtained for the entire structure. For the free vibration problem, the finite element equation is as follows:

$$([K] - \omega^2[M])\{\hat{q}\} = 0 \quad (30)$$

For the static problem, the finite element equation is as follows:

$$[K]\{q\} = \{F\} \quad (31)$$

For the buckling problem, the finite element equation is as follows:

$$([K] - P_{cr}[K_G])\{\hat{q}\} = 0 \quad (32)$$

where ω is the natural frequency, $\{\hat{q}\}$ is a vector of displacement amplitudes of the vibration, $\{F\}$ is the global load vector, $[K]$ is the stiffness matrix, $[M]$ is the mass matrix, and $[K_G]$ is the stability matrix. The stiffness matrix $[K]$ can be given as:

$$[K] = \begin{bmatrix} [K^A] & [0] \\ [0] & [K^D] \end{bmatrix} \quad (33)$$

where

$$[K^A] = \int_0^{L_e} EA \left[\frac{\partial \varphi^{(U)}}{\partial X} \right]^T \left[\frac{\partial \varphi^{(U)}}{\partial X} \right] dX \quad (34a)$$

$$[K^D] = \int_0^{L_e} \left(EI + \frac{1}{4} l^2 \mu A \right) \left[\frac{\partial^2 \varphi^{(V)}}{\partial X^2} \right]^T \left[\frac{\partial^2 \varphi^{(V)}}{\partial X^2} \right] dX \quad (34b)$$

The mass matrix $[M]$ can be expressed as the sum of four submatrices as follows:

$$[M] = [M_U] + [M_V] + [M_\emptyset] \quad (35)$$

where

$$[M_U] = \int_0^{L_e} \rho A [\varphi^{(U)}]^T [\varphi^{(U)}] dX \quad (36a)$$

$$[M_V] = \int_0^{L_e} \rho A [\varphi^{(V)}]^T [\varphi^{(V)}] dX \quad (36b)$$

$$[M_\emptyset] = \int_0^{L_e} \rho I [\varphi^{(\emptyset)}]^T [\varphi^{(\emptyset)}] dX \quad (36c)$$

The stability matrix $[K_G]$ can be given as:

$$[K_G] = \begin{bmatrix} [0] & [0] \\ [0] & [K_G^D] \end{bmatrix} \quad (37)$$

where

$$[K_G^D] = \int_0^{L_e} \left[\frac{\partial \varphi^{(V)}}{\partial X} \right]^T \left[\frac{\partial \varphi^{(V)}}{\partial X} \right] dX \quad (38)$$

The load vector $\{F\}$ is expressed as

$$\{F\} = \int_{x=0}^{L_e} \{\varphi(X)\}^T f dX + Q_i \quad (39)$$

In the solution of the free vibration and buckling problems, the eigenvalue procedure is performed in Eqs. (30) and (32). When the material length scale parameter (l) is equal to zero, the finite element formulations reduce to classical beam theory.

After integration processing, the finite element matrixes can be expressed as follows:

$$[K] = \begin{bmatrix} \frac{EA}{L_e} & 0 & 0 & -\frac{EA}{L_e} & 0 & 0 \\ 0 & \frac{12(EI + 0.25l^2\mu A)}{L_e^3} & \frac{-6(EI + 0.25l^2\mu A)}{L_e^2} & 0 & \frac{-12(EI + 0.25l^2\mu A)}{L_e^3} & \frac{-6(EI + 0.25l^2\mu A)}{L_e^2} \\ 0 & \frac{-6(EI + 0.25l^2\mu A)}{L_e^2} & \frac{4(EI + 0.25l^2\mu A)}{L_e} & 0 & \frac{6(EI + 0.25l^2\mu A)}{L_e^2} & \frac{2(EI + 0.25l^2\mu A)}{L_e} \\ -\frac{EA}{L_e} & 0 & 0 & \frac{EA}{L_e} & 0 & 0 \\ 0 & \frac{-12(EI + 0.25l^2\mu A)}{L_e^3} & \frac{6(EI + 0.25l^2\mu A)}{L_e^2} & 0 & \frac{12(EI + 0.25l^2\mu A)}{L_e^3} & \frac{6(EI + 0.25l^2\mu A)}{L_e^2} \\ 0 & \frac{-6(EI + 0.25l^2\mu A)}{L_e^2} & \frac{2(EI + 0.25l^2\mu A)}{L_e} & 0 & \frac{6(EI + 0.25l^2\mu A)}{L_e^2} & \frac{4(EI + 0.25l^2\mu A)}{L_e} \end{bmatrix} \quad (40a)$$

$$[M] = \begin{bmatrix} \frac{\rho AL_e}{3} & 0 & 0 & \frac{\rho AL_e}{6} & 0 & 0 \\ 0 & \left(\frac{13\rho AL_e}{35} + \frac{6\rho l}{5L_e} \right) & \left(\frac{-11\rho AL_e^2}{210} - \frac{\rho l}{10} \right) & 0 & \left(\frac{9\rho AL_e}{70} - \frac{6\rho l}{5L_e} \right) & \left(\frac{13\rho AL_e^2}{420} - \frac{\rho l}{10} \right) \\ 0 & \left(\frac{-11\rho AL_e^2}{210} - \frac{\rho l}{10} \right) & \left(\frac{\rho AL_e^3}{105} + \frac{2\rho l L_e}{15} \right) & 0 & \left(\frac{-13\rho AL_e^2}{420} + \frac{\rho l}{10} \right) & \left(\frac{-\rho AL_e^3}{140} - \frac{\rho l L_e}{30} \right) \\ \frac{\rho AL_e}{6} & 0 & 0 & \frac{\rho AL_e}{3} & 0 & 0 \\ 0 & \left(\frac{9\rho AL_e}{70} - \frac{6\rho l}{5L_e} \right) & \left(\frac{-13\rho AL_e^2}{420} + \frac{\rho l}{10} \right) & 0 & \left(\frac{13\rho AL_e}{35} + \frac{6\rho l}{5L_e} \right) & \left(\frac{11\rho AL_e^2}{210} + \frac{\rho l}{10} \right) \\ 0 & \left(\frac{13\rho AL_e^2}{420} - \frac{\rho l}{10} \right) & \left(\frac{-\rho AL_e^3}{140} - \frac{\rho l L_e}{30} \right) & 0 & \left(\frac{11\rho AL_e^2}{210} + \frac{\rho l}{10} \right) & \left(\frac{\rho AL_e^3}{105} + \frac{2\rho l L_e}{15} \right) \end{bmatrix} \quad (40b)$$

$$[K_G] = \begin{bmatrix} 0 & 0 & 0 & 0 & 0 & 0 \\ 0 & \frac{6}{5L_e} & \frac{-1}{10} & 0 & \frac{-6}{5L_e} & \frac{-1}{10} \\ 0 & \frac{-1}{10} & \frac{2L_e}{15} & 0 & \frac{1}{10} & \frac{-L_e}{30} \\ 0 & 0 & 0 & 0 & \frac{0}{10} & \frac{0}{30} \\ 0 & \frac{-6}{5L_e} & \frac{1}{10} & 0 & \frac{6}{5L_e} & \frac{1}{10} \\ 0 & \frac{1}{10} & \frac{-L_e}{30} & 0 & \frac{1}{10} & \frac{2L_e}{15} \end{bmatrix} \quad (40c)$$

3. Numerical results

In the numerical examples, the effects of the material length scale parameter and geometry parameters on the static, vibration, and buckling responses of the nanobeam are presented in both the classical beam theory (CBT) and MCST. Using the conventional assembly procedure for the finite elements, the system stiffness, mass, stability matrices, and the load vector are obtained from the element stiffness, mass, stability matrices, and load vectors. After that, the solution process outlined in the preceding section is used to obtain the solution for the problem of concern. In obtaining the numerical results, graphs and solution of the nonlinear finite element model, MATLAB program is used. The nanobeam is taken to be made of epoxy ($E = 1,44 \text{ GPa}$, $\nu = 0.38$, $l = 17.6 \text{ }\mu\text{m}$, $\rho = 1600 \frac{\text{kg}}{\text{m}^3}$). In the numerical calculations, the number of finite elements is taken as 100. In the numerical integrations, five-point Gauss integration rule is used.

In order to establish the accuracy of the present formulation and the computer program developed by the author, the results obtained from the present study are compared with the available results in the literature. For this purpose, the static deflections shapes of a simple supported beam with rectangular cross section, which is subjected to a point load, are calculated for MCST and compared with those of Alashti and Abolghasemi [41] by inserting the material and load properties used in this reference. It is clearly seen that the curves of **Figure 3** of the present study are very close to those of Alashti and Abolghasemi [41].

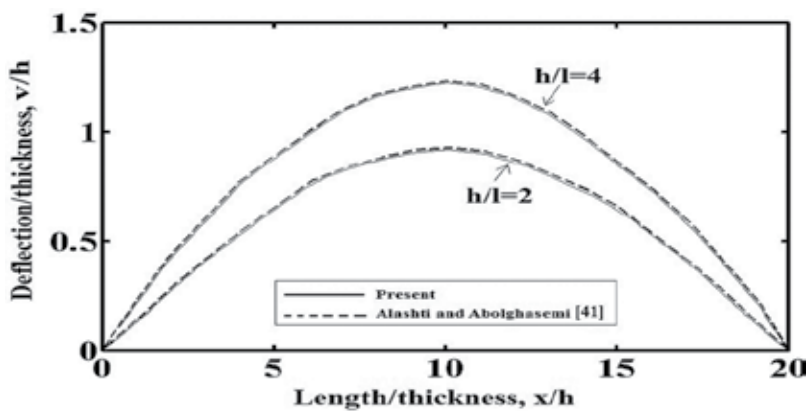


Figure 3. Comparison study: static deflections shape of the simple supported beam based on the MCST.

Figure 4a–c shows the effects of the thickness (h) on the static, vibration, and buckling responses of the nanobeam, respectively, in both the CBT and MCST. In these figures, static deflections, fundamental frequencies, and critical buckling loads are calculated and plotted for different values of the h for $b = l$ and $L = 30l$. In the calculation of **Figure 3a**, the nanobeam is subjected to a transversal point load ($P = 100 \mu\text{N}$) at the midpoint of the beam in the transverse direction.

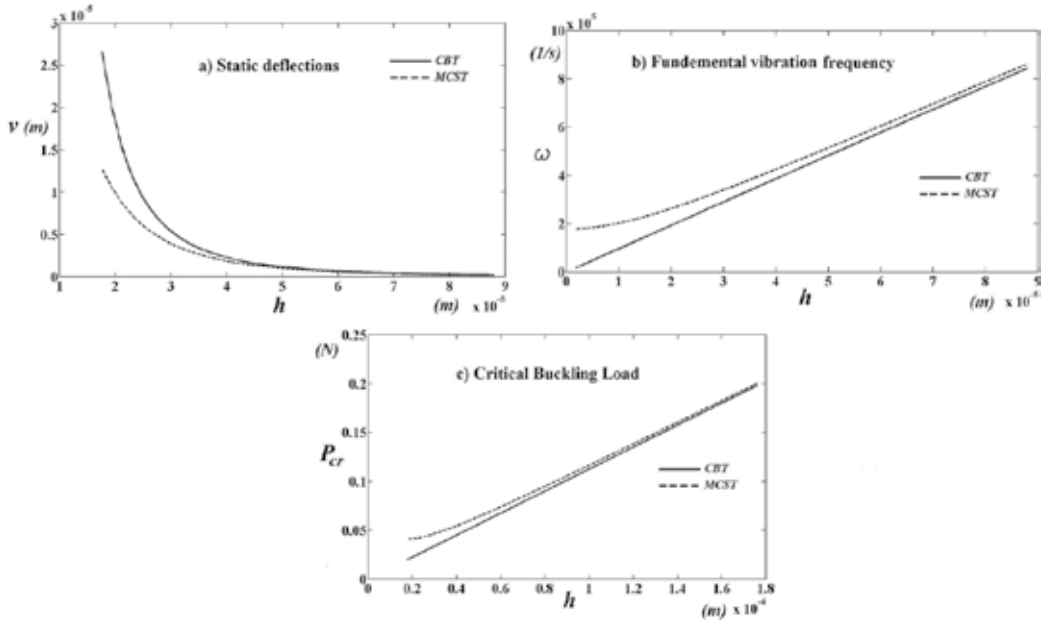


Figure 4. Effect of the thickness on the static, vibration, and buckling responses of the nanobeam for CBT and MCST; (a) static analysis, (b) free vibration analysis, and (c) buckling analysis.

As seen from **Figure 4**, the difference between the results of the MCST and CBT decreases significantly with the increase in the thickness of the nanobeam. Increase in the thickness of the nanobeam leads to a decline on effects of size effect and difference between the results of MCST and CBT.

In order to see the effect of material length scale parameter (l) on the static, vibration and buckling of the nanobeam, static deflections, fundamental frequencies, and critical buckling loads are displayed with different value of the dimensionless material length scale parameters (l/h) in both the CBT and MCST in **Figure 5** for $b = 1 \mu\text{m}$ and $L = 30 \mu\text{m}$. In this figure, for different values of the dimensionless material length scale parameters (l/h), the material length scale parameter (l) is varied when the thickness of the nanobeam (h) is kept constant as $1 \mu\text{m}$.

It is seen from **Figure 5** that with an increase in the dimensionless material length scale parameter l/h leads to a rise on the difference between the results of the MCST and CBT. Also, the dimensionless material length scale parameter has no effect on the mechanical responses for the classical theory, which is unable to capture the size effect. It is found that the deflections

of the nanobeam by the CBT are always larger than those by the MCST. However, fundamental frequencies and critical buckling loads by the MCST are always larger than those by the CBT. It can be seen from figures that the difference between the CBT and MCST is very large when the h and l/h increase. The material parameter and dimension of the nanobeam have a very important role on the mechanical behavior of nanobeams.

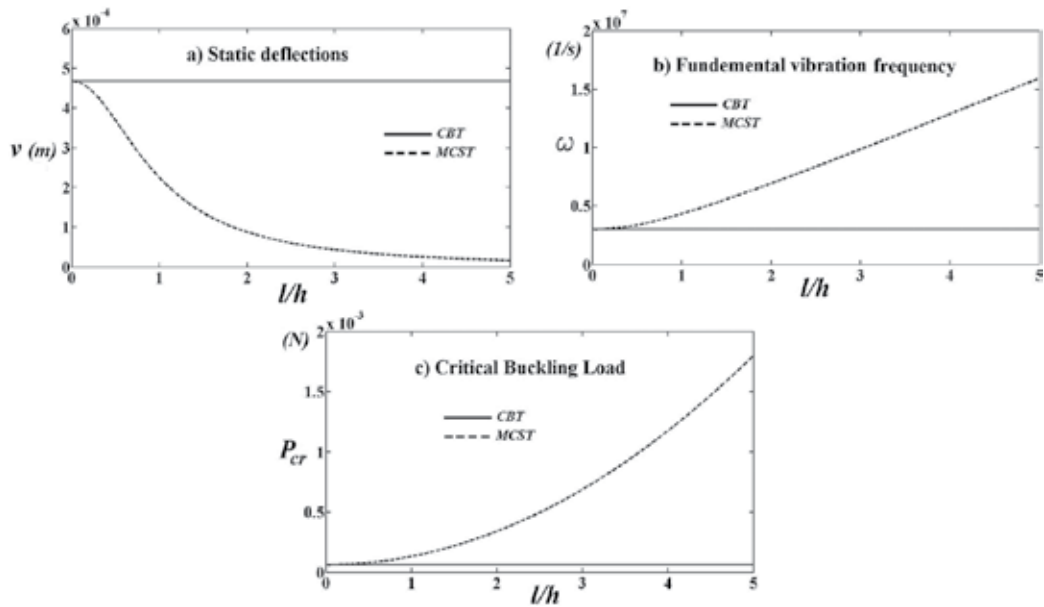


Figure 5. Effect of the dimensionless material length scale parameter (l/h) on the static, vibration, and buckling responses of the nanobeam for CBT and MCST; (a) static analysis, (b) free vibration analysis, and (c) buckling analysis.

4. Conclusions

Finite element solution of nanobeams is investigated based on modified couple stress theory within the Euler-Bernoulli beam theory. The finite element formulations are derived for static, free vibration, and buckling problems of nanobeams. The effect of the material length scale parameter and geometry parameters on the static, vibration, and buckling responses of the nanobeam is presented and discussed in the numerical study. Also, the difference between the classical beam theory and modified couple stress theory is investigated.

It is observed from the investigations that the material length scale parameter and dimension of the nanobeam have a big influence on the static, free vibration, and buckling behaviors of nanobeams. With the increase in the thickness of the nanobeam (h) and decrease in the dimensionless material length scale parameter (l/h), the difference between the classical beam theory and modified couple stress theory decrease considerably. It is observed from the results that modified couple stress theory must be used instead of the classical beam theory for small values of nanobeam height and high values of the material length scale parameter.

Author details

Şeref Doğuşcan Akbaş

Address all correspondence to: serefda@yahoo.com

Department of Civil Engineering, Bursa Technical University, Bursa, Turkey

References

- [1] Zook J.D., Burns D.W., Guckel H., Smegowsky J.J., Englestad R.L. and Feng Z. Characteristics of polysilicon resonant microbeams. *Sensors and Actuators*. 1992;**35**:31–59.
- [2] Pei J., Tian F. and Thundat T. Glucose biosensor based on the microcantilever. *Analytical Chemistry*. 2004;**76**:292–297.
- [3] Senturia S.D. CAD challenges for microsensors, microactuators, and microsystems. *Proceeding of IEEE*. 1998;**86**:1611–1626.
- [4] Rezazadeh G., Tahmasebi A. and Zubtsov M. Application of piezoelectric layers in electrostatic MEM actuators: controlling of pull-in voltage. *Journal of Microsystem Technologies*. 2006;**12**:1163–1170.
- [5] Eringen A.C. Nonlocal polar elastic continua. *International Journal Engineering and Science*. 1972;**10**(1):1–16.
- [6] Toupin R.A. Elastic materials with couple stresses. *Archive for Rational Mechanics and Analysis*. 1962;**11**:385–414.
- [7] Mindlin R.D. and Tiersten H.F. Effects of couple-stresses in linear elasticity. *Archive for Rational Mechanics and Analysis*. 1962;**11**:415–448.
- [8] Mindlin R.D. Influence of couple-stresses on stress concentrations. *Experimental Mechanics*. 1963;**3**:1–7.
- [9] Fleck H.A. and Hutchinson J.W. A phenomenological theory for strain gradient effects in plasticity. *Journal of Mechanics and Physics of Solids*. 1993;**41**:1825–57.
- [10] Yang F., Chong A., Lam D. and Tong P. Couple stress based strain gradient theory for elasticity. *International Journal of Solids and Structures*. 2002;**39**(10):2731–2743.
- [11] Lam D.C.C., Yang F., Chong A.C.M., Wang J. and Tong P. Experiments and theory in strain gradient elasticity. *Journal of Mechanics and Physics of Solids*. 2003;**51**(8):1477–508.
- [12] Park S.K. and Gao X.L. Bernoulli–Euler beam model based on a modified couple stress theory. *Journal of Micromechanics and Microengineering*. 2006;**16**:2355–2359.

- [13] Ma H.M., Gao X.L. and Reddy J.N. A microstructure-dependent Timoshenko beam model based on a modified couple stress theory. *Journal of Mechanics and Physics of Solids*. 2008;**56**:3379–3391.
- [14] Kong S.L., Zhou S., Nie Z. and Wang K. The size-dependent natural frequency of Bernoulli–Euler micro-beams. *International Journal of Engineering Science*. 2008;**46**:427–437.
- [15] Wang C.M., Xiang Y. and Kitipornchai S. Postbuckling of nano rods/tubes based on nonlocal beam theory. *International Journal of Applied Mechanics*. 2009;**1**(2):259–266.
- [16] Asghari M., Ahmadian M.T., Kahrobaiyan M.H. and Rahaeifard M. On the size dependent behavior of functionally graded micro-beams. *Materials Design*. 2010;**31**:2324–3249.
- [17] Wang L. Size-dependent vibration characteristics of fluid-conveying microtubes. *Journal of Fluids and Structure*. 2010;**26**:675–684.
- [18] Simsek M. Dynamic analysis of an embedded microbeam carrying a moving microparticle based on the modified couple stress theory. *International Journal of Engineering Science*. 2010;**48**:1721–1732.
- [19] Kahrobaiyan M.H., Asghari M., Rahaeifard M. and Ahmadian M.T. Investigation of the size dependent dynamic characteristics of atomic force microscope microcantilevers based on the modified couple stress theory. *International Journal of Engineering Science*. 2010;**48**:1985–1994.
- [20] Xia W., Wang L. and Yin L. Nonlinear non-classical microscale beams: static, bending, postbuckling and free vibration. *International Journal of Engineering Science*. 2010;**48**:2044–2053.
- [21] Ke L.L., Wang Y.S. and Wang Z.D. Thermal effect on free vibration and buckling of size-dependent microbeams. *Physica E: Low-Dimensional Systems and Nanostructures*. 2011;**43**(7):1387–1393.
- [22] Li, C., Lim C.W., Yu J.L. and Zeng Q.C. Analytical solutions for vibration of simply supported nonlocal nanobeams with an axial force. *International Journal of Structural Stability and Dynamics*. 2011;**11**:257–271.
- [23] Akgöz B. and Civalek Ö. Analysis of microtubules based on strain gradient elasticity and modified couple stress theories. *Advances in Vibration Engineering*. 2012;**11**(4):385–400.
- [24] Akgöz B. and Civalek Ö. Longitudinal vibration analysis for microbars based on strain gradient elasticity theory. *Journal of Vibration and Control*. 2012;**20**(4):606–616.
- [25] Ansari R., Gholami R. and Darabi M.A. A nonlinear Timoshenko beam formulation based on strain gradient theory. *Journal of Mechanics of Materials and Structures*. 2012;**7**(2):95–211.

- [26] Dos Santos J.A. and Reddy J.N. Free vibration and buckling analysis of beams with a modified couple-stress theory. *International Journal of Applied Mechanics*. 2012;**4**(3):1250026.
- [27] Simsek M., Kocatürk T. and Akbas S.D. Static bending of a functionally graded micro-scale Timoshenko beam based on the modified couple stress theory. *Composite Structures*. 2013;**95**:740–747.
- [28] Wang L., Xu Y.Y. and Ni Q. Size-dependent vibration analysis of three-dimensional cylindrical microbeams based on modified couple stress theory: a unified treatment. *International Journal of Engineering Science*. 2013;**68**:1–10.
- [29] Kocatürk T. and Akbas S.D. Wave propagation in a microbeam based on the modified couple stress theory. *Structural Engineering and Mechanics*. 2013;**46**:417–431.
- [30] Kong S.L. Size effect on natural frequency of cantilever micro-beams based on a modified couple stress theory. *Advanced Materials Research*. 2013;**694**:221–224.
- [31] Daneshmehr A.R., Abadi M.M. and Rajabpoor A. Thermal effect on static bending, vibration and buckling of reddy beam based on modified couple stress theory. *Applied Mechanics and Materials*. 2013;**332**:331–338.
- [32] Akgöz B. and Civalek Ö. Buckling analysis of linearly tapered micro-Columns based on strain gradient elasticity. *Structural Engineering and Mechanics*. 2013;**48**(2):195–205.
- [33] Ziaee S. Buckling of defective carbon nanotubes under axial and transverse loads. *International Journal of Applied Mechanics*. 2014;**6**(1):1450004.
- [34] Islam Z.M., Jia P. and Lim C.W. Torsional wave propagation and vibration of circular nanostructures based on nonlocal elasticity theory. *International Journal of Applied Mechanics*. 2014;**6**(2):1450011.
- [35] Miandoab E.M., Pishkenari H.N. and Yousefi-Koma A. Dynamic analysis of electrostatically actuated nanobeam based on strain gradient theory. *International Journal of Structural Stability and Dynamics*. 2015;**15**(4):1450059.
- [36] Liu C., Ke L., Yang Y., Yang J., and Kitipornchai S. Buckling and post-buckling of size-dependent piezoelectric timoshenko nanobeams subject to thermo-electro-mechanical loadings. *International Journal of Structural Stability and Dynamics*. 2013;**14**(4):1–22.
- [37] Tang M., Ni Q., Wang L., Luo Y. and Wang Y. Size-dependent vibration analysis of a microbeam in flow based on modified couple stress theory. *International Journal of Engineering Science*. 2014;**85**:20–30.
- [38] Hosseini S.A.H. and Rahmani O. Surface effects on buckling of double nanobeam system based on nonlocal Timoshenko model. *International Journal of Structural Stability and Dynamics*. 2016;**16**:1550077.
- [39] Akbas S.D. Analytical solutions for static bending of edge cracked micro beams. *Structural Engineering and Mechanics*. 2016;**59**(3):579–599.

- [40] Akbas S.D. Forced vibration analysis of viscoelastic nanobeams embedded in an elastic medium. *Smart Structures and Systems*. 2016;**18**(6):1125–1143.
- [41] Alashti R. A. and Abolghasemi A.H. A size-dependent Bernoulli-Euler beam formulation based on a new model of couple stress theory. *International Journal of Engineering-Transactions C: Aspects*. 2013; **27**(6):951–960.

Green Synthesis of Metallic and Carbon Nanostructures

R. Britto Hurtado, G. Calderon-Ayala,
M. Cortez-Valadez, L.P. Ramírez-Rodríguez and
M. Flores-Acosta

Additional information is available at the end of the chapter

<http://dx.doi.org/10.5772/intechopen.68483>

Abstract

The technological and biomedical applications of low toxicity and eco-friendly organic compounds are nowadays increasingly attracting the attention of researchers in nanoscience, who are aiming for more biocompatible and nanostructured systems for their application in antineoplastic therapies. This study presents the significance of “green components” in the production of graphene, metallic, and semiconductor nanoparticles, due to their antioxidant and antitumor properties. The formation of nanostructures is caused during green synthesis methods by organic molecules or carboxylic acid groups present in some plant extracts; for this reason, we include here a recapitulation and analysis of the role of carboxylic acids in those systems (organic). Furthermore, we propose the use of the extract from *Opuntia ficus-indica* cladodes to obtain metallic and carbon nanostructures, as an alternative biosynthesis method for the development of future nanobiotechnological applications.

Keywords: green synthesis, nanoparticles synthesis, carbon nanostructures, carboxylic acid

1. Introduction

Several nanoparticle synthesis methods are applied nowadays in different scientific fields; furthermore, based on the type of process (physical, chemical, or biological) and the conditions the synthesis is undertaken, they allow a control of the shape of the material, thus managing their application more accurately [1, 2]. With the objective of adopting eco-friendly methods that help to reduce the pollution caused by some toxic compounds and to exploit the local natural resources, the biosynthesis of nanostructured materials (green methods)

has been undertaken through antioxidant microorganisms and agents obtained from local plant extracts [3–5]. Thus, the use of green synthesis in nanotechnology is fundamental in scientific research in nanoscience, mainly, in order to find medical applications of the nanostructures that reduce toxicity risks while being biocompatible [6–8]. There is evidence of nanoparticles obtained through size-tunable biosynthesis [9, 10] and different technological and biocompatible applications. For instance, Ag nanoparticles show antibacterial and anti-tumor properties and have potential use in antineoplastic treatments [11–14]; furthermore, they are applicable in SERS (surface-enhanced Raman spectroscopy) [15]. Gold nanoparticles between 20 and 25 nm present catalytic activity [16], and ZnO nanoparticles with a range between 9.6 and 25.5 nm present antibacterial and photocatalytic applications [17]. Pooja et al. synthesized biocompatible gold nanoparticles using karaya gum, which can be used in the elaboration of antineoplastic medications [18]. Biocompatible silver nanoparticles were obtained from the extract of *Rosa damascen* petals, which have anticarcinogenic properties against pulmonary adenocarcinoma [19]. Patra et al. synthesized gold and silver nanoparticles with *Butea monosperma* leaves; this nanoparticle system inhibits the growth of cancer cells, and these authors consider that the synthesis of these nanoparticles is important in biomedicine for the development of cancer treatments [20]. The biosynthesis of nanostructured systems thus appears to be a valuable tool for nano-biotechnological applications in nanoscience around the world.

Similarly, the green synthesis is used in the graphene and bimetallic nanoalloys obtained. Coconut water and pomegranate juice were reported as reducing and capping agents of graphite oxide (OG) to obtain graphene [21, 22]. Other authors have obtained Au-Ag bimetallic nanoparticles with pomegranate juice [23] and extract from leaf of mahogany [24], as well as the bioreduction synthesis in bimetallic nanostructure-type core/shell of Ti/Ni between 1 and 4 nm employing *Medicago sativa* [25]. Shen and collaborators used plant extract of *Anacardium occidentale* for the formation of bimetallic nanoparticles of Au-Ag, considering that polyols play an important role in the reduction of metal ions [26].

Table 1 lists a variety of plants that have been recently used for the synthesis of metallic, bimetallic, and semiconductor nanoparticles.

Nanoparticle	Plant extract	Size	Reference
Ag	<i>Atrocarpus altilis</i>	34 nm; 38 nm	[27]
	<i>Artocarpus heterophyllus</i> Lam.	10.78 nm	[28]
	<i>Vigna sp. L</i>	24.35 nm	[29]
	<i>Hydrangea paniculata</i>	36–75 nm	[30]
	<i>Andrographis paniculata</i>	13–27 nm	[31]
	<i>Ficus religiosa</i>	5–35 nm	[32]
	<i>Alternanthera sessilis</i> Linn	20–30 nm	[33]
	<i>Lycium barbarum</i>	3–15 nm	[34]
	<i>Osmanthus fragrans</i>	2–30 nm	[35]
	<i>Sambucus nigra</i>	26 nm	[36]

Nanoparticle	Plant extract	Size	Reference
Au	<i>Citrus limon</i>	32.2 nm	[37]
	<i>Morinda citrifolia</i>	12.1–38.2 nm	[38]
	<i>Terminalia arjuna</i>	20–50 nm	[39]
	<i>Zingiber officinale</i>	5–15 nm	[40]
	<i>Dillenia indica</i>	5–50 nm	[41]
	<i>Plumeria alba flower</i>	15.6 ± 3.4 nm	[42]
	<i>Citrus maxima</i>	25.7 ± 10 nm	[43]
	<i>Gloriosa superba</i>	20 nm	[44]
	<i>Cinnamomum zeylanicum</i>	25 nm	[45]
	<i>Cassia auriculata</i>	15–25 nm	[46]
Cu	<i>Ginkgo biloba</i>	15–20 nm	[47]
	<i>Tamarind and lemon juice</i>	20–50 nm	[48]
Pt	<i>Azadirachta indica</i>	5–50 nm	[49]
Pd	<i>Chlorella vulgaris</i>	5–20 nm	[50]
	<i>Catharanthus roseus</i>	38 nm	[51]
Fe	<i>Citrus maxima</i>	10–100 nm	[52]
	<i>Eucalyptus</i>	20–80 nm	[53]
Ni	<i>Ocimum sanctum</i>	12–36 nm	[54]
Au-Ag	<i>Antigonon leptopus</i>	10–60 nm	[55]
	<i>Gloriosa superba</i>	10 nm	[44]
	<i>Guazuma ulmifolia</i>	10–25 nm	[56]
	<i>Ocimum basilicum</i>	3–25 nm	[57]
	<i>Commelina nudiflora</i>	20–80 nm	[58]
Au-Pd	<i>Cacumen platycladi</i>	~7 nm	[59]
CuO	<i>Calotropis gigantea</i>	20–30 nm	[60]
	<i>Carica papaya</i>	140 nm	[61]
	<i>Punica granatum</i>	10–100 nm	[62]
ZnO	<i>Solanum nigrum</i>	20–30 nm	[63]
	<i>Ocimum basilicum L.</i>	50 nm	[64]
	<i>Agathosma betulina</i>	15.8 nm	[65]
	<i>Aspalathus linearis</i>	4.08 nm	[66]
TiO ₂	<i>Jatropha curcas L.</i>	25–50 nm	[67]
	<i>Eclipta prostrata</i>	49.5 nm	[68]
	<i>Cicer arietinum L.</i>	14 nm	[69]
SnO ₂	<i>Aspalathus linearis</i>	2.1–19.3 nm	[70]
NiO	<i>Agathosma betulina</i>	15–55 nm	[71]

Table 1. Plant extracts used in the synthesis of metallic, bimetallic, and semiconductor nanoparticles.

2. The role of carboxylic acids in nanoparticles

Nano-biosynthesis is classified as a chemical method that promotes the growth of a system by the aggregation of the metallic atoms reduced from the atoms in precursor solutions. Literature reports show that certain organic compounds are responsible for oxidation-reduction (redox) reactions, which trigger the formation and stabilization of nanoparticles. For instance, in the cases of the biometallic alloys Au, Ag, and Au/Ag, it is observed that polyphenols and polyols that carry antioxidant properties present in plants have an important role in the formation of nanostructures [24, 72–74]. Quercetin (a flavonol with high antioxidant activity [75]) also appears in the reports as a main component in the formation of metallic nanostructures [76]. It is thus important to highlight the role that the antioxidant activity of the substances used in biosynthesis has on the fabrication of nanoparticles. Similarly, literature reports that carboxylic acids are commonly used in biological methods as reducing and sometimes stabilizing agents in the production and application of these materials. Yoosaf et al. show that it is possible to stabilize nanoparticles through electrostatic interactions with carboxylic groups (using gallic acid), which adhere to the surface of the nanoparticles [77]. This argument is supported by Amornkitbamrung et al. who attribute the reduction of $\text{Pd}^{+2} \rightarrow \text{Pd}^0$ to the functionality of the carboxylate ion (R-COO^-) [78]. On the other hand, Hosseini-M et al. address that carboxylic acids are crucial in the morphology, size, and distribution of Fe_3O_4 nanoparticles; furthermore, they present a co-catalyst effect [79]. Au nanoparticles were synthesized with dicarboxylic acids (oxalic, malonic, succinic, glutaric, and adipic) as reducing agents of HAuCl_4 , without the presence of any other surfactant agents, the synthesis resulted in different morphologies and SERS applications [80]. Similarly, other reports reiterate the importance of the carboxylic groups in the formation of nanoparticles [81, 82]. On nonmetals, Dwivedi et al. obtained selenium nanoparticles of 40–100 nm using carboxylic acids (acetic, oxalic, and gallic acids) for the synthesis method [83]. Propionic acid is used as a stabilizing agent in the fabrication of ZnO quantum dots (3.6–5.2 nm) [84]; similarly, carboxylic acids were used in manganese oxide nanoparticles, which work as catalysts in the conversion of CO to CO_2 [85]; additionally, pimelic dicarboxylic acid is used as a nucleating agent for the synthesis of TiO_2 nanoparticles [86]. Thus, the carboxylic acid groups stick to nanoparticles transferring stability (**Figure 1**), as reported by Zhi-Mei Qi et al. who synthesized gold nanoparticles through infrared (IR) spectroscopy [81].

Carboxylic acids are the most common type of organic acids in the carboxylic group (made by the fusion of one hydroxyl and carboxyl group) at the extreme end of the carbon chain. Under certain conditions, proton donors transfer H^+ hydrons through heterolysis. The general formula of the carboxylic acid group is R-COOH , where R is a monovalent functional group (one hydrogen or carbon chain), when the carbon structure is replaced by two functional carboxylic groups, the acid is dicarboxylic acid (HOOC-R-COOH). When the proton H^+ is transferred to the remaining ion, the formula changes into R-COO^- carboxylate [87]. These acids are used in the food and pharmaceutical industries and in the manufacture of detergent and surfactant agents, among other applications [88]. Recent reports have demonstrated that when COOH groups are applied to certain biological complexes, they present excellent antitumor and antioxidant activity [89]; furthermore, other reports indicate that the carboxylic acids in *Rhinacanthus nasutus* show antiviral activity [90].

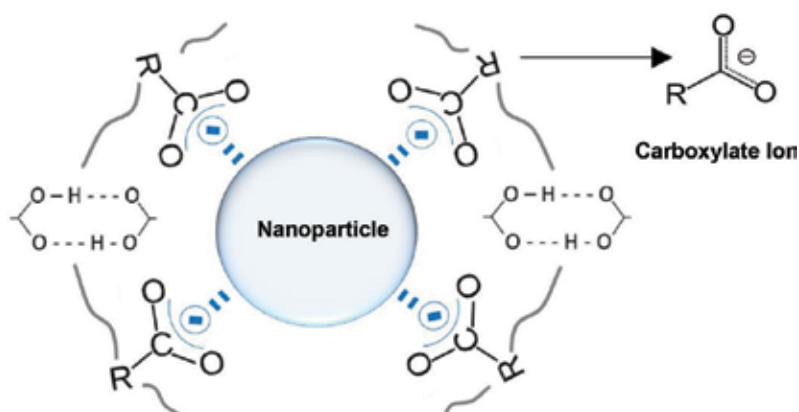
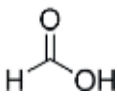
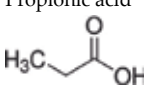
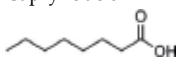
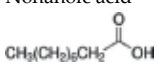
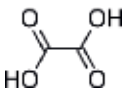


Figure 1. Representation of the electrostatic interaction of the carboxylic acid group on the nanoparticles.

The use of these compounds in the synthesis processes of metallic and nonmetallic nanoparticles is increasing due to the biocompatible and antioxidant properties of carboxylic acids.

Table 2 shows scientific reports on carboxylic acids used in biosynthesis for the production of nanomaterials; the table focuses on the different applications of the acids. In regard to the reduction-oxidation process of metallic ions, Zoya Zaheer and Rafiuddin [91] propose a reduction

Carboxylic acid	NPs	Size (nm)	Function report. used as:	Reference
Formic acid 	Ag Pd	13–25 4.1–5.7	Formic acid—used as a solvent and reducing agent of Ag precursor. Formic acid as a reducing agent in the presence of polyvinylpyrrolidone (PVP) for the synthesis of size-tunable Pd NCs.	[92] [93]
Propionic acid 	Au	12–41	Functionalization of gold nanoparticles synthesized on reaction of propionic acid with aqueous HAuCl ₄ .	[94]
Caprylic acid 	Au	5–15	Gold NPs—synthesized by reduction technique-based redox-active amphiphiles (e.g., caproic acid, caprylic acid, and capric acid).	[95]
Nonanoic acid 	Ag	7.6	Silver nanoparticles—stabilized in nonanoic acid. Capping agent.	[96]
Oxalic acid 	Ag	3.5–9	Colloidal silver nanoparticles were prepared with oxalic acid in the presence of CTAB.	[97]

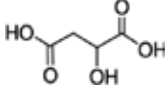
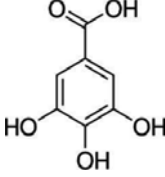
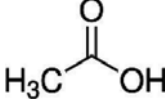
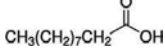

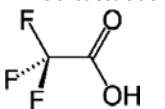
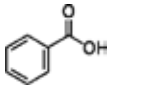
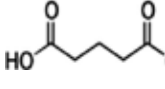
Carboxylic acid	NPs	Size (nm)	Function report. used as:	Reference
Malic acid 	Ag	~10	Citric acid present in <i>S. lycopersicums</i> fruit extract is used as reducing agent and malic acid is used as capping agent of the bio-reduced silver nanoparticles.	[98]
Gallic acid 	Au@Pt	~50 nm	Gallic acid (GA) as both a reducing and a protecting agent.	[99]
Acetic acid 	CuS CuInSe ₂	5 400	CuS nanoparticles using carboxylic acid (acetic, propionic) as a solvent have been developed. The CuInSe ₂ nanoparticles for thin-film solar cells were synthesized using acetic acid as a mineralizer.	[100] [101]
Decanoic acid 	ZnO	100	Zinc oxide (ZnO) nanoparticles were examined using surface modifiers (oleic acid and decanoic acid) in supercritical methanol.	[102]
Lauric acid 	Fe ₃ O ₄ Ag	9.4 ± 2.3 8	The nanostructured material was coated with lauric acid. Capping agents.	[103] [104]
Trifluoroacetic acid 	TiO ₂	5	Trifluoroacetic acid—used as an electron scavenger and a morphological control agent.	[105]
Benzoic acid 	ZnO	5–50	ZnO precursors—obtained by the intimate mixing of zinc acetate dihydrate and carboxylic acids as capping agents.	[106]
Glutaric acid 	Ag NiO-Ni	30–50 22–41	The morphologies of silver nanoparticles are impacted by glutaric acid. Nanocomposite has been fabricated via the thermal decomposition of nickel salts by using glutaric acid as a spacer agent.	[107] [108]

Table 2. Influence of some carboxylic and dicarboxylic acids on the synthesis of nanoparticles.

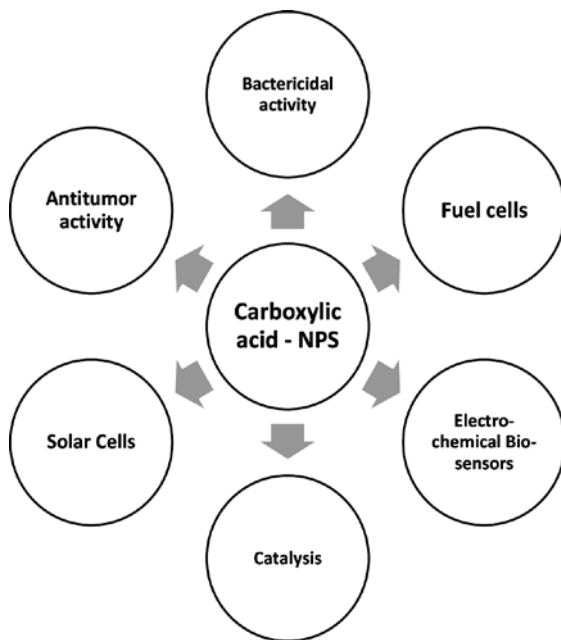
mechanism of Ag⁺ by oxalic acid (HOOC-COO⁻) with CTAB as the stabilizing agent; the reduction mechanism takes place in an aqueous solution with a pH control of pK = 1.2 and pK₂ = 4.2.

Since the organic compounds of carboxylic acids can be found in nature (for instance, in plants such as fungi) and they are not harmful for human consumption or the environment,

they are used in the food and pharmaceutical industries. Studies on the synthesis of metallic and semiconductor nanoparticles are beginning to be used in these fields in order to improve processes that are beneficial to the environment and human beings. It is important to mention that some carboxylic acids functionalized with nanoparticles are also used in technological applications (**Scheme 1**).

A recent study shows a simpler unsaturated carboxylic acid (acrylic acid) that works with silver nanoparticles in the process of membrane filtration that avoids nanoparticles to adhere to the surface of the modified membranes, which at the same time show antibacterial/bacteriostatic properties [109]. The main reaction of acrylic acid is polymerization; thus, it is commonly used in the production of plastics, paints, and adhesives. Due to these characteristics, Ag nanoparticles modified with polyacrylic acid was produced by the redox method showing excellent water solubility, stability, and biocompatibility, as well as antibacterial properties against *Escherichia coli*, *Staphylococcus aureus*, and *Pseudomonas aeruginosa* [110]. Nanoparticles and formic acid have a similar role, since the electrochemical oxidation process of formic acid is an efficient energy supplier in direct formic acid fuel cells (DFAFCs) for mobile and portable applications [111–113]. The biodegradability and low cost of formic acid makes it a valuable resource in energy storage, in spite of its toxicity [114–117]. Thus, metallic and bimetallic nanoparticles Pt [118], Pt-Cu [119], Pt-Au [120, 121], Pd-Ag [122], and so on are used as catalysts in the electro-oxidation of formic acid.

Reports also show oxalic acid functionalized with biocompatible magnetite nanobars (oxalic acid-Fe₃O₄) prepared through the co-precipitation method for applications in electrochemical



Scheme 1. Some nanobiotechnological applications of carboxylic acids functionalized with nanoparticles.

biosensors [123]. Additionally, oxalic acid and malic acid play an important role in the synthesis of tungstate nanoplates and nanoflowers (hydrated tungsten oxide: $\text{WO}_3 \cdot \text{H}_2\text{O}$) which show photocatalytic properties [124, 125]. Sedira et al. show that Ag nanoparticles oxidize easily in aqueous solutions, which in combination with acetic acid cause the liberation of Ag^+ and improve the bactericidal effect in a higher range than with zinc oxide quantum dots [126]. Similarly, benzoic acid in the surface of TiO_2 nanorods increases the power conversion efficiency of dye-sensitized solar cells (DSSCs), becoming at the same time an alternative and efficient method for the production of electrodes based on TiO_2 nanorods [127]. It has been shown recently that the synthesis of Se nanoparticles induced by carboxylic acids (acetic acid, pyruvic acid, and benzoic acid) has antitumor properties with good potential in the treatment of Dalton's lymphoma (DLA) cancer cells [128]. On the other hand, caffeic acid (containing the functional groups phenolic and acrylic) is used as a reducing and stabilizing agent in the preparation of silver nanoparticles, which show antitumor properties and works as an alternative agent in human hepatoma therapies [129]. Reports show that green synthesis of gold nanoparticles obtained with chlorogenic acid presents anti-inflammatory properties; additionally, it has promising applications in nanomedicine [130]. Maleic acid (dicarboxylic) functionalized with gold nanoparticles is used in the colorimetric detection of high efficiency of lead [131]; correspondingly, copper nanoparticles functionalized with carboxylic acid act as catalysts, when reducing 2-nitrophenol to 2-aminophenol in a few minutes [132]. Hence, it can be concluded that the different applications of metallic and nonmetallic nanoparticles in combination with organic agents such as carboxylic groups are of great importance in future medical applications for the development of antineoplastic therapies.

3. Biosynthesis of nanoparticles with *Opuntia ficus-indica*

The cladodes from *O. ficus-indica* are characterized by their antioxidant properties, vitamin content, and by the presence of flavonoids and gallic acids [133–137], in addition to their content of uronic acid, a type of sugar acid with carbonyl and carboxylic functional groups [138]. In recent studies, gallic acid is used as a reducing and stabilizing agent in the mass production of silver nanoparticles with antioxidant properties and low cytotoxicity for normal cells [139, 140]. Similarly, biocompatible gold nanoparticles are synthesized at environment temperature through the reduction of HAuCl_4 with gallic acid and poly-(N-vinyl-2-pyrrolidone) (PVP) [141]. Thus, carboxylic organic agents (gallic and uronic acids) in the cladode extract are responsible for the reduction and stabilization of the nanoparticles (**Figure 2**).

O. ficus-indica is well known for its anti-diarrheal, anti-inflammatory, antiviral, and anticarcinogen properties [142, 143], as well as for being used in treatments for diabetes and indigestion. The plant is commonly used as a nutritional complement, and its fruits and cladodes can be consumed in salads [144–146]. In general, this plant contains vitamins, minerals, and sugars, indispensable for human health. A recent study by E. Ramirez M et al. reports that *O. ficus-indica* cladodes improve the physicochemical properties of corn tortillas [147]; additionally, it increases the antioxidant activity in the blood and plasma of humans [148]. Furthermore, the extract has better anti-inflammatory potential than the drug indometacin [149]. Similarly, metallic and nonmetallic nanoparticles obtained with ecological methods are pioneering in the same fields as the extract *O. ficus-indica* (**Scheme 2**).

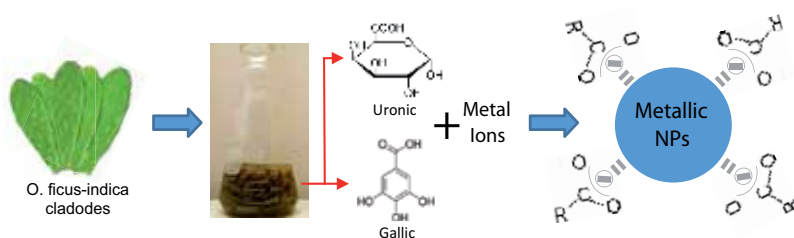
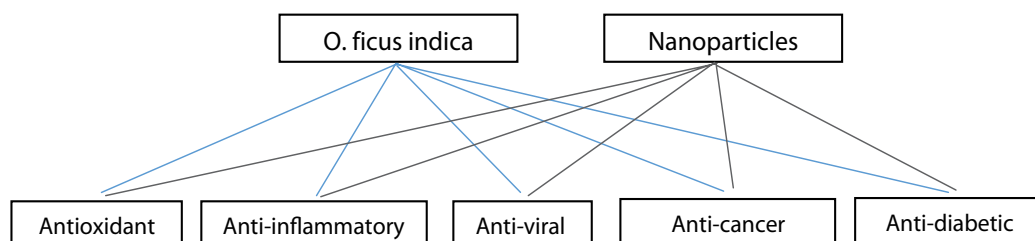


Figure 2. Carboxylic acids in *O. ficus-indica* play an important role in the formation of nanoparticles.



Scheme 2. Nanoparticles and cladodes from *O. ficus-indica* have similar range of technological applications.

For instance, silver nanoparticles obtained from the extracts of *R. indica* and *European black elderberry* show anti-inflammatory properties [150, 151]. Gold nanoparticles from *Inonotus obliquus* show antioxidant activity [152]. Synthesized ZnO nanoparticles from the root of *Polygala tenuifolia* show antioxidant and anti-inflammatory activity [153]. In the same way, Au and Ag nanoparticles obtained by biosynthesis are powerful nanomaterials in the control of diabetes [154–156]. Thus far, literature only reports in vitro studies with antibacterial activity using *O. ficus-indica* extract, applied in the biofabrication of silver nanoparticles, considering the synergic affects against *E. coli* and *S. aureus* [133]. As a consequence, the organic agents such as carboxylic acids, in the cladode extract of *O. ficus-indica*, and the nanoparticles obtained through eco-friendly methods, can improve the nanobiotechnological applications; furthermore, they secure innovative developments of the several application fields and the modern technology. It is still necessary to develop studies in order to validate the hypotheses presented in this study, concerning the nanoparticles obtained from the extracts from the cladodes.

4. Experimental section

4.1. Metallic nanoparticles

In this study, we synthesized metallic nanoparticles Ag, Au, Cd, Cu, Pb, and Ti with cladodes from *O. ficus-indica* in a colloidal medium. The synthesis presented excellent stability during long periods of time. The following were used as precursors during the synthesis processes: Nitrates AgNO_3 ; $\text{Cu}(\text{NO}_3)_2$; $\text{Pb}(\text{NO}_3)_2$; $\text{Cd}(\text{NO}_3)_2$; Chlorides: HAuCl_4 . Small fragments of metal underwent a thermal treatment in nitric acid for the synthesis of Ti nanoparticles (**Figure 2**).

The method used in this study was made in collaboration with other authors [157]: 25 g of the cladode was mixed in 50 ml of deionized water; subsequently, the solution underwent thermal treatment at a constant temperature of 60°C, and magnetic agitation for 1 h. The resulting solution is then filtered obtaining the *O. ficus-indica* extract. Three milliliters of the extract is mixed with 25 ml of the precursor solutions (nitrate and chlorides) for the reduction of the metallic ions. The solution undergoes the same thermal treatment and magnetic agitation described above. The nanoparticles are formed and stabilized during these processes.

4.2. Carbon nanostructures

The organic molecules containing the *O. ficus-indica* extract may have hydrophilic properties. This represents of the extract of the plant a strong candidate for the obtaining of laminar materials of carbon and small quantum dots both in colloidal means.

To obtain a few graphene sheets from commercial graphite, 5 ml of the extract of *O. ficus-indica* was used as mentioned in the previous section. Subsequently, 2 g of commercial graphite was added to 50 ml of deionized water and mixed with 5-ml extract of *O. ficus-indica*. The mixture was kept in an ultrasonic bath for 30 min. Finally, floating material was collected on the liquid surface with a slightly bright hue, to be analyzed by transmission electron microscopy (TEM), Raman, and X-ray photoelectron spectroscopy (XPS). To obtain carbon quantum dots (CQDs), a mixture with the same components was maintained under magnetic stirring and at 50°C for 30 min and then subjected to an ultrasonic bath for 30 min. In the first minutes of subjecting the sample in the ultrasonic bath, a tone change in the surface of the liquid is observed. In the same way, floating material was collected on the surface of the liquid, finding small CQD.

5. Results and discussions

Nanoparticles of the precursors mentioned in the experimental section were obtained and characterized by transmission electron microscopy. In the case of the silver nanoparticles, these mainly presented particle sizes that oscillate between 2 and 4 nm, and few cases are observed with sizes between 10 and 15 nm (**Figure 3a**). In both cases, morphologies of spherical type are observed. For the case of the precursor HAuCl_4 after performing the synthesis process mentioned in the experimental section, gold nanoparticles with different morphologies such as triangular, pentagonal, hexagonal, and quasi-spherical were obtained. The mentioned macroscopic parameters allowed a diversity of morphologies for this precursor as seen in **Figure 3b**. In the case of cadmium nanoparticles (**Figure 3c**), an irregular shape with sizes located between 2 and 8 nm approximately was obtained.

In some cases, the organic molecules contained in the plant extract are manifested by interacting with the surface of the nanoparticle, possibly as a consequence of molecular affinity. As is the case with copper nanoparticles (**Figure 3d**), in these, a region between 2 and 3 nm in thickness is observed that surrounds a nanoparticle with a diameter of approximately 10 nm. Another similar case was presented when synthesizing titanium nanoparticles; in the TEM image (**Figure 3f**), we observed clusters of nanoparticles were stabilized by an organic

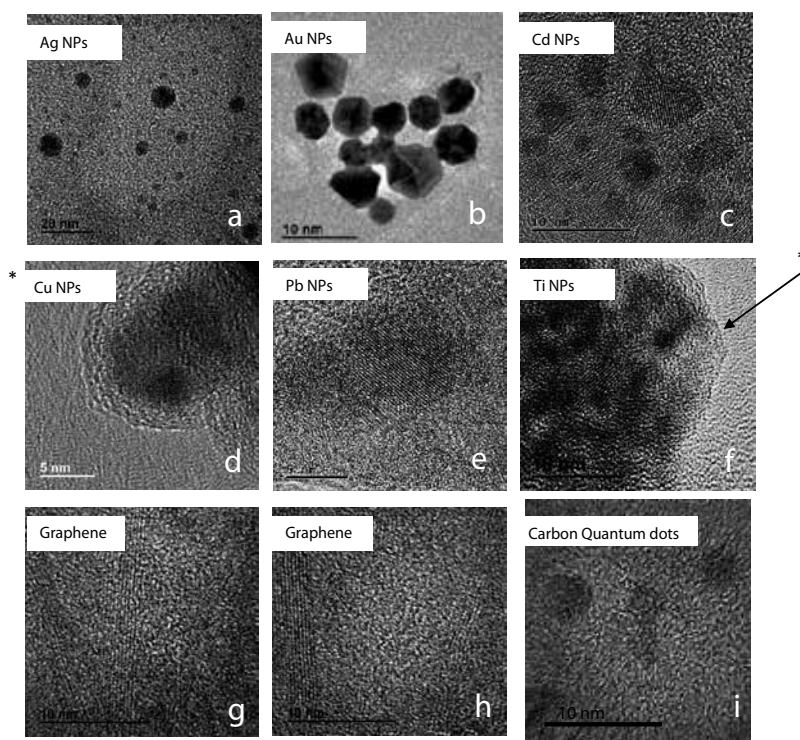


Figure 3. TEM images of metallic nanoparticles and carbon nanostructures synthesized with cladode extract from *O. ficus-indica*. a) Ag Nps, b) Au Nps, c) Cd Nps, d) Cu Nps, e) Pn Nps, f) Ti Nps, g) Graphene, h) Graphene, i) Carbon Quantum dots.

medium. The nanoparticles of titanium have sizes located at approximately 5 nm; we assume that this stabilizing medium may contain ascorbic acid, starches, proteins, and various vitamins naturally contained in the extract of the plant *O. ficus-indica*.

On the other hand, when using $PbNO_3$ as a precursor of lead nanoparticles by the synthesis method presented, nanoparticles below 10 nm were obtained with well-defined crystalline phase as seen in **Figure 3e**. For the case of the synthesized metallic nanoparticles, we observed that the extract of *O. ficus-indica* facilitates the obtaining for a size smaller than 10 nm. This has several advantages for analyzing biomedical applications such as drug delivery, therapeutic applications, bioimaging, and magnetic energy storage [158–160].

For the laminar carbon nanostructures obtained by green synthesis methods, there are currently published results that start from graphite oxide as a precursor [161, 162]. In the present investigation, we use commercial graphite as a precursor, further reducing the costs of synthesis for the nanostructured laminar final product. **Figure 3g** and **h** show graphene layers made up of less than 10 layers. These were obtained by the simple ultrasonic sonication method shown in the experimental section. We assume that the method presented can be made repeatedly until a smaller number of graphene sheets are obtained because the hydrophilic components in the extract of *O. ficus-indica* favor the exfoliation.

The use of green synthesis to obtain CQD is rarely documented. Few numbers of articles show evidence of the synthesis of CQD using plant extract [163, 164]. By combining the *O. ficus-indica* plant extract with a small amount of commercial graphite and maintaining the mixture at 60° C for 1 h, it was possible to collect the surface liquid from the solution for further analysis by TEM and to find CQD (**Figure 3i**). In the same way as the metallic nanoparticles, the extract allowed to obtain CQD with a size smaller than 5 nm. This favors the applications of chemical sensors, photodetectors, and so on [165, 166].

6. Optical properties in metallic nanoparticles

As is well known, the metallic and semiconductor nanoparticles have new optical properties in relation to the bulk material. These properties can be detected by ultraviolet/visible spectroscopy (UV/Vis) and are associated with the existence of surface plasmon. Surface plasmon resonance (SPR) physically represents the oscillation of free electrons on the surface of the nanoparticles, constituting a characteristic fingerprint of each nanostructured material. The nanoparticles obtained using the extract of *O. ficus-indica* were analyzed experimentally by UV/Vis spectroscopy. All spectra were considered from 200 to 800 nm.

In the case of silver nanoparticles, these showed an absorption band centered on 390-nm characteristic of the SPR due to quantum confinement in silver, as seen in **Figure 4a**. The dependence of the location of the SPR is associated with the morphology of the nanostructures as well as the size. Silver nanostructures can be found in the literature with an SPR located at 408, 430, 440, and so on [167–169], associated with different sizes of silver nanoparticles.

The gold nanoparticles probably represent the most studied metal nanostructured in terms of behavior and shifts of SPR. The gold nanoparticles have absorption bands located at 500, 550, 800, and so on, for nanoparticles with different morphologies. This indicates the dependence and sensitivity of the location of the SPR with the morphology of the gold nanostructures [170–172]. The gold nanoparticles obtained in this work show a large amplitude absorption band associated with the presence of the SPR centered at 55 nm. We assume that this band implicitly considers the contribution of several SPRs associated with the different morphologies obtained, as shown in **Figure 4b**. This can be seen in the large amplitude of the absorption band, with a range from 500 to 670 nm. For cadmium nanoparticles, an absorption band centered at 232 nm is shown in **Figure 4c**. For lead, there are reports of nanocubes with absorption bands located at approximately 320 and 400 nm [173]. A band detected at 300 nm was associated with SPR due to the confinement in these lead nanoparticles (**Figure 4e**).

The obtained copper nanoparticles had a well-defined absorption band centered at 580 nm approximately as shown in **Figure 4d**. The synthesis of copper nanoparticles it faces to copper oxidation easily in a colloidal medium, the extract of *O. ficus-indica* facilitates the stabilization of these nanoparticles. Prabsash et al. obtained nanoparticles of copper with a size of 10 nm, using chemical reduction by the reducing agent sodium borohydride [174].

On the other hand, titanium (metal) nanoparticles are difficult to find in the literature. There are reports from Mohammadi and Halali who used the electromagnetic levitation melting gas

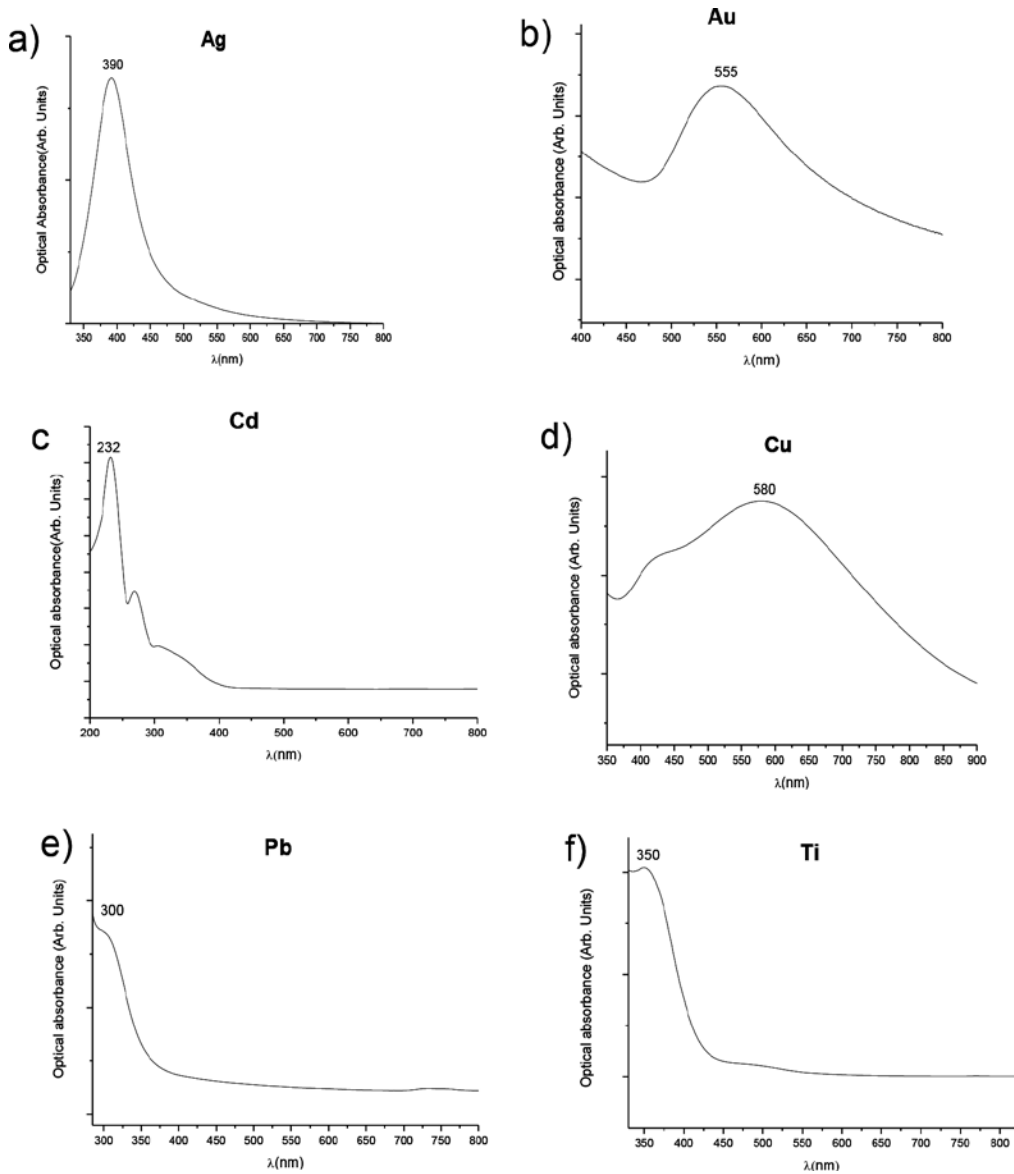


Figure 4. Optical absorbance of metallic nanoparticles synthesized by *O. ficus-indica* extract.

method to evaporate titanium particles [175]; the nanoparticles obtained by them have sizes between 28 and 40 nm. Although the method presented is effective, it represents a requirement of special equipment to carry out the synthesis of titanium nanoparticles. The titanium nanoparticles obtained in the present work were based on the modified method presented by R. Britto et al. [176], varying slightly the amount of extract of the plant *O. ficus-indica*. The absorption band obtained for titanium nanoparticles (**Figure 4f**) was located at 350 nm, associated with the SPR of this metal.

7. Conclusions

In conclusion, the current importance of organic agents functionalized with nanoparticles in the nanotechnological and biomedical fields has been exposed in this study. The properties of carboxylic acids make the fabrication of biocompatible nanostructured systems attractive for future attention. The biosynthesis process used in the fabrication of graphene layers and nanoparticles initiates an ecological and low-cost alternative in biocompatible applications for the treatment of diseases, mainly for antineoplastic therapies. The cladode extract from *O. ficus-indica* is highly efficient in the formation of nanoparticles, which can play an important role in the biocompatibility for the benefit of health and nutrition. Metallic and nonmetallic nanoparticles with nanobiotechnological applications synthesized with ecological methods (carboxylic groups) will be a fundamental tool for biocompatible applications in nanoscience and nanotechnology.

Author details

Ricardo Britto Hurtado¹, Gerardo Calderon-Ayala¹, Manuel Cortez-Valadez^{2*}, Luis Patricio Ramírez-Rodríguez³ and Mario Flores-Acosta¹

*Address all correspondence to: manuelcortez@live.com

1 Departamento de Investigación en Física, Universidad de Sonora, Apdo, Hermosillo, Sonora, Mexico

2 CONACYT—Departamento de Investigación en Física, Universidad de Sonora, Apdo, Hermosillo, Sonora, Mexico

3 Departamento de Física, Universidad de Sonora, Apdo, Hermosillo, Sonora, Mexico

References

- [1] Sahayaraj K, Rajesh S, A. Méndez-Vilas. Bionanoparticles synthesis and antimicrobial applications. In: Science against Microbial Pathogens: Communicating Current Research and Technological Advances. Formatex Research Center. 2011. pp. 228-244
- [2] Kaushik NT, Snehit SM, Rasesh YP. Biological synthesis of metallic nanoparticles. *Nanomedicine: Nanotechnology, Biology and Medicine*. 2010;**6**(2):257-262
- [3] Prashant M, Nisha KR, Sudesh KY. Biosynthesis of nanoparticles: Technological concepts and future applications. *Journal of Nanoparticle Research*. 2008;**10**:507-517
- [4] Xiangqian L, Huizhong X, Chen Z-S, Chen G. Biosynthesis of nanoparticles by microorganisms and their applications. *Journal of Nanomaterials*. 2011;**2011**, Article ID 270974:16
- [5] Amit KM, Yusuf C, Uttam CB. Synthesis of metallic nanoparticles using plant extracts. *Biotechnology Advances*. March–April 2013;**31**(2):346-356

- [6] Cristina B-A, Le Duc T, Nguyen TKT. Synthesis of nanoparticles for biomedical applications. *Annual Reports on the Progress of Chemistry, Section A: Inorganic Chemistry*. 2010;**106**:553-568
- [7] Adam S, Gabriela K, Ivo Š, Mirka Š, Ivan R, Leslie MS. Applications of biosynthesized metallic nanoparticles – A review. *Acta Biomaterialia*. October 2014;**10**(10):4023-4042
- [8] Khabat V, Sedigheh KD. Chapter 29 – Biosynthesis of silver nano-particles by trichoderma and its medical applications. *Biotechnology and Biology of Trichoderma*. Elsevier B. V. 2014;**1**:393-404
- [9] Mingxia G, Wei L, Feng Y, Huihong L. Controllable biosynthesis of gold nanoparticles from a *Eucommia ulmoides* bark aqueous extract. *Spectrochimica Acta Part A: Molecular and Biomolecular Spectroscopy*. 5 May 2015;**142**:73-79
- [10] Salman K, Syed MDR, Mohd A, Mohd A, Pramdeep B, Mohd SK. A novel process for size controlled biosynthesis of gold nanoparticles using bromelain. *Materials Letters*. 15 November 2015;**159**:373-376
- [11] Amit KM, Debabrata T, Alka C, Pavan KA, Anupam C, Inder PS, Uttam CB. Bio-synthesis of silver nanoparticles using *Potentilla fulgens* Wall. ex Hook. and its therapeutic evaluation as anticancer and antimicrobial agent. *Materials Science and Engineering: C*. 1 August 2015;**53**:120-127
- [12] Arthanari S, Mani G, Jayabalan J, Hyun TJ. Biosynthesis of silver nanoparticles using *Cassia tora* leaf extract and its antioxidant and antibacterial activities. *Journal of Industrial and Engineering Chemistry*. 25 August 2015;**28**:277-281
- [13] Debasis N, Sonali P, Sarbani A, Pradipta RR, Bismita N. Biologically synthesised silver nanoparticles from three diverse family of plant extracts and their anticancer activity against epidermoid A431 carcinoma. *Journal of Colloid and Interface Science*. 1 November 2015;**457**:329-338
- [14] Ramachandran R, Krishnaraj C, Stacey LH, Yun S-II, Thangavel Kalaichelvan P. Plant extract synthesized silver nanoparticles: An ongoing source of novel biocompatible materials. *Industrial Crops and Products*. August 2015;**70**:356-373
- [15] Monica P, Manisha B, Timea S, Swapnil G, Emilia L, Avinash I, Manuela B, Adriana V, Simion A, Mahendra R. Biosynthesized silver nanoparticles performing as biogenic SERS-nanotags for investigation of C26 colon carcinoma cells. *Colloids and Surfaces B: Biointerfaces*. 1 September 2015;**133**:296-303
- [16] Srinath BS, Ravishankar Rai V. Rapid biosynthesis of gold nanoparticles by *Staphylococcus epidermidis*: Its characterisation and catalytic activity. *Materials Letters*. 1 May 2015;**146**:23-25
- [17] Tamanna B, Kavita M, Manika K, Ram P, Ajit V. Biosynthesis of zinc oxide nanoparticles from *Azadirachta indica* for antibacterial and photocatalytic applications. *Materials Science in Semiconductor Processing*. April 2015;**32**:55-61
- [18] Deep Pooja D, Sravani P, Hitesh K, Bharathi R, Shyam SR, Ramakrishna S. Natural polysaccharide functionalized gold nanoparticles as biocompatible drug delivery carrier. *International Journal of Biological Macromolecules*. September 2015;**80**:48-56

- [19] Balaji V, Vimala S, Anusha T, Elangovan V. Rapid synthesis of biocompatible silver nanoparticles using aqueous extract of *Rosa damascena* petals and evaluation of their anticancer activity. *Asian Pacific Journal of Tropical Medicine*. September 2014; 7(Suppl 1):S294-S300
- [20] Sujata P, Sudip M, Ayan KB, Anirban G, Bojja S, Chitta RP. Green synthesis, characterization of gold and silver nanoparticles and their potential application for cancer therapeutics. *Materials Science and Engineering: C*. 1 August 2015;53:298-309
- [21] Kartick B, Srivastava SK, Srivastava I. Green synthesis of graphene. *Journal of Nanoscience and Nanotechnology*. 2013;13:4320-4324
- [22] Farnosh T, Masoud S-N, Alireza B, Fatemeh M. Green synthesis and characterization of graphene nanosheets. *Materials Research Bulletin*. 2015;63:51-57
- [23] Meena Kumari M, John J, Daizy P. Green synthesis and applications of Au–Ag bimetallic nanoparticles. *Spectrochimica Acta Part A: Molecular and Biomolecular Spectroscopy*. 2015;137:185-192
- [24] Samiran M, Nayan R, Rajibul AL, Ismail SK, Saswati B, Debabrata M, Naznin AB. Biogenic synthesis of Ag, Au and bimetallic Au/Ag alloy nanoparticles using aqueous extract of mahogany (*Swietenia mahogani* JACQ.) leaves. *Colloids and Surfaces B: Biointerfaces*. 2011;82:497-504
- [25] Schabes-Retchkiman PS, Canizal G, Herrera-Becerra R, Zorrilla C, Liu HB, Ascencio JA. Biosynthesis and characterization of Ti/Ni bimetallic nanoparticles. *Optical Materials*. 2006;29:95-99
- [26] Sheny DS, Joseph M, Daizy P. Phytosynthesis of Au, Ag and Au–Ag bimetallic nanoparticles using aqueous extract and dried leaf of *Anacardium occidentale*. *Spectrochimica Acta Part A*. 2011;79:254-262
- [27] Veerasamy R, Sethu V, Sivadasan S, Syed AAS, Rajak H. Green synthesis of silver nanoparticles using *Atrocarpus altilis* leaf extract and the study of their antimicrobial and antioxidant activity. *Materials Letters*. 2016;180:264-267
- [28] Umesh BJ, Vishwas AB. Green synthesis of silver nanoparticles using *Artocarpus heterophyllus* Lam. seed extract and its antibacterial activity. *Industrial Crops and Products*. 2013;46:132-137
- [29] Soheila M, Shahram P, Abbas A. Green synthesis of silver nanoparticles with a long lasting stability using colloidal solution of cowpea seeds (*Vigna* sp. L). *Journal of Environmental Chemical Engineering*. 2016;4:2023-2032
- [30] Gopalu K, Matheswaran J, Manickam V, Govindan SK, Evgeny K, Arkhipov D, Alexander G, Denis K. *Hydrangea paniculata* flower extract-mediated green synthesis of MgNPs and AgNPs for health care applications. *Powder Technology*. 2017;305:488-494
- [31] Udhayaraj S, Jacob JA, Subramanian S, Durairaj S, Raman S, Soundarrajan K, Tirupathi Pichiah PB, Shanmugam A. Hepatocurative activity of biosynthesized silver nanoparticles fabricated using *Andrographis paniculata*. *Colloids and Surfaces B: Biointerfaces*. 2013;102:189-194

- [32] Jacob JA, Mohamed AAS, Thomas AJ, Udhayaraj S, Arunachalam S, Durairaj S, Seenivasan K, Shanmugam A. In vivo antitumor activity of biosynthesized silver nanoparticles using *Ficus religiosa* as a nanofactory in DAL induced mice model. *Colloids and Surfaces B: Biointerfaces*. 2013;**108**:185-190
- [33] Niraimathi KL, Sudha V, Lavanya R, Brindha P. Biosynthesis of silver nanoparticles using *Alternanthera sessilis* (Linn.) extract and their antimicrobial, antioxidant activities. *Colloids and Surfaces B: Biointerfaces*. 2013;**102**:288-291
- [34] Chunfa Do Chuanliang C, Xianglin Z, Yanlong Z, Xiangjie W, Xiuzhi Y, Kui Z, Xinhua X, Bin Y. Wolfberry fruit (*Lycium barbarum*) extract mediated novel route for the green synthesis of silver nanoparticles. *Optik - International Journal for Light and Electron Optics*. 2017;**130**:162-170
- [35] Chunfa D, Xianglin Z, Hao C, Chuanliang C. Green synthesis of biocompatible silver nanoparticles mediated by *Osmanthus fragrans* extract in aqueous solution. *Optik - International Journal for Light and Electron Optics*. 2016;**127**:10378-10388
- [36] Bianca M, Luminița D, Marcela A, Simona C, Gabriela AF. A green approach to phyto-mediated synthesis of silver nanoparticles using *Sambucus nigra* L. fruits extract and their antioxidant activity. *Journal of Molecular Liquids*. 2016;**221**:271-278
- [37] Mohanan VS, Soundarapandian K. Green synthesis of gold nanoparticles using Citrus fruits (*Citrus limon*, *Citrus reticulata* and *Citrus sinensis*) aqueous extract and its characterization. *Spectrochimica Acta Part A: Molecular and Biomolecular Spectroscopy*. 2013;**102**:15-23
- [38] Suman TY, Radhika Rajasree SR, Ramkumar R, Rajthilak C, Perumal P. The green synthesis of gold nanoparticles using an aqueous root extract of *Morinda citrifolia* L. *Spectrochimica Acta Part A: Molecular and Biomolecular Spectroscopy*. 2014;**118**:11-16
- [39] Gopinath K, Venkatesh KS, Ilangovan R, Sankaranarayanan K, Arumugam A. Green synthesis of gold nanoparticles from leaf extract of *Terminalia arjuna*, for the enhanced mitotic cell division and pollen germination activity. *Industrial Crops and Products*. 2013;**50**:737-742
- [40] Praveen Kumar K, Willi P, Chandra PS. Green synthesis of gold nanoparticles with *Zingiber officinale* extract: Characterization and blood compatibility. *Process Biochemistry*. 2011;**46**:2007-2013
- [41] Arghya S, Manoj G, Pragya S, Manab D, Utpal B. Green synthesis of gold nanoparticles using aqueous extract of *Dillenia indica*. *Advances in Natural Sciences: Nanoscience and Nanotechnology*. 2016;**7**:025005 (8pp)
- [42] Rani M, Aswathy B, Sudha RS. Green-synthesized gold nanoparticles from *Plumeria alba* flower extract to augment catalytic degradation of organic dyes and inhibit bacterial growth. *Particuology*. 2016;**24**:78-86
- [43] Jia Y, Di X, Hua NG, Chao W, Li KH, De FC. Facile one-step green synthesis of gold nanoparticles using *Citrus maxima* aqueous extracts and its catalytic activity. *Materials Letters*. 2016;**166**:110-112

- [44] Kasi G, Shanmugasundaram K, Kasi B, Subramanian M, Kunga SV, Masanam E, Periyannan K, Naiyf SA, Shine K, Marimuthu G, Giovanni B, Ayyakannu A. Green synthesis of silver, gold and silver/gold bimetallic nanoparticles using the *Gloriosa superba* leaf extract and their antibacterial and antibiofilm activities. *Microbial Pathogenesis*. 2016;**101**:1-11
- [45] Smitha SL, Daizy P, Gopchandran KG. Green synthesis of gold nanoparticles using *Cinnamomum zeylanicum* leaf broth. *Spectrochimica Acta Part A: Molecular and Biomolecular Spectroscopy*. 2009;**74**:735-739
- [46] Ganesh Kumar V, Dinesh Gokavarapu S, Rajeswari A, Stalin Dhas T, Karthick V, Kapadia Z, Tripti Shrestha IAB, Anindita R, Sweta S. Facile green synthesis of gold nanoparticles using leaf extract of antidiabetic potent *Cassia auriculata*. *Colloids and Surfaces B: Biointerfaces*. 2011;**87**:159-163
- [47] Mahmoud N, Mohammad Sajadi S. Green synthesis of copper nanoparticles using *Ginkgo biloba* L. leaf extract and their catalytic activity for the Huisgen [3 + 2] cycloaddition of azides and alkynes at room temperature. *Journal of Colloid and Interface Science*. 2015;**457**:141-147
- [48] Sastry ABS, Karthik AamanchiCh RB, Sree Rama Linga Prasad BSM. Large-scale green synthesis of Cu nanoparticles. *Environmental Chemistry Letters*. 2013;**11**:183-187
- [49] Thirumurugan A, Aswitha P, Kiruthika C, Nagarajan S, Nancy Christy A. Green synthesis of platinum nanoparticles using *Azadirachta indica* – An eco-friendly approach. *Materials Letters*. 2016;**170**:175-178
- [50] Farzaneh A, Mohammad HS, Sara S. Green synthesis of palladium nanoparticles using *Chlorella vulgaris*. *Materials Letters*. 2017;**186**:113-115
- [51] Aasaithambi K, Selvaraj MR, Gunabalan M, Ramalingam C, Ganesh E. Synthesis and characterization of palladium nanoparticles using *Catharanthus roseus* leaf extract and its application in the photo-catalytic degradation. *Spectrochimica Acta Part A: Molecular and Biomolecular Spectroscopy*. 2015;**135**:116-119
- [52] Yufen W, Zhanqiang F, Liuchun Z, Lei T, Eric PT. Green synthesis of Fe nanoparticles using *Citrus maxima* peels aqueous extracts. *Materials Letters*. 2016;**185**:384-386
- [53] Ting W, Xiaoying J, Zuliang C, Mallavarapu M, Ravendra N. Green synthesis of Fe nanoparticles using eucalyptus leaf extracts for treatment of eutrophic wastewater. *Science of the Total Environment*. 2014;**466–467**:210-213
- [54] Chitra JP, Rameshthangam P, Solairaj D. Green synthesis of nickel nanoparticles using *Ocimum sanctum* and their application in dye and pollutant adsorption. *Chinese Journal of Chemical Engineering*. 2015;**23**:1307-1315
- [55] Ganaie SU, Abbasi T, Abbasi SA. Rapid and green synthesis of bimetallic Au–Ag nanoparticles using an otherwise worthless weed *Antigonon leptopus*. *Journal of Experimental Nanoscience*. 2015;**11**:6, 395-417

- [56] Viswanathan K, Ayyakannu A, Kasi G, Periyannan K, Marimuthu G, Naiyf SA, Shine K, Jamal MK, Giovanni B. Guazuma ulmifolia bark-synthesized Ag, Au and Ag/Au alloy nanoparticles: Photocatalytic potential, DNA/protein interactions, anticancer activity and toxicity against 14 species of microbial pathogens. *Journal of Photochemistry and Photobiology B: Biology*. 2017;**167**:189-199
- [57] Malapermal V, Mbatha JN, Gengan RM, Anand K. Biosynthesis of bimetallic Au-Ag nanoparticles using *Ocimum basilicum* (L.) with antidiabetic and antimicrobial properties. *Advanced Materials Letters*. 2015;**6**(12):1050-1057
- [58] Palaniselvam K, Soundharrajan I, Srisesharam S, Da HK, Natanamurugaraj G, Gaanty P, Maniam MM, Yusoff Ki CC. Synthesis of bimetallic nanoparticles (Au-Ag alloy) using *Commelina nudiflora* L. plant extract and study its on oral pathogenic bacteria. *Journal of inorganic and Organometallic Polymers and Materials*. 2017;**27**:562-568. DOI:10.1007/s10904-017-0498-8
- [59] Guowu Z, Jiale H, Mingming D, Ibrahim A-R, Yao M, Qingbiao L. Green synthesis of Au-Pd bimetallic nanoparticles: Single-step bioreduction method with plant extract. *Materials Letters*. 2011;**65**:2989-2991
- [60] Jitendra KS, Shaheer Akhtar M, Ameen S, Pratibha S, Gurdip S. Green synthesis of CuO nanoparticles with leaf extract of *Calotropis gigantea* and its dye-sensitized solar cells applications. *Journal of Alloys and Compounds*. 2015;**632**:321-325
- [61] Renu S, Perumal M, Viswanathan M, Tajudeennasrin F, Kanchi SS, Vilwanathan R. Green synthesis of colloidal copper oxide nanoparticles using *Carica papaya* and its application in photocatalytic dye degradation. *Spectrochimica Acta Part A: Molecular and Biomolecular Spectroscopy*. 2014;**121**:746-750
- [62] Alaa YG, Tawfiq Al-Antary M, Akl MA. Green synthesis of copper oxide nanoparticles using *Punica granatum* peels extract: Effect on green peach Aphid. *Environmental Nanotechnology, Monitoring & Management*. 2016;**6**:95-98
- [63] Ramesh M, Anbuvarannan M, Viruthagiri G. Green synthesis of ZnO nanoparticles using *Solanum nigrum* leaf extract and their antibacterial activity. *Spectrochimica Acta Part A: Molecular and Biomolecular Spectroscopy*. 2015;**136**:864-870
- [64] Hasna AS, Rajeshwari S, Venckatesh R. Green synthesis and characterization of zinc oxide nanoparticles from *Ocimum basilicum* L. var. *purpurascens* Benth.-Lamiaceae leaf extract. *Materials Letters*. 2014;**131**:16-18
- [65] Thema FT, Manikandan E, Dhlamini MS, Maaza M. Green synthesis of ZnO nanoparticles via *Agathosma betulina* natural extract. *Materials Letters*. 2015;**161**:124-127
- [66] Diallo A, Ngom BD, Park E, Maaza M. Green synthesis of ZnO nanoparticles by *Aspalathus linearis*: Structural & optical properties. *Journal of Alloys and Compounds*. 2015;**646**:425-430

- [67] Manish H, Shreeram J, Mayur D, Kisan K. Green synthesis of TiO₂ nanoparticles by using aqueous extract of *Jatropha curcas* L. latex. *Materials Letters*. 2012;**75**:196-199
- [68] Rajakumar G, Abdul Rahuman A, Priyamvada B, Gopiesh Khanna V, Kishore Kumar D, Sujin PJ. *Eclipta prostrata* leaf aqueous extract mediated synthesis of titanium dioxide nanoparticles. *Materials Letters*. 2012;**68**:115-117
- [69] Anil AK, Ketan PG, Kalyani G, Vijay HI, Swapnali D, Ramphal S, Chang J-Y, Anil VG. Biomediated green synthesis of TiO₂ nanoparticles for lithium ion battery application. *Composites Part B: Engineering*. 2016;**99**:297-304
- [70] Diallo A, Manikandan E, Rajendran V, Maaza M. Physical & enhanced photocatalytic properties of green synthesized SnO₂ nanoparticles via *Aspalathus linearis*. *Journal of Alloys and Compounds*. 2016;**681**:561-570
- [71] Thema FT, Manikandan E, Gurib-Fakim A, Maaza M. Single phase Bunsenite NiO nanoparticles green synthesis by *Agathosma betulina* natural extract. *Journal of Alloys and Compounds*. 2016;**657**:655-661
- [72] Shiv Shankar S, Akhilesh R, Absar A, Murali S. Rapid synthesis of Au, Ag, and bimetallic Au core–Ag shell nanoparticles using Neem (*Azadirachta indica*) leaf broth. *Journal of Colloid and Interface Science*. 2004;**275**:496-502
- [73] Huang J, Li Q, Sun D, Lu Y, Su Y, Yang X, Wang H, Wang Y, Shao W, He N, Hong J, Chen C. Biosynthesis of silver and gold nanoparticles by novel sundried *Cinnamomum camphora* leaf. *Nanotechnology*. 2007;**18**:105104-105114
- [74] Sheny DS, Joseph M, Daizy P. Phytosynthesis of Au, Ag and Au–Ag bimetallic nanoparticles using aqueous extract and dried leaf of *Anacardium occidentale*. *Spectrochimica Acta, Part A*. 2011;**79**
- [75] Wieslaw W, Dorota S-N, Joanna T, Katarzyna O, Henryk Z, Mariusz KP. Metabolites of dietary quercetin: Profile, isolation, identification, and antioxidant capacity. *Journal of Functional Foods*. November 2014;**11**:121-129
- [76] Egorova EM, Revina AA. Synthesis of metallic nanoparticles in reverse micelles in the presence of quercetin. *Colloids and Surfaces A: Physicochemical and Engineering Aspects*. 31 July 2000;**168**(1):87-96
- [77] Karuvath Y, Binil II, Cherumuttathu HS, George Thomas K. In situ synthesis of metal nanoparticles and selective naked-eye detection of lead ions from aqueous media. *Journal of Physics and Chemistry C*. 2007;**111**:12839-12847
- [78] Lunjakorn A, Prompong P, Chuchaat T, Sanong E. Palladium nanoparticles synthesized by reducing species generated during a successive acidic/alkaline treatment of sucrose. *Spectrochimica Acta Part A: Molecular and Biomolecular Spectroscopy*. 2014;**122**:186-192
- [79] Hassan H-M, Fatemeh P, Sohaila A. Carboxylic acid effects on the size and catalytic activity of magnetite nanoparticles. *Journal of Colloid and Interface Science*. 1 January 2015;**437**:1-9

- [80] Ravi Kumar DV, Kumavat SR, Chamundeswari VN, Partha PP, Kulkarni A, Prasad BLV. Surfactant-free synthesis of anisotropic gold nanostructures: Can dicarboxylic acids alone act as shape directing agents? *RSC Advances*. 2013;**3**:21641
- [81] Qi Z-M, Zhou H-S, Naoki M, Itaru H, Kayori S, Akiko T, Kenji K. Characterization of gold nanoparticles synthesized using sucrose by seeding formation in the solid phase and seeding growth in aqueous solution. *Journal of Physics and Chemistry B*. 2004;**108**
- [82] Naheed A, Seema S, Radheshyam R. Rapid green synthesis of silver and gold nanoparticles using peels of *Punica granatum*. *Advanced Materials Letters*. 2012;**3**(5):376-380
- [83] Charu D, Chetan PS, Krishankant S, Manmohan K, Parma NB. An organic acid-induced synthesis and characterization of selenium nanoparticles. *Journal of Nanotechnology*. 2011;**2011**, Article ID 651971, p. 6
- [84] Aleksandra S, Mathieu F, Commenge J-M, Lavinia B, Laurent F, Raphaël S. Size-controlled synthesis of ZnO quantum dots in microreactors. *Nanotechnology*. 2014;**25**:145606 (9pp) 1-9
- [85] Stanton C, David AK, Kurt ML, Eric CN, Steven LS. Self-assembly of manganese oxide nanoparticles and hollow spheres. Catalytic activity in carbon monoxide oxidation. *Chemical Communications*. 2011;**47**:8286-8288
- [86] Amir G, Elías P, Armando A, Antonio V, Javier V-M. Calcium pimelate supported on TiO₂ nanoparticles as isotactic polypropylene prodegradant. *Polymer Bulletin*. 2015;**1**:13
- [87] Keyshawn C. Chemistry of carboxylic acid. In: Research World. 2012 [Otra ref. por si acaso: Saul Patai. *The Chemistry of Carboxylic Acids and Esters*. Ansari Road, Darya Ganj, Delhi: Interscience Publisher, Chichester; 1969]
- [88] Ashton Acton Q. *Carboxylic Acids—Advances in Research and Application*. Atlanta, GA: Scholarly Editions; 2013.
- [89] Kamatchi TS, Chitrapriya N, Kim SK, Fronczek FR, Natarajan K. Influence of carboxylic acid functionalities in ruthenium (II) polypyridyl complexes on DNA binding, cytotoxicity and antioxidant activity: Synthesis, structure and in vitro anticancer activity. *European Journal of Medicinal Chemistry*. January 2013;**59**:253-264
- [90] Thongchuai B, Tragoolpua Y, Sangthong P, Trisuwan K. Antiviral carboxylic acids and naphthoquinones from the stems of *Rhinacanthus nasutus*. *Tetrahedron Letters*. 9 September 2015;**56**(37):5161-5163
- [91] Rafiuddin Zoya Zaheer. Silver nanoparticles to self-assembled films: Green synthesis and characterization. *Colloids and Surfaces B: Biointerfaces*. 2012;**90**:48-52
- [92] Jeong L, Park WH. Preparation and characterization of gelatin nanofibers containing silver nanoparticles. *International Journal of Molecular Science*. 2014;**15**:6857-6879
- [93] Wang Q, Wang Y, Guo P, Li Q, Ding R, Wang B, Li H, Liu J, Zhao XS. Formic acid-assisted synthesis of palladium nanocrystals and their electrocatalytic properties. *Langmuir*. 2014;**30**:440-446

- [94] Venkatachalam M, Govindaraju K, Mohamed Sadiq A, Tamilselvan S, Ganesh Kumar V, Singaravelu G. Functionalization of gold nanoparticles as antidiabetic nanomaterial. *Spectrochimica Acta Part A: Molecular and Biomolecular Spectroscopy*. 2013;**116**:331-338
- [95] Dinda E, Harunar Rashid MD, Mandal TK. Amino acid-based redox active amphiphiles to in situ synthesize gold nanostructures: From sphere to multipod. *Crystal Growth and Design*. 2010;**10**(5):2421-2433
- [96] Henneke DE, Malyavanatham G, Kovar D, O'Brien DT, Becker MF, Nichols WT, Keto JW. Stabilization of silver nanoparticles in nonanoic acid: A temperature activated conformation reaction observed with surface enhanced Raman spectroscopy. *The Journal of Chemical Physics*. 2003;**119**:6802
- [97] Khan Z, Hussain JI, Kumar S, Hashmi AA, Malik MA. Silver nanoparticles: Green route, stability and effect of additives. *Journal of Biomaterials and Nanobiotechnology*. 2011;**2**:390-399
- [98] Umadevi M, Bindhu MR, Sathe V. A novel synthesis of malic acid capped silver nanoparticles using solanum lycopersicums fruit extract. *Journal of Materials Science & Technology*. April 2013;**29**(4):317-322
- [99] Zhang G, Zheng H, Shen M, Wang L, Wang X. Green synthesis and characterization of Au@Pt core-shell bimetallic nanoparticles using gallic acid. *Journal of Physics and Chemistry of Solids*. 2015;**81**:79-87
- [100] Armelao L, Camozzo D, Gross S, Tondello E. Synthesis of copper sulphide nanoparticles in carboxylic acids as solvent. *Journal of Nanoscience and Nanotechnology*. 2006 Feb;**6**(2):401-408
- [101] Shim JB, Kim CG, Jeon DJ, Chung T-M, An K-S, Lee SS, Lim JS, Jeong SJ, Park BK, Lee YK. Hydrothermal synthesis of CuInSe₂ nanoparticles in acetic acid. *Journal of Physics and Chemistry of Solids*. June 2013;**74**(6):867-871
- [102] Veriansyah B, Kim J-D, Min BK, Shin YH, Lee Y-W, Kim J. Continuous synthesis of surface-modified zinc oxide nanoparticles in supercritical methanol. *The Journal of Supercritical Fluids*. February 2010;**52**(1):76-83
- [103] Mamani JB, Costa-Filho AJ, Cornejo DR, Vieira ED, Gamarra LF. Synthesis and characterization of magnetite nanoparticles coated with lauric acid. *Materials Characterization*. July 2013;**81**:28-36
- [104] Dong CF, Zhang XL, Cao CL, Cai H. Synthesis of monodispersed lauric acid capped silver nanoparticles by wet-chemical reduction method. *Applied Mechanics and Materials*. December 2013;**477-478**:1246-1252
- [105] Calatayud DG, Jardiel T, Peiteado M, Rodríguez CF, Rocio Espino Estévez M, Doña Rodríguez JM, Palomares FJ, Rubio F, Fernández-Hevia D, Caballero AC. Highly photoactive anatase nanoparticles obtained using trifluoroacetic acid as an electron scavenger and morphological control agent. *Journal of Material Chemistry A*. 2013;**1**:14358-14367
- [106] Estruga M, Domingo C, Ayllón JA. Solution-processable ZnO nanoparticles obtained by low-temperature solventless synthesis. *Journal of Material Chemistry*. 2011;**21**:4408-4415

- [107] Xiong N, Wang M, Zhang H, Xie H, Zhao Y, Wang Y, Li J. Sintering behavior and effect of silver nanoparticles on the resistivity of electrically conductive adhesives composed of silver flakes. *Journal of Adhesion Science and Technology*. 2014;**28**(24):2402-2415
- [108] Rahimipour HR, Hosseinian A. Preparation of NiO-Ni nanocomposite by using of glutaric acid in neutral condition. *Advanced Materials Research*. November 2013;**829**:554-558
- [109] Bojarska M, Piatkiewicz W. Antibacterial properties of membranes modified by acrylic acid with silver nanoparticles. *Desalination and Water Treatment*. 2014:1-7
- [110] Ni Z, Wang Z, Sun L, Li B, Zhao Y. Synthesis of poly acrylic acid modified silver nanoparticles and their antimicrobial activities. *Materials Science and Engineering: C*. 1 August 2014;**41**:249-254
- [111] Rejal SZ, Masdara MS, Kamarudin SK. A parametric study of the direct formic acid fuel cell (DFAFC) performance and fuel crossover. *International Journal of Hydrogen Energy*. 24 June 2014;**39**(19):10267-10274
- [112] Yu X, Pickup PG. Recent advances in direct formic acid fuel cells (DFAFC). *Journal of Power Sources*. 15 July 2008;**182**(1):124-132
- [113] Baik SM, Kim J, Han J, Kwon Y. Performance improvement in direct formic acid fuel cells (DFAFCs) using metal catalyst prepared by dual mode spraying. *International Journal of Hydrogen Energy*. September 2011;**36**(19):12583-12590
- [114] Liu X, Li S, Liu Y, Cao Y. Formic acid: A versatile renewable reagent for green and sustainable chemical synthesis. *Chinese Journal of Catalysis*. September 2015;**36**(9):1461-1475
- [115] Chen D, Cui P, He H, Liu H, Yang J. Highly catalytic hollow palladium nanoparticles derived from silver@silver-palladium core-shell nanostructures for the oxidation of formic acid. *Journal of Power Sources*. 25 December 2014;**272**:152-159
- [116] Zhong X, Wang Z, Huang Y, Yu Y, Feng Q, Li Q. Fabrication of Pt nanoparticles on ethylene diamine functionalized graphene for formic acid electrooxidation. *International Journal of Hydrogen Energy*. 23 September 2014;**39**(28):15920-15927
- [117] Sáez A, Expósito E, Solla-Gullón J, Montiel V, Aldaz A. Bismuth-modified carbon supported Pt nanoparticles as electrocatalysts for direct formic acid fuel cells. *Electrochimica Acta*. 29 February 2012;**63**:105-111
- [118] Moghaddam RB, Pickup PG. Oxidation of formic acid at polycarbazole-supported Pt nanoparticles. *Electrochimica Acta*. 1 May 2013;**97**:326-332
- [119] Hosseini SR, Hosseinzadeh R, Ghasemi S, Farzaneh N. Synthesis of poly (2-Methoxyaniline)/sodium dodecyl sulfate film including bimetallic Pt-Cu nanoparticles and its application for formic acid oxidation. *International Journal of Hydrogen Energy*. 9 February 2015;**40**(5):2182-2192
- [120] Oko DN, Zhang J, Garbarino S, Chaker M, Ma D, Tavares AC, Guay D. Formic acid electro-oxidation at PtAu alloyed nanoparticles synthesized by pulsed laser ablation in liquids. *Journal of Power Sources*. 15 February 2014;**248**:273-282

- [121] Liaoa M, Xiong J, Fan M, Shi J, Luo C, Zhong C-J, Chen BH. Phase properties of carbon-supported platinum–gold nanoparticles for formic acid electro-oxidation. *Journal of Power Sources*. 30 October 2015;**294**:201-207
- [122] Mandal K, Bhattacharjee D, Dasgupta S. Synthesis of nanoporous PdAg nanoalloy for hydrogen generation from formic acid at room temperature. *International Journal of Hydrogen Energy*. 20 April 2015;**40**(14):4786-4793
- [123] Sharma A, Baral D, Bohidara HB, Solanki PR. Oxalic acid capped iron oxide nanorods as a sensing platform. *Chemico-Biological Interactions*. 5 August 2015;**238**:129-137
- [124] Li L, Zhao J, Wang Y, Li Y, Ma D, Zhao Y, Hou S, Hao X. Oxalic acid mediated synthesis of $\text{WO}_3 \cdot \text{H}_2\text{O}$ nanoplates and self-assembled nanoflowers under mild conditions. *Journal of Solid State Chemistry*. July 2011;**184**(7):1661-1665
- [125] Miao B, Zenga W, Xu S, Zeng S, Chen Y, Wu S. Synthesis and controlled growth of monodisperse $\text{WO}_3 \cdot \text{H}_2\text{O}$ square nanoplates with the assistance of malic acid. *Materials Letters*. 15 December 2013;**113**:13-16
- [126] Sedira S, Ayachi AA, Lakehal S, Fateh M, Achour S. Silver nanoparticles in combination with acetic acid and zinc oxide quantum dots for antibacterial activities improvement—A comparative study. *Applied Surface Science*. 30 August 2014;**311**:659-665
- [127] Liu J, Wang Y, Sun D. Enhancing the performance of dye-sensitized solar cells by benzoic acid modified TiO_2 nanorod electrode. *Renewable Energy*. 2012;**38**(1):214-218
- [128] Kumar S, Tomar MS, Acharya A. Carboxylic group-induced synthesis and characterization of selenium nanoparticles and its anti-tumor potential on Dalton's lymphoma cells. *Colloids and Surfaces B: Biointerfaces*. 1 February 2015;**126**:546-552
- [129] Guo D, Dou D, Ge L, Huang Z, Wanga L, Gu N. A caffeic acid mediated facile synthesis of silver nanoparticles with powerful anti-cancer activity. *Colloids and Surfaces B: Biointerfaces*. 1 October 2015;**134**:229-234
- [130] Hwang SJ, Jun SH, Park Y, Cha S-H, Yoon M, Cho S, Lee H-J, Park Y. Green synthesis of gold nanoparticles using chlorogenic acid and their enhanced performance for inflammation. *Nanomedicine: Nanotechnology, Biology and Medicine*. October 2015;**11**(7):1677-1688
- [131] Ratnarathorn N, Chailapakul O, Dungchai W. Highly sensitive colorimetric detection of lead using maleic acid functionalized gold nanoparticles. *Talanta*. 15 January 2015;**132**:613-618
- [132] Poupart R, Droumaguet BL, Guerrouache M, Carbonnier B. Copper nanoparticles supported on permeable monolith with carboxylic acid surface functionality: Stability and catalytic properties under reductive conditions. *Materials Chemistry and Physics*. 1 August 2015;**163**:446-452
- [133] Gade A, Gaikwad S, Tiwari V, Yadav A, Ingle A, Rai M. Biofabrication of silver nanoparticles by *Opuntia ficus-indica*: In vitro antibacterial activity and study of the mechanism involved in the synthesis. *Current Nanoscience*. 2010;**6**(4):370-375

- [134] Chougui N, Djerroud N, Naraoui F, Hadjal S, Aliane K, Zeroual B, Larbat R. Physicochemical properties and storage stability of margarine containing *Opuntia ficus-indica* peel extract as antioxidant. *Food Chemistry*. 15 April 2015;**173**:382-390
- [135] El-Mostafa K, El Kharrassi Y, Badreddine A, Andreoletti P, Vamecq J, El Kebbaj MHS, Latruffe N, Lizard G, Nasser B, Cherkaoui-Malki M. Nopal cactus (*Opuntia ficus-indica*) as a source of bioactive compounds for nutrition, health and disease. *Molecules*. 2014;**19**:14879-14901
- [136] Zhong X-K, Jin X, Lai F-Y, Lin Q-S, Jiang J-G. Chemical analysis and antioxidant activities in vitro of polysaccharide extracted from *Opuntia ficus indica* Mill. cultivated in China. *Carbohydrate Polymers*. 15 October 2010;**82**(3):722-727
- [137] Habibi Y, Heyraud A, Mahrouz M, Vignon MR. Structural features of pectic polysaccharides from the skin of *Opuntia ficus-indica* prickly pear fruits. *Carbohydrate Research*. 28 April 2004;**339**(6):1119-1127
- [138] Cárdenas A, Goycoolea FM, Rinaudo M. On the gelling behaviour of 'nopal' (*Opuntia ficus indica*) low methoxyl pectin. *Carbohydrate Polymers*. 2008;**73**:212-222
- [139] Kim D-Y, Sung JS, Kim M, Ghodake G. Rapid production of silver nanoparticles at large-scale using gallic acid and their antibacterial assessment. *Materials Letters*. 15 September 2015;**155**:62-64
- [140] Li D, Liu Z, Yuan Y, Liu Y, Niu F. Green synthesis of gallic acid-coated silver nanoparticles with high antimicrobial activity and low cytotoxicity to normal cells. *Process Biochemistry*. March 2015;**50**(3):357-366
- [141] Wang W, Chen Q, Jiang C, Yang D, Liu X, Xu S. One-step synthesis of biocompatible gold nanoparticles using gallic acid in the presence of poly-(N-vinyl-2-pyrrolidone). *Colloids and Surfaces A: Physicochemical and Engineering Aspects*. 5 July 2007;**301**(1-3):73-79
- [142] Morales P, Ramírez-Moreno E, de Cortes Sanchez-Mata M, Carvalho AM, Ferreira ICFR. Nutritional and antioxidant properties of pulp and seeds of two xoconostle cultivars (*Opuntia joconostle* F.A.C. Weber ex Diguët and *Opuntia matudae* Scheinvar) of high consumption in Mexico. *Food Research International*. 2012;**46**:279-285
- [143] López-Romero P, Pichardo-Ontiveros E, Avila-Nava A, Vázquez-Manjarrez N, Tovar AR, Pedraza-Chaverri J, Torres N. The effect of nopal (*Opuntia Ficus Indica*) on post-prandial blood glucose, incretins, and antioxidant activity in Mexican patients with type 2 diabetes after consumption of two different composition breakfasts. *Journal of the Academy of Nutrition and Dietetics*. November 2014;**114**(11):1811-1818
- [144] Kaur M, Kaur A, Sharma R. Pharmacological actions of *Opuntia ficus indica*: A review. *Journal of Applied Pharmaceutical Science*. 2012;**02**(07):15-18
- [145] Ahmad A, Davies J, Randall S, Skinner GR. Antiviral properties of extract of *Opuntia streptacantha*. *Antiviral Research*. May 1996;**30**(2-3):75-85

- [146] Sreekanth D, Arunasree MK, Roy KR, Reddy TC, Reddy GV, Reddanna P. Betanin a betacyanin pigment purified from fruits of *Opuntia ficus-indica* induces apoptosis in human chronic myeloid leukemia cell line-K562. *Phytomedicine*. 2007;**14**:739-746
- [147] Ramírez-Moreno E, Cordoba-Díaz M, de Cortes Sánchez-Mata M, Díez Marqués C, Goñi I. The addition of cladodes (*Opuntia ficus indica* L. Miller) to instant maize flour improves physicochemical and nutritional properties of maize tortillas. *LWT - Food Science and Technology*. June 2015;**62**(1), Part 2:675-681
- [148] Avila-Nava A, Calderón-Oliver M, Medina-Campos ON, Zou T, Gu L, Torres N, Tovar AR, Pedraza-Chaverri J. Extract of cactus (*Opuntia ficus indica*) cladodes scavenges reactive oxygen species in vitro and enhances plasma antioxidant capacity in humans. *Journal of Functional Foods*. 2014;**10**:13-24
- [149] Antunes-Ricardo M, Gutiérrez-Urbe JA, López-Pacheco F, Alvarez MM, Serna-Saldívar SO. In vivo anti-inflammatory effects of isorhamnetin glycosides isolated from *Opuntia ficus-indica* (L.) Mill cladodes. *Industrial Crops and Products*. 2015;**76**:803-808
- [150] Manikandan R, Manikandan B, Raman T, Arunagirinathan K, Marimuthu Prabhu N, Jothi Basu M, Perumal M, Palanisamy S, Munusamy A. Biosynthesis of silver nanoparticles using ethanolic petals extract of *Rosa indica* and characterization of its antibacterial, anticancer and anti-inflammatory activities. *Spectrochimica Acta Part A: Molecular and Biomolecular Spectroscopy*. 5 March 2015;**138**:120-129
- [151] David L, Moldovan B, Vulcu A, Olenic L, Perde-Schrepler M, Fischer-Fodor E, Florea A, Crisan M, Chiorean I, Clichici S, Adriana Filip G. Green synthesis, characterization and anti-inflammatory activity of silver nanoparticles using European black elderberry fruits extract. *Colloids and Surfaces B: Biointerfaces*. 1 October 2014;**122**:767-777
- [152] Lee KD, Nagajyothi PC, Sreekanth TVM, Park S. Eco-friendly synthesis of gold nanoparticles (AuNPs) using *Inonotus obliquus* and their antibacterial, antioxidant and cytotoxic activities. *Journal of Industrial and Engineering Chemistry*. 25 June 2015;**26**:67-72
- [153] Nagajyothi PC, Cha SJ, Yang IJ, Sreekanth TVM, Kim KJ, Shin HM. Antioxidant and anti-inflammatory activities of zinc oxide nanoparticles synthesized using *Polygala tenuifolia* root extract. *Journal of Photochemistry and Photobiology B: Biology*. May 2015;**146**:10-17
- [154] Ganesh Kumar V, Dinesh Gokavarapu S, Rajeswari A, Stalin Dhas T, Karthick V, Kapadia Z, Shrestha T, Barathy IA, Roy A, Sinha S. Facile green synthesis of gold nanoparticles using leaf extract of antidiabetic potent *Cassia auriculata*. *Colloids and Surfaces B: Biointerfaces*. 1 October 2011;**87**(1):159-163
- [155] Venkatachalam M, Govindaraju K, Mohamed Sadiq A, Tamilselvan S, Ganesh Kumar V, Singaravelu G. Functionalization of gold nanoparticles as antidiabetic nanomaterial. *Spectrochimica Acta Part A: Molecular and Biomolecular Spectroscopy*. December 2013;**116**:331-338

- [156] Rajaram K, Aiswarya DC, Sureshkumar P. Green synthesis of silver nanoparticle using *Tephrosia tinctoria* and its antidiabetic activity. *Materials Letters*. 1 January 2015;138:251-254
- [157] Álvarez RAB, Cortez-Valadeza M, Britto-Hurtado R, Oscar Neira Bueno L, Flores-Lopez NS, Hernández-Martínez AR, Gámez-Corrales R, Vargas-Ortiz R, Bocarando-Chacon J-G, Arizpe-Chavez H, Flores-Acosta M. Raman scattering and optical properties of lithium nanoparticles obtained by green synthesis. *Vibrational Spectroscopy*. March 2015;77:5-9
- [158] Ghosh P, Han G, De M, Kim CK, Rotello VM. Gold nanoparticles in delivery applications. *Advanced Drug Delivery Reviews*. 2008;60(11):1307-1315
- [159] Zhang L, Gu FX, Chan JM, Wang AZ, Langer RS, Farokhzad OC. Nanoparticles in medicine: Therapeutic applications and developments. *Clinical Pharmacology & Therapeutics*. 2008;83:761-769
- [160] Frey NA, Peng S, Cheng K, Sun S. Magnetic nanoparticles: Synthesis, functionalization, and applications in bioimaging and magnetic energy storage. *Chemical Society Reviews*. 2009;38:2532-2542
- [161] Zhu C, Guo S, Fang Y, Dong S. Reducing sugar: New functional molecules for the green synthesis of graphene nanosheets. *ACS Nano*. 2010;4(4):2429-2437
- [162] Wang Y, Shi ZX, Yin J. Facile synthesis of soluble graphene via a green reduction of graphene oxide in tea solution and its biocomposites. *ACS Applied Materials & Interfaces*. 2011;3(4):1127-1133
- [163] Mewada A, Pandey S, Shinde S, Mishra N, Oza G, Thakur M, Sharon M, Sharon M. Green synthesis of biocompatible carbon dots using aqueous extract of *Trapa bispinosa* peel. *Materials Science and Engineering: C*. 2013;33(5):2914-2917
- [164] Mehta VN, Jha S, Kailasa SK. One-pot green synthesis of carbon dots by using *Saccharum officinarum* juice for fluorescent imaging of bacteria (*Escherichia coli*) and yeast (*Saccharomyces cerevisiae*) cells. *Materials Science and Engineering: C*. 2014;38:20-27
- [165] Dong Y, Wang R, Li H, Shao J, Chi Y, Lin X, Chen G. Polyamine-functionalized carbon quantum dots for chemical sensing. *Carbon*. 2012;50(8):2810-2815
- [166] Keuleyan S, Lhuillier E, Brajuskovic V, Guyot-Sionnest P. Mid-infrared HgTe colloidal quantum dot photodetectors. *Nature Photonics*. 2011;5:489-493
- [167] Qin Y, Ji X, Jing J, Liu H, Wu H, Yang W. Size control over spherical silver nanoparticles by ascorbic acid reduction. *Colloids and Surfaces A: Physicochemical Engineering Aspects*. 2010;372:172-176
- [168] Vijayaraghavana K, Kamala Nalini SP, Udaya Prakash N, Madhankumar D. One step green synthesis of silver nano/microparticles using extracts of *Trachyspermum ammi* and *Papaver somniferum*. *Colloids and Surfaces B: Biointerfaces*. 2012;94:114-117

- [169] Bindhu MR, Umadevi M. Antibacterial and catalytic activities of green synthesized silver nanoparticles. *Spectrochimica Acta Part A: Molecular and Biomolecular Spectroscopy*. 2015;**135**:373-378
- [170] Jain PK, El-Sayed IH, El-Sayed MA. Au nanoparticles target cancer. *Nano Today*. 2007;**2**:18-29
- [171] Zheng YB, Juluri BK, Mao X, Walker TR, Huang TJ. Systematic investigation of localized surface plasmon resonance of long-range ordered Au nanodisk arrays. *Journal of Applied Physics*. 2008;**103**:014308
- [172] Prathap Chandran S, Chaudhary M, Pasricha R, Ahmad A, Sastry M. Synthesis of gold nanotriangles and silver nanoparticles using aloe vera plant extract. *Biotechnology Progress*. 2006;**22**(2):577-583
- [173] Xiong Y, Chen J, Wiley B, Xia Y, Yin Y, Li Z-Y. Size-dependence of surface plasmon resonance and oxidation for Pd nanocubes synthesized via a seed etching process. *Nano Letters*. 2005;**5**(7):1237-1242
- [174] Prabhasha PG, Haritha VS, Nair SS, Pilankatta R. Localized surface plasmon resonance based highly sensitive room temperature pH sensor for detection and quantification of ammonia. *Sensors and Actuators B: Chemical*. 2017;**240**:580-585
- [175] Vahid Mohammadi A, Halali M. Synthesis and characterization of pure metallic titanium nanoparticles by an electromagnetic levitation melting gas condensation method. *RSC Advances*. 2014;**4**:7104-7108
- [176] Britto-Hurtado R, Cortez-Valadez M, Álvarez-Bayona R, Horta-Fraijo P, Bocarando-Chacon J-G, Gámez-Corrales R, Pérez-Rodríguez A, Martínez-Suárez F, Arizpe-Chávez H, Flores-Acosta M. Green synthesis and optical properties of Ti nanoparticles. *NANO*. 2015;**10**, 1550069:1-7

Perspective of the Structuration Process Use in the Optoelectronics, Solar Energy, and Biomedicine

Natalia Vladimirovna Kamanina

Additional information is available at the end of the chapter

<http://dx.doi.org/10.5772/68123>

Abstract

In the current chapter, the results of the optimized organic and inorganic materials features have been presented and discussed under the conditions when the material volumetric body and their surfaces have been structured. The dramatic change of the main characteristics of the inorganic matrix which surface has been modified with oriented carbon nanotubes and additionally treated by surface electromagnetic waves has been established. The transmittance and reflection spectral change, of the micro-hardness and of the wetting angle increase have been discussed due to the covalent bonding of the carbon nanotubes with the near-surface materials layers. Analytic and molecular dynamics simulations have supported the data. The essential change of the basic macro-parameters of the organic matrix, including the liquid crystal one, via their structuration with the nano- and/or bio-objects such as the fullerenes, carbon nanotubes, shungites, quantum dots, graphene oxides, DNA has been found. The spectral, photorefractive, and photoconductive characteristics modification has been discussed due to the drastic increase of the dipole moment. The laser-induced change of the refractive index has been considered as the indicator of the basic materials macro-parameters changing. It has been predicted that a scientific knowledge and the technology advances can be useful for the solar energy, display technique, for the system to absorb the gas and impurities, for the schemes with the compacted information recording as well as for the biomedicine.

Keywords: structuration process, carbon nanotubes, surfaces, coatings, conducting quasi-graphene layers, inorganic and organic materials, spectra, mechanical properties, refractive features, laser-mater interaction

1. Introduction

Careful investigations of the structural, refractive, conductive, and wetting properties of the innovative hybrid materials modified with effective nano- and bio-objects are timely and quite popular [1–6] because of the relevance study of new physical and chemical effects in them. Structured inorganic and organic materials, including liquid crystal ones, are able to optimize the technological processes for nano- and bio-technologies, as well as to extend the possible their application for the purposes of telecommunications, display, laser, biomedical engineering, industrial production, etc.

It should be said that the study of the structural and optical effects in the materials has a special place in the development of modern innovative technologies. This is due to the substantial increase in applications last, as the photon energy lies in the range of electronic and vibrational transitions in matter, and therefore, this circumstance allows the use of light and more particularly laser radiation, to obtain unique information about structural and dynamic refractive properties of the materials. Moreover, it permits to manifest new and classic confirmation of the effects in them and to use laser sources for modeling properties of the investigated matrix systems.

This chapter partially summarizes the prospects of the process of surface structuring (e.g., some inorganic materials) and the volume (e.g., some organic systems) in order to create and advocate new composites with unique improved their physical and chemical properties.

1.1. Features of structuration of the surface of inorganic model materials

Covalent bonding of the CNTs, as an indicator of enlightenment, the strengthening of materials, changing their resistance and laser strength.

Among other perspective nanoparticles and nanostructures, the carbon nanotubes (CNTs) occupy the special place. The basic features of carbon nanotubes are regarded to their branched surface, high conductivity, strong hardness of their C–C bonds, little value of the refractive index as well as to their complicated, and unique mechanisms of charge carrier moving [7–10]. These characteristics permit to apply the CNTs materials with good advantage in order to improve the physical and chemical properties of the inorganic systems especially when the CNTs have been deposited on the material surfaces.

It should be mentioned that to modify the properties of the inorganic materials via their surface treatment, the SWCNTs type #704121 with the diameter placed in the range of 0.7–1.1 nm purchased from Aldrich Co. has been used. These nanotubes have been deposited on the material surface using IR CO₂-laser with *p*-polarized irradiation at wavelength of 10.6 μm and power of 30 W. Moreover, CNTs have been placed at the materials interface under the conditions when an additional electric field of 100–600 V cm⁻¹ has been applied in order to orient the nanotubes in the vertical position during the deposition process. This procedure has been partially shown in the RU patents [11, 12]. The spectra of the nanotubes-treated materials have been obtained using Perkin-Elmer Lambda 9 and Furrier FSM-1202 instruments as well as using VIS SF-26 device operated in the range of 250–1200 nm. Surface mechanical hardness

has been revealed using the CM-55 instrument as well as via using of the micro-hardness device PMT-3M (produced by “LOMO”, Saint-Petersburg, Russia) with the ability to vary an indenter forces. The laser strength has been checked with pulsed nanosecond Nd-laser. The special accent has been given to observe the relief at the material surface via checking the wetting angle. In this case, the camera with parameters as Compact F1.6 1/3 CS Mount 6.0–60 mm Manual Focal Iris Zoom Lens for CCTV Camera (Black) has been applied. The modified surface analysis has been made using Solver Next AFM (purchased from NT MDT Co., Zelenograd, Moscow region, Russia).

1.2. ITO conducting layer: spectral parameters, wetting phenomenon, laser and mechanical characteristics

It should be mentioned that an emphasis has been given on the ITO-conducting layers modification due to the reason that these structures have so broad area of the application in the general telecommunication systems, solar energy area, and biomedicine as well as in display, gas storage and laser technique [13–20]. For example, if one of the optoelectronic key element, such as electrically or light-addressed spatial light modulators (SLMs) can be considered, it should be said that besides of the solution to obtain the high resistivity and good speed, some other important problem should be resolved. It connected with the possible increase of the transparency, mechanical and laser strength of the SLM elements as well. Thus, nanostructuration process permits to find new ways to resolve the problem mentioned above with good advantage. In this case, the influence of the surface treatment procedure on the materials basic characteristics can be taken into account.

The data showed in **Figures 1** and **2** as well as in **Tables 1** and **2** support the spectral evidences, the mechanical properties, the laser features, the resistance values, and the wetting angles. It should be mentioned that an additional surface electromagnetic wave (SEW) treatment has

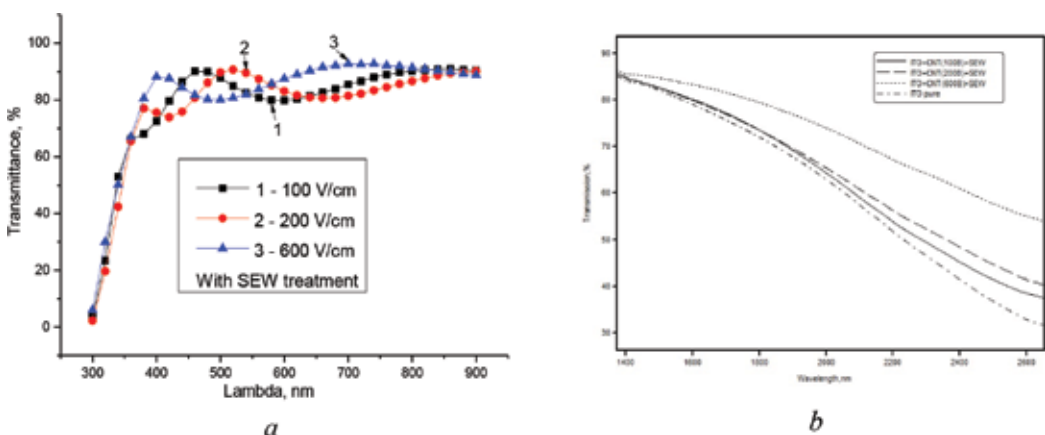


Figure 1. VIS (a) and near IR-range (b) transmittance spectra of the ITO-layer covered with the vertically aligned CNTs under the different electric field applied.

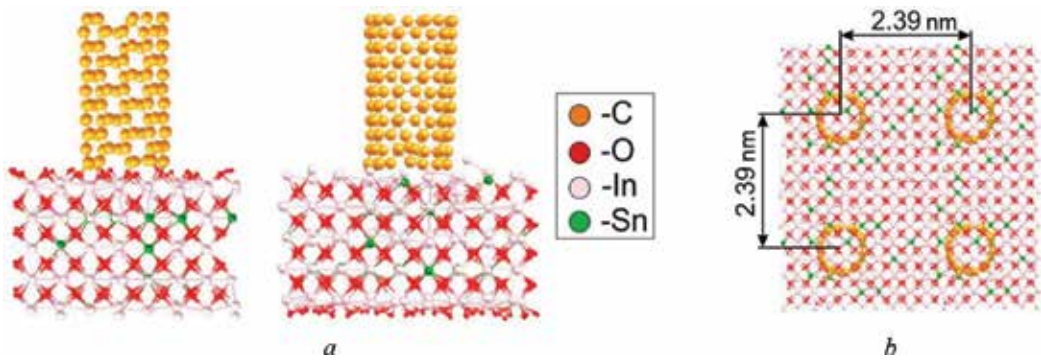


Figure 2. Possible CNTs placement on the ITO surfaces: general view (a) and the dimension one (b).

been made to modify the ITO relief in order to decrease the roughness and resistivity as well as to apply one as an orienting coating for the classical nematic liquid crystal cells [21, 22].

One can see from **Figure 1** data that the structuration of the ITO surfaces with oriented CNTs provokes the shift of the spectral parameters (a) and increase the transparency (b). The molecular dynamics method based on the LAMMPS program [23, 24] has been made to support these results. Data of this simulation have supported the bonding existing effect and testified that the one has been coincided with the diameter and speed of the CNTs under the laser-oriented deposition (LOD) conditions. The data presented in **Figure 2** show the possible bonding between carbon atoms and atomic surface layer.

It should be mentioned that this ITO surface modification revealed by LOD has provoked the dramatically decrease of the resistivity. It can be explained by the formation of the possible quasi-graphene layer due to the fact that CNTs reveal the large charge carrier moving from the core of the nanotubes and show the donor acceptor properties too. **Figure 3a** presented

Resistivity before treatment, Ohm	Resistivity after treatment, Ohm
1570	700
1400	500
600	200
390	120
195	70
155	52
150	43
100	46
100	40

Table 1. Comparative values of the resistivity of the pure ITO and of the transparent conducting layers under the nanostructure process treatment.

Materials	Micro-hardness, Pa	Micro-hardness increase, times	Energy density, $J \times cm^{-2}$	Destruction provoked energy density, $J \times cm^{-2}$
ITO	2.2×10^9	0	0.3–0.4	0.65
ITO + CNTs	3.5×10^9	~1.6	0.6–0.7	~0.75
ITO + CNTs + SEW	4.7×10^9	2	0.9	~1.5

Table 2. Comparative values of the mechanical hardness and laser strength of the pure ITO and of the transparent conducting layers under the nanostructure process treatment.

the tentative model picture to form the quasi-graphene layers on the ITO surfaces structured by LOD. As an additional, the AFM-image is shown in **Figure 3b** in order to present the real structured optimized relief.

To observe the change of the resistivity, one can see **Table 1** data. Thus, the resistivity parameters can be change up to 2–3 times. It can be important for the future design of the telecommunication systems, such as light-addressed and electrically addressed SLMs, electrically controlled display and holographic elements, etc., because it should provoke the essential decrease of the applied voltage. Indeed, the data presented in **Table 1** have been obtained for the initial different pure ITO coatings with different their thickness and treated at different annealing temperatures.

Among these advantages, the mechanical hardness and laser strength improvement have been shown as well. The data of **Table 2** support this fact. It should be testified that the mechanical hardness and laser strength of the ITO-conducting layer can be successfully increased via CNTs treatment. It should be mentioned that traditionally the HfO_2 coatings have been

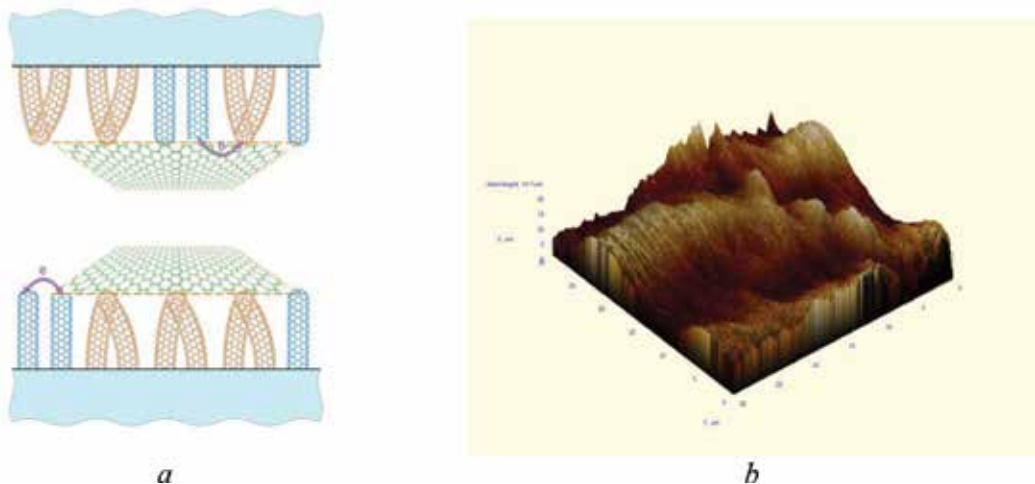


Figure 3. Possible model presentation to form the quasi-graphene layers on the ITO surfaces coated with oriented CNTs (a) and AFM-image of the structured ITO relief (b).

deposited on the ITO surface to eliminate their roughness and increase the strength, but the CNTs modification can provoke the better results via applying the LOD technique.

Some evidences to increase the wetting angle have been obtained too for the ITO relief studied. Thus, the pure ITO coatings additionally treated with the surface electromagnetic waves have revealed the wetting angle close to 70–75°. After nanostructuring process using LOD technique, the wetting angle has been increased and placed in the range of 85–89°.

Analyzing these evidences, it should be noticed that the ITO-relief obtained can be sufficiently used especially in the display and SLM technique due to the fact that the modified relief at the ITO surfaces can be considered as the conducting layer with the decreased resistivity as well as the orienting one to align the LC dipoles with good advantage. Moreover, these structured ITO can be prospectively using in the solar energy area and in the biomedicine as well as in the general optoelectronics too especially due to their increased transparency.

1.3. MgF_2 and relative structures: spectral parameters, wetting phenomenon, and mechanical hardness

Using the mentioned above designed laser technologies based on the oriented deposition of the carbon nanotubes [11, 12] on the surface of optical materials including as well MgF_2 , CaF_2 , BaF_2 , LiF, NaCl, KBr, KCl, etc. materials operated in the UV and in the IR spectral range, the study of the spectrum of transmittance, micro-hardness, changing the ability to water absorption, etc. is important. Results for the obtained transmittance and the reflection spectra of the group of randomly selected samples are shown in **Figure 4**. One can observe the essential change of the spectral characteristics for the 200–500 nm and for the near-IR spectral range. Moreover, for the BaF_2 structures, the reflection spectrum change has been obtained up to 16 micrometers.

Analyzing these data, it is evident that the process of laser deposition of CNTs on the surface of the studied materials changes the spectral parameters, leading to a substantial increase of transmittance and decrease of Fresnel losses due to the covalent binding of the CNTs to the surface of the material [25, 26] with regard to the small value of the imaginary part of permittivity of CNTs and their small refractive index that can be <1.1 .

Moreover, dramatically change of the micro-hardness and the wetting angle has been obtained for these systems. The comparative data before and after laser deposition of the CNTs are shown in **Table 3**. Thus, micro-hardness can be increased more than 6–10%, and the angle of wettability can be changed from 1.5 to 5 times. Of course, not only essential mechanical properties of carbon nanotubes should be considered when one analyzes these data, but also the formation of predicted covalent bonds between carbon nanotubes and the surface atoms of the investigated materials. It should be mentioned that the analytical calculations presented in the paper [26] for the model MgF_2 structure have shown that in order to destroy the structured material surface we should firstly to bend the vertically oriented nanotubes with energy of 1.8×10^{-20} J, which is in five times larger than the one, which can be applied to simply remove the nanotubes from the surface after

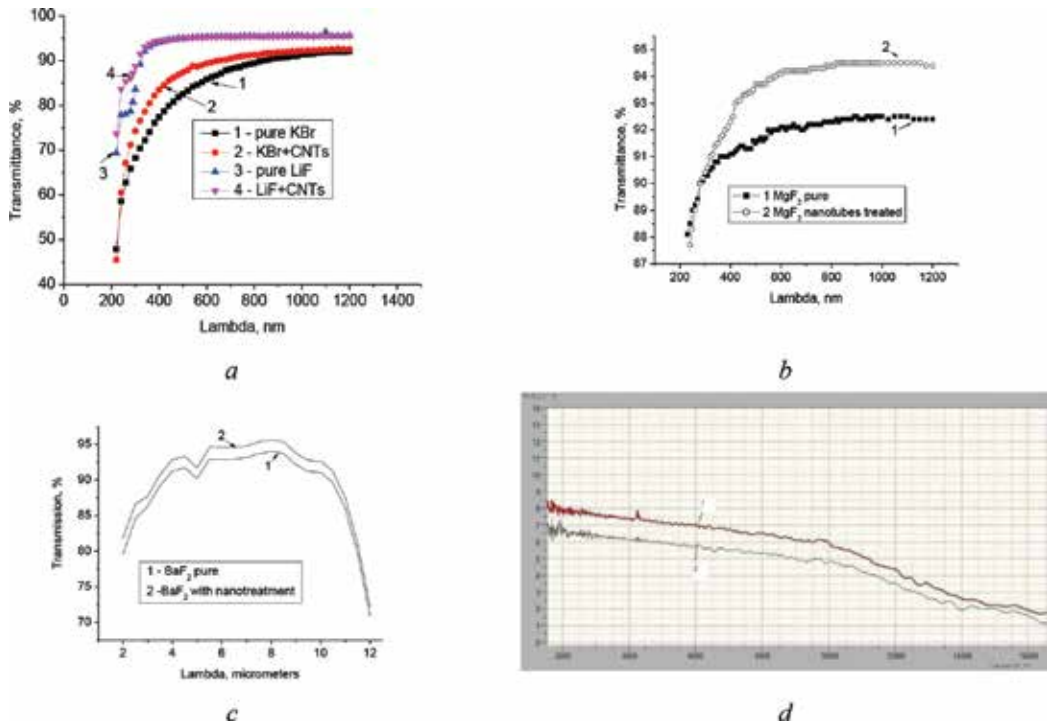


Figure 4. Transmittance spectral change of the LiF and KBr (a); MgF₂ (b), BaF₂ materials (c), and reflection spectral parameters of BaF₂ (d). Curve 1 and curve 2 are regarded to the systems before and after nanotreatment. The sample thickness was ~2 nm.

destroying MgC bonding. This simple model can be used to explain the results of the dramatic increase of mechanical surface hardness of MgF₂ covered with nanotubes placed by LOD technique.

No	Materials	Indenter, g	Increase of the micro-hardness, %	Wetting angle, before CNTs deposition, degrees	Wetting angle, after CNTs deposition, degrees
1	NaCl	2	6–8	7	25
2	KCl	10	4–6	10	30
3	LiF	10	3–5		
4	KBr	10	6–10	5-7	25–30
5	MgF ₂	40	6	83-85	89–90
6	BaF ₂	2	12–15	55-56	67–70
7	CaF ₂	40	9–10		

Table 3. Comparative values of the mechanical hardness of the UV-IR materials under the nanostructure process treatment.

Analyzing these evidences, one can propose that some hydrophilic properties of the functional UV-IR materials can be changed to reveal the hydrophobic features. That is very important in the Fourier spectrometry devices, for the microscopy area, as well as for the biomedicine. For example, the output windows of magnesium fluoride are used in the lamps for quartz treatment of medical institutions. It also can be required for the some substrate of the spatial light modulators which area of their operation should be extended to the UV and IR spectral ranges.

In addition, registered increase of the spectral characteristics, macro-hardness parameters and of the wetting phenomena too indicates the novel tendency to find unique way to improve the technical parameters of these materials under the condition of the oriented CNTs laser deposition technique for the purpose of the general optoelectronics, solar energy, and biomedicine systems.

1.4. Metal and semiconductor materials: spectral parameters, wetting phenomenon, and mechanical hardness

Some materials from the metal and semiconductor groups have been studied in order to accept the knowledge about the influence of the nanostructuration process on the basic physical parameters of this type of the materials. Partially, the data are presented in **Figure 5**. It should be noticed that in the case of the analysis of the spectra, one took into account the change of the spectrum with one-sided processing of the material and processing from two their sides.

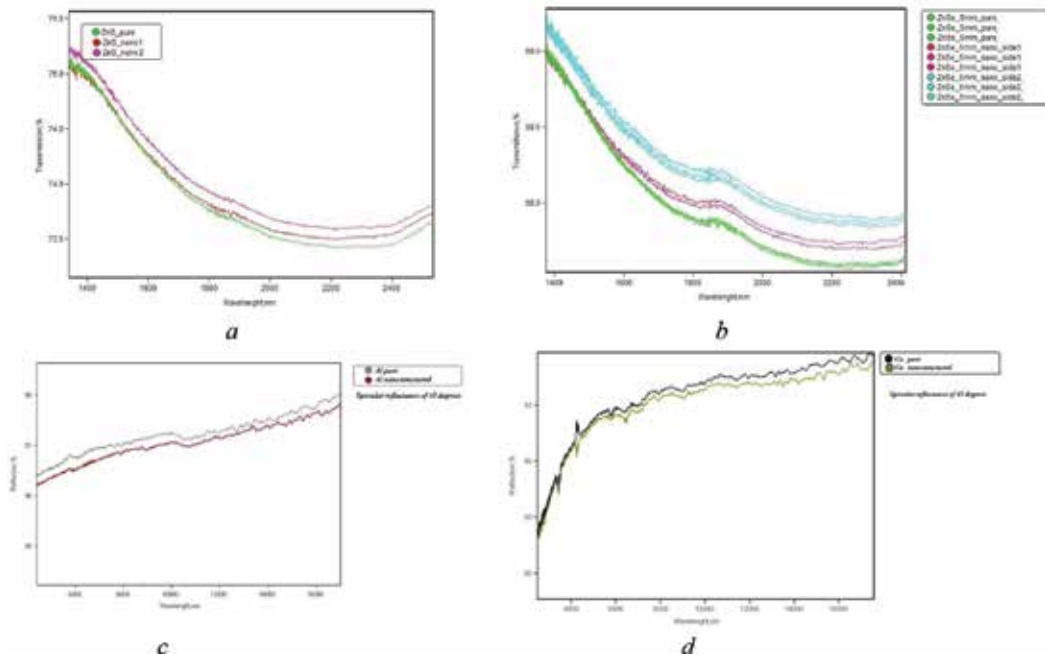


Figure 5. Transmittance spectral change of the ZnS (a); ZnSe (b) materials, and reflection spectral parameters of Al (c), and Cu (d).

The micro-hardness results reveal the increase of these parameters too. Thus, for the Al, Cu, ZnS, ZnSe materials, the micro-hardness has been increased up to 7, 9, 5, 5%, respectively. It should be mentioned that the indenter with the forces of 30 and 20 g has been used to treat the metal and semiconductor materials, respectively.

The molecular dynamics method has supported the results of the spectral and the mechanical properties changing due to the incorporation of the CNTs into the materials surfaces and due to form the possible bonding between the carbon atom and the original material surface atoms of Al and ZnS materials. It should be mentioned that the penetration depth has been depended on the velocity of the CNTs and their diameters. The molecular dynamics results are shown in **Figure 6**. This analysis has been made using the procedure in the framework of the LAMMPS program [23, 24].

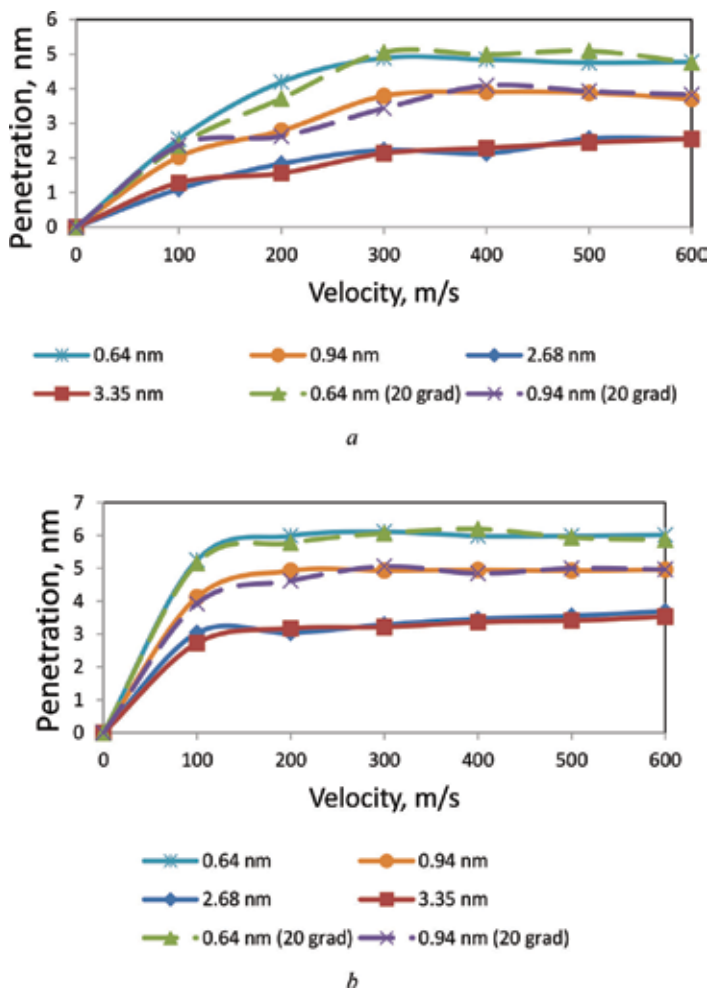


Figure 6. Dependence of the penetration on the CNTs velocity for the studied Al (a) and ZnS (b) materials under the laser-oriented deposition process using the different diameter of the CNTs.

It should be noticed that the interaction between Zn and S atoms in the penetration process of CNT into Zn-S surface was described using Tersoff many-body potential in which parameters are given in publication [27]. Interaction between Al atoms was described using embedded atom method (EAM) [28] parametrized according to Ref. [29].

To describe the interaction between CNT and Al substrate, the 12–6 potential $E = 4\epsilon\left[\left(\frac{\sigma}{r}\right)^{12} - \left(\frac{\sigma}{r}\right)^6\right]$ has been used. The interaction parameters were fit as: $\epsilon = 2.63$ eV, $\sigma = 1.91$ Å based on inter-layer distance between graphene and Al surface. To describe the interaction between CNT and Zn atoms of the substrate, the parameters for 12–6 potential were fitted as $\epsilon = 0.011$ eV, $\sigma = 1.80$ Å. Interaction between C and S was taken two times smaller than for Zn-C. The interaction between carbon atoms in the CNT was described using Tersoff many-body potentials with parameters described in Ref. [23].

The molecular dynamics simulations have been carried out at constant temperature about 300 K. The total time of simulation has been of 60 ps with the time step of 1 fs. The velocities of the tubes have been varied from 100 to 600 m×s⁻¹ according to the experiments.

Thus, using the consideration based on the ITO, MgF₂ and relative structures, Al, Cu, ZnS and ZnSe materials, the current study can propose the CNTs laser treatment as the innovative way to modify the important physical and chemical characteristics of these inorganic materials.

Analyzing these evidences, one can remember that Al is the material used to fabricate the aviation, aerospace, food processing and the production of tableware; copper is a material for the manufacture of wires for electrical industry; ZnS and ZnSe are the materials for the manufacture of space components and devices of technical sensors, etc. Thus, all of the mentioned above area of the application of the materials under the consideration can be essentially exceeded via using the LOD technique with good advantage.

2. Features of the structuring of the volume of model polymers and liquid crystals: change of the refractive parameters as indicator of the changes of the photoconductive, spectral and structural properties

Using four-wave mixing of laser beams (see **Figure 7**) in the nanosecond range of durations, at the wavelength of the second harmonic of a neodymium laser $\lambda = 532$ nm, with variation, as energy density or spatial frequency λ , the investigation of the change of refractive properties of a large group of conjugated organic materials by recording the diffraction efficiency in the diffraction Raman-Nath has been made. The scheme and the conditions are coincided to that considered before in the papers [14, 30]. It should be mentioned that for all materials studied, the threshold value of the input energy density at which the reversible process has been transfer to the irreversible one has been detected. Some AFM-image is shown in **Figure 8**, which corresponded to thermal replica on the material surface to indicate this fact. One can see that the spatial frequency approximately equaled to 90–100 mm⁻¹ has been formed.

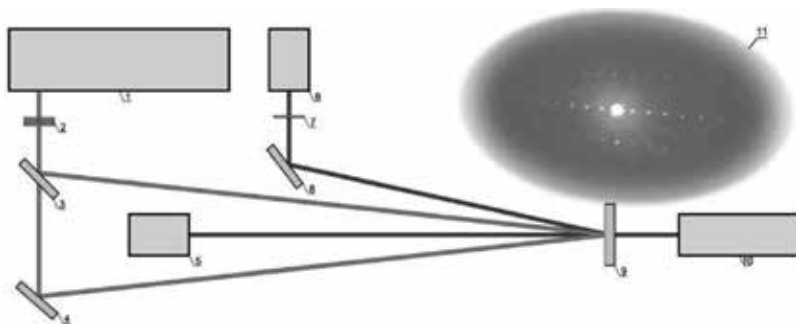


Figure 7. Experimental setup. 1—Nd-laser with the second harmonic convertor (532 nm), 2,7—filters, 3,4,8—mirrors, 5,6—photo detectors, 9—samples, 10—an additional Nd- or He-Ne-laser to read-out, 11—recorded diffractive grating.

The values of light-induced additives to the refractive index have been calculated, and the range of variation of cubic nonlinearity and nonlinear refraction has been defined. It is established that these values are comparable with those obtained for three-dimensional silicon structures. But, it should be noticed that the technology of obtaining thin films of conjugated organic materials significantly easier and their thickness is an order of magnitude less. The main results of the largest light-induced change of the refractive index Δn_i in a number of structured organic materials, for example, polyimide PI, 2-cyclooctylamino-5-nitropyridine (COANP) and nematic liquid crystals (NLC) with different concentrations of the sensitizers and treated at different energy densities are systematic and presented in the comparative **Table 4**.

As nano- and bio-sensitizers the fullerenes, shungites, carbon nanotubes (CNT), quantum dots (QD), oxides graphene, DNA has been used. The explanation of the change of the refractive properties of the organic conjugated systems with structuring volume of the medium is given in the framework of the significant growth of the polarizability, dipole moment, and the way of the transfer of charge carriers from intramolecular electron donor is not on the

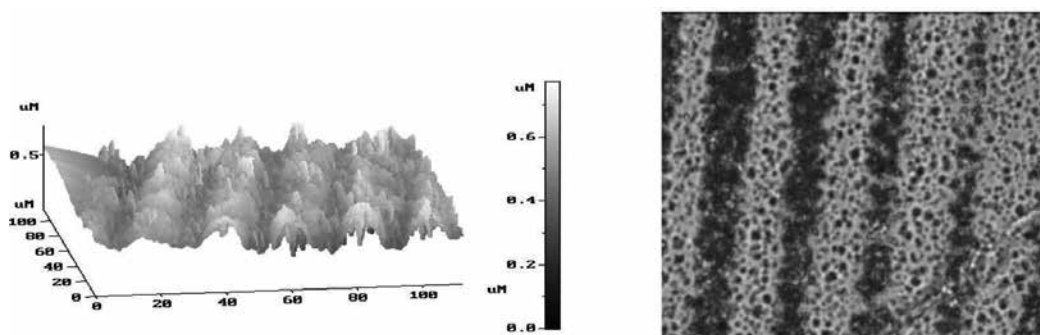


Figure 8. AFM and optical images of the relief obtained on the material surfaces under the conditions when reversible process becomes the irreversible one.

Materials	Nano-object content, wt.%	Energy density, J cm ⁻²	Δn_i
Pure polyimide	0	0.5–0.6	10^{-4} – 10^{-5}
Polyimide + QDs CdSe(ZnS)	0.003	0.2–0.3	2.0×10^{-3}
Polyimide + graphene oxide	0.05	0.2	2.7×10^{-3}
Polyimide + graphene oxide	0.1	0.2	3.4×10^{-3}
Polyimide + C ₆₀	0.2	0.5–0.6	4.2×10^{-3}
Polyimide + C ₇₀	0.2	0.6	4.68×10^{-3}
Polyimide + shungite	0.1	0.5	3.46×10^{-3}
Polyimide + shungite	0.2	0.1	5.3×10^{-3}
Polyimide + CNTs	0.1	0.5–0.6	5.7×10^{-3}
Pure COANP	0	0.8–0.9	$\sim 10^{-5}$
2-cyclooctylamino-5-nitropyridine (COANP) + C ₆₀	5	0.9	6.21×10^{-3}
COANP + C ₆₀	5	0.9	6.89×10^{-3}
LC + polyimide + C ₇₀	0.2	0.1	1.2×10^{-3}
LC + COANP + C ₇₀	5	17.5×10^{-3}	1.4×10^{-3}
LC + COANP + C ₇₀	1	30×10^{-3}	1.45×10^{-3}
LC + QDs CdSe(ZnS) + DNA	0.1	0.1	1.35×10^{-3}

Table 4. Refractive characteristics modification via checking of the laser-induced change of the refractive index.

intramolecular acceptor but to the intermolecular acceptor with high electron affinity and ability to delocalize of not one, but a larger number of carriers [31, 32]. Qualitative picture is shown in **Figure 9**.

Analyzing the basic experimental data presented in **Table 4**, it should be remembered that the different types of the sensitizers, their content, and energy density have been applied. Moreover, the experiments have been performed at the close spatial frequencies and at the same laser pulse width. One can see that the values of the laser-induced refractive index have been exceeded the ones obtained for the chosen pure matrix systems. It should be mentioned that the refractive features have been connected with the increase of the charge carrier mobility obtained via photoconductive experiments. The comparative analysis to check the increase of the charge carrier mobility has been made via procedure shown in the paper [33].

It should be said that the calculated values of nonlinear refraction n_2 and third-order nonlinear susceptibility $\chi^{(3)}$ are included in a range of values: $n_2 = 10^{-10}$ – 10^{-9} cm²×W⁻¹ и $\chi^{(3)} = 10^{-10}$ – 10^{-9} cm³×erg⁻¹ [30, 31, 34–36]. The growth of refractive coefficients correlated with the change of the photoconductive (increase of mobility of charge carriers), and it is connected with the changes in the order parameter of the studied materials and with the infrared shift of their spectral characteristics. It has been registered to the photosensitivity and has been

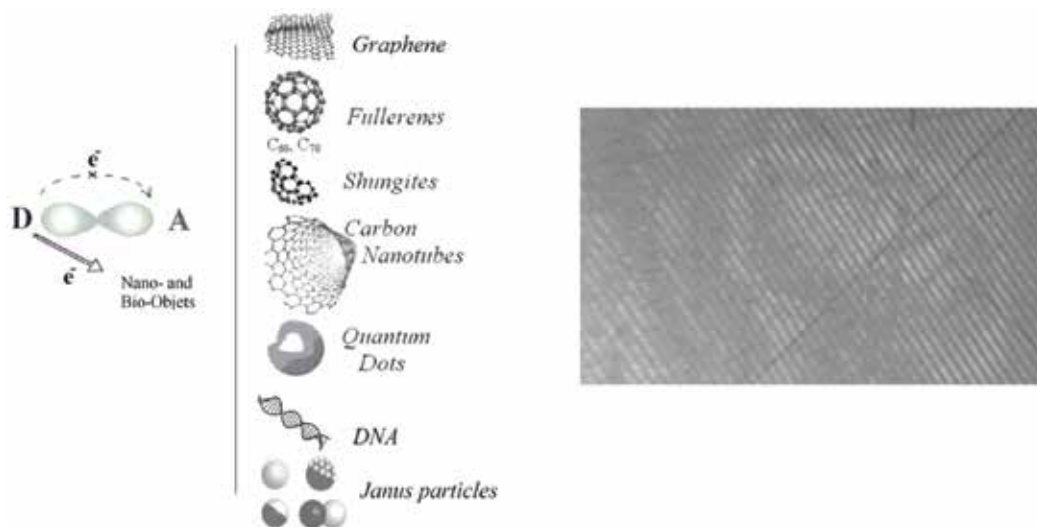


Figure 9. Model to explain the formation of the intermolecular charge transfer complex between an organic matrix donor and nano- or bio-objects as an effective acceptor (*left*) and the picture of the observed diffractive grating (*right*).

calculated via checking the charge carrier mobility. Moreover, the tendency of the change of the nano-doping to bio-doping one has been discussed because the bio-doped organics have shown the same refractive parameters change [37, 38]. The correlations indicated above can be used, on the one hand, for the basis of the predicted paths to extend the use of organic conjugated structured materials for the industrial and the biomedical applications, on the other hand, for the assessing of the ability of the competing influence of bio-objects, in comparison with nano-objects, due to nontoxicity and easy renewability from the World Ocean these biological structures.

3. Conclusion

Analyzing the obtained and discussed data, it should be concluded the followings:

1. Structuration of the inorganic material surfaces (based, e.g., on the ITO structures, MgF_2 and relative systems, Al, Cu, ZnS and Znse ones) has predicted the spectral, mechanical and wetting features change. The increase of the transparency, hardness, and wetting angle has been revealed.
2. Structuration of the inorganic material surfaces based on ITO has shown and supported the essential decrease of the resistivity. It can provoke the decrease of the applied voltage when these ITO coatings are considered as the transparent conducting layers in the spatial light modulators and in the related devices.

3. Structuration of the inorganic material surfaces based on ITO via CNTs-oriented laser deposition technique can provoke to form the possible quasi-graphene layers, which can easily explain the change of the ITO resistivity due to large charge from the core of the CNTs and their donor-acceptor properties.
4. Doping of the organic materials by studied nanoparticles has revealed the drastic change of the laser-induced refractive index that is larger than the ones obtained for the pure organic conjugated matrixes.
5. Calculated refractive parameters of the nanoparticles doped organics can be compared with the analogous refractive parameters obtained for the classical inorganic bulk crystals.
6. The laser-induced change of the refractive index of the nano-doped organics can be compared with the analogous refractive parameters obtained for the bio-doped organics materials based, for example, on the liquid crystal ones.
7. Applications of the materials, which body and interface can be modified with effective nanoparticles, can be extended essentially. The solar energy, gas storage systems, information technology, displays, and the biomedicine can accumulate the knowledge and the practical results.

Acknowledgements

The results have been obtained in the Department "Photophysics of media with nanoobjects" and have been partially supported by RFBR grant no.13-03-00044 (2013–2015) and project "Nanocoating-GOI" (2012–2015), as well as by international FP7 Program, Marie Curie Action, Project "BIOMOLEC" (2011-2015). Author wishes to thank their colleagues D.G. Kvashnin (Emanuel Institute of biochemical physics RAS, Institute of Science and Technology "MISiS") and P.B. Sorokin (Technological Institute for Superhard and Novel Carbon Materials, Institute of Science and Technology "MISiS") for the help with the molecular dynamics calculations. The author appreciates their colleagues from the department for "Photophysics of media with nanoobjects," Vavilov State Optical Institute and abroad too for the helpful discussion at the seminars and conferences.

Author details

Natalia Vladimirovna Kamanina

Address all correspondence to: nvkamanina@mail.ru

1 Vavilov State Optical Institute, St. Petersburg, Russia

2 St. Petersburg Electrotechnical University ("LETI"), St. Petersburg, Russia

References

- [1] Hosoda K., Tada R., Ishikawa M., Yoshino K.: Effect of C60 doping on electrical and optical properties of poly[[disilanylene]oligophenylenes]. *Jpn. J. Appl. Phys. Part 2.* 1997; 36(3B): L372–L375.
- [2] Brabec C.J., Padinger F., Sariciftci N.S., Hummelen J.C.: Photovoltaic properties of conjugated polymer/methanofullerene composites embedded in a polystyrene matrix. *J. Appl. Phys.* 1999; 85(9): 6866–6872.
- [3] Smalyukh I.I., Shiyanovskii S.V., Lavrentovich O.D.: Three dimensional imaging of orientation order by fluorescence confocal polarizing microscopy. *Chem. Phys. Lett.* 2001; 336: 88–96.
- [4] Poole Jr C.P. and Owens F.J. *Introduction to Nanotechnology.* Wiley Interscience, New York; 2003. 400 p.
- [5] Khoo I.C., Yana Zh.W., Lewis B., Mallouk T.: Photorefractive CdSe and gold nanowire-doped liquid crystals and polymer-dispersed-liquid-crystal photonic crystals. *Mol. Cryst. Liq. Cryst.* 2006; 446: 233–244.
- [6] Yu D., Park K., Durstock M., Dai L.: Fullerene-grafted graphene for efficient bulk heterojunction polymer photovoltaic devices. *J. Phys. Chem. Lett.* 2011; 2: 1113–1118.
- [7] Namila S., Chandra N., Shet C.: Mechanical behavior of functionalized nanotubes. *Chem. Phys. Lett.* 2004; 387: 247–252. doi:10.1016/j.cplett.2004.01.104
- [8] Fa W., Yang X., Chen J., Dong J.: Optical properties of the semiconductor carbon nanotube intramolecular junctions. *Phys. Lett.* 2004; A323: 122–131. www.elsevier.com/locate/pla
- [9] Taherpour A.A., Aghagolnezhad-Gerdroudbari A., Rafiei S.: Theoretical and quantitative structural relationship studies of reorganization energies of [SWCNT(5,5)-Armchair-C_nH₂₀] (n = 20–310) nanostructures by neural network CFFBP method. *Int. J. Electrochem. Sci.* 2012; 7: 2468–2486. www.electrochemsci.org
- [10] Yang Z.-P., Ci L., Bur J.A., Lin S.-Y., Ajayan P.M.: Experimental observation of an extremely dark material made by a low-density nanotube array. *Nano Letters.* 2008; 8(2): 446–451. Published on Web 01/09/2008. DOI: 10.1021/nl072369t
- [11] Kamanina N.V. and Vasilyev P.Y. Optical coatings based on CNTs for the optical devices and nanoelectronics. RU Patent 2 355 001 C2 with the priority on 09.01.2007; registered on the RF State inventory on 10.05.2009.
- [12] Kamanina N.V., Vasilyev P.Y., Studeonov V.I. Optical coating based on oriented in the electric field CNTs for the optical devices, micro- and nanoelectronics under the conditions when the interface: solid substrate-coating can be eliminated. RU Patent 2 405 177 C2 with the priority on 23.12.2008; registered on the State inventory on 27.11.2010.

- [13] Lowans B.S., Bates B., Greer R.G.H., Aiken J.: Binary phase modulation properties of a programmable liquid crystal television display. *Appl. Opt.* 1992; 31: 7393–7395.
- [14] Kamanina N.V. and Vasilenko N.A. Influence of operating conditions and of interface properties on dynamic characteristics of liquid-crystal spatial light modulators. *Opt. Quantum Electron.* 1997; 29(1): 1–9. doi:10.1023/A:1018506528934
- [15] Kamanina N.V. and Vasilenko N.A.: High-speed SLM with a photosensitive polymer layer. *Electron. Lett.* 1995; 31(5): 394–395. doi:10.1049/el:199502585
- [16] Lekshmy S.S. and Joy K.: Structural and optoelectronic properties of indium doped SnO₂ thin films deposited by sol gel technique. *J. Mater. Sci.: Mater. Electron.* 2014; 25: 1664–1672. doi:10.1007/s10854-014-1781
- [17] Xu J., Yang Z., Zhang X., Wang H., Xu H.: Structural, electrical, optical properties and reliability of ultrathin tin doped indium oxide films for touch panels. *J. Mater. Sci.: Mater. Electron.* 2014; 25: 1792–1797. doi:10.1007/s10854-014-1800
- [18] Dhinakar K.G., Selvalakshmi T., Sundar S.M., Bose A.C.: Structural, optical and impedance properties of SnO₂ nanoparticles. *J. Mater. Sci.: Mater. Electron.* 2016; 27(6): 5818–5824.
- [19] Zhang S., Tsonev D., Videv S., Ghosh S., Turnbull G.A., Samuel I.D.W., Haas H.: Organic solar cells as high-speed data detectors for visible light communication. *Optica.* 2015; 2(7): 607–610. doi:10.1364/OPTICA.2.000607
- [20] Joshi S., Krishnamurthy L., Shekar G.L.: Randomly oriented rectangular shaped structures of CuO on NiO/ITO surfaces. *Adv. Mater. Lett.* 2016; 7(9): 735–742. doi:10.5185/amlett.2016.6102
- [21] Kamanina N.V. and Vasilyev P.Y.: New method to improve the dynamic parameters of liquid crystals: Surface wave treatment of the interface between solid phase and mesophase. *J. Soc. Information Disp.* 2007; 15(12): 1099–1101.
- [22] Kamanina N.V., Vasilyev P.Y., Vangonen A.I., Studeonov V.I., Usanov Y.E., Kajzar F., Attias A.-J.: Photophysics of organic structures doped with nanoobjects: Optical limiting, switching and laser strength. *Mol. Cryst. Liq. Cryst.* 2008; 485: 197–206.
- [23] Tersoff J. Modeling solid-state chemistry: Interatomic potentials for multicomponent systems. *Phys. Rev. B* 1989; 39(8): 5566–5568. doi:10.1103/PhysRevB.39.5566
- [24] Plimpton S.: Fast parallel algorithms for short-range molecular dynamics. *J. Comput. Phys.* 1995; 117: 1–19.
- [25] Kamanina N.V., Vasilyev P.Y., Studeonov V.I.: Using nanotechnologies in optics: On the possibility of enhancing the transparency and increasing the mechanical surface strength of materials in the UV and IR regions. *J. Opt. Technol.* 2008; 75(12): 806–808.
- [26] Kamanina N.V., Bogdanov K.Yu., Vasilyev P.Y., Studeonov V.I.: Enhancing the mechanical surface strength of “soft” materials for the UV and IR ranges and increasing their transmission spectrum: Model MgF₂-nanotube system. *J. Opt. Technol.* 2010; 77(2): 145–147.

- [27] Benkabou F., Aourag H., Certier M.: Atomistic study of zinc-blende CdS, CdSe, ZnS, and ZnSe from molecular dynamics. *Mater. Chem. Phys.* 2000; 66(1): 10–16. doi:10.1016/S0254-0584(00)00239-X
- [28] Daw M.S. and Baskes M.I.: Semiempirical, quantum mechanical calculation of hydrogen embrittlement in metals. *Phys. Rev. Lett.* 1983; 50(17): 1285. doi:10.1103/PhysRevLett.50.1285
- [29] Mishin Y., Farkas D., Mehl M.J., Papaconstantopoulos D.A.: Interatomic potentials for monoatomic metals from experimental data and ab initio calculations. *Phys. Rev. B.* 1999; 59(5): 3393. doi:10.1103/PhysRevB.59.3393
- [30] Kamanina N.V.: Nonlinear optical study of fullerene-doped conjugated systems: new materials for nanophotonics applications. *Proceedings of the NATO Advanced Research Workshop on Organic Nanophotonics.* 2003; II/100: 177–192.
- [31] Kamanina N.V.: Fullerene-dispersed liquid crystal structure: dynamic characteristics and self-organization processes. *Physics-Uspokhi.* 2005; 48 (4): 419–427.
- [32] Kamanina N.V.: *Features of Optical Materials Modified with Effective Nanoobjects: Bulk Properties and Interface.* New York, Physics Research and Technology, “Novinka”, Published by Nova Science Publishers, Inc., New York, 2014. 116 p. ISBN: 978-1-62948-033-6
- [33] Mikhailova M.M., Kosyreva M.M., Kamanina N.V.: On the increase in the charge carrier mobility in fullerene-containing conjugated organic systems. *Tech. Phys. Lett.* 2002; 28 (6): 450–453.
- [34] Kamanina N.V., Emandi A., Kajzar F., Attias A.-J.: Laser-induced change in the refractive index in the systems based on nanostructured polyimide: Comparative study with other photosensitive structures. *Mol. Cryst. Liq. Cryst.* 2008; 486: 1–11.
- [35] Kamanina N.V. and Uskokovic D.P.: Refractive index of organic systems doped with nano-objects. *Mater. Manufacturing Processes.* 2008; 23: 552–556.
- [36] Kamanina N.V., Serov S.V., Shurpo N.A., Likhomanova S.V., Timonin D.N., Kuzhakov P.V., Rozhkova N.N., Kityk I.V., Plucinski K.J., Uskokovic D.P.: Polyimide-fullerene nanostructured materials for nonlinear optics and solar energy applications. *J. Mater. Sci.: Mater. Electron.* 2012; 23(8): 1538–1542. doi:10.1007/s10854-012-0625-9
- [37] Kamanina N.V., Serov S.V., Bretonniere Y., Chantal A.: Organic systems and their photorefractive properties under the nano- and biostructuration: Scientific view and sustainable development”. *J. Nanomater.* 2015; 5 pages. Hindawi Publishing Corporation, Article ID 278902. doi:10.1155/2015/278902
- [38] Kamanina N.V., Serov S.V., Zubtsova Y.A., Bretonniere Y., Andraud C., Baldeck P., Kajzar F.: Photorefractive properties of some nano- and bio-structured organic materials. *J. Nanotechnol. Diagn. Treat.* 2014; 2(1): 2–5. <http://savvysciencepublisher.com/downloads/jndtv2n1a1/>

Edited by Alexander Vakhrushev

In recent years, nanotechnology is the basis for the development of modern production. This determined the urgency of the intensive development of the new direction of mechanics and nanomechanics, for the scientific description of nanotechnological processes and the solution of several topical nanotechnology problems. Topics included in the book cover a wide range of research in the field of nanomechanics: thermomass theory of nanosystems; deformation of nanomaterials; interface mechanics of assembly carbon nanotube; nanomechanics on surface; molecular interactions and transformations; nanomechanical sensors, nanobeams, and micromembranes; nanostructural organic and inorganic materials; green synthesis of metallic nanoparticles. The main goal of these works is the establishment of the nanosystem macroparameter dependence on its nanoparameters using nanomechanics. This book will be useful for engineers, technologists, and researchers interested in methods of nanomechanics and in advanced nanomaterials with complex behavior and their applications.

Photo by ktsimage / iStock

IntechOpen

